

**IMPERIAL COLLEGE OF SCIENCE, TECHNOLOGY AND MEDICINE**

UNIVERSITY OF LONDON

**LAMB WAVE INSPECTION OF LARGE STRUCTURES  
USING PERMANENTLY ATTACHED TRANSDUCERS**

by

**Paul David Wilcox**

A thesis submitted to the University of London for the degree of

**Doctor of Philosophy**

Department of Mechanical Engineering

Imperial College of Science, Technology and Medicine

London SW7 2BX

**March 1998**

## Abstract

---

This thesis investigates some aspects of the fundamental science necessary for the development of an integral structural inspection system based on the use of ultrasonic Lamb waves. It is particularly concerned with the long range propagation of Lamb wave modes, the selection of suitable modes and the design of permanently attached transducers.

An analytical investigation into the effect of plate curvature on Lamb wave propagation is presented, since this is highly relevant to the inspection of structures such as pipes and pressure vessels. It is shown that when the radius of plate curvature to plate thickness ratio is greater than approximately 10:1, the effect of curvature on the propagation of lower order Lamb wave modes is negligible. Quantitative studies into the effects of dispersion on the long range propagation of Lamb waves are presented. It is demonstrated that at any point on any dispersion curve, there is an optimum number of cycles required in an input signal to maximise the spatial resolution obtainable over a particular propagation distance.

The design of inter-digital transducers (IDTs) made from the piezoelectric polymer PVDF for the transmission and reception of Lamb waves is investigated. A one-dimensional transducer model is used to investigate the frequency response of PVDF bulk wave transducers. Results from this model are used to develop various types of PVDF IDTs which work over a frequency range from 65 kHz to 2.5 MHz. These transducers are shown to be able to propagate Lamb waves over several metres in structures between 1 and 13 mm thick.

A model based on Huygens' principle of superposition is developed for predicting the acoustic field from an IDT. This model has been shown to be of equal accuracy to an existing finite element model and several orders of magnitude faster. The model has also been successfully validated against experimental data and used to elucidate guidelines for the design of two common configurations of IDT.

## Acknowledgements

---

I would like to sincerely thank my supervisors, Prof. Peter Cawley and Dr. Mike Lowe, who have provided invaluable guidance, technical knowledge and grammatical superiority throughout this project. Excellent advice was also given by Prof. Bert Auld during his two visits to Imperial College.

Welcome input, in various forms, has been provided by the members of the non-destructive testing group at Imperial College. They are, in approximately the order of appearance, David Alleyne, Andrew Chan, Bruce Drinkwater, Michel Castaings, Mark Evans, Richard Monkhouse, Keith Vine, Brent Zeller, Brian Pavlakovic, Rob Long, Roger Dalton, Pierre Marty, Arnaud Bernard and Christophe Aristégui.

The project was funded under the Postgraduate Training Partnership Award (PTP) scheme by the Water Research Centre (WRc) and the Engineering and Physical Sciences Research Council (EPSRC).

The acknowledgements would be incomplete without personal thanks to my father and sister, various flatmates (Nick, Milla, Jonathan, Jim, Mark and Jackie) and of course to Kathryn.

# Contents

---

List of figures.....	8
List of tables.....	17
<b>1. Introduction.....</b>	<b>18</b>
1.1 BACKGROUND.....	18
1.2 LAMB WAVES, TRANSDUCERS AND SMART STRUCTURES.....	18
1.2.1 <i>Conventional ultrasonic inspection</i>	
1.2.2 <i>Lamb wave inspection and applications</i>	
1.2.3 <i>Permanently attached transducers and smart structures</i>	
1.2.4 <i>Towards an integrated structural inspection system</i>	
1.3 OVERVIEW OF THESIS.....	20
<b>2. Lamb wave theory .....</b>	<b>23</b>
2.1 INTRODUCTION.....	23
2.2 BACKGROUND.....	23
2.2.1 <i>Wave propagation in isotropic elastic media</i>	
2.2.2 <i>Waves in a free flat plate</i>	
2.3 EFFECT OF CURVATURE ON LAMB WAVE PROPAGATION.....	30
2.3.1 <i>Introduction</i>	
2.3.2 <i>Theoretical analysis</i>	
2.3.3 <i>Dispersion curves for waves propagating in curved plates</i>	
2.3.4 <i>Conclusions</i>	
2.4 EFFECT OF DISPERSION ON LAMB WAVE PROPAGATION.....	36
2.4.1 <i>Introduction</i>	
2.4.2 <i>Dispersivity</i>	
2.4.3 <i>Resolvable distance</i>	
2.4.4 <i>Optimum number of cycles in input signal</i>	
2.4.5 <i>Conclusions</i>	
2.5 CONCLUSIONS.....	44
<b>3. Development and validation of one-dimensional transducer model.....</b>	<b>61</b>
3.1 INTRODUCTION.....	61
3.2 DEVELOPMENT OF ONE-DIMENSIONAL TRANSDUCER MODEL.....	62
3.2.1 <i>Modelling the different elements in the transducer system</i>	
3.2.2 <i>Assembly of the model components to perform specific calculations</i>	
3.2.3 <i>Inclusion of losses in the model</i>	
3.2.4 <i>Software implementation of model</i>	

3.3	VALIDATION OF ONE-DIMENSIONAL MODEL USING PVDF TRANSDUCERS .....	72
3.3.1	<i>PVDF as a transducer material</i>	
3.3.2	<i>Experimental methods</i>	
3.3.3	<i>Results</i>	
3.4	PARAMETRIC STUDIES MADE USING ONE-DIMENSIONAL MODEL .....	75
3.4.1	<i>Effect of parametric perturbations</i>	
3.4.2	<i>General parametric studies</i>	
3.5	CONCLUSIONS .....	77
4.	<b>High frequency PVDF inter-digital transducers.....</b>	<b>89</b>
4.1	INTRODUCTION .....	89
4.2	BACKGROUND .....	89
4.2.1	<i>Requirements for the transmission and reception of Lamb waves</i>	
4.2.2	<i>Transducers to transmit and receive Lamb waves</i>	
4.3	PVDF INTER-DIGITAL TRANSDUCER DESIGN AND CONSTRUCTION .....	93
4.3.1	<i>Construction of PVDF inter-digital transducers</i>	
4.3.2	<i>Frequency response</i>	
4.3.3	<i>Wavelength selectivity</i>	
4.4	TRANSMISSION AND RECEPTION OF FUNDAMENTAL ANTI-SYMMETRIC MODE IN THIN PLATES.....	98
4.4.1	<i>Introduction</i>	
4.4.2	<i>Transmission and reception of <math>A_0</math> mode in 1.2 mm thick aluminium plate</i>	
4.4.3	<i>Transmission and reception of <math>A_0</math> mode in 1.2 mm thick steel plate with artificial defect</i>	
4.4.4	<i>Conclusions</i>	
4.5	TRANSMISSION AND RECEPTION OF HIGHER ORDER MODES IN THICKER PLATES.....	102
4.5.1	<i>Introduction</i>	
4.5.2	<i>Transmission and reception of <math>A_2</math> mode in ductile iron pipe with 6.5 mm thick walls</i>	
4.5.3	<i>Transmission and reception of <math>S_4</math> mode in ductile iron pipe with 6.5 mm thick walls</i>	
4.5.4	<i>Conclusions</i>	
4.6	CONCLUSIONS .....	106
5.	<b>Use of Huygens' principle to predict acoustic fields generated by inter-digital transducers .....</b>	<b>127</b>
5.1	INTRODUCTION .....	127
5.1.1	<i>Strategies for IDT modelling</i>	
5.2	THEORY.....	129
5.2.1	<i>Calculation of displacements resulting from continuous excitation of a plate at a point</i>	

5.2.2	<i>Use of model to predict acoustic fields due to inputs of finite duration</i>	
5.2.3	<i>Calculation of acoustic field due to multiple sources</i>	
5.2.4	<i>Application of Huygens' principle to IDTs generating Lamb waves</i>	
5.3	SOFTWARE IMPLEMENTATION .....	140
5.3.1	<i>Program for calculating acoustic field due to a point source</i>	
5.3.2	<i>Program for performing Huygens' superposition</i>	
5.4	VALIDATION.....	142
5.4.1	<i>Validation of displacements resulting from point excitation of a plate</i>	
5.4.2	<i>Validation of displacement field associated with an IDT</i>	
5.5	CONCLUSIONS .....	144
6.	<b>Low frequency inter-digital transducers .....</b>	<b>165</b>
6.1	INTRODUCTION .....	165
6.2	DESIGN AND TESTING OF LOW FREQUENCY INTER-DIGITAL TRANSDUCERS .....	165
6.2.1	<i>Initial considerations using one-dimensional model</i>	
6.2.2	<i>Initial experimental tests using bulk wave transducers</i>	
6.2.3	<i>Initial experimental tests using inter-digital transducers</i>	
6.2.4	<i>Example of a four phase IDT</i>	
6.3	IMPROVED EXPERIMENTAL METHODS FOR MEASURING THE ACOUSTIC FIELD FROM INTER-DIGITAL TRANSDUCERS.....	173
6.3.1	<i>Methods which correct for coupling inconsistencies</i>	
6.4	FURTHER USE OF HUYGENS' MODEL FOR INTER-DIGITAL TRANSDUCER DESIGN.....	177
6.4.1	<i>Design of straight-finger inter-digital transducers</i>	
6.4.2	<i>Design of curved-finger inter-digital transducers</i>	
6.5	CONCLUSIONS .....	181
7.	<b>Conclusions and future work .....</b>	<b>205</b>
7.1	REVIEW OF THESIS.....	205
7.2	SUMMARY OF FINDINGS .....	206
7.2.1	<i>Effect of curvature on Lamb wave propagation</i>	
7.2.2	<i>Effect of dispersion on Lamb wave propagation</i>	
7.2.3	<i>Inter-digital transducers</i>	
7.2.4	<i>Inspection of thick plate-like structures</i>	
7.2.5	<i>Huygens' modelling of the field from inter-digital transducers</i>	
7.3	FUTURE WORK .....	207
7.3.1	<i>Effect of curvature on Lamb wave propagation</i>	
7.3.2	<i>Inter-digital transducers</i>	
7.3.3	<i>Huygens' modelling of inter-digital transducers</i>	

**References.....209**

**Appendix A: Equations for wave propagation in a curved plate.....217**

**Appendix B: Bandwidths of Hanning windowed tonebursts.....220**

**Appendix C: Publications list.....223**

## List of figures

---

Figure 2.1	Diagram of flat isotropic plate, showing orientation of axes, wave propagation direction and wavefronts. ....	45
Figure 2.2	Examples of Lamb wave mode shapes in aluminium, showing, on the left, the variation of in-plane ( $u_x$ ), out-of-plane ( $u_z$ ) particle displacements and strain energy density (SED) through the plate thickness. The diagrams on the right show the deformation of the plate for each case. The modes and dimensionless frequencies are (a) $A_0$ at 0.44, (b) $S_0$ at 0.05, (c) $S_0$ at 0.80 and (d) $S_4$ at 4.17. ....	46
Figure 2.3	Phase velocity dispersion curves for aluminium (continuous lines) and steel (dashed lines) on dimensionless axes.....	47
Figure 2.4	Group velocity dispersion curves for aluminium (continuous lines) and steel (dashed lines) on dimensionless axes.....	48
Figure 2.5	Schematic diagram showing nomenclature for wave propagation in curved plates.....	49
Figure 2.6	Phase velocity dispersion curves for aluminium on dimensionless axes for radius:thickness ratios of (a) 10:1, (b) 5:1, (c) 2:1 and (d) 1:1. The dispersion curves for a flat plate of the same thickness are indicated by the dotted lines.....	50
Figure 2.7	Group velocity dispersion curves for aluminium on dimensionless axes for radius:thickness ratios of (a) 10:1, (b) 5:1, (c) 2:1 and (d) 1:1. The dispersion curves for a flat plate of the same thickness are indicated by the dotted lines.....	51
Figure 2.8	Example of low dispersion. (a) Distance-time plot showing propagation of $A_0$ mode Lamb waves at 1.343 MHz mm. (b), (c) and (d) show time-traces that would be received at distances of 0, 50 and 100 mm from the source.....	52
Figure 2.9	Example of high dispersion. (a) Distance-time plot showing propagation of $S_0$ mode Lamb waves at 2.000 MHz mm. (b), (c) and (d) show time-traces that would be received at distances of 0, 50 and 100 mm from the source.....	52
Figure 2.10	Predicted time-traces showing (a) two 20 cycle tonebursts completely separated in time. The effect of reducing the separation is shown in (b), (c) and (d). (e) shows the effect of reducing the number of cycles to 5 while maintaining the separation shown in (d). ....	53

Figure 2.11	Group velocity dispersion curves for aluminium with stationary points marked by the white circles. ....	54
Figure 2.12	Dispersivity curves for aluminium using input signals with (a) 10, (b) 20 and (c) 50 cycles. ....	55
Figure 2.13	(a) Phase and (b) group velocity dispersion curves for aluminium plotted on dimensionless logarithmic axes. ....	56
Figure 2.14	Dispersivity curves for aluminium using input signals with durations of (a) 10, (b) 20 and (c) $50 d/v_t$ , where $d$ is the plate thickness and $v_t$ is the bulk transverse wave velocity.....	57
Figure 2.15	Resolvable distance vs. cycles in input toneburst for the $S_1$ mode in aluminium at 4.03 MHz mm (its maximum group velocity), for various propagation distances. The dotted line marks the location of the minima in resolvable distance as the propagation distance is varied.....	58
Figure 2.16	Minimum resolvable distance curves for aluminium at propagation distances of (a) 100, (b) 500 and (c) 1000 $d$ , where $d$ is the plate thickness.....	59
Figure 2.17	Optimum number of cycles in input signal for aluminium at propagation distances of (a) 100, (b) 500 and (c) 1000 $d$ , where $d$ is the plate thickness. ....	60
Figure 3.1	(a) Physical transducer configuration and (b) representation as an electrical network. ....	81
Figure 3.2	(a) Piezoelectric layer and (b) representation of the piezoelectric layer as a three port network. ....	81
Figure 3.3	Representation of a non-piezoelectric layer as a two port network.....	82
Figure 3.4	(a) Reduction of two port network and impedance to (b) a single impedance.....	82
Figure 3.5	Model used to predict acoustic response. $Z_A$ is the apparent impedance looking into the semi-infinite medium, A.....	82
Figure 3.6	Model of the complete system, including the output impedance of the pulser. ....	82
Figure 3.7	(a) The network used in the transmit case and (b) the corresponding network ignoring the time delay in medium A.....	83
Figure 3.8	(a) The network used in the receive case using a Thévenin driving circuit, (b) using a Norton diving circuit and (c) ignoring the time delay in medium A. ....	83

Figure 3.9	Experimental set-up for measuring the pulse-echo response of PVDF transducers bonded to solid substrates. ....	84
Figure 3.10	Comparison of experimentally measured and predicted input impedance of PVDF film in air. ....	84
Figure 3.11	(a) Experimentally measured and (b) predicted pulse-echo time-traces for the case of an air-PVDF-perspex transducer configuration. ....	85
Figure 3.12	(a) Experimentally measured and (b) predicted pulse-echo time-traces for the case of an air-PVDF-aluminium transducer configuration. ....	85
Figure 3.13	(a) Experimentally measured and (b) predicted pulse-echo time-traces for the case of a water-PVDF-aluminium transducer configuration. ....	86
Figure 3.14	(a) Experimentally measured and (b) predicted pulse-echo time-traces for the case of a water-PVDF-aluminium transducer configuration with a thicker (75 $\mu\text{m}$ ) bond layer between the PVDF and the aluminium. ....	86
Figure 3.15	Example predicted pulse-echo response vs. frequency graph, showing the effect of perturbing an input parameter (in this case the thickness of the PVDF layer) by $\pm 10\%$ . ....	87
Figure 3.16	Effect of varying the acoustic impedance of the material under interrogation on predicted pulse-echo response. ....	87
Figure 3.17	Effect of varying the acoustic impedance of the backing material on predicted pulse-echo response. ....	88
Figure 3.18	Effect of varying the bond layer thickness on predicted pulse-echo response. ....	88
Figure 4.1	Example predictions of time-traces that would be measured 100 mm away from a source on a 1 mm thick aluminium plate, if (a) the source was a broadband pulse (b) the source was a 20 cycle toneburst and (c) the source was a 20 cycle toneburst and only excited a single mode, in this case $A_1$ . ....	108
Figure 4.2	Excitation of Lamb waves by (a) immersion coupling and (b) variable angle wedge transducer. ....	108
Figure 4.3	(a) Excitation of Lamb waves by electromagnetic acoustic transducer. (b) A surface acoustic wave device generating Rayleigh waves in a piezoelectric substrate (after Kino 1987). ....	109
Figure 4.4	Schematic cross section, showing the construction of a high frequency PVDF IDT (a) before and (b) after assembly. ....	110

Figure 4.5	(a) Example electrode pattern for a single phase IDT and (b) the associated distribution of surface tractions. (c) Example electrode pattern for a two phase IDT and (d) the associated distribution of surface tractions.....	110
Figure 4.6	Experimental set-up to investigate effect of backing layer thickness on bulk wave transducer response.....	111
Figure 4.7	(a) Experimentally measured and (b) predicted effect of increasing the thickness of backing layer on acoustic response of the PVDF bulk wave transducer system shown in figure 4.6.....	112
Figure 4.8	(a) Cross section through an IDT and plate and (b) the idealised distribution of surface tractions associated with the IDT. (c) Shows the wavenumber spectrum of the IDT.....	113
Figure 4.9	Example dispersion curves showing operating lines and regions associated with both an IDT and a toneburst. ....	113
Figure 4.10	DLV plot for aluminium plate. The inset graphs indicate the temporal and spatial bandwidths on the main graph which are associated with different lengths of toneburst and different lengths of IDT respectively.....	114
Figure 4.11	(a) Phase and (b) group velocity dispersion curves for 1.2 mm thick aluminium plate, showing the operating line of a 2.4 mm wavelength IDT.....	115
Figure 4.12	Geometry of 2.4 mm wavelength IDT. ....	116
Figure 4.13	Experimental set-up of 2.4 mm wavelength IDTs operating in pitch-catch mode on 1.2 mm thick aluminium plate.....	116
Figure 4.14	Received time-traces from experiment shown in figure 4.13. The complete received signal when using a 20 cycle toneburst at 1.02 MHz is shown in (a). The effects of using 5, 10, 20 and 50 cycles are shown in (b), (c), (d) and (e) respectively. The complete time-trace obtained using a 20 cycle toneburst at 2.51 MHz is shown in (f). ....	117
Figure 4.15	<i>F-scan</i> plot of the received signals from the experiment shown in figure 4.13. The analytically predicted group velocity dispersion curves are also superimposed after being mapped into group delay space and scaled appropriately.....	118
Figure 4.16	(a) Phase and (b) group velocity dispersion curves for 1.2 mm thick steel plate, showing the operating line of a 2.4 mm wavelength IDT. ....	119

Figure 4.17	Experimental set-up of 2.4 mm wavelength IDTs operating in pitch-catch mode on 1.2 mm thick steel plate with an artificial defect. ....	120
Figure 4.18	Received time-traces from experiment shown in figure 4.17. The complete received signal when using a 20 cycle toneburst at 1.04 MHz is shown in (a). The effects of using 5, 10, 20 and 50 cycles are shown in (b), (c), (d) and (e) respectively . The complete time-trace obtained using 20 cycles at 2.58 MHz is shown in (f). ....	121
Figure 4.19	(a) Phase and (b) group velocity dispersion curves for 6.5 mm thick ductile iron plate, showing the operating lines of a 6.0 mm and 2.7 mm wavelength IDTs. ....	122
Figure 4.20	Geometry of 6.0 mm wavelength IDT. ....	123
Figure 4.21	Experimental set-up of 6.0 mm wavelength IDTs operating in pitch-catch mode around circumference of ductile iron pipe. The details of the electrical connections to the IDTs are omitted for clarity.....	123
Figure 4.22	Received time-traces from experiment shown in figure 4.21. (a) is the complete received signal when the excitation was a 20 cycle toneburst at 1.05 MHz. The effects of using 5, 10, 20 and 50 cycles are shown in (b), (c), (d) and (e) respectively. ....	124
Figure 4.23	Geometry of 2.7 mm wavelength IDT. ....	125
Figure 4.24	Experimental set-up of 2.7 mm wavelength IDTs operating in pitch-catch mode around circumference of ductile iron pipe. The details of the electrical connections to the IDTs are omitted for clarity.....	125
Figure 4.25	Received time-traces from experiment shown in figure 4.24. (a) is the complete received signal when the excitation was a 20 cycle toneburst at 2.7 MHz. The effects of using 5, 10, 20 and 50 cycles are shown in (b), (c), (d) and (e) respectively. ....	126
Figure 5.1	(a) Excitability of straight crested Lamb wave modes in aluminium plate when the excitation is by an infinitely long line source. In (b) the attenuation curves for the same plate immersed in water are shown for comparison. ....	146
Figure 5.2	Excitability of circular crested Lamb wave modes in aluminium plate when the excitation is by a point source.....	147
Figure 5.3	An example displacement-distance curve for the case of an aluminium plate being excited at a dimensionless frequency of 0.4287, by a harmonic force of dimensionless amplitude 1.0.....	147

Figure 5.4	An example displacement-distance-time plot for the case of an aluminium plate being excited at a dimensionless frequency of 0.4287, by a harmonic force of dimensionless amplitude 1.0.....	148
Figure 5.5	An example displacement-distance curve for the case of an aluminium plate 14 $\mu$ s after excitation by a 10 cycle, Hanning windowed toneburst at a dimensionless centre frequency of 0.4287 and a dimensionless peak amplitude 1.0. ....	149
Figure 5.6	Representation of a small area of an IDT by a point source.....	149
Figure 5.7	Geometry of single finger of an IDT being modelled with varying numbers of sources across its width.....	150
Figure 5.8	Effect of using (a) 2, (b) 4, (c) 6, (d) 8 and (e) 10 sources per wavelength across the width of a finger of an IDT in Huygens' model.....	151
Figure 5.9	Angular sections at a distance of 100 $\lambda$ through the acoustic fields in figure 5.9. ....	152
Figure 5.10	Geometry of single finger of an IDT being modelled with varying numbers of sources along its length. ....	153
Figure 5.11	Effect of using (a) 1, (b) 2, (c) 3, (d) 4 and (e) 10 sources per wavelength along the length of a finger of an IDT in Huygens' model.....	154
Figure 5.12	Angular sections at a distance of 100 $\lambda$ through the acoustic fields in figure 5.11. ....	155
Figure 5.13	Screen shot of the input screen for the software written to calculate displacement-distance-time matrices. ....	156
Figure 5.14	Screen shot of the output screen for the software written to calculate displacement-distance-time matrices. ....	157
Figure 5.15	Screen shot of the software written to perform the Huygens' calculations.....	158
Figure 5.16	Geometry of the FE model used to validate analytic predictions of the acoustic field due to a point source. ....	159
Figure 5.17	Out-of-plane surface displacement vs. distance for a 1.0 mm thick steel plate 15 $\mu$ s after excitation with a 10 cycle toneburst at 1.0 MHz predicted by (a) analytic and (b) FE model.....	160

Figure 5.18	Out-of-plane surface displacement vs. distance for a 1.0 mm thick steel plate 10 $\mu$ s after excitation with a 10 cycle toneburst at 2.5 MHz predicted by (a) analytic and (b) FE models. (c) Shows the results from analytic model, but ignoring modes with phase velocities exceeding 10 mm/ $\mu$ s. ....	160
Figure 5.19	Experimental set-up for measuring displacement-time curves. ....	161
Figure 5.20	Schematic diagram showing the construction of conical point contact transducers used for making surface displacement measurements, after Evans (1997). ....	161
Figure 5.21	Time-traces (a) predicted using the analytic model and (b) measured experimentally when a 5 mm thick aluminium plate was excited with a 5 cycle toneburst at 0.2 MHz, 250 mm away from the monitoring point. ....	162
Figure 5.22	Time-traces (a) predicted using the analytic model and (b) measured experimentally when a 5 mm thick aluminium plate was excited with a 5 cycle toneburst at 0.5 MHz, 250 mm away from the monitoring point. ....	162
Figure 5.23	Geometry of transducer used in validation, and experimental set-up. ....	163
Figure 5.24	(a) Acoustic field predicted by the Huygens' model. Comparison of field cross sections at (b) 50 mm, (c) 100 mm and (d) 150 mm between Huygens' model, experimental point measurements and FE model. ....	164
Figure 6.1	Predicted pulse-echo response of a single 1.1 mm thick active PVDF layer and a 0.1 mm thick layer of active PVDF sandwiched between two layers of 0.5 mm thick passive PVDF. Both systems are backed by 1.25 mm thick copper and mounted on an aluminium substrate. No bond layers are included in the model. ....	183
Figure 6.2	Predicted pulse-echo response of a 0.1 mm thick PVDF layer and a 0.1 mm thick PVDF layer sandwiched between two 0.5 mm thick passive layers of PVDF. In both cases, the systems are backed by 1.25 mm thick copper layers and bonded to aluminium substrates. ....	184
Figure 6.3	Typical measured pulse-echo response of a monolithic bulk wave transducer, in this case showing a device with passive layers, with and without lead backing. ....	184
Figure 6.4	Construction of first low frequency IDTs. The fingers are (a) cut from PVDF sheet and configured as shown in (b). The layered assembly of the IDT is shown in (c), in this case for a passive layers design. ....	185

Figure 6.5	Experimental set-up for testing low frequency IDTs. ....	185
Figure 6.6	Received time-traces obtained from T <sub>1</sub> (passive layer device). The time-trace shown in (a) is with both sets of fingers connected, and the time-traces in (b) and (c) show the effect of connecting each set individually.....	186
Figure 6.7	Received time-traces obtained from T <sub>2</sub> (single layer device). The time-trace shown in (a) is with both sets of fingers connected, and the time-traces in (b) and (c) show the effect of connecting each set individually.....	187
Figure 6.8	Geometry of a four phase IDT designed to produce a uni-directional divergent beam over a 90° sector. ....	188
Figure 6.9	(a) Predicted acoustic field from the four phase IDT shown in figure 6.8 and (b) angular cross section along the dotted line in (a). The experimentally measured values are also plotted in (b). ....	189
Figure 6.10	Construction of four phase IDT showing (a) the electrode shapes and polarity and (b) the electrical connections. The experimental set-up for measuring the acoustic field from the IDT is shown in (c). ....	190
Figure 6.11	Time-traces measured at the locations (a) P, (b) Q and (c) R from the IDT in figure 6.10 when the IDT was driven at 91 kHz.....	191
Figure 6.12	Time-traces measured at the locations (a) P, (b) Q and (c) R from the IDT in figure 6.10 when the IDT was driven at 65 kHz.....	192
Figure 6.13	Phase velocity dispersion curves for 5 mm thick aluminium plate (Al) and 5 mm thick aluminium plate (Al) in perfect ‘welded’ contact with 1.3 mm thick lead plate (Pb).....	193
Figure 6.14	<b>Technique 2</b> for measuring the acoustic field from an IDT, using two conical transducers and the IDT as the transmitter. ....	193
Figure 6.15	<b>Technique 3</b> for measuring the acoustic field from an IDT, using two conical transducers and the IDT as a receiver. ....	194
Figure 6.16	Geometry of experimental set-up to measure the acoustic field around a point source by various methods. ....	194
Figure 6.17	Three sets of angular cross section measurements through the acoustic field from a point source before being corrected for coupling inconsistencies.....	195
Figure 6.18	The three sets of angular cross section measurements from figure 6.17 after being corrected for coupling inconsistencies by <b>technique 3</b> . ....	195

Figure 6.19	Measured cross sections through the acoustic fields from single straight fingers of lengths 2, 5 and 10 wavelengths. Predicted cross sections from Huygens' model are also shown. The diamonds on the cross sections indicate the minima on either side of the main lobe of the beam. ....	196
Figure 6.20	Predicted beam divergence angle as a function of finger length for a single straight finger. The function for the beam divergence of a bulk wave transducer with diameter equal to the finger length is indicated by the dashed line. An improved curve fitted to the predicted beam divergences is also plotted. ....	197
Figure 6.21	Predicted beam cross sections though the acoustic field from a straight finger IDT, 10 wavelengths wide, and with 1, 5 and 10 fingers. In (a) the relative amplitudes of the three fields are correct, but in (b) the amplitude of each cross section has been normalised by the number of fingers. ....	198
Figure 6.22	Nomenclature used to describe a curved finger IDT. ....	199
Figure 6.23	Predicted angular cross sections through the acoustic field from an IDT with a single curved finger of angle $90^\circ$ as the radius of the finger is increased from (a) 1, (b) 2, (c) 3, (d) 4, (e) 5 and (f) 10 wavelengths. Cross sections through the ideal fields are shown with lighter lines and where applicable, experimental measurements are shown by black circles. ....	200
Figure 6.24	Predicted angular cross sections through the acoustic field from an IDT with a single curved finger of radius 5 wavelengths as the angle of the finger is increased from (a) $15^\circ$ , (b) $30^\circ$ , (c) $45^\circ$ , (d) $60^\circ$ , (e) $75^\circ$ and (f) $90^\circ$ . Cross sections through the ideal fields are shown with lighter lines and where applicable, experimental measurements are shown by black circles. ....	201
Figure 6.25	Schematic diagram illustrating the discrepancy between the actual and ideal angular beam profiles from a curved finger IDT. ....	202
Figure 6.26	Predicted beam quality of a single curved finger IDT as a function of radius of finger for various angles of finger. The critical radius is indicated by circles in the inset graph of the low radius region. ....	203
Figure 6.27	Critical radius of a single curved finger. ....	204
Figure 6.28	Radius and angle combinations required to produce particular beam qualities for an IDT with a single curved finger. The critical radius is also plotted. ....	204

## List of tables

---

Table 3.1	Material properties of PVDF from Amp Inc. published data.....	79
Table 3.2	Material properties used in one-dimensional model. ....	79
Table 3.3	Pulse-echo tests performed.....	80
Table 3.4	The effect of parametric perturbations on the location of the resonant peaks in the one-dimensional transducer model. ....	80
Table 3.5	Summary of parametric perturbations on one-dimensional model. ....	80

# 1. Introduction

---

## 1.1 BACKGROUND

In the hypothetical ‘smart material’ of the future, it is anticipated (Clark 1998) that monitoring, data processing and actuation will all take place at a microscopic or even molecular level. Unfortunately, other than in nature, genuinely smart materials are still a long way from being engineered. However, there are many existing situations in which some form of continuous structural monitoring and assessment would be desirable, even if this is not achieved at a microscopic level. This leads to the concept of integrated structural inspection systems and the somewhat misleading notion of ‘smart structures’. Potential candidates for integrated structural inspection systems include pressure vessels, storage tanks, airframes, pipelines and so forth.

By using ultrasonic Lamb waves a large area of a structure can be monitored by transducers at only one or two fixed locations. If these transducers are permanently attached or even integrated into the structure, then with the appropriate telemetry and information processing, continuous monitoring of the structure becomes feasible. This type of monitoring is particularly well suited to detecting and locating defects, such as corrosion pitting or fatigue cracks.

The Lamb wave inspection of large structures is a relatively new field and there is still much work to be done before a practical integrated structural inspection system can be developed. This thesis examines some of the fundamental issues and aims to provide a foundation for future work in this area. Experimental results and theoretical models which address various aspects of the topic are presented, and where appropriate, conclusions are drawn. In particular, the selection of Lamb wave modes for testing, and the construction and modelling of inter-digital transducers are investigated.

In section 1.2 below, a general review of the subject area is given in order to provide a context for the work described in the rest of the thesis. For readability, this section does not include detailed literature reviews which may be found at the appropriate points in the relevant chapters. An overview of this thesis is given in section 1.3.

## 1.2 LAMB WAVES, TRANSDUCERS AND SMART STRUCTURES

### 1.2.1 *Conventional ultrasonic inspection*

The use of bulk stress waves at sonic and ultrasonic frequencies in many non-destructive and non-invasive inspection applications is a well documented subject (see for example the text by Szilard 1980). This type of ultrasonic inspection will be referred to as conventional ultrasonic inspection to distinguish it from ultrasonic inspection using Lamb waves and other guided waves. In most conventional ultrasonic inspection some form of transducer is used to transmit a pulse of ultrasonic energy into a structure. After this, two modes of operation are possible: either the same transducer can be used to listen for reflected echoes of the original signal (pulse-echo mode) or a second transducer can be

used at a separate location to detect the arrival of the original signal (pitch-catch mode). In pulse-echo mode, internal defects in the structure can be detected and located by the existence and arrival time of echoes. Single sided thickness measurement is also possible by the same principle. In pitch-catch mode, the velocity of sound and attenuation within the structure can be calculated, and these can be used to infer the condition of the material. In both modes of operation, only the area of the structure immediately below the transmitting transducer is inspected at any one time. Although, such testing methods allow very accurate and reliable inspection, the time and effort needed to inspect an entire structure can be considerable.

### *1.2.2 Lamb wave inspection and applications*

Lamb waves are guided acoustic waves which propagate in the plane of a plate and, like bulk acoustic waves, their interaction with defects means that they can be used for inspection purposes. Because they propagate in the plane of a plate, a reasonably large area of a suitable structure can potentially be inspected from a single location although with some reduction in resolution and sensitivity compared to the conventional single point ultrasonic inspection described above.

In unbounded isotropic solids longitudinal and transverse modes of acoustic wave propagation are possible and these are generally non-dispersive. However, in the case of Lamb waves an infinite number of modes can exist, all of which are dispersive, hence the use of Lamb waves for inspection purposes is, in general, not as straightforward as the use of bulk waves.

Although Lamb produced his famous dispersion equations for acoustic wave propagation in plates in 1917, it was not until Worlton (1961) provided 'experimental confirmation of Lamb waves at megacycle frequencies' that the possibility of using Lamb waves for non-destructive testing began to be investigated in earnest. Since then, much work has been done on the use of Lamb waves and other guided waves for inspection purposes. A comprehensive review of applications may be found in Alleyne (1991). Very broadly speaking, the use of Lamb waves for non-destructive inspection purposes falls into two categories depending on the distance of propagation. Firstly, there are short range applications, where Lamb waves and other guided waves are used to obtain information which cannot be obtained by more conventional means. These areas include the determination of the elastic properties of materials (Chimenti and Nayfeh 1990), the detection of defects near to interfaces such as in the inspection of adhesive joints (Mal *et al.* 1990), and temperature and thickness measurement of thin films (Khuri-Yakub *et al.* 1996). In these cases, sensitivity is of key importance and generally this is the main selection criterion for a suitable Lamb wave mode. Effects such as dispersion are not so important as the propagation distances are small.

The second area which is of greater relevance here is in applications where the propagation distance is large. Applications of long range Lamb wave inspection include the detection of delaminations in rolled steel (Lehfeltd and Höller 1967, Ball and Shewring 1973) and composites (Guo and Cawley 1992), and pipeline inspection (Alleyne and Cawley 1994a). In long range applications, the aim is to inspect large areas rapidly. Major considerations are the minimisation of coherent noise by using pure mode

excitation and maximising the propagation distance by using modes with minimal dispersion.

### 1.2.3 *Permanently attached transducers and smart structures*

Conventional active ultrasonic techniques are not a feasible basis for a permanently attached structural inspection system, due to large number of transducers needed to monitor an entire structure. A possible solution is to only monitor certain areas where it is known *a priori* that defects such as corrosion or cracks are likely to occur. This has proved to be viable in some circumstances as in the case of the Fleximat transducer system (manufactured by AEA Technology plc.) which is used for monitoring pipes and fixtures in the petrochemical industry. However, if an entire structure is to be monitored, then a single transducer must be capable of inspecting a reasonable area of the surrounding structure. Potentially this can be achieved by using permanently attached Lamb wave transducers. Several methods are available for the excitation and detection of Lamb waves which are reviewed in chapter 4, but in this thesis attention is focused on the use of inter-digital transducers. Inter-digital transducers are low profile and can be designed to have a minimal impact on both the appearance and mechanical performance of the structure to which they are attached.

The transducers described here use the piezoelectric polymer PVDF as the transduction element. However, the conclusions which are drawn in most cases are not specific to this material and would be applicable to the design of inter-digital transducers made from other piezoelectric elements, such as 0-3 composites (Tran-Huu-Hue *et al.* 1997) or ceramic platelets embedded in a polymer matrix (Gachagan *et al.* 1996).

### 1.2.4 *Towards an integrated structural inspection system*

Although the work described in this thesis concentrates on the development of the basic ultrasonic and transduction science for integrated structural inspection systems, it is important to be aware of the wider issues which are likely to arise later. These include considerations such as transducer lifetime, data telemetry, data processing and very importantly, economics.

Furthermore, there are several fundamental issues which are relevant to general long range Lamb wave testing which have been intentionally omitted from this thesis. These topics include the interaction of Lamb waves with defects (for example, Alleyne and Cawley 1992a and Datta *et al.* 1991) and the effect which fluid loading on structures and other attenuation mechanisms have on Lamb wave propagation (for example Alers 1994, Rose 1995). The work in these areas complements the work described in chapter 2 and will help to provide further criteria for the selection of suitable Lamb wave modes.

## 1.3 OVERVIEW OF THESIS

Each of the following five chapters in this thesis is largely self-contained and describes work on a particular aspect of the project. The order of the chapters approximately follows the chronological order in which the work was carried out by the author. Much of the work can also be found in the publications list given in appendix C.

Theoretical aspects of Lamb waves are covered in chapter 2. First, the mathematical analysis of their propagation in a flat plate is summarised following the method of Viktorov (1967). The investigation of the effect of plate curvature on Lamb wave propagation is then investigated. It was thought, at the time when this work was performed by the author, to be the first time it had been done. Subsequently, however, Qu *et al.* (1996) have presented a similar analysis for wave propagation in a curved plate, although they do not offer comparisons with the familiar flat plate case. The final section in this chapter presents quantitative assessments of the relative dispersion of different Lamb wave modes as functions of frequency. It is thought that this is the first time any quantitative studies of this type have been performed.

Chapter 3 describes work on the development of a one-dimensional computer model for polymer film transducer systems which was carried out by the current author and his colleague Mr. R. Monkhouse with technical advice from Prof. B. Auld, whose contributions at several stages of this project are gratefully acknowledged. The contribution of the author was predominantly in the mathematical development of the model and its manipulation to perform specific calculations. Although one-dimensional transducer models have existed for around half a century since the work of Mason (1948), a variety of approaches have been taken, and most literature does not give details on how general models are used to perform specific calculations. Here, a modular, matrix based approach is adopted, and use of the model is described in some detail. This model is used later in chapters 4 and 6 in order to gain an understanding of the frequency response characteristics of more complex transducers.

The concept of inter-digital transducers (IDTs) for the transmission and reception of Lamb waves is introduced in chapter 4 together with a review of other methods. The chapter goes on to describe the design, fabrication and testing of the first generation of PVDF IDTs on 1-2 mm thick aluminium plates which was carried out by the author, again in conjunction with his colleague Mr. R. Monkhouse. The success of these initial tests has stimulated further work in this field by other workers at Imperial College including Mr. R. Dalton, Mr. P. Marty and Mr. A. Bernard. The author then discusses the use of IDTs of a similar design to transmit and receive higher order Lamb wave modes ( $A_2$  and  $S_4$ ) in a thicker (6.5 mm) structure. The experimental test results show some success, but suggest problems of obtaining mode purity. It is concluded that the use of higher order modes is not a good strategy for the long range Lamb wave inspection of thick structures.

In order to use an IDT to monitor a structure using Lamb waves, it is important to know what area of the structure the IDT is inspecting. Chapter 5 moves away from the physical construction of IDTs and describes the development of a model based on Huygens' principle to predict the acoustic field generated by an IDT. Subject to certain assumptions being satisfied by the transducer, the model is valid for all IDTs. The chapter begins by defining an excitability function for Lamb waves which may be viewed as a modal property in much the same way as the phase or group velocity. Using the excitability and other modal properties enables the exact Lamb wave acoustic field from a point source to be predicted as a function of distance and time and this has been implemented in software by the author. This model, finite element predictions and experimental measurements are all compared. Next, the discretisation of an IDT into point sources and the summation of the acoustic field from each to obtain the total acoustic field from the IDT is described. This forms the basis of the software implementation of the Huygens' model. Results from

the Huygens' model are compared with FE predictions and experimental measurements of the acoustic field from an IDT.

The construction of IDTs is returned to in chapter 6, in which the development of low frequency PVDF transducers is described. Use of the one-dimensional model from chapter 3 in conjunction with further experimental tests with bulk wave transducers indicates that by using a heavy backing layer, transducers which operate at around 100 kHz may be constructed from 110  $\mu\text{m}$  thick PVDF. Successful tests using PVDF IDTs with such a layered construction to transmit and receive Lamb waves at 97 kHz in a 12.5 mm thick aluminium bar are presented. The section concludes with an example of a more complex design of low frequency IDT which has also been fabricated and tested.

The large size and simple construction of low frequency IDTs has been exploited to provide further experimental data for comparison with Huygens' model. The remainder of chapter 6 uses such experimental data in conjunction with Huygens' model to elucidate several guidelines governing the geometry of IDTs with either straight or curved fingers. An improved experimental technique for making measurements of the strength of the Lamb wave field from an IDT using point transducers is also described.

The main conclusions of chapters 2 to 6 in this thesis are summarised in chapter 7. Specific issues which have been raised in this thesis and require further investigation are summarised and possible future work is proposed.

## 2. Lamb wave theory

---

### 2.1 INTRODUCTION

The modal properties of acoustic waves which propagate along the free surface of a semi-infinite isotropic elastic solid were first identified by Rayleigh (1885), after whom this class of waves were named. Although the propagation of waves in layered media was of considerable interest to seismologists, before the age of digital computers such cases were too complex to be solved numerically. Lamb realised that a preliminary step would be to algebraically solve the problem of wave propagation in a flat isotropic plate in vacuum which he succeeded in doing in 1917.

In this chapter, attention is focused on theoretical aspects of Lamb wave propagation, starting with a summary of the derivation of the basic two-dimensional equations for Lamb waves in flat plates, which follows the method of Viktorov (1967). Section 2.3 contains an analysis of two-dimensional Lamb wave propagation in curved plates and a comparison with the case of a flat plate. Section 2.4 investigates the effect of dispersion on Lamb wave propagation and its implications for long range non-destructive testing.

### 2.2 BACKGROUND

This section summarises the derivation of the Lamb wave dispersion equations, starting from the wave equations which must be satisfied by all waves in elastic isotropic media.

#### 2.2.1 *Wave propagation in isotropic elastic media*

The propagation of elastic waves in an infinite isotropic, homogeneous solid is well understood and the derivation of the wave equations may be found in numerous texts (for example, Brekhovskikh and Goncharov 1985). Only the key equations will be reproduced here, as they are the foundation of all acoustic wave theory and will be a starting point for several later calculations.

#### *The wave equations*

A system of fixed Cartesian axes in the  $x$ ,  $y$  and  $z$  directions is defined in the material being studied. If the material has density  $\rho$ , then by considering the equilibrium of an infinitesimal cube of material and using Hooke's law (see for example Howatson *et al.* 1972) to relate stresses to strains the following differential equation for the displacement field may be deduced (Brekhovskikh and Goncharov 1985):

$$\begin{aligned}
 \rho \frac{\partial^2 u_x}{\partial t^2} &= (\lambda + \mu) \frac{\partial}{\partial x} \left( \frac{\partial u_x}{\partial x} + \frac{\partial u_y}{\partial y} + \frac{\partial u_z}{\partial z} \right) + \mu \left( \frac{\partial^2}{\partial x^2} + \frac{\partial^2}{\partial y^2} + \frac{\partial^2}{\partial z^2} \right) u_x \\
 \rho \frac{\partial^2 u_y}{\partial t^2} &= (\lambda + \mu) \frac{\partial}{\partial y} \left( \frac{\partial u_x}{\partial x} + \frac{\partial u_y}{\partial y} + \frac{\partial u_z}{\partial z} \right) + \mu \left( \frac{\partial^2}{\partial x^2} + \frac{\partial^2}{\partial y^2} + \frac{\partial^2}{\partial z^2} \right) u_y \\
 \rho \frac{\partial^2 u_z}{\partial t^2} &= (\lambda + \mu) \frac{\partial}{\partial z} \left( \frac{\partial u_x}{\partial x} + \frac{\partial u_y}{\partial y} + \frac{\partial u_z}{\partial z} \right) + \mu \left( \frac{\partial^2}{\partial x^2} + \frac{\partial^2}{\partial y^2} + \frac{\partial^2}{\partial z^2} \right) u_z
 \end{aligned} \quad (2.1)$$

where  $u_x$ ,  $u_y$  and  $u_z$  are the components of the displacement field in the  $x$ ,  $y$  and  $z$  directions,  $\lambda$  and  $\mu$  are the Lamé stiffness constants for the material and  $t$  represents time. These are the differential equations of motion which must be satisfied by all elastic waves propagating in the material and will be referred to as the wave equations. Any displacement field which satisfies the wave equations implicitly satisfies the equilibrium and compatibility conditions, so the only remaining constraints on the displacement field must come from external boundary conditions. It should be noted that the wave equations are linear and hence the superposition of two or more valid solutions for the displacement field will still yield a valid solution. The wave equations cannot be solved directly, but various displacement fields can be shown to satisfy them, as will be demonstrated in subsequent sections.

#### *Longitudinal and transverse waves*

The solution of the wave equations that will be considered here is for continuous homogeneous plane waves propagating in the positive  $x$  direction. In such a wave, each wavefront is an infinite plane parallel to the  $yz$  plane, and the displacement field is independent of the  $y$  and  $z$  directions. Hence a harmonic spatial dependence, given by  $\exp(ikx)$ , is included in any proposed solutions, where  $k$  is the wavenumber and  $i$  is defined as  $\sqrt{-1}$ . Two forms of solution are possible, depending on whether or not the particle displacement is parallel or perpendicular to the direction of wave propagation.

Consider the case where the particle displacement is parallel to the direction of wave propagation. The displacement field is then given by:

$$\begin{aligned}
 u_x &= A_x \exp(kx - i\omega t) \\
 u_y &= 0 \\
 u_z &= 0
 \end{aligned} \quad (2.2)$$

where  $A_x$  is an arbitrary constant,  $\omega$  represents an angular frequency. This solution may easily be shown to satisfy the wave equations. Also, this displacement field can be shown to be irrotational, the wave propagation being effected by localised compressions and rarefractions of the material. By substitution into equation 2.1, the angular frequency and wavenumber can be shown to be related by:

$$\frac{\omega}{k} = \sqrt{\frac{\lambda + 2\mu}{\rho}} = v_l \quad (2.3)$$

The ratio of angular frequency to wave number,  $v_l$ , defines the phase velocity of the waves, that is, the velocity at which the wave crests propagate. In this case, since the

particle motion has been constrained to being in the direction of wave propagation, the waves are usually described as being longitudinal waves, and hence  $v_l$  is referred to as the bulk longitudinal wave velocity.

The second solution to the wave equations is when the particle displacements are perpendicular to the direction of propagation. Hence the displacement field may be described by:

$$\begin{aligned} u_x &= 0 \\ u_y &= A_y \exp(kx - i\omega t) \\ u_z &= A_z \exp(kx - i\omega t) \end{aligned} \quad (2.4)$$

where, again,  $A_y$  and  $A_z$  are arbitrary constants. Unlike, the displacement field for longitudinal waves, this displacement field is purely rotational and has zero divergence. Hence, there are no localised changes in volume of the material as the wave propagates. Substitution of equation 2.4 into equation 2.1 yields the following relationship between  $\omega$  and  $k$ :

$$\frac{\omega}{k} = \sqrt{\frac{\mu}{\rho}} = v_t \quad (2.5)$$

Again, the quantity  $v_t$  is the phase velocity of the propagating waves, and is referred to as the bulk transverse or bulk shear wave velocity, since the particle motion is at right angles to the direction of propagation. The direction of particle motion is in a specific direction in the  $yz$  plane (given by the vector  $[0 \ A_x \ A_y]^T$ ) which is referred to as the polarization direction of the transverse waves.

The bulk transverse and longitudinal wave velocities are both material properties and they are widely used in wave propagation calculations. It should be stressed that the bulk wave velocities derived above only apply to waves with infinite plane wavefronts. The same solutions are not, in general, valid for other geometries of propagation, such as in the case of waves with concentric spherical wavefronts propagating away from a point.

### *Potential functions*

An elegant way of manipulating the wave equation (equation 2.1) is by using potential functions to decompose the displacement field  $\underline{u}$  into two fields, one associated with longitudinal waves and one associated with transverse waves.

As shown, the displacement field associated with longitudinal waves is irrotational and that associated with transverse waves is non-divergent. If a displacement field is defined as being the *grad* of some scalar field  $\phi$ , then basic vector identities (see for example, Howatson *et al.* 1972) show that the displacement field is irrotational. Likewise, if a displacement field is defined as being the *curl* of some vector field  $\underline{\psi}$ , then the displacement field can be shown to be non-divergent. Since it can be shown (Malvern 1969) that any vector field can be decomposed into an irrotational component and a non-divergent component, so any particle displacement field can be written as:

$$\underline{u} = \nabla \phi + \nabla \times \underline{\psi} \quad (2.6)$$

where  $\phi$  and  $\underline{\psi}$  are the potential functions. Provided they are both continuous functions, with continuous derivatives, the displacement field will also be a continuous function and hence compatibility will be satisfied. The wave equations may now be rewritten in terms of the potential functions to obtain:

$$\begin{aligned}\rho \frac{\partial^2 \phi}{\partial t^2} &= (\lambda + 2\mu) \nabla^2 \phi \\ \rho \frac{\partial^2 \underline{\psi}}{\partial t^2} &= \mu \nabla^2 \underline{\psi}\end{aligned}\tag{2.7}$$

where the first equation is for longitudinal waves, and the second is for transverse waves.

### 2.2.2 Waves in a free flat plate

#### *Boundary conditions and reduced wave equation*

Attention is now turned to the consideration of waves propagating in a flat isotropic plate in vacuum. The derivation of the Lamb wave equations summarised here follows the method of Viktorov (1967), although some changes of nomenclature are introduced for consistency with other calculations in this thesis.

Cartesian axes are defined with the  $x$  and  $y$  axes in the plane of the plate and the  $z$  axis normal to the plane of the plate. The plate is assumed to extend to infinity in the  $x$  and  $y$  directions, and the origin of the  $z$  axis is located midway through the thickness of the plate as shown in figure 2.1. The thickness of the plate is  $d$  and hence the boundary conditions which all waves within the plate must satisfy are given by:

$$\begin{aligned}\sigma_{zz} \Big|_{z=\pm d/2} &= 0 \\ \sigma_{xz} \Big|_{z=\pm d/2} &= 0 \\ \sigma_{yz} \Big|_{z=\pm d/2} &= 0\end{aligned}\tag{2.8}$$

In this calculation only straight crested Lamb waves propagating in the  $x$  direction will be considered. This means that the wavefronts are assumed to be infinite in the  $y$  direction as illustrated schematically in figure 2.1, and that the behaviour of the waves is independent of the  $y$  coordinate, hence  $\partial/\partial y = 0$ . Plane strain conditions in the  $xz$  plane are therefore assumed. A final condition necessary to reduce the solution set to include only genuine Lamb waves (and not to include, for example, SH waves which are transverse waves with rotation about the  $z$  axis) is to require that there is no component of particle displacement in the  $y$  direction, so  $u_y=0$ . To ensure that there is rotation only about axes in the  $y$  direction, the vector potential function defining shear waves,  $\underline{\psi}$ , only has a component in the  $y$  direction,  $\psi_y$ . Under these conditions, the wave equations (equation 2.7) reduce to:

$$\begin{aligned}\rho \frac{\partial^2 \phi}{\partial t^2} &= (\lambda + 2\mu) \left( \frac{\partial^2 \phi}{\partial x^2} + \frac{\partial^2 \phi}{\partial z^2} \right) \\ \rho \frac{\partial^2 \psi_y}{\partial t^2} &= \mu \left( \frac{\partial^2 \psi_y}{\partial x^2} + \frac{\partial^2 \psi_y}{\partial z^2} \right)\end{aligned}\tag{2.9}$$

Defining longitudinal and transverse wave numbers,  $k_l$  and  $k_t$  respectively, as follows:

$$\begin{aligned}k_l &= \omega \sqrt{\frac{\rho}{\lambda + 2\mu}} = \omega v_l \\ k_t &= \omega \sqrt{\frac{\rho}{\mu}} = \omega v_t\end{aligned}\tag{2.10}$$

and assuming a temporal harmonic dependence of  $\exp(i\omega t)$  enables the wave equations to be further reduced to:

$$\begin{aligned}\frac{\partial^2 \phi}{\partial x^2} + \frac{\partial^2 \phi}{\partial z^2} + k_l^2 \phi &= 0 \\ \frac{\partial^2 \psi_y}{\partial x^2} + \frac{\partial^2 \psi_y}{\partial z^2} + k_t^2 \psi_y &= 0\end{aligned}\tag{2.11}$$

#### *Solution of wave equations*

The calculation is concerned with waves propagating along the plate, hence a new wavenumber,  $k$ , in this direction is introduced. As the wave crests are straight, a spatially harmonic solution of the potential functions governed by  $\exp(ikx)$  is assumed (this is the fundamental difference between the solution for straight crested Lamb waves and that for circular crested Lamb waves as will be shown later in chapter 5). It can be shown that the following potential functions satisfy the reduced wave equations (equation 2.11 above):

$$\begin{aligned}\phi &= (S_l \cosh q_l z + A_l \sinh q_l z) \exp i(kx - \omega t) \\ \psi_y &= (S_t \sinh q_t z + A_t \cosh q_t z) \exp i(kx - \omega t)\end{aligned}\tag{2.12}$$

where  $q_l = \sqrt{k^2 - k_l^2}$  and  $q_t = \sqrt{k^2 - k_t^2}$ .

#### *Satisfying boundary conditions*

The displacement field associated with the potential functions given in equation 2.12 is then calculated using equation 2.6. From the displacement field, the strain field may be calculated and finally Hooke's law (Howatson *et al.* 1972) is used to obtain the relevant components of the stress field:

$$\begin{aligned}\sigma_{zz} &= \mu \left[ S_l (k^2 + q_l^2) \cosh q_l z + A_l (k^2 + q_l^2) \sinh q_l z + 2A_t i k q_t \sinh q_t z + 2S_t i k q_t \sinh q_t z \right] \exp i(\omega t - kx) \\ \sigma_{xz} &= \mu \left[ 2S_l i k q_l \sinh q_l z + 2A_l i k q_l \sinh q_l z + A_t (k^2 + q_t^2) \cosh q_t z + S_t (k^2 + q_t^2) \sinh q_t z \right] \exp i(\omega t - kx)\end{aligned}\tag{2.13}$$

The equations for the stresses,  $\sigma_{zz}$  and  $\sigma_{xz}$ , may be evaluated at  $z = +/- d$  and set to zero to satisfy the boundary conditions at the free surfaces. In this way, four homogeneous equations are found:

$$\begin{bmatrix} \sigma_{zz}|_{z=d/2} \\ \sigma_{zz}|_{z=-d/2} \\ \sigma_{xz}|_{z=d/2} \\ \sigma_{xz}|_{z=-d/2} \end{bmatrix} = \mu \begin{bmatrix} (k^2 + q_i^2) \cosh q_i d/2 & (k^2 + q_i^2) \sinh q_i d/2 & 2iks \sinh q_i d/2 & 2iks \cosh q_i d/2 \\ (k^2 + q_i^2) \cosh q_i d/2 & -(k^2 + q_i^2) \sinh q_i d/2 & -2iks \sinh q_i d/2 & 2iks \cosh q_i d/2 \\ 2ikq \sinh q_i d/2 & 2ikq \cosh q_i d/2 & -(k^2 + q_i^2) \cosh q_i d/2 & -(k^2 + q_i^2) \sinh q_i d/2 \\ -2ikq \sinh q_i d/2 & 2ikq \cosh q_i d/2 & -(k^2 + q_i^2) \cosh q_i d/2 & (k^2 + q_i^2) \sinh q_i d/2 \end{bmatrix} \begin{bmatrix} S_i \\ A_i \\ A_i \\ S_i \end{bmatrix} \\ = \begin{bmatrix} 0 \\ 0 \\ 0 \\ 0 \end{bmatrix} \quad (2.14)$$

For non-trivial solutions to this equation, the determinant of the 4 x 4 matrix must be zero. This is an Eigenvalue problem, which yields a modal solution for waves which can propagate along the plate without the external input of energy. The determinant of the 4 x 4 matrix in equation 2.14 can be shown to be the product of the two factors  $\Delta_A$  and  $\Delta_S$  given below:

$$\Delta_S = (k^2 + q_i^2)^2 \cosh q_i d/2 \sinh q_i d/2 - 4k^2 q_i q_i \cosh q_i d/2 \sinh q_i d/2 = 0 \\ \Delta_A = (k^2 + q_i^2)^2 \sinh q_i d/2 \cosh q_i d/2 - 4k^2 q_i q_i \sinh q_i d/2 \cosh q_i d/2 = 0 \quad (2.15)$$

These are the famous Lamb wave dispersion relationships, originally derived by Lamb himself (1917). The first equation is associated with waves propagating along the plate with symmetrically distributed displacements about the centre line of the plate, and the second is associated with similar waves with anti-symmetric displacements. As the determinant of the 4 x 4 matrix in equation 2.14 will be zero when either  $\Delta_A$  or  $\Delta_S$  equals zero, either of part of equation 2.15 may be solved independently. For any frequency,  $\omega$ , one or more values of wavenumber,  $k$ , can be found which satisfy either  $\Delta_A = 0$  or  $\Delta_S = 0$ . In this way two sets of dispersion data are obtained, one giving frequency-wavenumber pairs which correspond to anti-symmetric waves and the other giving frequency-wavenumber pairs which correspond to symmetric waves.

### Mode shapes

Valid wavenumber-frequency pairs may be plotted against one another to yield wavenumber-frequency dispersion curves. The curves are an infinite set of continuous lines, each of which is called a mode of the system. At any point on a curve, there is a distribution of particle displacements through the thickness of the plate which is associated with that particular combination of wavenumber and frequency. For a flat plate in vacuum, the particle displacements associated with a particular modal solution may be evaluated by calculating the appropriate Eigenvector of equation 2.14 and then using equation 2.12 to obtain the potential fields.

The distribution of particle displacements through the thickness of the plate is called the mode shape, but this name is slightly misleading as the mode shape varies with frequency along each mode.

For a single flat plate in either vacuum or fluid, a naming convention for the modes exists based on their mode shapes. The first identifier in the name is either A or S depending on whether or not the particle displacements are symmetric or anti-symmetric about the centre line of the plate, and the second identifier, the mode number or order, is used to differentiate between the modes within each type. The higher the mode number, the greater the complexity of the mode shape. For example at low frequencies, the fundamental  $A_0$  mode corresponds to simple flexural waves and the  $S_0$  mode corresponds to simple compression waves propagating along the plate, while the higher order modes correspond to more complex displacement fields. Some examples of mode shapes are shown in figure 2.2. The dimensionless frequency,  $\bar{f}$ , referred to in figure 2.2 is defined as  $\bar{f} = fd/v_t$ .

### Dispersion curves

Although the solution of the modal problem yields wavenumber-frequency pairs, it is more usual to present dispersion curves of phase velocity vs. frequency. The phase velocity,  $v_{ph}$ , is defined thus:

$$v_{ph} = \frac{\omega}{k} \quad (2.16)$$

The phase velocity is the velocity at which the wave peaks of a continuous wave at a single frequency propagate. If the phase velocity is plotted against the product of frequency and the characteristic dimension of the system (the plate thickness) rather than the absolute frequency, the dispersion curves become independent of the actual size of the system. For generality, both axes can be made dimensionless by dividing the phase velocity by a characteristic velocity, which is taken as being the bulk transverse wave velocity in the plate material.

An interesting consequence of plotting phase-velocity dispersion curves on such dimensionless axes, is that they are then only dependent on the ratio of the bulk longitudinal and transverse wave velocities of the plate material. This can readily be seen by re-arrangement of the dispersion equation 2.15, using the  $\bar{v}_{ph}$  to denote dimensionless phase velocity ( $v_{ph}/v_t$ ),  $\bar{\omega}$  to denote dimensionless circular frequency ( $\omega d/v_t$ ) and  $\bar{v}_l = v_l/v_t$ :

$$\begin{aligned} \left( \frac{2}{\bar{v}_{ph}^2} - 1 \right) \cosh \frac{\bar{\omega}}{2} \left( \frac{1}{\bar{v}_{ph}^2} - \frac{1}{\bar{v}_l^2} \right)^{\frac{1}{2}} \sinh \frac{\bar{\omega}}{2} \left( \frac{1}{\bar{v}_{ph}^2} - 1 \right)^{\frac{1}{2}} - \frac{4}{\bar{v}_{ph}^2} \left( \frac{1}{\bar{v}_{ph}^2} - \frac{1}{\bar{v}_l^2} \right)^{\frac{1}{2}} \left( \frac{1}{\bar{v}_{ph}^2} - 1 \right)^{\frac{1}{2}} \cosh \frac{\bar{\omega}}{2} \left( \frac{1}{\bar{v}_{ph}^2} - 1 \right)^{\frac{1}{2}} \sinh \frac{\bar{\omega}}{2} \left( \frac{1}{\bar{v}_{ph}^2} - \frac{1}{\bar{v}_l^2} \right)^{\frac{1}{2}} = 0 \\ \left( \frac{2}{\bar{v}_{ph}^2} - 1 \right) \sinh \frac{\bar{\omega}}{2} \left( \frac{1}{\bar{v}_{ph}^2} - \frac{1}{\bar{v}_l^2} \right)^{\frac{1}{2}} \cosh \frac{\bar{\omega}}{2} \left( \frac{1}{\bar{v}_{ph}^2} - 1 \right)^{\frac{1}{2}} - \frac{4}{\bar{v}_{ph}^2} \left( \frac{1}{\bar{v}_{ph}^2} - \frac{1}{\bar{v}_l^2} \right)^{\frac{1}{2}} \left( \frac{1}{\bar{v}_{ph}^2} - 1 \right)^{\frac{1}{2}} \sinh \frac{\bar{\omega}}{2} \left( \frac{1}{\bar{v}_{ph}^2} - 1 \right)^{\frac{1}{2}} \cosh \frac{\bar{\omega}}{2} \left( \frac{1}{\bar{v}_{ph}^2} - \frac{1}{\bar{v}_l^2} \right)^{\frac{1}{2}} = 0 \end{aligned} \quad (2.17)$$

The ratio of the bulk velocities of a material,  $\bar{v}_l$ , can be written in terms of the Lamé constants of the material, or perhaps more usefully in terms of the elastic constants  $E$  and  $\nu$ :

$$\frac{\bar{v}_l}{v_t} = \frac{v_l}{v_t} = \sqrt{\frac{\lambda + 2\mu}{\mu}} = \sqrt{2 \frac{1-2\nu}{1-\nu}} \quad (2.18)$$

Hence the shape of the dimensionless phase velocity dispersion curves for a flat plate in vacuum is dependent only on the Poisson's ratio of the plate material.

The dimensionless phase-velocity dispersion curves for aluminium (Poisson's ratio = 0.34) are shown with continuous lines in figure 2.3 and those for steel (Poisson's ratio = 0.30) are shown with dashed lines. It can be seen that the differences are minimal on the fundamental modes but become significant on the higher order modes. A much more detailed investigation into the effect of Poisson's ratio on the shape of the dispersion curves may be found in the three works by Freedman (1990a, b and c).

The phase velocity describes the velocity of wave peaks in a continuous single frequency wave, but a wave packet of finite duration and therefore of finite bandwidth will propagate at a different velocity. This is called the group velocity,  $v_{gr}$ , and is defined as:

$$v_{gr} = \frac{\partial \omega}{\partial k} \quad (2.19)$$

Again, examples of the group-velocity dispersion curves for aluminium and steel are plotted on dimensionless axes and are shown in figure 2.4, with the dimensionless group velocity being defined as  $\bar{v}_{gr} = v_{gr}/v_t$ . The group velocity is also the velocity at which energy propagates.

### *Multi-layer systems and general solution methods*

The Lamb wave dispersion equations given above are specific to the case of a flat isotropic plate in vacuum. Several approaches to modelling wave propagation in general layered media systems are possible. In the first case, the transmission line method may be used, as developed by Thomson (1950) and Haskell (1953). However, *Disperse* (Pavlakovic *et al.* 1997), the software which was used for most dispersion calculations described in this thesis uses the alternative global matrix method, as it is numerically more stable at high frequency thickness values (see Lowe 1995 for a discussion of why this is the case). A detailed description of the global matrix method may be found in Lowe (1995).

## 2.3 EFFECT OF CURVATURE ON LAMB WAVE PROPAGATION

### 2.3.1 Introduction

The previous section summarised the well known analysis for wave propagation in a flat plate under 2-dimensional plane strain conditions. In this section, a similar analysis is presented for the case of waves propagating in plates with a constant radius of curvature. Unfortunately, the results of this calculation have not lead to elegant dispersion equations analogous to those for a flat plate given in equation 2.15. However, expressions have been derived for the stress and displacement fields associated with waves propagating in curved plates, and these have been used in the global matrix formulation used by *Disperse*

in order to obtain dispersion curves. Dispersion curves for plates with varying degrees of curvature will be compared to those for a flat plate of the same thickness in section 2.3.3.

Much work has been reported on the axial propagation of waves in cylinders (Gazis 1958, 1959, Pao and Mindlin 1960 and Fitch 1963 amongst others), including work on fluid filled cylinders in vacuum (Kumar 1971, 1972) and vacuum filled cylinders in fluid (Metsaveer and Klauson 1996). All these cases are fundamentally different systems to that which is under consideration here, primarily because the propagation is in the axial direction, but also because continuity of displacements and stresses is assumed around the circumference of the cylinder. In the analysis presented here, for reasons which will be discussed below, the angular co-ordinate is assumed to extend to infinity and this continuity condition is not applied.

Work has been reported on wave propagation in the circumferential direction in various curved systems. Surprisingly, these cases are almost invariably more complex than the simple curved plate in vacuum considered here. A particular avenue of research has been concerned with examining the reflection of bulk compression waves in a fluid by immersed spheres and cylinders (Numerich and Dale 1984 for instance). The size of the reflections have been found to depend on whether the immersed body is solid or not, and this observation has stimulated interest in the mechanics of the wave propagation around the body. A component of the reflected signal may be attributed to the superposition of Lamb and Rayleigh type waves which are excited and propagate around the surface of the body, re-radiating energy into back into the fluid as they do so. If the circumference of the body coincides with an integral number of wavelengths of the excited Lamb or Rayleigh waves, a resonance in the reflection is observed. For this reason, much of this work has been concerned with examining what are effectively standing Rayleigh and Lamb waves, which satisfy the continuity condition described in the preceding paragraph. Recently, Kaduchak and Marston (1995) have investigated the effect of exciting a hollow immersed cylinder with a short toneburst, to set up two packets of Lamb type waves (equivalent to the  $S_2$  mode) which propagate circumferentially in opposite directions around the cylinder. They also present a portion of the phase and group velocity dispersion curves for this mode.

Work on Rayleigh wave propagation on curved substrates is considerably more developed. In particular, the work of Rulf (1968) examined the effect of arbitrary substrate curvature on Rayleigh wave propagation, Epstein (1976, 1979) and Kawald *et al.* (1996) have examined circumferential wave propagation for thin layers on solid cylindrical substrates. The problem formulation by Kawald *et al.* (1996) forms the basis of that which is used here for Lamb waves. Recently Hassan and Nagy (1997) have investigated the propagation of so-called 'creeping waves' around a cylindrical fluid filled cavity in an elastic host medium, with emphasis on the coupling of the wave modes in the fluid and the Rayleigh type wave modes in the host medium.

It appeared that no work had previously been reported on the modal propagation of Lamb waves in an unloaded curved plate, although the algebraic basis of the calculation could be constructed from other work, in particular Kawald *et al.* (1996), Hassan and Nagy (1997) and even Rulf (1968).

Subsequent to the analysis described here being completed, conference proceedings of work by Qu *et al.* (1996) have been published which investigate the same problem. Their

results are presented in the form of angular wavenumber vs. frequency plots for various degrees of curvature, but somewhat surprisingly the results are not directly compared to those for a flat plate. They do not offer any qualitative remarks on the degree of curvature which a plate must have before it should be regarded as a curved plate rather than a flat plate, and nor do they present group velocity dispersion curves.

### 2.3.2 Theoretical analysis

The analysis concerns waves propagating in the circumferential direction around an infinitely long cylinder. Cylindrical coordinates ( $r$ ,  $\theta$  and  $z$ ) are used throughout the analysis, and isotropic material is assumed. The plane perpendicular to the axis of the cylinder (the  $z$  direction) contains the  $r$  (radial) and  $\theta$  (circumferentially) directions, as shown in figure 2.5. Plane strain is assumed in the plane of  $r$  and  $\theta$ , and the wavefronts are considered to be infinitely long in the  $z$  direction. The angular direction,  $\theta$ , extends from zero to infinity, with no account being made for the continuity of displacements and stresses around the circumference of the cylinder (i.e. at  $0$ ,  $2\pi$ ,  $4\pi$  etc.), hence the number of wavelengths around the circumference need not be an integer (unlike in the case of axially propagating waves discussed by Gazis 1959 for example). For this reason, the system being modelled cannot exist physically. However, in practical applications where tonebursts rather than continuous waves are used, the analysis will be valid providing that the spatial length of a toneburst is smaller than the circumference of the cylinder.

The analysis is performed using the scalar and vector potential functions,  $\phi$  and  $\underline{\psi}$  discussed previously. The associated wave equations (equation 2.7) are independent of the coordinate system used and are therefore still valid for the cylindrical geometry, as long as the correct form of the vector operators is used.

#### *Calculation of suitable potential functions*

In the same manner as for the flat plate case, a basic form for the potential functions is proposed which specifies wave propagation in the desired direction. In the curved case, a harmonic spatial dependence on the angle  $\theta$  is assumed, hence both potential functions have an  $\exp(ik_\theta\theta)$  term, where  $k_\theta$  is the angular wavenumber. Again, rotation is only permitted about axes in the  $z$  direction. Hence the vector potential field only has a component in this direction. The following functions for  $\phi$  and  $\underline{\psi}$  are used (after Kawald *et al.* 1996):

$$\begin{aligned} \phi &= f(r)\exp i(k_\theta\theta - \omega t) \\ \underline{\psi} &= \begin{bmatrix} 0 \\ 0 \\ g(r)\exp i(k_\theta\theta - \omega t) \end{bmatrix} \end{aligned} \quad (2.20)$$

The remaining terms,  $f(r)$  and  $g(r)$ , in the potential functions are functions of the radius,  $r$ , and specify that there will also be a dependence on the radial position in the cylinder. These functions are not yet known and the next stage of the calculation is to determine them.

The  $\nabla^2$  operator in cylindrical co-ordinates is (Howatson *et al.* 1972):

$$\nabla^2 = \frac{1}{r} \frac{\partial}{\partial r} \left( r \frac{\partial}{\partial r} \right) + \frac{1}{r^2} \frac{\partial^2}{\partial \theta^2} + \frac{\partial^2}{\partial z^2} \quad (2.21)$$

Using this definition, the scalar potential function given in equation 2.20 may be substituted into the wave equation 2.7 to obtain:

$$\frac{\partial^2}{\partial r^2} f(r) + \frac{1}{r} \frac{\partial}{\partial r} f(r) - \frac{k_\theta^2}{r^2} f(r) = -\frac{\omega^2}{v_l^2} f(r) \quad (2.22)$$

$\omega/v_l$  is now replaced by  $k_l$ , the longitudinal bulk wavenumber. Then, by substituting  $x/k_l$  for  $r$  and defining a new function  $f_2(x)=f(x/k_l)$ , equation 2.22 can be manipulated to obtain:

$$\left[ \frac{\partial^2}{\partial x^2} + \frac{1}{x} \frac{\partial}{\partial x} + \left( 1 - \frac{k_\theta^2}{x^2} \right) \right] f_2(x) = 0 \quad (2.23)$$

which is Bessel's differential equation. As  $k_\theta$  can be any real number (i.e. not necessarily an integer), the solution for  $f_2(x)$  is:

$$\begin{aligned} f_2(x) &= A^{l+} H_{k_\theta}^{(1)}(x) + A^{l-} H_{k_\theta}^{(2)}(x) \\ \text{or } f_2(rk_l) &= f(r) = A^{l+} H_{k_\theta}^{(1)}(rk_l) + A^{l-} H_{k_\theta}^{(2)}(rk_l) \end{aligned} \quad (2.24)$$

where  $H^{(1)}$  and  $H^{(2)}$  are Hankel functions of the first and second kind.  $A^{l-}$  and  $A^{l+}$  may be interpreted as the amplitudes of two partial waves, the former propagating inwards towards the centre of the cylinder and the latter propagating outwards.

The calculation of  $g(r)$  follows the same procedure and yields an almost identical result. When the wave equation 2.7 is applied to the vector potential function,  $\underline{\psi}$ , only the following equation is obtained, since the components of  $\underline{\psi}$  in the  $r$  and  $\theta$  directions are both zero.

$$\frac{\partial^2}{\partial r^2} g(r) + \frac{1}{r} \frac{\partial}{\partial r} g(r) - \frac{k_\theta^2}{r^2} g(r) = -\frac{\omega^2}{v_t^2} g(r) \quad (2.25)$$

So replacing  $\omega/v_t$  with  $k_t$  (the bulk transverse wavenumber) the solution for  $g_2(rk_t)=g(y/k_t)$  is:

$$\begin{aligned} g_2(x) &= A^{t+} H_{k_\theta}^{(1)}(x) + A^{t-} H_{k_\theta}^{(2)}(x) \\ \text{or } g_2(rk_t) &= g(r) = A^{t+} H_{k_\theta}^{(1)}(rk_t) + A^{t-} H_{k_\theta}^{(2)}(rk_t) \end{aligned} \quad (2.26)$$

$A^{t-}$  and  $A^{t+}$  may be interpreted as the wave amplitudes of two partial waves, again with the former propagating inwards towards the centre of the cylinder and the other propagating outwards.

The following potential functions have now been found which satisfy the wave equations (and hence equilibrium and compatibility conditions) and which also specify wave propagation in the circumferential direction:

$$\begin{aligned}\phi &= \left( A^{l+} H_{k_\theta}^{(1)}(rk_l) + A^{l-} H_{k_\theta}^{(2)}(rk_l) \right) \exp i(k_\theta \theta - \omega t) \\ \psi_z &= \left( A^{t+} H_{k_\theta}^{(1)}(rk_t) + A^{t-} H_{k_\theta}^{(2)}(rk_t) \right) \exp i(k_\theta \theta - \omega t)\end{aligned}\tag{2.27}$$

*Calculation of field matrix*

The displacement field is straightforward to calculate using the cylindrical form of the vector operators in equation 2.6 to give:

$$\begin{aligned}u_r &= \frac{\partial \phi}{\partial r} + \frac{1}{r} \frac{\partial \psi_z}{\partial \theta} \\ u_\theta &= \frac{1}{r} \frac{\partial \phi}{\partial \theta} - \frac{\partial \psi_z}{\partial r} \\ u_z &= 0\end{aligned}\tag{2.28}$$

The relevant components of the strain field may then be calculated from the strain-displacement relationships, which in cylindrical coordinates are:

$$\begin{aligned}\varepsilon_{rr} &= \frac{\partial u_r}{\partial r} \\ \varepsilon_{\theta\theta} &= \frac{u_r}{r} + \frac{1}{r} \frac{\partial u_\theta}{\partial \theta} \\ \varepsilon_{r\theta} &= \frac{\partial u_\theta}{\partial r} - \frac{u_\theta}{r} + \frac{1}{r} \frac{\partial u_r}{\partial \theta}\end{aligned}\tag{2.29}$$

Finally Hooke's law (Howatson *et al.* 1972) may be applied to the strain field to obtain the required stress components. The equations obtained are not reproduced here (see appendix A) as they are exceedingly cumbersome. Due to the Hankel functions and the fact that the geometry of the curved plate is not symmetrical about the centre line of the plate, it is not possible to obtain elegant dispersion equations for curved plates which are analogous to the dispersion equations 2.15 for flat plates.

However, a field matrix for a particular curved layer can be calculated which gives the stresses,  $\sigma_{rr}$  and  $\sigma_{r\theta}$  and the displacements,  $u_r$  and  $u_\theta$  at any radius  $r$ , for use in the global matrix method. This matrix has been added to *Disperse* (Pavlakovic *et al.* 1997) which uses it to calculate the dispersion characteristics of waves propagating in curved plates in the direction of curvature. Some results which illustrate the effects of curvature on Lamb wave propagation in plates are illustrated in the following section.

### 2.3.3 Dispersion curves for waves propagating in curved plates

In the case of curved plates, the modal solution will calculate pairs of angular wavenumber,  $k_\theta$  and frequency,  $\omega$ , values which satisfy the wave equation and the relevant boundary conditions. The angular phase velocity,  $\theta'_{ph}$ , and group velocity,  $\theta'_{gr}$ , are then given by similar relations to those used to calculate the linear phase and group velocities for a flat plate:

$$\begin{aligned}\theta'_{ph} &= \frac{\omega}{k_\theta} \\ \theta'_{gr} &= \frac{\partial\omega}{\partial k_\theta}\end{aligned}\tag{2.30}$$

For comparison with a flat plate, it is preferable to convert these angular velocities to linear velocities by multiplying them by a distance, which is taken as the mean radius of the cylinder,  $\bar{r} = \frac{1}{2}(r_i + r_o)$ , where  $r_i$  = inner radius and  $r_o$  = outer radius.

The dispersion curves will again be independent of the actual size of the system if they are expressed as functions of frequency-thickness product and the thickness to radius ratio,  $\bar{r}:d$ , is maintained. In figure 2.6 dimensionless phase velocity curves for aluminium are plotted for  $\bar{r}:d$  ratios of 10:1, 5:1, 2:1 and for a flat plate. The apparent cut-off of some modes at low frequencies is actually an artefact of the calculation. This is due to certain elements in the field matrix containing the terms  $J_{k_\theta-1}(\dots)$ ,  $J_{k_\theta-2}(\dots)$ ,  $Y_{k_\theta-1}(\dots)$  and  $Y_{k_\theta-2}(\dots)$ . Unfortunately, the current calculation routines are unable to evaluate these if the order of the Bessel function is negative, as will occur if the angular wavenumber is small. In the future it is intended to use Bessel function recurrence relationships to re-write these terms so that only Bessel functions of order  $k_\theta$  or higher are required for the field matrix.

Figure 2.7 shows the dimensionless group velocity curves corresponding to the dimensionless phase velocity curves shown in figure 2.6.

It can be seen from figure 2.6 that for a radius:thickness ratio of 10:1, the difference between the phase velocity dispersion curves for a flat plate and a curved plate appear to be minimal for all modes. It is not until the radius:thickness ratio falls to below 5:1 that significant curvature effects can be visually observed on the phase velocity dispersion curves.

Consider the point where the  $A_2$  and  $S_2$  modes cross in the case of a flat plate, as shown in the inset in figure 2.6(a). In the curved case, the corresponding modes do not cross, but instead ‘repel’ and ‘swap’. This means that the mode which at one side of the crossing point followed the locus of the  $A_2$  mode afterwards follows the locus of the  $S_2$  mode and *vice versa*. This swapping effect is much more apparent on the group velocity dispersion curves shown in figure 2.7(a) even at this relatively large radius:thickness ratio. It can also be seen to be occurring on several pairs of higher order modes, most notably in the region close to the maximum of the  $S_4$  mode in the flat plate.

### 2.3.4 Conclusions

It has been shown that the effect of plate curvature on the phase velocity dispersion curves is negligible if the radius:thickness ratio is greater than around 10:1. However, the effect of curvature at certain points on the group velocity dispersion curves is significant, even at this radius:thickness ratio. There is obviously a considerable amount of further investigation required into these effects and their practical implications need to be assessed and validated.

Another interesting avenue of research is where a structure contains plates with abrupt bends or folds separating flat areas. If it is desired to propagate Lamb waves from one flat section to another around the fold, the analysis presented above will give an indication of the difference between the wave propagation characteristics in the flat and folded areas. From the difference in phase velocity of a mode between the flat and folded regions, it should be possible to infer an approximate value for the reflection coefficient of that mode when incident on the fold. This assumes that the material properties of the plate remain constant around the fold, which may not be a valid assumption in cases where the folded structure is manufactured by plastic deformation of an initially flat plate, such as in vehicle body panels.

### 2.4 EFFECT OF DISPERSION ON LAMB WAVE PROPAGATION

#### 2.4.1 Introduction

In most long range Lamb wave testing applications, Lamb waves are not excited continuously. Instead they are excited by short bursts of energy applied at one location on a plate and after propagation through the material and interaction with any defects they are received by transducers at either the same location (pulse-echo) or at other locations (pitch-catch).

A direct consequence of using an excitation signal of finite duration is that single frequency excitation can never be achieved; the excitation must have a finite bandwidth. In bulk wave ultrasonic testing this is not important since, to a first approximation, bulk waves are non-dispersive in all elastic isotropic materials. For this reason, many bulk wave NDT systems, such as thickness gauges and flaw detectors, use short pulses of energy with broadband frequency spectra. In such systems, the pulse of energy propagates without dispersion, i.e. its shape does not change as it propagates.

However, when exciting Lamb waves, broadband excitation is not ideal for two reasons: firstly because of the problems of interpreting results if more than one mode is excited (which will generally be the case if broadband excitation is used), and secondly because each Lamb wave mode is, in general, dispersive. This section is concerned with quantitatively examining the effect of dispersion on the propagation of Lamb waves. To the best knowledge of the author, this is the first time such quantitative studies have been undertaken.

#### *Manifestation of dispersion effects*

The effect of broadband excitation of a dispersive Lamb wave mode is that the energy at different frequencies propagates at different speeds. This manifests itself physically as a spreading of the Lamb wave in space and time as it propagates through the material.

This is illustrated in figures 2.8(a) and 2.9(a) (a full discussion on the calculation of these figures may be found in chapter 4), which show graphically the propagation of packets of Lamb waves in space and time. The greyscale indicates the amount of out-of-plane displacement on the plate surface at any point. In figure 2.8, the  $A_0$  mode is excited with a five cycle toneburst in aluminium plate at 1.343 MHz mm, which is a point of reasonably low dispersion. As can be seen, the 'size' of the packet remains fairly constant as it

propagates, and this is confirmed by the three cross sections on the right of the figure which represent the time signal that would be received at locations 0, 50 and 100 mm from the source. However, figure 2.9 shows the effect of exciting the  $S_0$  mode at 2.0 MHz mm with a five cycle toneburst. Here, the energy packet can be seen to be spreading out in distance and time. This is demonstrated in the cross sections shown in the figure which again represent time signals that would be measured at 0, 50 and 100 mm from the source. In these graphs, the effect of dispersion is manifested as an increase in the duration of the signal in time and a decrease in its amplitude.

Both the dispersion effects of signal spreading and the reduction in signal amplitude are undesirable in long range Lamb wave testing.

The spreading of wave packets in space and time reduces the amount of resolution available. Consider a packet of Lamb waves which have propagated a distance  $l$  from a transmitting transducer when they arrive at a reflector. Some of the energy packet is reflected back towards the transducer and some continues past the reflector. A distance  $\delta$ , which is assumed to be small compared to  $l$ , beyond the first reflector is a second reflector from which a second packet of energy is reflected back towards the transducer. If the transducer is being used in pulse-echo mode, then the presence of both reflectors will only be detectable if the two reflections can be resolved. A common practical situation is when one of the reflectors is the edge of a plate which produces a large reflection, and the second reflector is a defect near the edge which produces a smaller reflection. In such a case, the defect can only be detected if the two reflections can be resolved.

As an example, figure 2.10 illustrates the effect of two reflectors generating two signals in a received time-trace. Both reflected signals are assumed to be identical tonebursts with a centre frequency of 1 MHz although they differ in amplitude by a factor of two. In figure 2.10(a), the spatial separation of the reflectors is such that the two reflected signals are completely separated in time. As the separation between the reflectors is reduced, the reflected signals begin to overlap, as illustrated in figure 2.10(b) and (c) until they become indistinguishable as shown in (d). However, if the received signals from the two reflectors were 5 rather than 20 cycle tonebursts, then the two signals would be separated in time as shown in (e), although the separation of the reflectors is the same as in (d). This simple example shows how the resolution of a long range inspection system is improved if the duration of received signals can be reduced. The exact separation at which the two signals become indistinguishable is somewhat subjective and in a practical application would depend on the sophistication of any signal processing techniques being used. However, it is assumed for the purposes of this work, that the signals must be completely separated in time to guarantee resolvability.

The reduction in amplitude of a dispersive signal reduces the sensitivity of the testing system, and hence the maximum propagation distance which can be achieved before the signal becomes undetectable is also reduced. The studies presented here are primarily concerned with the temporal effects of dispersion, but as a first approximation it can be assumed that the fractional change in amplitude is inversely proportional to the fractional change in duration of a signal due to dispersion.

### *Avoiding dispersion effects*

Lockett (1973) stated that to avoid dispersion effects when using broadband pulses of energy, the operating point on a Lamb wave mode should be at a point where the phase velocity is independent of frequency. Practically, this constrains the operating point on a mode to be well into the high frequency thickness region, in which all Lamb wave modes tend towards being Rayleigh waves on the surfaces of the plate. If tonebursts of limited bandwidth are used instead of pulses, many more operating points appear to become viable in regions where the group velocity curves are stationary with respect to frequency, as noted by Alleyne and Cawley (1992). Operating points of this type are marked by circles on the group velocity dispersion curves for aluminium shown in figure 2.11. As will be shown in the following sections, this qualitative method of selecting operating points is not only limiting, but also somewhat misleading in terms of predicting the amount of dispersion likely, particularly when looking at higher order modes.

By developing a quantitative measure of the dispersion associated with any point on the Lamb wave dispersion curves, this section will show how this measure can be used to:

- increase the size of perceived suitable operating regions on the fundamental and lower order modes.
- demonstrate that points of stationary group velocity on higher order Lamb wave modes may still be unusable for NDT applications.
- select the optimum input signal for a particular operating point

### **2.4.2 Dispersivity**

Consider a packet of Lamb wave energy propagating as a single mode through an isotropic, lossless plate in vacuum. The plate is also assumed to be two dimensional, that is, the Lamb waves are straight crested and are assumed to extend to infinity in the direction normal to the direction of propagation. The packet of Lamb waves starts to pass a fixed station at some position in the plate at time  $t_1$  and finishes passing at time  $t_2$ . Some distance,  $l$ , further along the plate the same packet of energy later passes a second station, starting to pass at time  $t_3$  and finishing passing at time  $t_4$ . At the first station, the duration of the wave packet in time is  $t_2-t_1$ , and at the second station the duration is  $t_4-t_3$ . If the wave packet is propagating without dispersion then  $(t_4-t_3)=(t_2-t_1)$ , but if dispersion is present then  $(t_4-t_3)>(t_2-t_1)$ . Thus a change in signal duration,  $\Delta T$ , may be defined:

$$\begin{aligned} \Delta T &= T_{out} - T_{in} \\ &= (t_4 - t_3) - (t_2 - t_1) \end{aligned} \tag{2.31}$$

If the packet of Lamb waves contains waves with a range of group velocities from  $v_{min}$  to  $v_{max}$ , then the temporal limits of the wave packet as it passes the second station may be expressed in terms of these velocities. The time,  $t_3$ , when the wave packet first reaches the second station cannot be earlier than the time taken for the fastest propagating waves to travel the distance  $l$  starting at time  $t_1$ . Similarly, the time,  $t_4$ , when the signal finishes passing the second station cannot be later than the time taken for the slowest propagating waves to travel the distance  $l$  starting at time  $t_2$ . Hence:

$$\begin{aligned}
 t_3 &= t_1 + \frac{l}{v_{\max}} \\
 t_4 &= t_2 + \frac{l}{v_{\min}}
 \end{aligned}
 \tag{2.32}$$

And equation 2.31 can be re-written as:

$$\begin{aligned}
 \Delta T &= \left( (t_2 + l/v_{\min}) - (t_1 + l/v_{\max}) \right) - (t_2 - t_1) \\
 &= l(1/v_{\min} - 1/v_{\max})
 \end{aligned}
 \tag{2.33}$$

This shows, as should be expected, that the duration of the wave packet will increase linearly with the distance travelled. This obviously assumes that the exact bounds of the group velocity range can be identified, which in turn means that the frequency bandwidth of the input signal must be exactly defined. In practice the bandwidth of the input signal can only be specified in terms of the points where its spectrum drops below  $n$  dB with respect to its maximum value. Within this bandwidth,  $x$  % of the energy of the signal is contained. If the group velocity limits are calculated within this frequency bandwidth, equations 2.32 and 2.33 then give the temporal limits of the wave packet in which  $x$  % of the total energy is contained. Without *a priori* knowledge of the relationship between group velocity and frequency over the signal bandwidth, it is not possible to infer directly what the amplitude of the signal at the times  $t_3$  and  $t_4$  are, with respect to the peak amplitude - i.e. these times are not necessarily the times at which the signal drops  $n$  dB below the peak value.

Although a spreading of a signal in time is the way in which dispersion will generally be observed, it is the spatial size of a signal which will limit the spatial resolution which can be obtained. However, at a particular point in space, the spatial duration will actually be increasing as the signal passes that point, so in order to convert the change in temporal size of a signal given by equation 2.33 to a change in spatial size, equation 2.33 is multiplied by a nominal group velocity,  $v_0$ , to give a measure of the mean spatial size of a signal as it passes a point in space:

$$\Delta L = v_0 l(1/v_{\min} - 1/v_{\max})
 \tag{2.34}$$

Finally, equation 2.34 can be differentiated with respect to distance,  $l$ , to obtain the rate of increase in spatial duration:

$$\frac{d}{dl} \Delta L = v_0 (1/v_{\min} - 1/v_{\max})
 \tag{2.35}$$

This quantity is constant for a particular signal, and will be defined as the dispersivity of the signal. The dispersivity is therefore a dimensionless quantity that measures the rate of spatial increase in size of a signal with respect to distance travelled.

The dispersivity is a measure of the dispersion of a packet of Lamb waves generated by a particular input signal, the input signal being associated with a particular frequency. But in order to investigate the dispersivity at different frequencies and hence different points on the dispersion curves, the frequency associated with the input signal must be variable. Hence, equation 2.35 cannot, in itself, provide a measure of the relative dispersion of different points on the Lamb wave dispersion curves. In order to obtain a relative measure

of this type, the frequency content of the input signal must be altered, and this can be effected in two ways which are discussed below.

*Dispersivity curves calculated using a constant shape of input signal*

Firstly, consider an input signal with a particular shape, such as a Hanning windowed toneburst of  $n$  cycles. To adjust the frequency content, this signal is stretched or compressed in time. For a Hanning windowed toneburst of  $n$  cycles and a centre frequency  $f_c$ , the bandwidth is between the frequencies  $f_{min}$  and  $f_{max}$ . These frequency limits can be shown (see appendix B) to be given by the following equations:

$$\begin{aligned} f_{min} &= f_0 \left( 1 - \frac{k}{n} \right) \\ f_{max} &= f_0 \left( 1 + \frac{k}{n} \right) \end{aligned} \tag{2.36}$$

where  $k$  is a constant depending on the bandwidth measure being used. In this section the bandwidth will be considered to be defined by the 40 dB down points of the spectrum (the points where the frequency spectrum drops below 40 dB with respect to its maximum value) in which case a value of 2.8 is used for  $k$ . Clearly, if the number of cycles,  $n$ , in the toneburst is kept constant then the absolute bandwidth of the signal is proportional to the centre frequency,  $f_c$ .

In order to use this method to calculate the amount of dispersivity as a function of frequency for a given Lamb wave mode, a standard input signal with a fixed number of cycles must be selected. For a particular centre frequency,  $f_0$ , the bandwidth limits,  $f_{min}$  and  $f_{max}$ , of the toneburst are calculated using equation 2.36. The maximum group velocity,  $v_{max}$ , and minimum group velocity,  $v_{min}$ , of the Lamb wave mode being examined are then found in that frequency range, and the value for the nominal group velocity,  $v_0$ , is taken as being the group velocity of that mode at the centre frequency,  $f_0$ . A measure of the dispersivity at any centre frequency,  $f_0$ , may then be calculated from equation 2.35.

As an illustration, figures 2.12(a), (b) and (c) show the dispersivity curves for 10, 20 and 50 cycle Hanning windowed tonebursts in aluminium plate.

The sharp dips in all the curves shown in figures 2.12(a), (b) and (c) are points of minimum dispersion, and comparison with the group velocity curves in figure 2.11 reveal that these points correspond, as expected, with the points of stationary group velocity. It is interesting to compare the relative amplitudes of the minimum dispersivity between modes. Considering figure 2.12(a) only, it can be seen that the minimum in dispersivity of the  $A_0$  mode at a dimensionless frequency of 0.487 is almost zero, whereas none of the minima for other modes fall much below 0.2, except in the case of the  $S_0$  mode as the frequency tends to zero. Even for larger numbers of cycles in the toneburst, the absolute values of the dispersivity are reduced, but the ratio between the minimum dispersivity of  $A_0$  and the minima in dispersivities of the other modes is approximately maintained. The obvious conclusion is that the almost negligible dispersivity which can be achieved by using the  $A_0$  mode at a dimensionless frequency 0.487 can never be matched when using higher order modes at their points of stationary group velocity.

Another interesting feature of the graphs in figures 2.12(a), (b) and (c) is the dispersivity of the  $A_0$  mode at dimensionless frequencies below 0.487. Although rising, the level of dispersivity in this region is still lower than can be achieved using most higher modes. This result appears somewhat surprising, due to the rapidly changing group velocity in this region (see figure 2.11) but becomes understandable if the dispersion curves are re-plotted on logarithmic axes, as has been done in figure 2.13. This type of scale means that the bandwidth of a tonebursts with a fixed number of cycles is represented by a vertical band of fixed width, independent of the centre frequency. It can be seen that in the low frequency region, the group velocity of the  $A_0$  mode in figure 2.13(b) is not changing particularly rapidly with respect to the logarithmic frequency, hence explaining the low dispersivity in this region.

The method described above for calculating the dispersivity is straightforward to compute and presents an immediately obvious measure of relative dispersion.

However, this method is biased towards predicting higher dispersivities at higher frequencies since the bandwidth of the input signal is increasing linearly with frequency. But as the frequency is increased, the temporal duration of the input signal decreases, so a greater degree of dispersion ought to be tolerated for a given target resolution. An alternative method of calculating the relative dispersivities of different points on a Lamb wave mode is to maintain an input signal of constant duration, and this is described below.

*Dispersivity curves calculated using a constant duration of input signal*

The duration of a Hanning windowed toneburst of  $n$  cycles at a centre frequency,  $f_0$ , is  $n/f_0$ . Hence for a toneburst of duration  $T_0$ , the number of cycles must be made equal to  $T_0 f_0$ . If this is done then the bandwidths in equations 2.36 become:

$$\begin{aligned} f_{\min} &= f_c \left( 1 - \frac{k}{f_c (t_2 - t_1)} \right) \\ f_{\max} &= f_c \left( 1 + \frac{k}{f_c (t_2 - t_1)} \right) \end{aligned} \tag{2.37}$$

Hence, the bandwidth  $f_{\max} - f_{\min}$  is now frequency independent. The dispersivity curves for a 1 mm thick aluminium plate may now be recalculated. Using the ratio of the plate thickness,  $d$ , to the bulk shear velocity,  $v_s$ , as a measure of time, figures 2.14(a), (b) and (c), show dispersivity curves with durations of 10, 20 and 50  $v_s/d$  respectively.

The graphs in figure 2.14 show a somewhat different picture of the dispersivity to those in figure 2.12. In particular, the lower order modes now look considerably less attractive, with the minimum in the dispersivity of the  $A_0$  mode no longer significantly lower than the minima on many higher order modes. From this perspective, the use of higher order modes appears more feasible, but there are other concerns which make them less attractive, such as the problems of modal selectivity and attenuation, both of which will be covered in later chapters.

If the examination of dispersivity using a toneburst with a fixed number of cycles corresponds to the dispersion curves plotted on a logarithmic frequency scale, then the

method described above, using a fixed duration of toneburst corresponds to the dispersion curves plotted on a linear frequency scale.

### 2.4.3 Resolvable distance

The two methods of investigating the effects of dispersion described above are based on examining the rate of signal spreading in space - the dispersivity. However, there is an alternative route of investigation that lends itself to a more direct physical application, and which also removes the ambiguity of how to compare different points on the dispersion curves.

Instead of considering the rate of signal spreading, the propagation of waves over a fixed distance,  $l$ , is examined. From equations 2.31 and 2.33, the duration of a signal received a distance  $l$  from the source is:

$$\begin{aligned} T_{out} &= \left( (t_2 + l/v_{\min}) - (t_1 + l/v_{\max}) \right) \\ &= l(1/v_{\min} - 1/v_{\max}) + (t_2 - t_1) \\ &= l(1/v_{\min} - 1/v_{\max}) + T_{in} \end{aligned} \quad (2.38)$$

The temporal duration of the received signal,  $T_{out}$ , may again be converted to a spatial duration,  $l_{out}$ , by multiplying by a nominal group velocity  $v_0$ , which is again taken as being the group velocity of the mode at the centre frequency,  $f_0$ , of the input signal. To obtain a dimensionless quantity, the spatial duration,  $l_{out}$ , is divided by the thickness of the plate  $d$ :

$$l_{out}/d = \frac{v_0(l(1/v_{\min} - 1/v_{\max}) + T_{in})}{d} \quad (2.39)$$

The quantity  $l_{out}/d$  will be termed the resolvable distance, as it indicates the spatial duration of a Lamb wave signal a distance  $l$  from a source, as a multiple of the plate thickness.

On first inspection, the concept of resolvable distance has merely introduced another variable into the problem, namely the propagation distance,  $l$ , in addition to the variable nature of the input signal. However, as will be shown below, for any particular propagation distance,  $l$ , and at any point on the dispersion curves, a single input signal can be found which minimises the resolvable distance.

#### *Minimum resolvable distance curves*

Let the input signal again be constrained to being a Hanning windowed toneburst of  $n$  cycles and centre frequency  $f_c$ . The resolvable distance given by equation 2.39 can be seen to be governed by two components, firstly the duration of the input signal,  $T_{in}$ , and secondly by the increase in duration of the signal due to dispersion given by  $l(1/v_{\min} - 1/v_{\max})$ . At a particular frequency, and with a small number of cycles in the input toneburst,  $T_{in}$  will be small, but the bandwidth will be large and dispersion effects will be significant. As the number of cycles is increased, the bandwidth is reduced and dispersion effects become less significant but  $T_{in}$  becomes larger. At some point in between, a minimum in the resolvable distance will be found. This is demonstrated for the  $S_1$  mode at a centre frequency of 4.03 MHz mm in figure 2.15. The figure shows a graph of

resolvable distance vs. number of cycles in the input signal for various propagation distances. Hence, at any particular centre frequency the duration of the received signal,  $T_{out}$ , may be minimised by adjusting the number of cycles. The dotted line through the minima of the resolvable distance curves in figure 2.15 shows clearly how the number of cycles in the input signal should be varied, depending on the propagation distance, to minimise the resolvable distance. The only condition for a minimum to exist, is that the Lamb wave mode being examined must exhibit some dispersion, otherwise the duration of  $T_{out}$  will increase monotonically with  $n$ , and the minimum of  $T_{out}$  will always be zero. Example resolvable distance curves calculated at distances of 100, 500 and 1000  $d$  from the source are shown in figure 2.16. It should be stressed that the resolvable distance curves do not simply scale linearly with distance, due to the non-linear nature of the group velocity curves.

It can be seen from the figure that at low frequencies, the  $A_0$  mode has a minimum resolvable distance at a dimensionless frequency of 0.487 which is around half that of the other modes. This will be a common operating point for the inter-digital transducers which will be described in later chapters. Even at frequencies of around half of this value, the  $A_0$  mode still has smaller resolvable distances than the low frequency minima of the  $A_1$  and  $S_1$  modes. The abrupt increase in resolvable distance of the  $S_0$  mode at very low frequencies arises because the software written to perform the calculation does not allow the input signal to contain less than one cycle. Figure 2.16(c) indicates that several points on modes at higher frequencies have minimum resolvable distances which are comparable to the  $A_0$  mode at its low frequency minimum, notably the  $S_1$ ,  $A_2$ ,  $S_2$ ,  $A_3$  and  $S_3$  modes. However, the resolvable distance of the  $A_0$  and  $S_0$  modes at higher frequencies is always lower than the minima in other modes. At these frequencies, the fundamental Lamb waves are effectively propagating as two Rayleigh waves, one on each surface of the plate. Although such waves exhibit low dispersion, it should be noted that the energy within them is concentrated close to the surfaces of the plate. Hence, as the fundamental Lamb wave modes tend towards Rayleigh waves, so their sensitivity to defects within the thickness of the plate is reduced.

### 2.4.4 Optimum number of cycles in input signal

An obvious by-product of the minimum resolvable distance curves is that the optimum number of cycles in the input signal is also calculated. These are plotted for the same distances in figure 2.17. As expected, the optimum number of cycles tends to increase as the propagation distance is increased and dispersion effects outweigh the initial duration of the signal. Even in the case of the  $A_0$  mode at the dimensionless frequency of 0.487, the optimum number of cycles required increases from 5 to 10 as the propagation distance is increased. An obvious question which arises from this observation is whether or not the number of cycles required reaches a limit as the propagation distance is increased further. Although such a study has not been performed, it is the opinion of the author that such a limit will not be reached, and that the optimum number of cycles at any operating point will increase monotonically (but not linearly) with propagation distance.

### 2.4.5 Conclusions

In this section, the effect of dispersion on the propagation of Lamb wave signals has been quantified. The two ways of calculating the dispersivity which have been described have

been shown to correspond to two different ways in which the group velocity dispersion curves can be viewed. If the input signal is a toneburst with a fixed number of cycles then the group velocity dispersion curves must be considered on a logarithmic frequency scale. On the other hand, if the input signal is a toneburst with constant duration the group velocity dispersion curves may be considered on a linear frequency scale.

The concept of a minimum resolvable distance which is associated with any point on the dispersion curves has been introduced and used to provide a comparison of the resolution which may be obtained between different modes over a particular propagation distance.

### 2.5 CONCLUSIONS

This chapter has been concerned with theoretical considerations of Lamb wave characteristics. In addition to reviewing the existing theory of Lamb wave propagation in free flat plates, two new topics have been addressed, the effect of curvature and the effect of dispersion.

The effect of curvature has been shown to have a minor effect on the phase velocity dispersion curves for moderate degrees of curvature. However, the group velocity dispersion curves which have been produced for curved plates indicate that mode repulsion takes place at some of the locations where modes cross in the flat plate case, even at moderate degrees of curvature. These effects have not been verified here since they are of somewhat academic interest from the perspective of the work described here. However, if more work is to be done on the propagation of Lamb waves along plates with bends, this area will become more important.

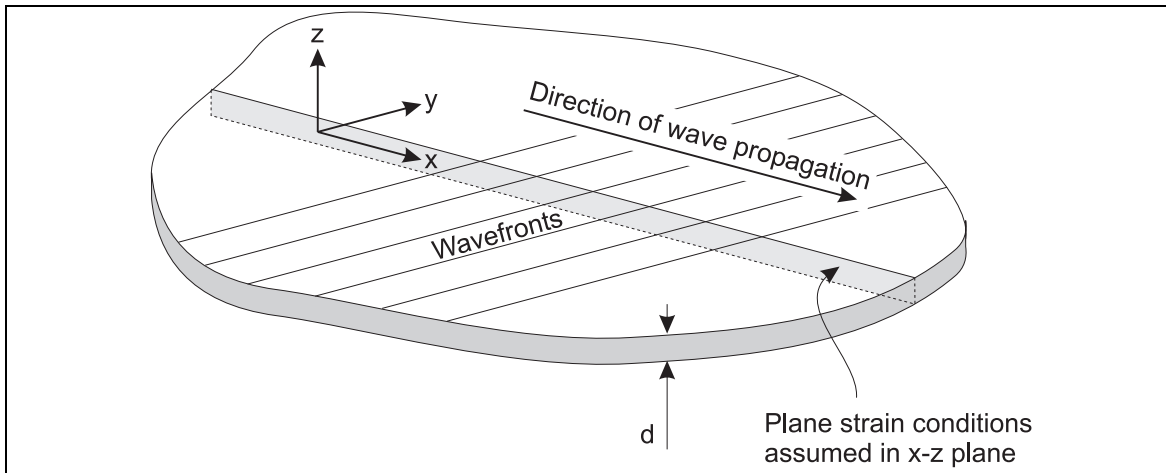


Figure 2.1 Diagram of flat isotropic plate, showing orientation of axes, wave propagation direction and wavefronts.

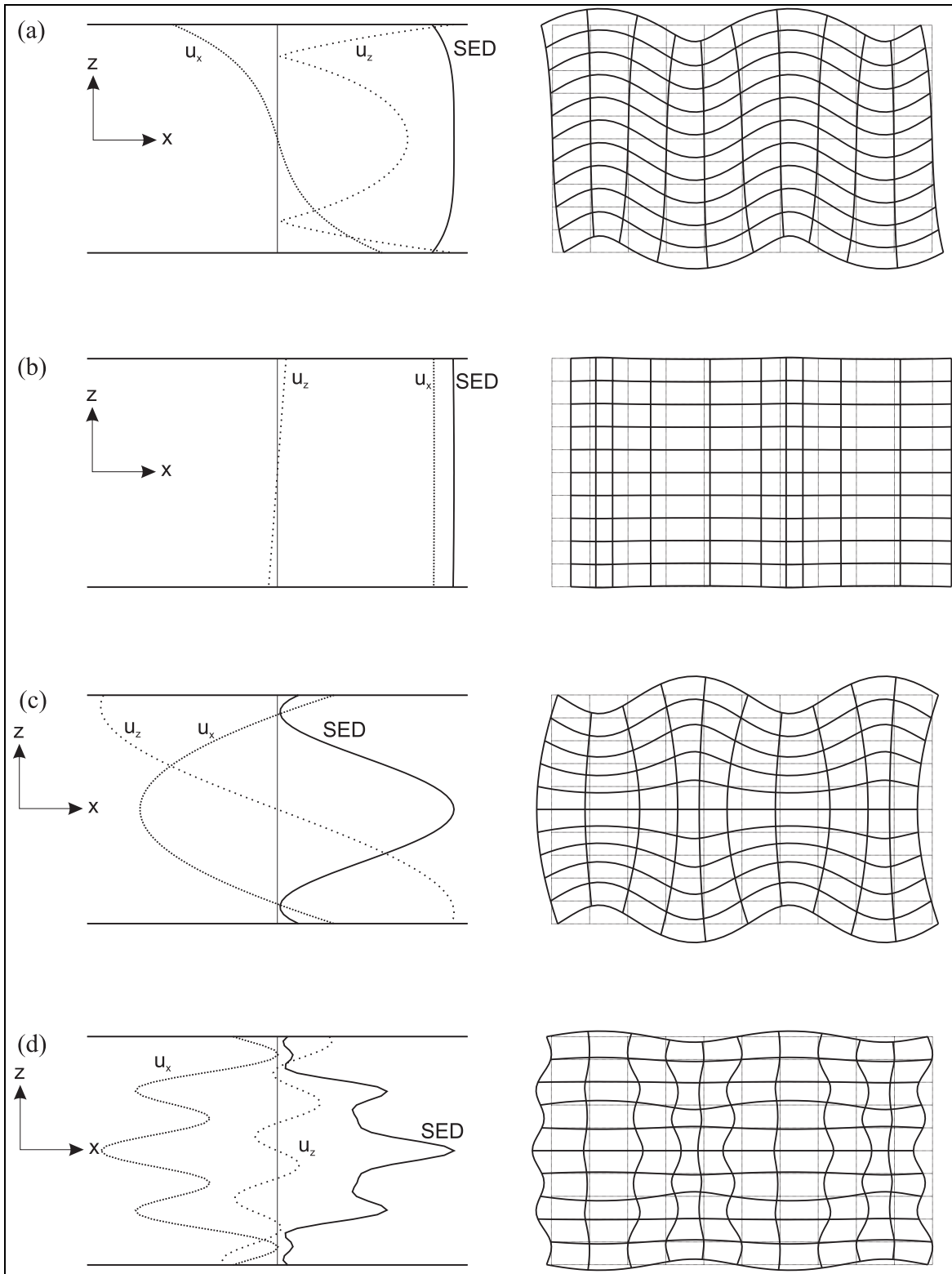


Figure 2.2 Examples of Lamb wave mode shapes in aluminium, showing, on the left, the variation of in-plane ( $u_x$ ), out-of-plane ( $u_z$ ) particle displacements and strain energy density (SED) through the plate thickness. The diagrams on the right show the deformation of the plate for each case. The modes and dimensionless frequencies are (a)  $A_0$  at 0.44, (b)  $S_0$  at 0.05, (c)  $S_0$  at 0.80 and (d)  $S_4$  at 4.17.

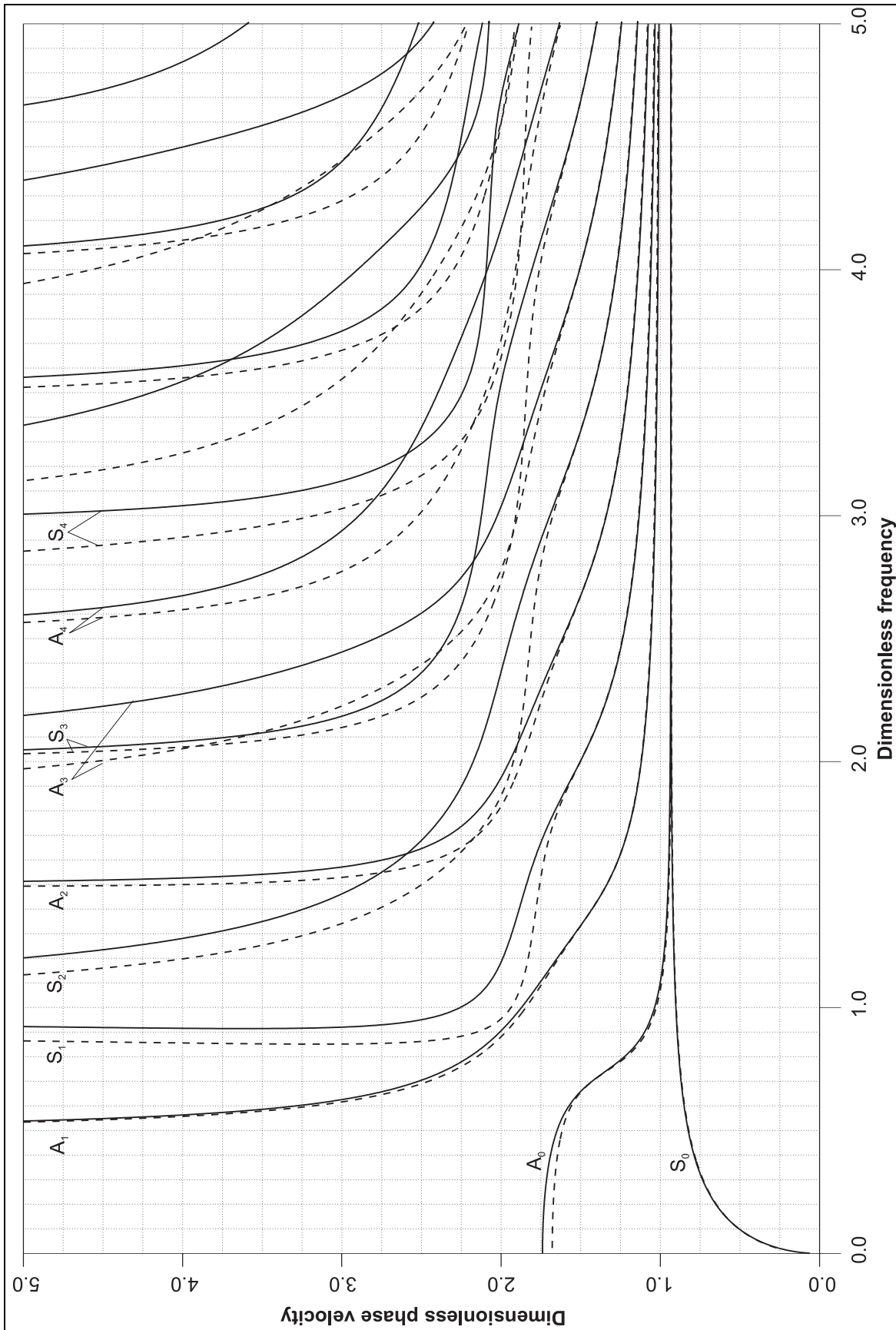


Figure 2.3 Phase velocity dispersion curves for aluminium (continuous lines) and steel (dashed lines) on dimensionless axes.

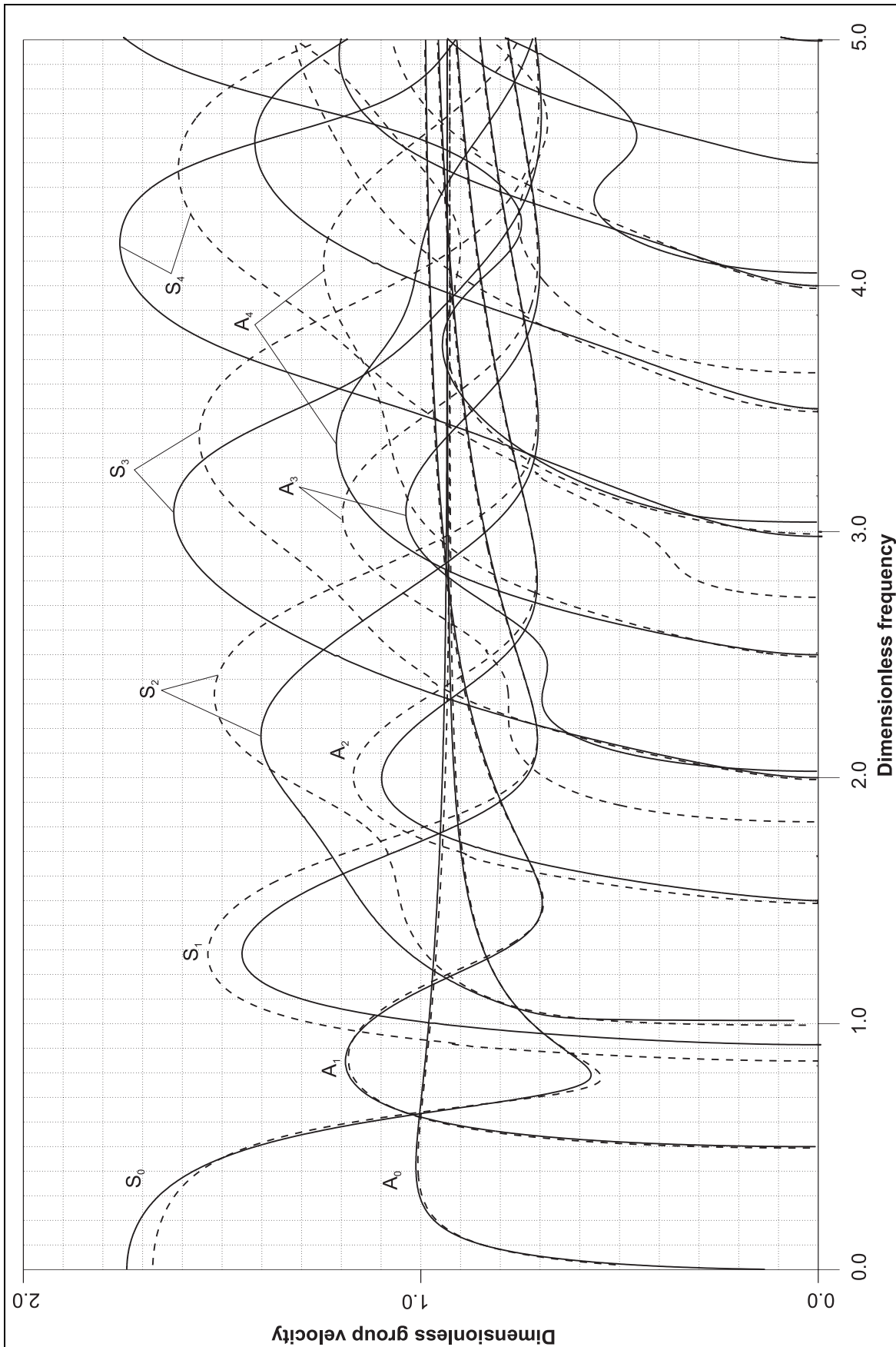


Figure 2.4 Group velocity dispersion curves for aluminium (continuous lines) and steel (dashed lines) on dimensionless axes.

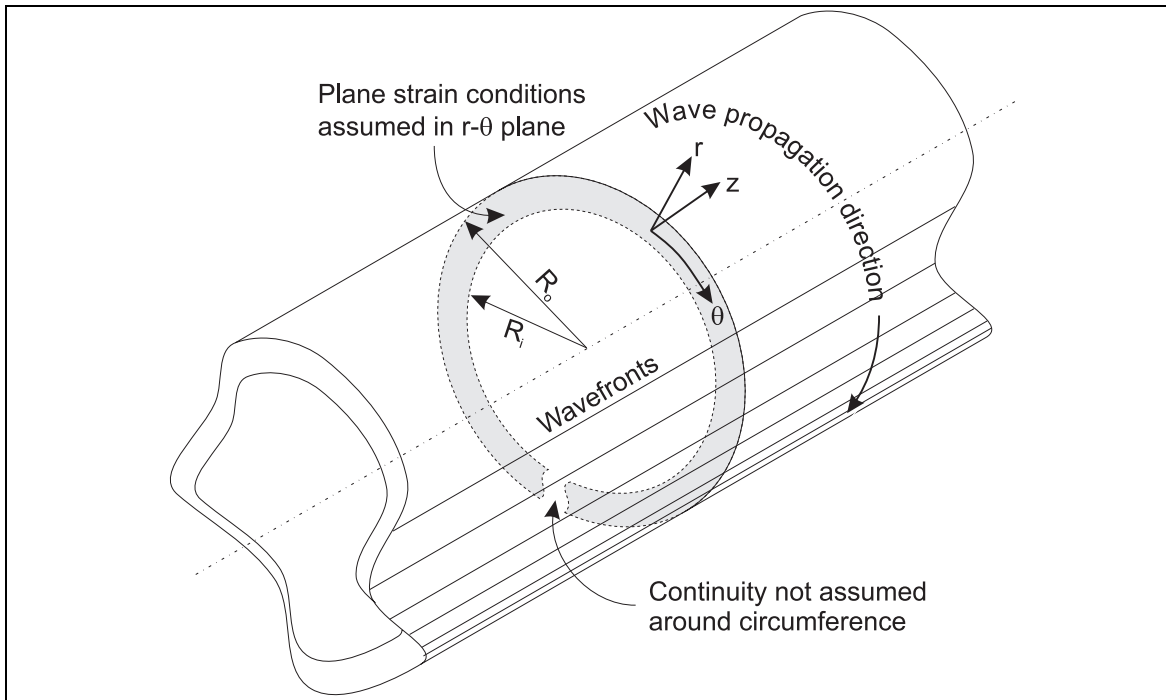


Figure 2.5 Schematic diagram showing nomenclature for wave propagation in curved plates.

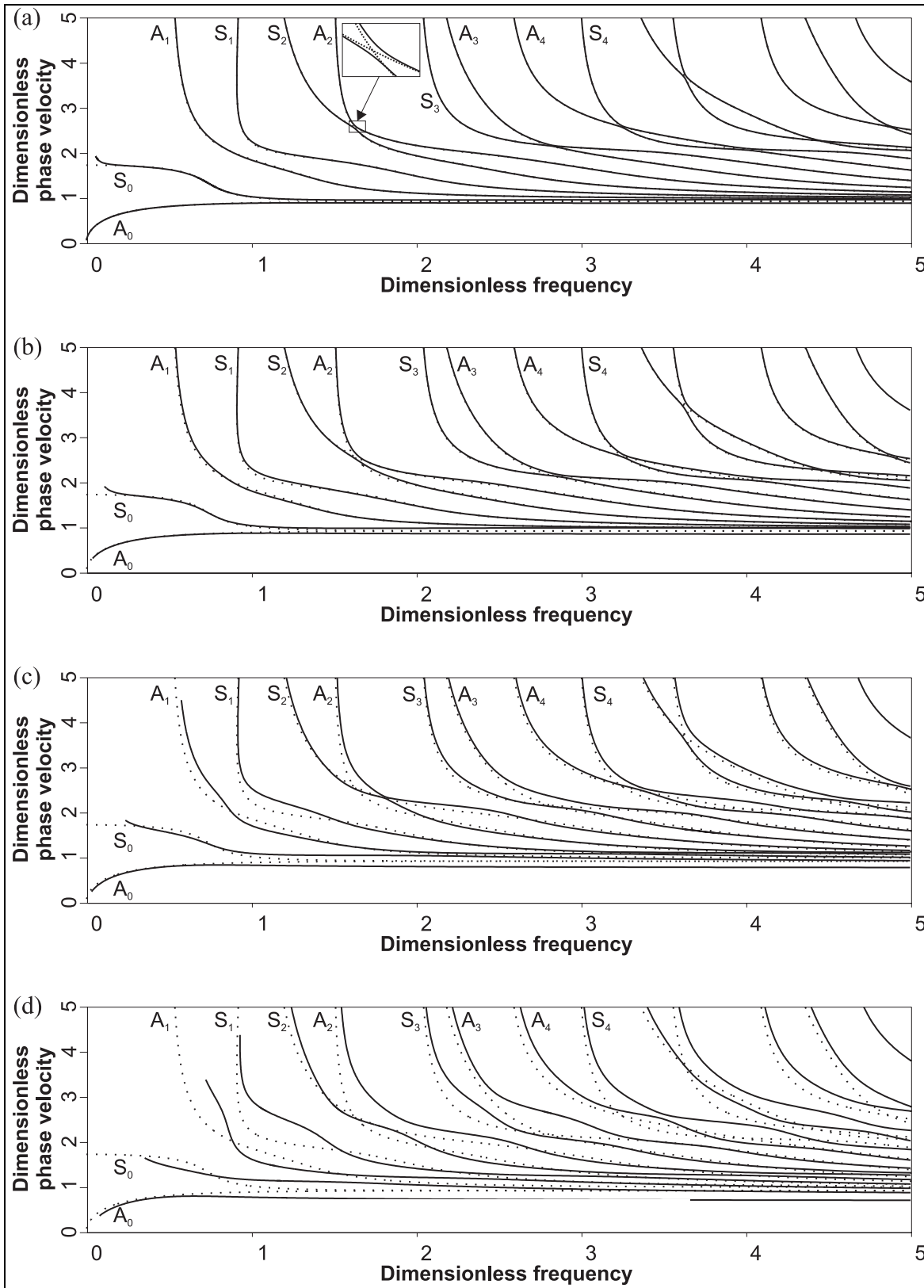


Figure 2.6 Phase velocity dispersion curves for aluminium on dimensionless axes for radius:thickness ratios of (a) 10:1, (b) 5:1, (c) 2:1 and (d) 1:1. The dispersion curves for a flat plate of the same thickness are indicated by the dotted lines.

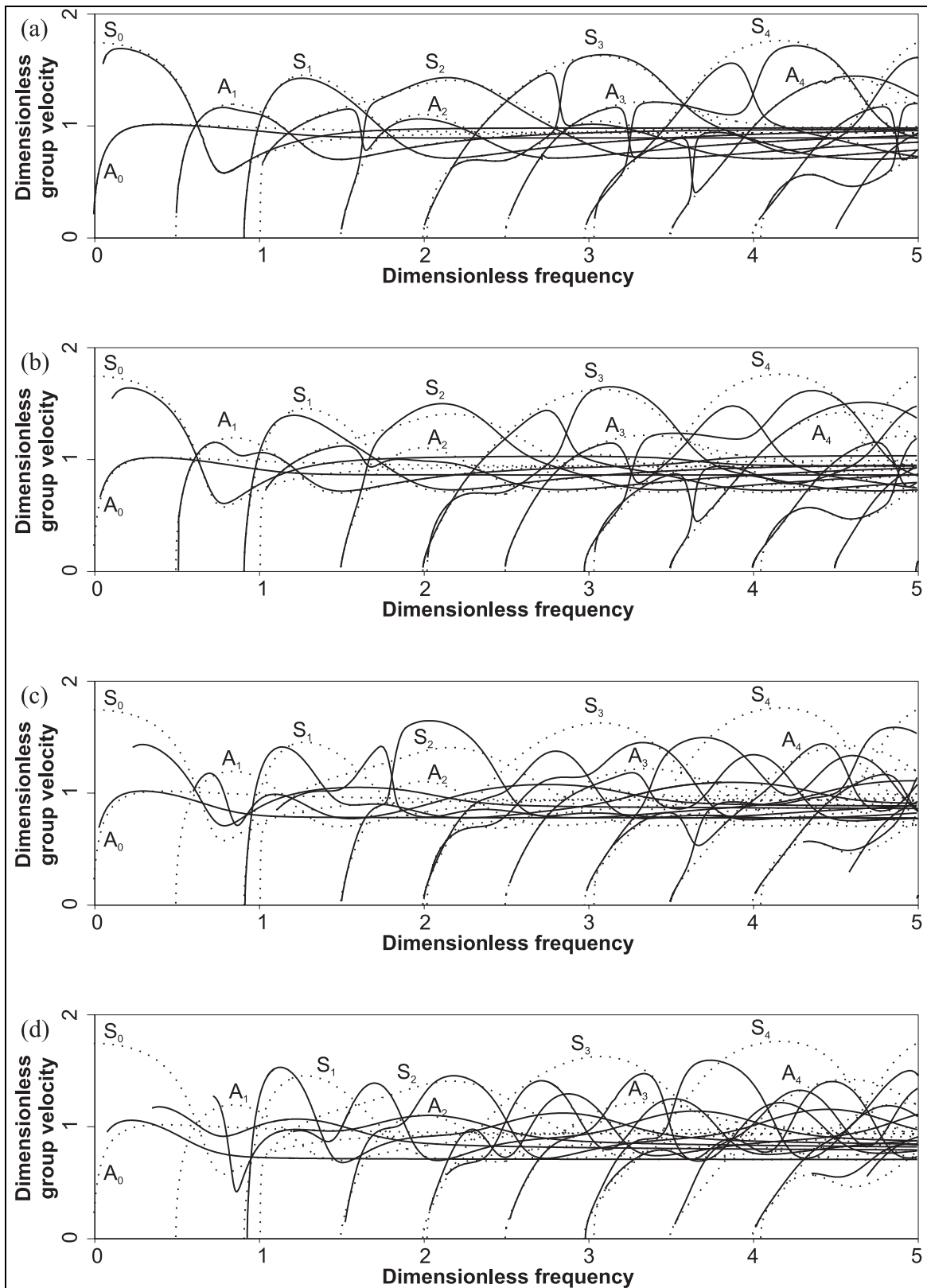


Figure 2.7 Group velocity dispersion curves for aluminium on dimensionless axes for radius:thickness ratios of (a) 10:1, (b) 5:1, (c) 2:1 and (d) 1:1. The dispersion curves for a flat plate of the same thickness are indicated by the dotted lines.

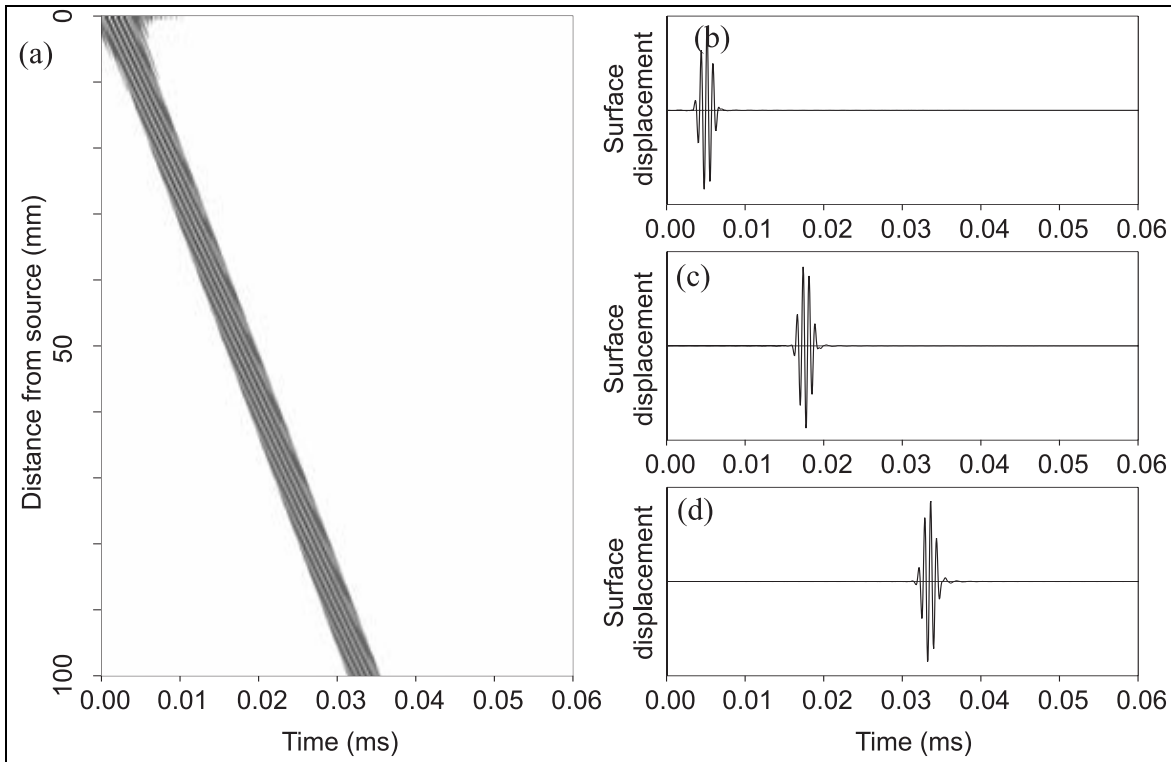


Figure 2.8 Example of low dispersion. (a) Distance-time plot showing propagation of  $A_0$  mode Lamb waves at 1.343 MHz mm. (b), (c) and (d) show time-traces that would be received at distances of 0, 50 and 100 mm from the source.

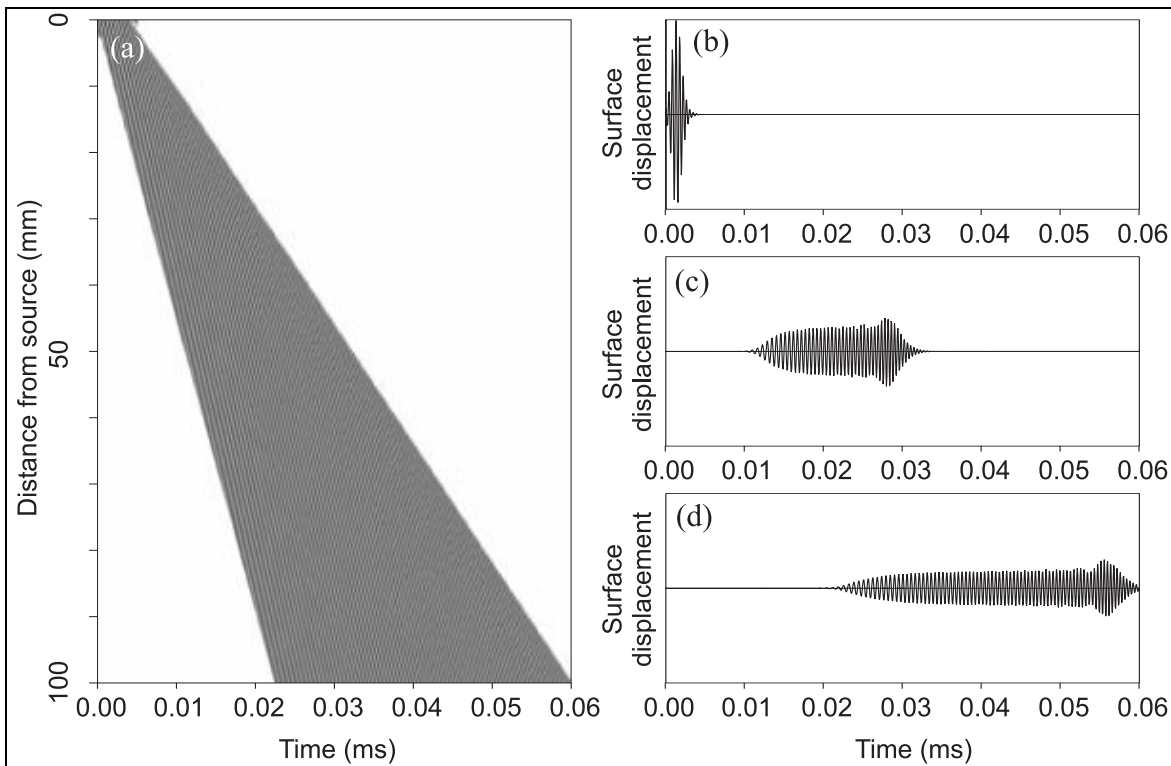


Figure 2.9 Example of high dispersion. (a) Distance-time plot showing propagation of  $S_0$  mode Lamb waves at 2.000 MHz mm. (b), (c) and (d) show time-traces that would be received at distances of 0, 50 and 100 mm from the source.

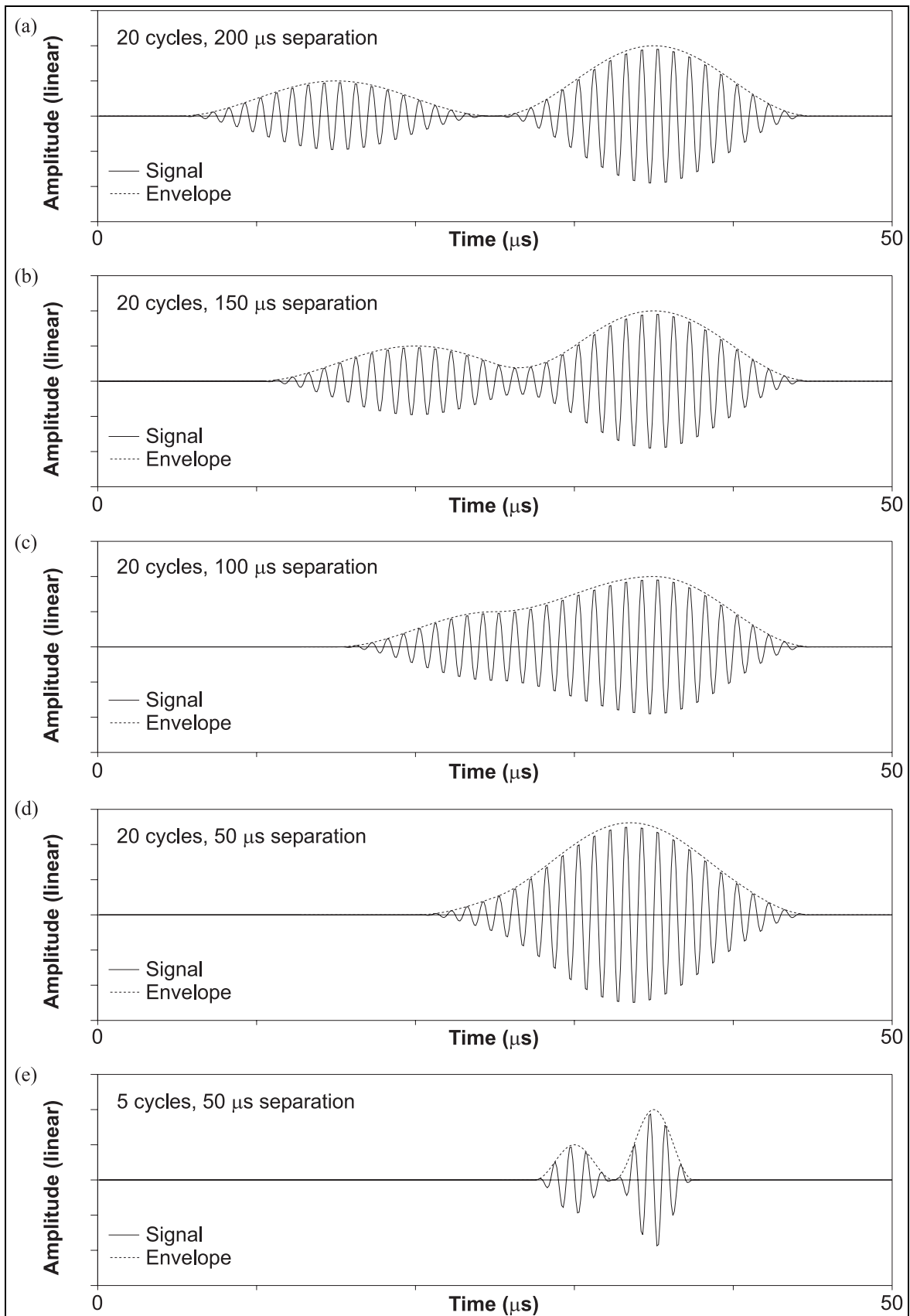


Figure 2.10 Predicted time-traces showing (a) two 20 cycle tonebursts completely separated in time. The effect of reducing the separation is shown in (b), (c) and (d). (e) shows the effect of reducing the number of cycles to 5 while maintaining the separation shown in (d).

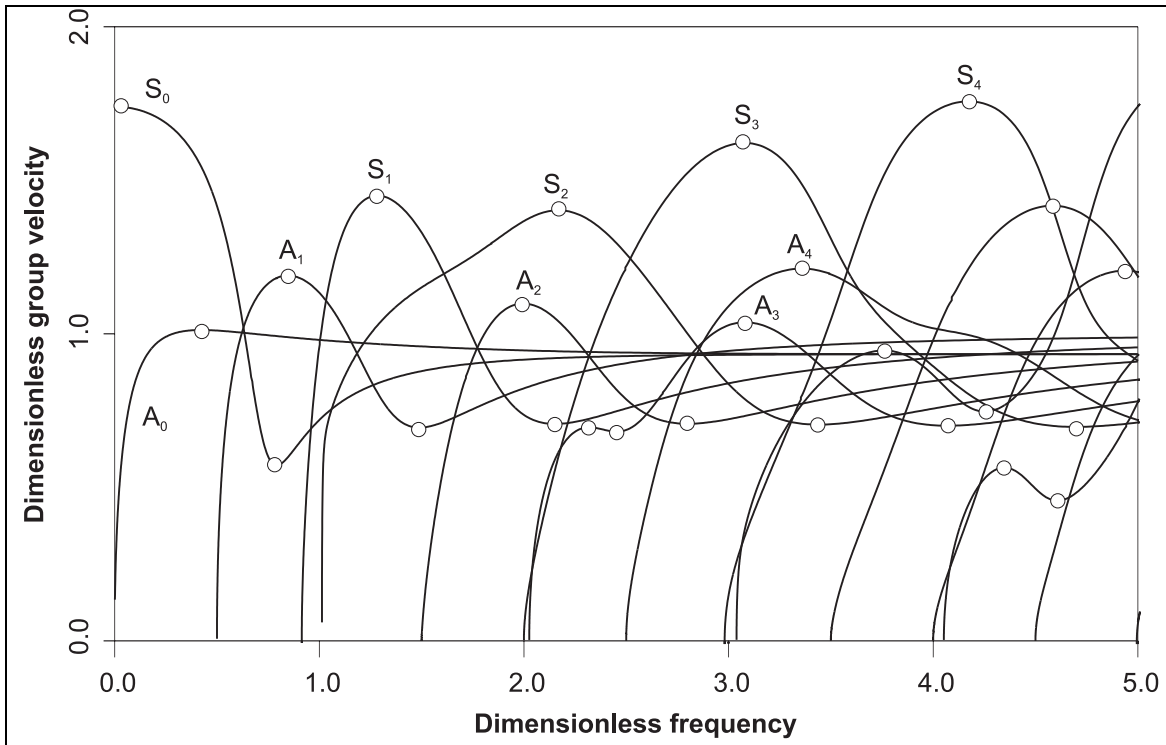


Figure 2.11 Group velocity dispersion curves for aluminium with stationary points marked by the white circles.

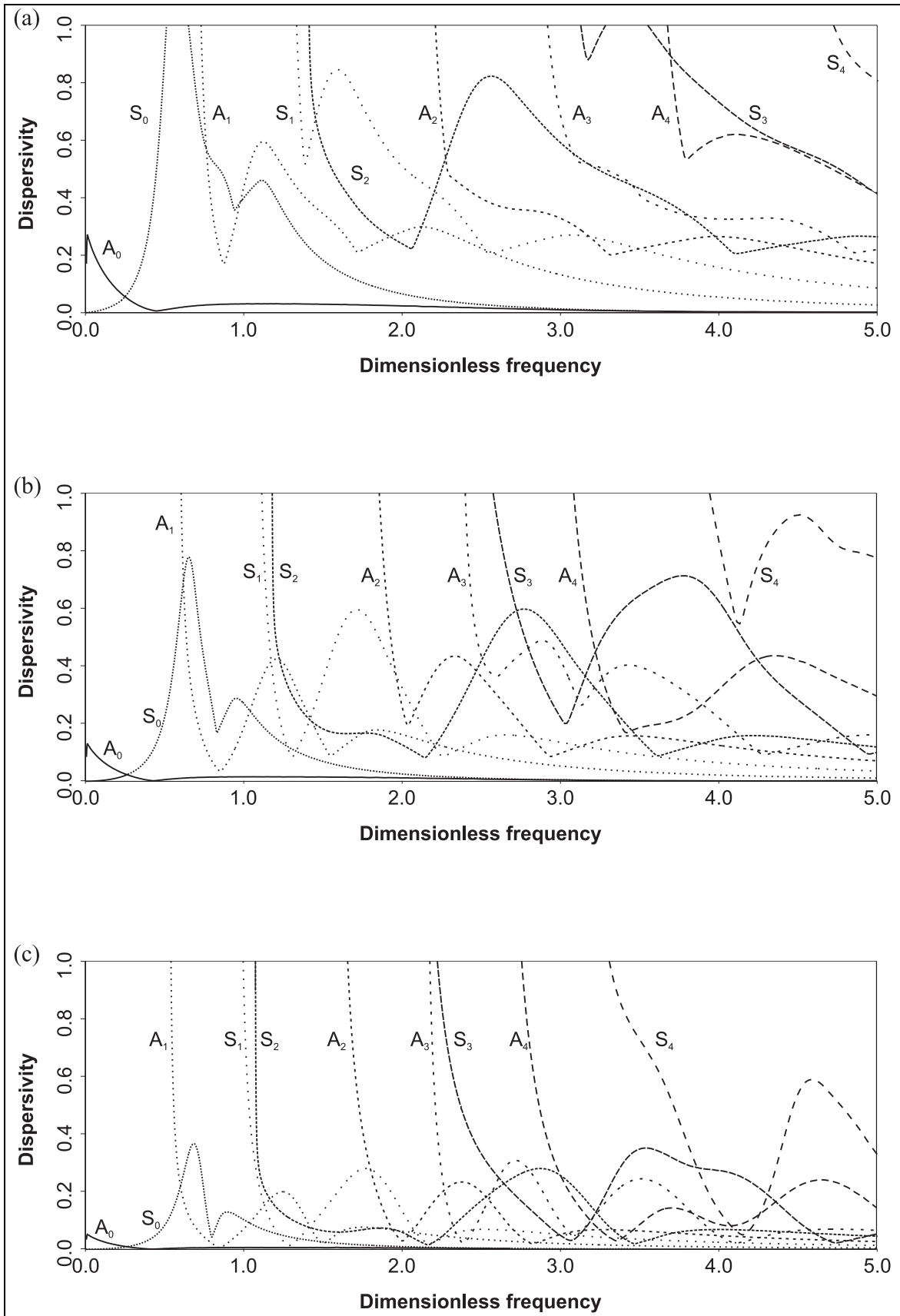


Figure 2.12 Dispersivity curves for aluminium using input signals with (a) 10, (b) 20 and (c) 50 cycles.

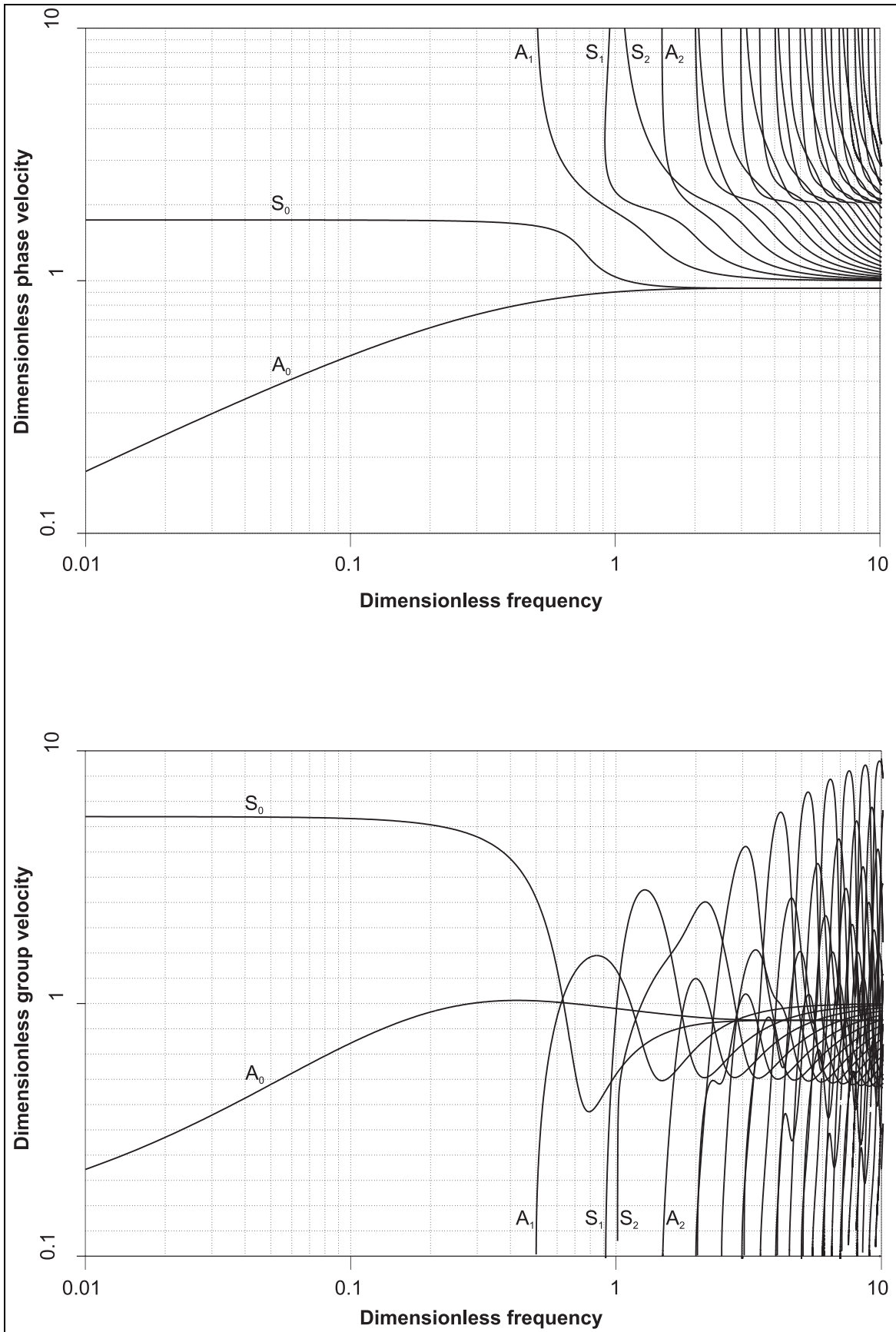


Figure 2.13 (a) Phase and (b) group velocity dispersion curves for aluminium plotted on dimensionless logarithmic axes.

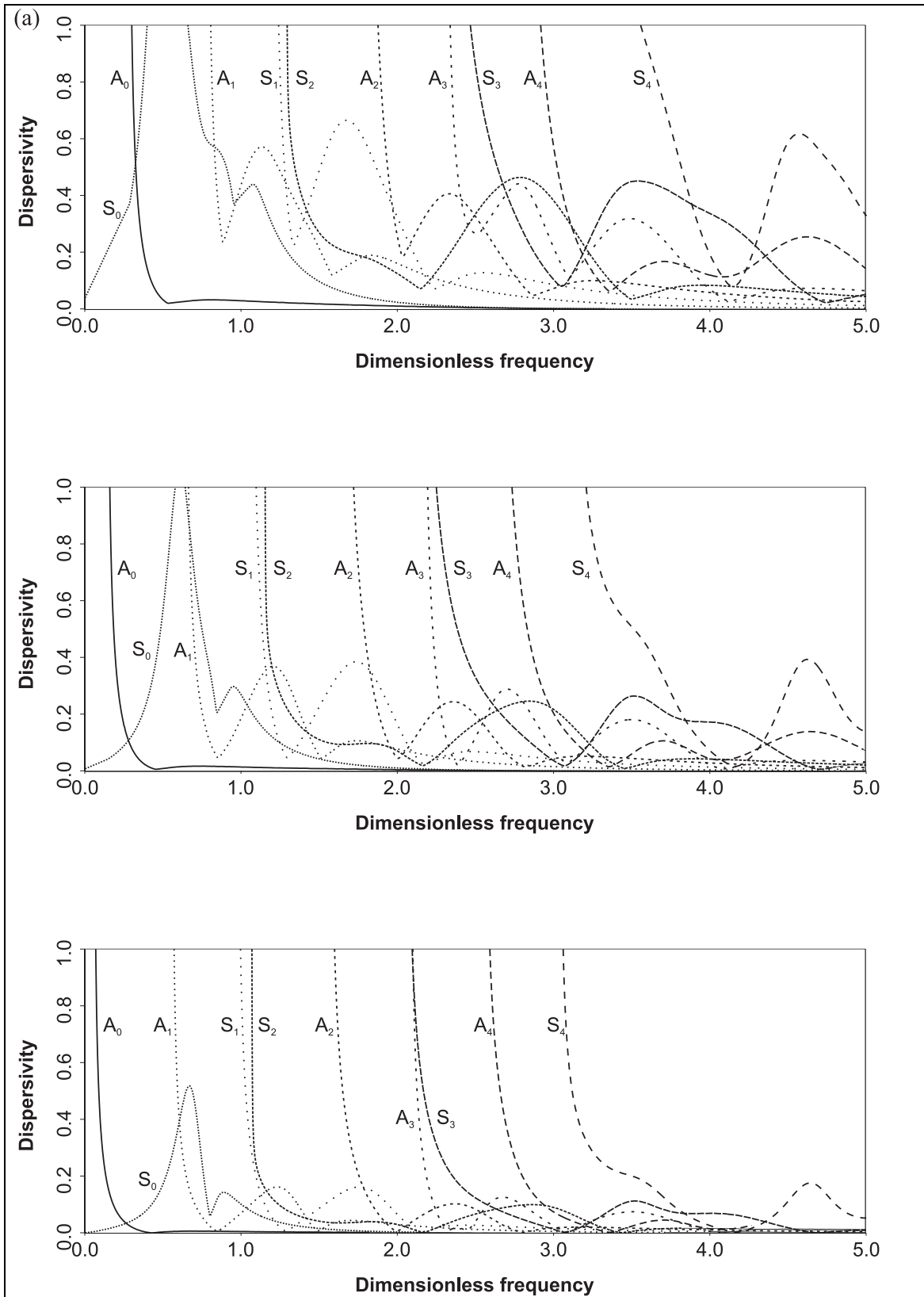


Figure 2.14 Dispersivity curves for aluminium using input signals with durations of (a) 10, (b) 20 and (c) 50  $d/v_t$ , where  $d$  is the plate thickness and  $v_t$  is the bulk transverse wave velocity.

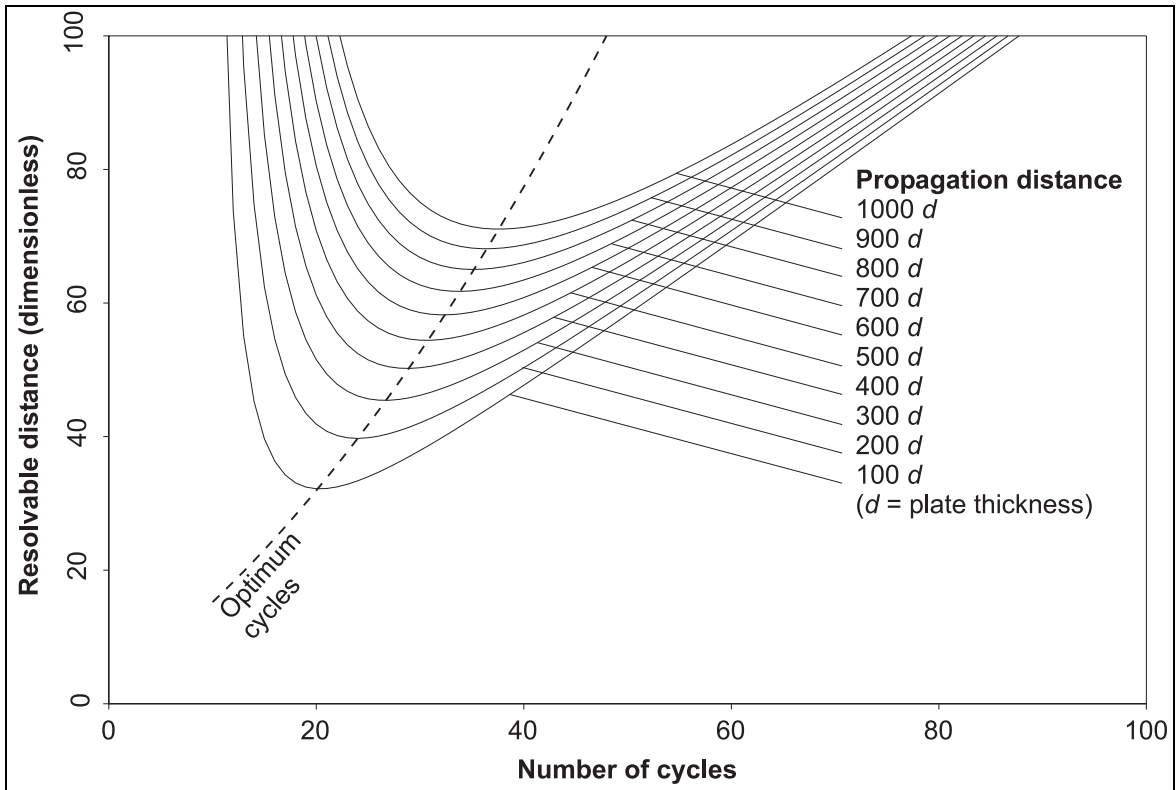


Figure 2.15 Resolvable distance vs. cycles in input toneburst for the  $S_1$  mode in aluminium at 4.03 MHz mm (its maximum group velocity), for various propagation distances. The dotted line marks the location of the minima in resolvable distance as the propagation distance is varied.

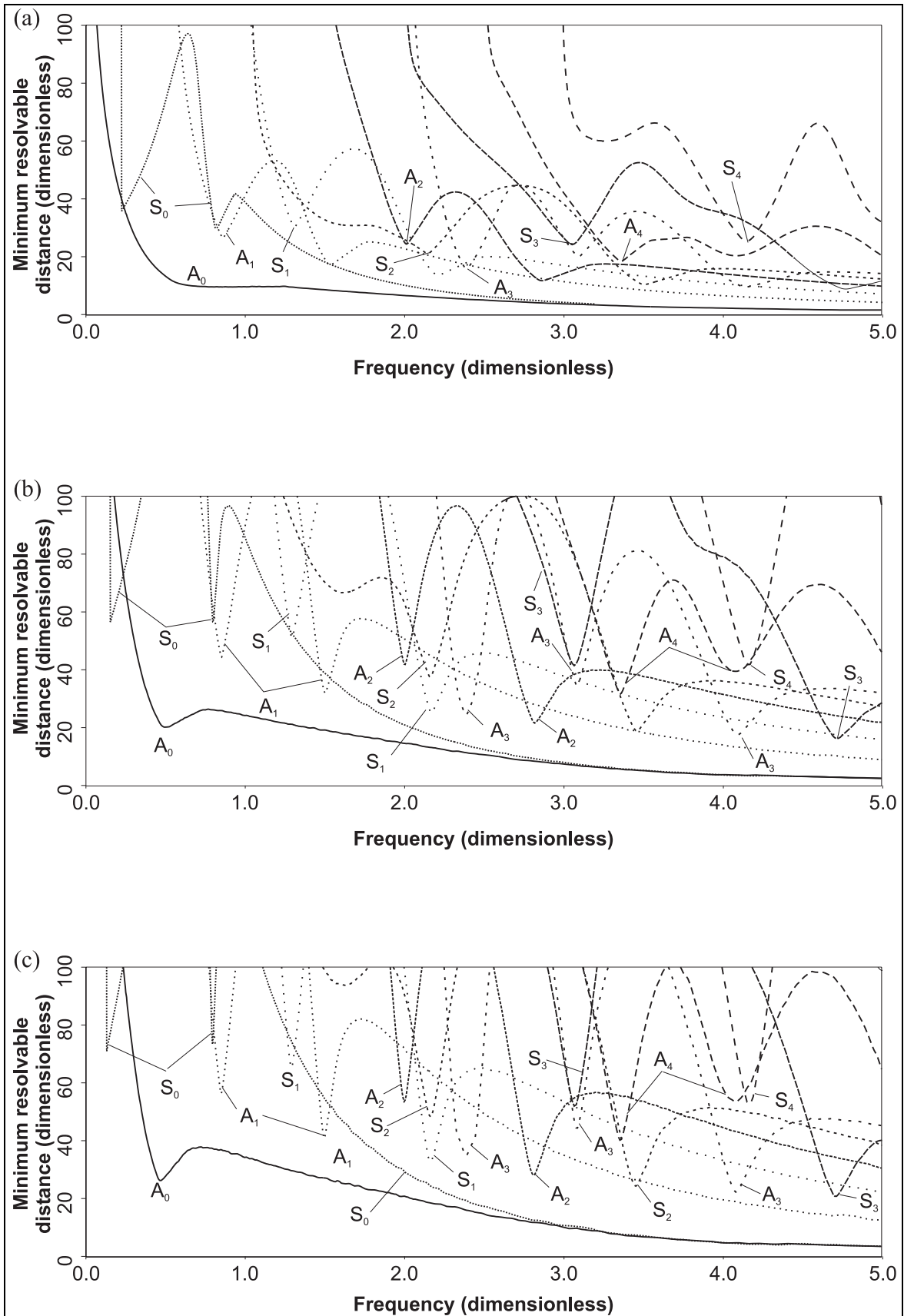


Figure 2.16 Minimum resolvable distance curves for aluminium at propagation distances of (a) 100, (b) 500 and (c) 1000  $d$ , where  $d$  is the plate thickness.

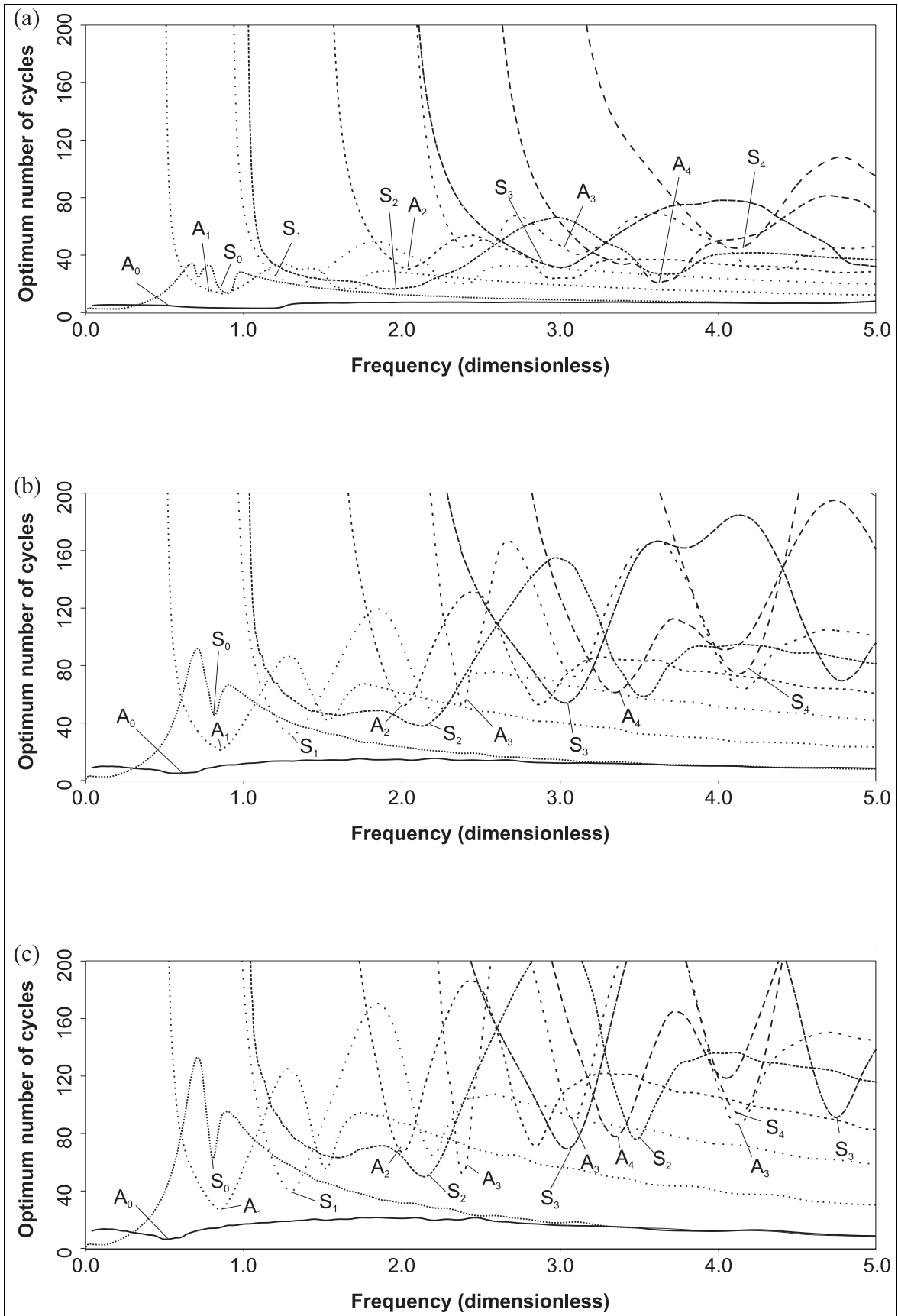


Figure 2.17 Optimum number of cycles in input signal for aluminium at propagation distances of (a) 100, (b) 500 and (c) 1000  $d$ , where  $d$  is the plate thickness.

### 3. Development and validation of one-dimensional transducer model

---

#### 3.1 INTRODUCTION

In this chapter, the development of a one-dimensional transducer model is described. Although the model is not directly applicable to transducers for transmitting and receiving Lamb waves, it provides a useful starting point in understanding the frequency response of thin piezoelectric polymer films which form the basis of the inter-digital transducers that will be described in later chapters.

The work in this chapter forms the basis of the Wilcox *et al.* (1998a) paper. The model was developed jointly by the current author and his colleague R. Monkhouse, in consultation with Prof. B. Auld. The contributions of the current author were mostly in the original mathematical derivation of the model and the subsequent improvements which were made to the model as experimental data was obtained. The original software implementation of the model, which was designed for a fairly standard transducer configuration was written by R. Monkhouse who was also responsible for setting up the pulse-echo specimens used for model validation. The later, more general software implementation of the one-dimensional model was written by the current author, and is the software used to produce the predictions in this thesis.

A one-dimensional transducer model can be used to predict the performance of a layered transducer system transmitting or receiving bulk longitudinal or transverse waves, although here, only bulk longitudinal waves will be considered. In such a layered transducer system, the length and breadth of each layer is assumed to be large compared to the thickness, hence the three dimensional transducer system may be reduced to a one-dimensional one. The one-dimensional assumption allows the mechanical elements in the system to be modelled as two port electrical networks, and hence the complete electromechanical system may be represented by a purely electrical network.

Numerous workers (beginning with Mason 1948) have used one-dimensional electrical networks for transducer analysis. In this chapter, a modular matrix based approach to one-dimensional transducer modelling is presented which is easily adaptable and intuitive to understand. The matrix method used here is compatible with that used by other workers such as Sittig (1967) and Lewis (1980). An alternative method proposed by Hayward *et al.* (1984) is to use a systems based approach with feedback loops in order to account for the various transduction phenomena.

The pulse-echo response of transducers which have been predicted by one-dimensional models are often presented (Desilets *et al.* 1978, Silk 1983, Ohigashi *et al.* 1988, Kimura and Ohigashi 1988, Brown and Carlson 1989, Hayward and Hossack 1990, Dias *et al.* 1993, Lockwood and Foster 1994 and many more), but the exact method by which these results are obtained is not always clear. Using the reciprocity theorem (see for example Sachse and Hsu 1979 or Auld 1990), the assumptions inherent in the calculation of pulse-echo response are considered and justified in section 3.2.2.

The first part of this chapter is concerned with the mathematical basis of the one-dimensional transducer model, and its implementation in software. The remainder of the chapter focuses on the piezoelectric polymer, PVDF, which is used as the piezoelectric element in most of the transducers described in this thesis. Although PVDF has been studied as a transducer material using one-dimensional models before (Bui *et al* 1977, Kimura and Ohigashi 1988, Brown and Carlson 1989, Dias *et al.* 1993 amongst others), most work has been concerned with the development transducers for high frequency (10 MHz and higher) applications and the transmission of acoustic energy into fluids such as water (e.g. Bainton *et al.* 1980) or human tissue (e.g. Swartz and Plummer 1980). In the context of the work covered in this thesis, the emphasis is on the properties of PVDF when bonded to a solid substrate and operated at frequencies below 10 MHz. Impedance and pulse-echo measurements on layered transducers made from PVDF are described in section 3.3, these experiments enabling the model to be both tuned and validated as it was developed. The final section of the chapter uses the model to perform parametric studies, firstly by examining the relative significance of the input parameters, and secondly by investigating the effect of several major parameters on the overall performance of a transducer.

## 3.2 DEVELOPMENT OF ONE-DIMENSIONAL TRANSDUCER MODEL

The one-dimensional model is based on mapping a complete electromechanical transducer system shown in figure 3.1(a) into a purely electrical network (figure 3.1(b)) which may then be analysed using conventional electrical circuit analysis techniques. After describing how the circuit equations for the different elements in the model are developed in section 3.2.1, section 3.2.2 will describe the assembly of the complete model to perform specific calculations.

### 3.2.1 *Modelling the different elements in the transducer system*

The complete transducer system may be divided into two parts: a layered mechanical system through which bulk acoustic waves may propagate in a direction perpendicular to the plane of the layers and an electrical system. The two systems are coupled in a piezoelectric layer, which converts electrical signals into mechanical strains and *vice versa*. As well as the piezoelectric layer, which is of finite thickness, the model also requires that the mechanical system is terminated by two semi-infinite end layers which may be either continuous media or vacua. Between the piezoelectric layer and either of the semi-infinite layers, there may be any number of finite thickness layers of other materials, such as electrodes or adhesives, as indicated in figure 3.1(a). The electrical system may contain any number of linear passive components as well as current and voltage sources. In this section, each of the layers in the mechanical system is described and an equivalent electrical network is presented. Finally the electrical network analogue of the complete transducer system is assembled.

#### *Piezoelectric layer*

For the piezoelectric material, equivalent circuits were proposed originally by Mason (1948) and refined by Krimholz, Leedom and Matthaei (Krimholz *et al.* 1971) who developed the so called KLM model. The governing circuit equations in these models are

the same, the differences being in the components used within the circuits. The equations can also be derived directly (for example, Auld 1990) by fitting solutions of the coupled wave equations for plane waves propagating in a piezoelectric material to the boundary conditions. All methods result in the circuit equation shown below in equation 3.1.

Figures 3.2(a) and (b) show respectively the piezoelectric layer and its representation as a three port electrical network described by the 3x3 impedance matrix:

$$\begin{bmatrix} F_1 \\ F_2 \\ V_3 \end{bmatrix} = -i \begin{bmatrix} AZ_0 \cot kd & AZ_0 \csc kd & h_{x1} / \omega \\ AZ_0 \csc kd & AZ_0 \cot kd & h_{x1} / \omega \\ h_{x1} / \omega & h_{x1} / \omega & 1 / \omega C_0 \end{bmatrix} \begin{bmatrix} v_1 \\ v_2 \\ I_3 \end{bmatrix} \quad (3.1)$$

where  $A$  is the area of the transducer,  $Z_0$  is the characteristic acoustic impedance of the piezoelectric material,  $k$  is the acoustic wave number (note that the wave number  $k$  used here is equal to  $i\gamma$  where  $\gamma$  is the propagation constant used by some authors such as Bui *et al.* 1977),  $d$  is the thickness of the film,  $h_{x1}$  is the piezoelectric charge constant (in Newtons per Coulomb) for the material corresponding to longitudinal plane waves propagating in the  $x$  direction,  $\omega$  is the angular frequency and  $C_0$  is the clamped capacitance of the piezoelectric layer (the capacitance that would be measured if zero-strain conditions could be achieved in the piezoelectric material).

The properties at ports one and two are acoustic ones, current representing particle velocity ( $v_i$ ) and voltage representing force ( $F_i$ ) due to normal stress ( $T_{xx}$ ). It should be noted that the sign convention for this circuit is that positive current flows in at all ports.

#### *Non-piezoelectric layers*

A layer (L) of an acoustic medium with characteristic acoustic impedance  $Z_0$ , finite thickness  $t$  and area  $A$  can be modelled as a length of transmission line (for example, Dias *et al.* 1993) in the electrical model, the two port network representation of which is shown in figure 3.3. The relationship between the output variables ( $F_2$  and  $v_2$ ) and input variables ( $F_1$  and  $v_1$ ) is then given by (see for example Howatson *et al.* 1991):

$$\begin{bmatrix} F_1 \\ v_1 \end{bmatrix} = \begin{bmatrix} \cos kt & iAZ_0 \sin kt \\ (i/AZ_0) \sin kt & \cos kt \end{bmatrix} \begin{bmatrix} F_2 \\ v_2 \end{bmatrix} \quad (3.2)$$

$$= \mathbf{T}_L \begin{bmatrix} F_2 \\ v_2 \end{bmatrix}$$

where  $\mathbf{T}_L$  is known as the transfer matrix for that particular layer. It should be noted that when using transfer matrices, the sign convention used for particle velocity  $v$  (current in the electrical analogue) is important, and it is for this reason that the matrix to convert from  $F_1$  and  $v_1$  to  $F_2$  and  $v_2$  is not the same as that given above but instead is:

$$\begin{aligned} \begin{bmatrix} F_2 \\ v_2 \end{bmatrix} &= \begin{bmatrix} \cos kt & -iAZ_0 \sin kt \\ -(i/AZ_0) \sin kt & \cos kt \end{bmatrix} \begin{bmatrix} F_1 \\ v_1 \end{bmatrix} \\ &= \mathbf{T}_L^{-1} \begin{bmatrix} F_1 \\ v_1 \end{bmatrix} \end{aligned} \quad (3.3)$$

### *Semi-infinite layers*

For a semi-infinite medium, the impedance seen looking into it is just the characteristic acoustic impedance of that material multiplied by the area of the transducer  $A$ . Hence the semi-infinite media at the front and back of the transducer are represented as impedances connected across the terminals of the last transmission lines.

### *Equivalent electrical network of the complete transducer*

A complete system as shown in figure 3.1(a) consists of the layer of piezoelectric material, a number of layers of other materials on either side of it and beyond them, two semi-infinite media. For clarity, one of the semi-infinite media will be defined as corresponding to a material under interrogation by the transducer and the other to a backing medium. The layer of piezoelectric material is then defined as having a back (B) and front (A), the back being the side towards the backing material and the front being the side towards the material under interrogation. The layers between the back of the piezoelectric material and the backing material are denoted as  $B_1, B_2$ , etc. (counting away from the piezoelectric material) and the layers on the front as  $A_1, A_2$ , etc. All the layers, including the piezoelectric one, make up what will be defined as the transducer.

The electrical network analogue of the transducer is shown in figure 3.1(b). It has a three port network representing the piezoelectric layer (PZ) described by a 3x3 impedance matrix (equation 3.1), a number of two port layers representing non-piezoelectric layers ( $A_i$  and  $B_i$ ) which are described by 2x2 transfer matrices (equation 3.3) and two terminating impedances to represent the material under interrogation ( $Z_A$ ) and the backing medium ( $Z_B$ ).

### **3.2.2 Assembly of the model components to perform specific calculations**

Except for any external electrical components (which may easily be added directly to the network) the description of the transducer system as an electrical network is now complete. This section is devoted to describing how the model is manipulated in order to obtain certain quantities of interest.

#### *Calculation of the input impedance of the transducer system*

The input impedance of a transducer system is a readily measurable function of frequency, and is hence a useful parameter for the model to be able to predict.

Firstly, the transfer matrices,  $\mathbf{T}_{Ai}$ , describing each of the front layers may be multiplied together to obtain a single transfer matrix,  $\mathbf{T}'_A$ , which relates the force,  $F_I$ , and particle velocity,  $-v_I$ , at the interface of the piezoelectric layer and the first front layer to those quantities measured between the last front layer and the material under interrogation ( $F_{ZA}$

and  $v_{ZA}$ ) as shown in equation 3.4. The minus sign for  $v_I$  is necessary since  $v_I$  has already been defined by equation 3.1 and figure 3.2 as being into the piezoelectric layer.

$$\begin{aligned} \begin{bmatrix} F_1 \\ -v_1 \end{bmatrix} &= \mathbf{T}_{A1} \mathbf{T}_{A2} \cdots \mathbf{T}_{A(n-1)} \mathbf{T}_{A(n)} \begin{bmatrix} F_{ZA} \\ v_{ZA} \end{bmatrix} \\ &= \mathbf{T}'_A \begin{bmatrix} F_{ZA} \\ v_{ZA} \end{bmatrix} \\ &= \begin{bmatrix} A & B \\ C & D \end{bmatrix} \begin{bmatrix} F_{ZA} \\ v_{ZA} \end{bmatrix} \end{aligned} \quad (3.4)$$

Since the ratio of  $F_{ZA}$  to  $v_{ZA}$  is given by the acoustic impedance of the material under interrogation,  $Z_A$ , the ratio of  $F_1$  and  $-v_1$  may then be expressed as an impedance,  $Z'_A$ , given by:

$$Z'_A = -\frac{F_1}{v_1} = \frac{AZ_A + B}{BZ_A + D} \quad (3.5)$$

This process has reduced a system of multiple layers and terminating impedance,  $Z_A$ , to a single impedance,  $Z'_A$ , as shown in figure 3.4.

The same process may be used to reduce the backing medium and intervening layers to a similar impedance,  $Z'_B$ , connected across the back port of the piezoelectric material. These impedances,  $Z'_B$  and  $Z'_A$ , provide ratios between  $F_1$  and  $-v_1$  and  $F_2$  and  $-v_2$  respectively in equation 3.1. Thus the symmetrical 3x3 matrix from equation 3.1:

$$\begin{bmatrix} F_1 \\ F_2 \\ V_3 \end{bmatrix} = \begin{bmatrix} Z_{11} & Z_{12} & Z_{13} \\ Z_{21} & Z_{22} & Z_{23} \\ Z_{31} & Z_{32} & Z_{33} \end{bmatrix} \begin{bmatrix} v_1 \\ v_2 \\ I_3 \end{bmatrix} \quad (3.6)$$

may be reduced to a 2x2 matrix,  $\mathbf{Z}_{PZ}$ , by using  $F_1/v_1 = -Z'_B$ :

$$\begin{aligned} \begin{bmatrix} F_2 \\ V_3 \end{bmatrix} &= \begin{bmatrix} Z_{22} - Z_{12}Z_{21}/(Z'_B + Z_{11}) & Z_{23} - Z_{21}Z_{13}/(Z'_B + Z_{11}) \\ Z_{32} - Z_{12}Z_{31}/(Z'_B + Z_{11}) & Z_{33} - Z_{13}Z_{31}/(Z'_B + Z_{11}) \end{bmatrix} \begin{bmatrix} v_2 \\ I_3 \end{bmatrix} \\ &= \begin{bmatrix} Z'_{22} & Z'_{23} \\ Z'_{32} & Z'_{33} \end{bmatrix} \begin{bmatrix} v_2 \\ I_3 \end{bmatrix} \\ &= \mathbf{Z}_{PZ} \begin{bmatrix} v_2 \\ I_3 \end{bmatrix} \end{aligned} \quad (3.7)$$

which, it should be noted, is still symmetrical. Then, by using  $F_2/v_2 = -Z'_A$ , the ratio between  $V_3$  and  $I_3$  may be found, which is the electrical input impedance,  $Z_{IN}$ , of the transducer:

$$\begin{aligned}
 Z_{IN} &= Z'_{33} - \frac{Z'^2_{23}}{Z'_A + Z'_{22}} \\
 &= Z'_{33} - \frac{Z'^2_{13}(Z'_A + Z'_{22}) + Z'^2_{23}(Z'_B + Z'_{11}) - 2Z'_{12}Z'_{13}Z'_{23}}{(Z'_A + Z'_{22})(Z'_B + Z'_{11}) - Z'^2_{12}}
 \end{aligned} \tag{3.8}$$

*Calculation of acoustic response*

The acoustic response is a somewhat abstract quantity which will be defined here as the ratio of the force measured at the interface of the material under interrogation to the current driving the transducer. It can be used to give an indication of the acoustic power being generated by the transducer, but, as will be shown in the next section, it is also an important intermediate quantity in the calculation for determining the pulse-echo response of the transducer.

In equation 3.8, the piezoelectric layer, backing layers and backing material were reduced to a two port network represented by the 2x2 impedance matrix,  $\mathbf{Z}_{PZ}$ . This has been achieved by effectively closing the back port of the three port network representing the piezoelectric layer, to leave a two port network, which will be referred to as the backed piezoelectric layer. One port of the backed piezoelectric layer is the electrical terminals and the other is the mechanical interface with the first of the front layers. As the backed piezoelectric layer is a two port device, the impedance matrix,  $\mathbf{Z}_{PZ}$ , may be re arranged into a transfer matrix,  $\mathbf{T}_{PZ}$ . In terms of the model network, the backed piezoelectric layer may then be treated in the same way as the other layers. For consistency with the other transfer matrices in the system it is necessary to change the sign convention for the piezoelectric layer, so that the particle velocity  $v_2$ , is now positive out of port two.

$$\begin{aligned}
 \begin{bmatrix} F_2 \\ v_2 \end{bmatrix} &= \begin{bmatrix} Z'_{22}/Z'_{32} & Z'_{23} - Z'_{22}Z'_{33}/Z'_{32} \\ 1/Z'_{32} & -Z'_{33}/Z'_{32} \end{bmatrix} \begin{bmatrix} V_3 \\ I_3 \end{bmatrix} \\
 &= \mathbf{T}_{PZ} \begin{bmatrix} V_3 \\ I_3 \end{bmatrix}
 \end{aligned} \tag{3.9}$$

The system is now extended back on the electrical side to include a pulser-receiver instrument used to drive the transducer. This is represented as a Norton equivalent circuit with an ideal current source ( $I_p$ ) in parallel with an output impedance  $Z_p$  as shown in figure 3.5. The transfer matrix representing the system from the terminals of  $I_p$  to the electrical terminals of the backed piezoelectric layer is defined as  $\mathbf{T}_p$ . Hence, if the transfer matrix,  $\mathbf{T}_{PZ}$ , for the backed piezoelectric layer is pre-multiplied by the matrices representing the layers in front of it (A1, A2, etc.) and post-multiplied by  $\mathbf{T}_p$ , a single transfer matrix,  $\mathbf{T}$ , is obtained:

$$\begin{aligned}
 \mathbf{T} &= \mathbf{T}_{An} \dots \mathbf{T}_{A2} \mathbf{T}_{A1} \mathbf{T}_{PZ} \mathbf{T}_P \\
 &= \begin{bmatrix} A & B \\ C & D \end{bmatrix} \\
 \therefore \begin{bmatrix} F_{OUT} \\ v_{OUT} \end{bmatrix} &= \begin{bmatrix} A & B \\ C & D \end{bmatrix} \begin{bmatrix} V_P \\ I_P \end{bmatrix}
 \end{aligned} \tag{3.10}$$

$\mathbf{T}$  represents the entire backed transducer, from input electric quantities,  $V_P$  and  $I_P$ , to the resulting mechanical output quantities,  $F_{OUT}$  and  $v_{OUT}$ , and includes the output impedance of the driving instrument,  $Z_P$ .  $V_P$  and  $I_P$  are the voltage and current at an ideal driving current source, and  $F_{OUT}$  and  $v_{OUT}$  are the force and particle velocity at the interface with the material being interrogated.

The acoustic response is the ratio of force,  $F_{OUT}$ , at the interface with the material under interrogation to the current,  $I_P$ , applied by the ideal current source. Since the ratio of  $F_{OUT}$  and  $v_{OUT}$  at the interface with the material under interrogation is  $Z_A$ , equation 3.10 may be rearranged to give the acoustic response:

$$\frac{F_{OUT}}{I_P} = \frac{BC - AD}{C - A/Z_A} \tag{3.11}$$

#### *Calculation of pulse-echo response*

The pulse-echo response of a transducer when it is bonded to a solid substrate of finite thickness is, like the input impedance, readily measurable experimentally. Although simple and in some ways intuitively obvious, the method by which the model is used to predict the pulse-echo response is quite subtle and deserves some further justification.

The goal is to predict the voltage which would be measured at the electrical terminals of the transducer as the first echo is received from an acoustic pulse generated by an input electrical pulse. The echo is that reflected back from a free surface normal to the transducer element which is assumed to exist somewhere within the material being interrogated. This signal therefore must make two passes through the backed transducer network described in the previous section, once in the electrical to mechanical direction and once in the mechanical to electrical direction.

A possible method to proceed with this calculation would be to consider the material under interrogation as finite and terminated with a free surface (a short circuit across the port furthest from the piezoelectric layer in the electrical analogue). This would enable the response of the entire system to be predicted in the frequency domain. Then, by using an inverse Fourier transform, the time domain response to a current impulse at the electrical terminals could be predicted and this would implicitly include echoes from the free surface. However, the time between pulse and echo is long compared to the portion of the signal which is of interest (the reflected echo), hence the amount of temporal resolution that could be obtained on the echo itself for a given size of inverse Fourier transform is small.

The method used in this analysis makes the assumption that the material under interrogation is very much thicker than any of the layers in the backed transducer system.

Thus the approximation that the backed transducer is connected to an infinite non-dispersive and non-attenuating medium (a reasonable approximation for the materials likely to be encountered in many practical applications) is justifiable. As will be shown, this enables the transmission and reception cases to be considered separately, with parameters in the transmit case being denoted by a  $t$  superscript and those in the receive case by a  $r$  superscript. Superposition of these two cases is then used to achieve the required boundary condition of a free surface at some point in the material.

Consider the complete system represented as the block diagram shown in figure 3.6. Again, it has been extended back at the electrical end to include a Norton equivalent circuit to represent the pulser-receiver instrument used to drive the transducer, with its own output impedance,  $Z_P$ , and an ideal current source,  $I_P$ , connected at point P, which supplies the pulse. In the transmit case,  $I_P^t$  can be calculated from the measurable voltage,  $V_P^t$ , as the input electrical impedance of the system,  $Z_{IN}$ , has already been calculated:

$$I_P^t = \frac{Z_{IN} + Z_P}{Z_{IN}Z_P} V_P^t \quad (3.12)$$

At the acoustic end the final front layer is connected to the material under interrogation (Material A) at interface Q. Point R in the model corresponds to the position of the free surface in the real material from which the pulse will be reflected.

In the transmit case, the material is represented up to this point R as a length of transmission line with characteristic impedance  $Z_A$  and length  $d$ , as shown in figure 3.7(a). The continuation (to infinity) beyond point R is represented as an impedance,  $Z_A$ , equal to the characteristic impedance of the material multiplied by the area of the transducer. It can be shown using the method described in equation 3.5 that the apparent impedance looking from point Q into the material is just  $Z_A$ , hence the material still appears to be infinite looking from point Q. Furthermore, the force,  $F_R^t$ , and particle velocity,  $v_R^t$ , at point R are the same as those at point Q except for a time delay due to the distance  $d$ . It is thus reasonable to replace the length of transmission line and terminating impedance,  $Z_A$ , with the same impedance connected directly at point Q and to say that the force measured there would be the same as that measured in the material at point R, except for the time delay. For the transmit case, the block diagram of figure 3.6 may now be re-drawn as that shown in figure 3.7(b), where the input is an electrical current,  $I_P^t$ , at point P and the output is a mechanical force measured (for consistency with the receive case) at the new terminals at point S.  $F_S^t$  is equal to the force,  $F_R^t$ , generated at the point R in the material except for a time delay.

In the receive case it is necessary to generate a force,  $F_R^r$ , at the point R in the medium as shown in figure 3.8(a), such that  $F_R^r$  equals  $-F_R^t$ . This means that when superposition of the transmit and receive cases is applied, the boundary condition required for a free surface at R will be achieved:

$$F_R^t + F_R^r = 0 \quad (3.13)$$

This cannot be simulated by connecting a forcing device directly at the point R in figure 3.8(a), as the length of material between points R and Q, would no longer be semi-infinite, as required for consistency with the transmit case. Instead a Thévenin type

driving circuit with an ideal voltage source (i.e. a forcing device),  $F_T^t$ , in series with an output impedance,  $Z_A$ , must be used as shown in figure 3.8(a), which due to the impedance matching means that the material does now appear to be semi-infinite looking away from the transducer. Unfortunately, it is the size of force at point R,  $F_R^r$ , that is the known quantity and not the force  $F_T^t$ . In order to be able to calculate  $F_T$  exactly, the impedance looking towards the transducer from point R would need to be known. However, it is a reasonable approximation to say that the length of material between points R and Q is large enough compared to the other layers involved to be considered as presenting an impedance of just  $Z_A$  to the driving circuit. Therefore  $F_T^t$  needs to be twice the size as the force required at point R,  $F_R^r$ . For reasons that will become apparent, it is more useful to use a Norton equivalent circuit (rather than a Thévenin one) with a current source (i.e. a shaking device) of magnitude  $v_N^r$  equal to  $F_T/Z_A$  in parallel with an impedance  $Z_A$  as shown in figure 3.8(b). Thus:

$$v_N^r \approx -2 \frac{F_R^r}{Z_A} \quad (3.14)$$

The receive model may now be further reduced by combining the transmission line between Q and R and the Norton circuit connected at point R, into a single Norton circuit connected at point Q. It can be shown that this has an output impedance still equal to  $Z_A$  and a current source of the same magnitude as in the original circuit but time delayed due to the length of intervening material. If, as in the transmit case, this time delay is ignored, the receive model is now as shown in figure 3.8(c), where the output is an electrical potential,  $V_P^r$ , measured at point P and the input is a mechanical displacement,  $v_N^r$ , imposed at point S.

Normally the transmit and receive models would now be superposed to satisfy the boundary condition at point R and so to fully predict the electrical pulse-echo response equal to the sum of  $V_P^t$  and  $V_P^r$ . This cannot be done in this case as both models have neglected the time delays within the material, hence the transmitted and received pulses would occur simultaneously. Instead, it is assumed that in practice the time interval between pulse and echo is sufficiently long for the effects of the transmitted pulse within the transducer to have completely died away before the echo is received. Thus the pulse-echo output is approximated as being solely due to the voltage  $V_P^r$  at the electrical terminals that is predicted by the receive model.

Comparison of figure 3.7(b) and figure 3.8(c) reveal that between points P and S, the circuits in the transmit and receive cases are now identical. The backed piezoelectric layer has a symmetrical impedance matrix, and all other components within the network are linear resistive, capacitive or inductive elements. This means that the impedance matrix relating properties for the entire network between points P and S will also be symmetrical. Writing this out for a general case gives:

$$\begin{bmatrix} V_P \\ F_S \end{bmatrix} = \begin{bmatrix} z_{11} & z_{12} \\ z_{21} & z_{22} \end{bmatrix} \begin{bmatrix} I_P \\ v_S \end{bmatrix} \quad (3.15)$$

In the transmit case  $F_S = F_S^t$ ,  $I_P = I_P^t$  and  $v_S = 0$ , so

$$\begin{aligned}
 F_S^t &= z_{21} I_P^t \\
 \therefore \frac{F_S^t}{I_P^t} &= z_{21}
 \end{aligned} \tag{3.16}$$

In the receive case  $V_P = V_P^r$ ,  $v_S = v_N^r$  and  $I_S = 0$ , so

$$\begin{aligned}
 V_P^r &= z_{12} v_N^r \\
 \therefore \frac{V_P^r}{v_N^r} &= z_{12}
 \end{aligned} \tag{3.17}$$

But  $z_{12} = z_{21}$ , so

$$V_P^r = \frac{v_N^r F_S^t}{I_P^t} \tag{3.18}$$

and using equation 3.14:

$$V_P^r = -2 \frac{F_S^t}{Z_A} \frac{F_S^t}{I_P^t} \tag{3.19}$$

The pulse-echo response is  $V_P^r/V_P^t$  and is obtained by combining equations 3.12 and 3.19 to give:

$$\begin{aligned}
 \frac{V_P^r}{V_P^t} &= -2 \cdot \frac{Z_{IN} Z_P}{Z_{IN} + Z_P} \cdot \frac{1}{Z_A} \cdot \frac{F_S^t}{I_P^t} \cdot \frac{F_S^t}{I_P^t} \\
 &= -\frac{2 Z_{IN} Z_P}{Z_A (Z_{IN} + Z_P)} \left( \frac{F_S^t}{I_P^t} \right)^2
 \end{aligned} \tag{3.20}$$

However,  $F_S^t/I_P^t$  is just the acoustic response as calculated previously. Hence, given the approximations described, the pulse-echo response is found simply to be proportional to the square of the acoustic response.

### 3.2.3 Inclusion of losses in the model

Loss mechanisms in the transducer system are in two categories. Mechanical losses due to scattering and true absorption are incurred by propagating acoustic waves in all the layers, the absorption ultimately converting all the non-propagating energy to heat. In the piezoelectric layer there are also dielectric losses to be considered, which manifest themselves as the conversion of some of the stored capacitive energy to heat.

#### *Dielectric Losses*

The dielectric losses in the piezoelectric layer are modelled by making the permittivity a complex value, where the imaginary component is associated with losses and is usually expressed as a loss tangent (the work of Leung and Yung 1979, Chen 1983 and Ohigashi *et al.* 1988 is particularly relevant), so that  $\epsilon_{xx}$  becomes  $\epsilon_{xx} (1 - i \tan \delta_e)$ . The loss tangent is generally frequency dependent.

*Mechanical Losses*

The mechanical losses in any acoustic medium can be modelled by making the material stiffness include an imaginary loss tangent term, so that  $c_{11}$  becomes  $c_{11}(1+i \tan \delta_m)$  where the imaginary term may be frequency dependent. If this is then used to solve the wave equation the wavenumber,  $k$ , must now also contain an imaginary term:

$$k = \omega \sqrt{\frac{\rho}{c_{11}(1+i \tan \delta_m)}} \quad (3.21)$$

where  $\rho$  is the material density and  $\omega$  is the angular frequency of the waves. If  $\tan \delta_m$  is assumed to be considerably less than unity, so that terms of order  $\tan^2 \delta_m$  or higher are negligible, then the complex wavenumber can be approximated as:

$$\begin{aligned} k &= \omega \sqrt{\frac{\rho}{c_{11}}} \frac{(1-i \tan \delta_m)^{1/2}}{(1+\tan^2 \delta_m)^{1/2}} = \omega \sqrt{\frac{\rho}{c_{11}}} \frac{\left(1-\frac{1}{2}i \tan \delta_m + O[\tan^2 \delta_m]\right)}{\left(1+O[\tan^2 \delta_m]\right)} \\ &\approx \omega \sqrt{\frac{\rho}{c_{11}}} \left(1-\frac{1}{2}i \tan \delta_m\right) \end{aligned} \quad (3.22)$$

Since the characteristic acoustic impedance of the material is defined as being:

$$Z_0 = \sqrt{\rho c_{11}} \quad (3.23)$$

then, using the same approximation as above, this becomes for a lossy material:

$$\begin{aligned} Z_0 &= \sqrt{\rho c_{11}} (1+i \tan \delta_m)^{1/2} = \sqrt{\rho c_{11}} \left(1+\frac{1}{2}i \tan \delta_m + O[\tan^2 \delta_m]\right) \\ &\approx \sqrt{\rho c_{11}} \left(1+\frac{1}{2}i \tan \delta_m\right) \end{aligned} \quad (3.24)$$

Various models have been suggested to predict the variation of the mechanical loss tangent with frequency, the most common being the Kelvin-Voigt model which represents a solid as a continuum of springs and ideal viscous dampers (see Malvern 1969 for a full description). This leads to a loss tangent term which is proportional to frequency. If the wavenumber is split into its real and imaginary components, then the imaginary component is the attenuation of a wave with distance. Based on the Kelvin-Voigt model, it can be seen from the above that, since  $\tan \delta_m$  is proportional to  $\omega$  then the attenuation must increase with the square of the frequency, although the approximations must break down at higher frequencies when  $\tan \delta_m$  ceases to be small compared to unity. Other workers (Lowe 1995 for example) have assumed that the attenuation per metre is proportional to frequency, which has the physical significance that the attenuation per wavelength is constant. From equation 3.22 it can be seen that this assumption requires that the mechanical loss tangent,  $\tan \delta_m$ , is constant at all frequencies. This assumption also agrees well with measurements made on common structural materials in the frequency range used in ultrasonic NDT, and is the assumption that is used in the model described here.

#### 3.2.4 Software implementation of model

The model was initially implemented in an interactive program written in Borland Pascal by R. Monkhouse, (who worked with the present author on the work described in the Wilcox, Monkhouse *et al.* 1998a paper). This program enabled very fast studies of transducer systems in a particular configuration to be performed. The second implementation of the model was written by the present author as a Matlab M-file, and was designed to be more general, and also enabled more complex modelling functions to be included if desired. The drawback of this implementation was that it did not have an interactive user interface. Results presented in the remainder of this thesis are from the second implementation.

### 3.3 VALIDATION OF ONE-DIMENSIONAL MODEL USING PVDF TRANSDUCERS

Attention is now turned to the piezoelectric polymer, polyvinylidene fluoride (PVDF), which forms the piezoelectric element in the majority of transducers described in this thesis. Kawai (1969) published the first description of the piezoelectric properties of PVDF. Subsequently, it has been used in many transducer applications as reviewed by Chen and Payne (1995).

Poled PVDF film (un-poled PVDF is not piezoelectric, but has applications as a general purpose thermoplastic engineering material in certain chemical processing applications) is supplied in a variety of thicknesses, the thickest which is available commercially is 110  $\mu\text{m}$ , including thin printed electrode layers. The PVDF used in this work was supplied by Amp (Harrisburg, USA), and their published data values which are shown in table 3.1 will be used unless stated otherwise. Its relatively low cost compared to piezoelectric ceramics, such as PZT, make it an attractive material for permanently attached transducers. In later chapters, the use of PVDF to make inter-digital Lamb wave transducers will be described, but in this chapter, the use of PVDF as a bulk wave transducer material will be examined using the one-dimensional transducer model described in the previous section.

#### 3.3.1 PVDF as a transducer material

PVDF is acoustically a much higher loss material than piezoelectric ceramics, its mechanical loss tangent,  $\tan\delta_m$ , is of the order of 0.1 compared to 0.02 for PZT 5A (all piezoelectric ceramic properties are taken from Morgan-Matroc technical data book). This means that PVDF film in vacuum has a low  $Q$  value and broadband frequency response characteristics. However, its piezoelectric coupling constant,  $k_t$ , is only around 14 % (compared to around 60 % for PZT 5A), and this fact combined with the low  $Q$  value of PVDF means that even resonant PVDF transducers tend to be significantly less sensitive than their ceramic equivalents. A major attraction of PVDF as a transducer material is due to its low acoustic impedance ( $\sim 4$  Mrayl) compared to piezo-ceramics ( $\sim 30$  Mrayl for PZT 5A), which enables it to couple much more efficiently to water and human tissue. For this reason, PVDF has been suggested for use in medical imaging (see for example Swartz and Plummer 1980, Ohigashi *et al.* 1984). For the applications considered in this thesis, the low acoustic impedance of PVDF is if anything a negative factor, since the PVDF is usually coupled directly onto a metallic substrate which will have high acoustic impedance (17 MRayl for aluminium, 45 MRayl for steel). However, the low cost, high

flexibility and ease of cutting make PVDF an ideal material for laboratory based experiments, as will be demonstrated in later chapters.

High frequency (~20 MHz) monolithic transducer arrays which utilise a PVDF elements fabricated directly onto MOSFET gates have been the source of some interest (for example Swartz and Plummer 1980) in imaging applications. However, in this thesis, the very high frequency characteristics are not important since the applications which will be discussed are in the frequency range below 5 MHz. This enables several simplifying approximations to be made in the model which are described below.

Numerous workers (Ohigashi 1976, Leung and Yung 1979, Swartz and Plummer 1980, Chen 1983, Ohigashi *et al.* 1984, Ohigashi *et al.* 1988, Dias *et al.* 1993, Kimura and Ohigashi 1988, Brown and Carlson 1989, Brown and Mason 1995) have made detailed investigations of the mechanical and dielectric losses, and the piezoelectric coupling parameter,  $k_t$ , all of which exhibit both frequency and temperature dependence. These results are also indicated in table 3.2. It will be shown later in section 3.4.1, that the exact value of the loss tangents has a very small effect on the results obtained from the model over the frequency range of interest. For this reason, they are both given constant (frequency independent) values, although it is recognised that if PVDF was being used at very high frequencies, the exact behaviour of the loss tangents would need to be included in the model. The variation of  $k_t$  over the frequency range of interest is also assumed to be minimal and is therefore taken as being constant. The complete list of material properties for PVDF and the non-piezoelectric materials which are used in the model is given in table 3.2.

#### 3.3.2 *Experimental methods*

PVDF film may be supplied with electrodes of various materials (Cu/Ni, Ni/Al, Ag ink) printed on both surfaces. Although the silver ink electrodes are the heaviest per unit area which significantly modifies the mechanical behaviour of the PVDF film, they also have the lowest resistivity. This factor is important when making electrical connections to a sheet of PVDF, since if the resistivity is high, there will be significant spatial variations in the potential difference between the electrodes, which will render the one-dimensional model invalid and will also make the design of efficient transducers difficult. For this reason, all PVDF used in this work has the low resistivity silver ink electrode option. A variety of techniques was explored to make the electrical connections to the film. Soldered connections are impossible, as the PVDF melts very easily. The most successful solution was to use fine multi-strand (10/0.1 mm) insulated wire bonded to the silver ink electrode on the PVDF by means of silver loaded epoxy resin (supplied by RS, UK). Due to the fragile nature of these connections, additional mechanical strength was achieved using a small quantity of hot-melt glue. For experimental purposes, all specimens were rigidly mounted in die-cast boxes to provide electrical screening and mechanical protection. The connections to the PVDF were made via BNC electrical connectors mounted in the box walls. A typical transducer configuration would be approximately 20 mm by 30 mm in area. These dimensions are two orders of magnitude greater than the thickness of the transducer, hence the assumptions inherent in the one-dimensional model should be valid.

#### *Input impedance measurements*

The input impedance of PVDF (with silver ink electrodes) in air was measured using a Schlumberger complex impedance meter, over the range from 10 kHz to 20 MHz. The specimen was mounted in a die-cast box as described above.

#### *Pulse-echo measurements*

Samples of PVDF were bonded to substrates of different materials as shown in table 3.3. The substrate thickness was typically between 10 mm and 20 mm. Studies with the one-dimensional model indicated that in the frequency range below 20 MHz, the bond layer thickness is only significant above about 15  $\mu\text{m}$ . In order to make bond layers below this thickness, a low viscosity epoxy without fillers (Araldite 2019) was used. The effect of using thicker bond layers was also investigated by using one or two layers of double sided adhesive tape, each layer of adhesive tape being approximately 75  $\mu\text{m}$  thick. The completed samples were mounted in die-cast boxes as described above. For the water backed cases, the diecast boxes were simply filled with water, the electrical impedance due to the water being sufficiently higher than the output impedance of the pulser-receiver for its effects to be ignored. The results from these tests were compared with time-traces predicted by the one-dimensional model using the values shown in table 3.2.

The pulse-echo response was then measured using a Panametrics 5052PR pulser-receiver using the experimental set-up shown in figure 3.9. It was shown in section 0 that the pulse-echo response depends on the output impedance of the pulser-receiver used, which in this case was variable from 10  $\Omega$  to 1000  $\Omega$  by a 'damping' control on the pulser-receiver. For consistent results and to minimise electrical reflections within the connecting cables, the damping control was set to maximum and a 50  $\Omega$  terminating impedance was connected externally to give a combined impedance of 47.5  $\Omega$ . The length of the connecting lead between the pulser-receiver and the transducer configuration under test was also kept as short as possible. Treating the input/output impedance of the pulser-receiver instrument as being this purely real value is known to be a gross approximation since the circuitry also contains capacitive and inductive elements. However, good agreement is still obtained between model predictions and experimental results, as will be demonstrated.

### **3.3.3 Results**

#### *Input impedance measurements*

The measured complex impedance of the PVDF film in air is plotted as a function of frequency in figure 3.10. It can be seen that there is a resonance (a peak in the real part of the input impedance) at around 7.5 MHz. This can be attributed to the half wavelength resonance of the film. It is interesting to note that for 110  $\mu\text{m}$  PVDF film without electrodes, the half wave resonance would occur at around 10 MHz (this can be calculated by dividing the speed of sound in PVDF, 2.2 mm/ $\mu\text{s}$ , by twice the thickness of the film, 220  $\mu\text{m}$ ). The depression in resonant frequency is due to the mass loading effect of the electrodes.

#### *Pulse-echo measurements*

Figures 3.11(a) and (b) show respectively the measured and predicted pulse-echo responses of an air-backed layer of PVDF bonded to a perspex substrate with a 15  $\mu\text{m}$  thick bond layer. Excellent agreement is achieved. Good agreement with the model is demonstrated with the PVDF bonded to an aluminium substrate as shown in figure 3.12. If the transducer is water backed, the results shown in figure 3.13 indicate that the duration of the signal is reduced. This is to be expected, as the water provides a second medium for the PVDF to dissipate energy into. The effect of using a thicker bond layer is dramatically illustrated in figure 3.14. The thicker bond layer reduces the acoustic impedance presented to the PVDF on the substrate side sufficiently for the PVDF to resonate in its half wavelength mode at around 7.5 MHz. This effect will be demonstrated more clearly in section 3.4.2.

In all cases, the agreement between the experimental results and the one-dimensional model are good. Any discrepancies are likely to be due to experimental limitations at high frequencies, rather than actual phenomena. For instance, the material layers may not be perfectly flat, which will lead to a time smearing of received signals and a corresponding roll-off in frequency response at high frequencies.

#### *Comments*

In this section, the accuracy of the one-dimensional model has been demonstrated for PVDF transducer systems which satisfy the one-dimensional criteria. By developing the model in parallel with these experiments, it has been possible to gain an intuitive grasp of the relative importance of the various parameters. In particular, the exact values of the loss tangents actually make very little difference to the pulse-echo response at the frequencies which are of interest here. In the next section these effects will be quantified more accurately.

## **3.4 PARAMETRIC STUDIES MADE USING ONE-DIMENSIONAL MODEL**

### **3.4.1 *Effect of parametric perturbations***

The one-dimensional transducer model requires seven material parameters to describe the piezoelectric layer, four material parameters to describe each finite layer and one parameter to describe each of the semi-infinite layers. In practice, accurate values may not be available or readily measurable for all of these parameters. For this reason, it is instructive to quantitatively examine the effect which small perturbations of each input parameter have on the output of the model. By doing this, key parameters which must be accurately specified may be identified, and parameters which have only minor effects on the output may be given nominal values, without the overall accuracy of the output of the model being compromised.

#### *Method*

To investigate the effect of every parameter for every possible transducer system would require the examination of an infinite number of permutations. Instead, a standardized

PVDF transducer configuration was examined which consisted of the following layers: a 5  $\mu\text{m}$  thick back electrode, a 100  $\mu\text{m}$  thick PVDF layer, a 5  $\mu\text{m}$  thick front electrode and a 15  $\mu\text{m}$  thick bond layer. This transducer was considered to be bonded to an aluminium substrate without backing (i.e. there was assumed to be a vacuum behind the back electrode). The effect of separately adjusting each of the input parameters required in the model by either +10 % or -10 % was then examined. The output of the model which was monitored was the prediction of pulse-echo response over the range 0-20 MHz, which is plotted as a solid line in figure 3.15. This exhibits two resonant peaks at  $f_1$  (~4 MHz) and  $f_2$  (~12 MHz) with amplitudes of  $a_1$  and  $a_2$  respectively. When a particular input parameter, for example the thickness of PVDF, was perturbed by -10 %, the pulse-echo response was re-plotted, as shown by the dotted line in figure 3.15. Although the general shape of the pulse-echo response remains the same, the positions of the two resonant peaks shift in both frequency and amplitude, and it is the amplitudes of these shifts which are used to quantify the effect of the perturbation of the input parameter. After the perturbation, a numerical algorithm was used to calculate the magnitudes of the change in frequency of the two resonant peaks,  $\Delta f_1$  and  $\Delta f_2$ , and the magnitudes of their change in amplitude,  $\Delta a_1$  and  $\Delta a_2$ .

### Results

The complete results are given in table 3.4, which shows the effect of either increasing or decreasing each parameter on the position of both resonant peaks.

For clarity, these results are averaged in two stages. Firstly, the average fractional changes in frequency and amplitude are calculated:

$$\begin{aligned} \Delta f / f &= \frac{1}{4} \left( \overbrace{\Delta f_1 / f_1 + \Delta f_2 / f_2}^{-10\%} + \overbrace{\Delta f_1 / f_1 + \Delta f_2 / f_2}^{+10\%} \right) \\ \Delta a / a &= \frac{1}{4} \left( \overbrace{\Delta a_1 / a_1 + \Delta a_2 / a_2}^{-10\%} + \overbrace{\Delta a_1 / a_1 + \Delta a_2 / a_2}^{+10\%} \right) \end{aligned} \quad (3.25)$$

Secondly, an overall measure of the input parameter perturbation effect is obtained by averaging these two quantities. These results are shown in table 3.5.

### Conclusions

It can be seen from table 3.5 that the parameters which have the greatest effect on the pulse-echo response are those of the PVDF. It is surprising to note that the longitudinal wave velocity and, to a lesser extent, the density of the bond layer are also fairly significant, despite the thickness of the bond layer being only 15  $\mu\text{m}$ . This is because the acoustic impedance which the electroded PVDF ‘sees’ on the substrate side is a combination of the substrate impedance and the intervening bond layer. It is instructive to note that in the case of the electrodes, the longitudinal wave velocity has almost no effect whereas the thickness and density do. At the frequencies used here, the wavelength of the waves in the electrodes is significantly longer than their thickness, and the electrodes therefore appear as mass loading rather than layers of finite thickness. It is also interesting to observe how little effect the loss parameters have on the pulse-echo response. Furthermore it should be noted that all the loss parameters, together with the PVDF

coupling, the PVDF permittivity and wave velocity in the electrodes only affect the amplitude and not the frequencies of the peaks in the pulse-echo response.

#### 3.4.2 General parametric studies

##### *Acoustic impedance of material under interrogation*

The effect of varying the acoustic impedance of the material under interrogation is shown in figure 3.16, where the transducer is a layer of electroded PVDF bonded to the substrate with a 15  $\mu\text{m}$  bond layer. For substrate impedances of less than about 7 MRayl, the pulse-echo response is dominated by the half wavelength resonance of the electroded PVDF at around 7.5 MHz. For substrate impedances in excess of 7 MRayl, the pulse-echo response changes to one which is dominated by two resonances, one tending to a frequency of 3.75 MHz and the second tending to a frequency of around 11.25 MHz. These correspond to the quarter and three quarter wavelength resonances across the PVDF film, where a node exists at the interface with the substrate.

##### *Acoustic impedance of backing material*

Next, consider a similar transducer bonded to an aluminium substrate and backed by a semi-infinite medium which is not necessarily a vacuum. The effect of increasing the acoustic impedance of the backing medium on the pulse-echo response is shown in figure 3.17. With no backing material, the pulse-echo response is again dominated by the quarter and three quarter wavelength resonances across the electroded film. As the acoustic impedance of the backing medium is increased, these resonant peaks are rapidly reduced and the frequency response becomes increasingly flat. It is also interesting to note that at very low frequencies the pulse-echo response is actually increased. This effect will be exploited in the work described in later chapters.

##### *Effect of bond layer thickness*

The effect of varying the bond layer thickness for an unbacked transducer on an aluminium substrate is demonstrated in figure 3.18. The effect of increasing the bond layer thickness is to effectively reduce the combined impedance presented by the bond layer and the substrate to the PVDF. As expected from the previous studies, this causes the half wavelength resonance of the PVDF at 7.5 MHz to become dominant when thick bond layers are used. This also explains the increased ringing that was predicted and observed experimentally in the case of a water backed transducer with a 75  $\mu\text{m}$  thick bond layer, the pulse-echo response of which is shown in figure 3.14.

### 3.5 CONCLUSIONS

In this chapter a one-dimensional transducer model has been developed, and its accuracy has been proven for the case of planar bulk wave transducers made from 110  $\mu\text{m}$  thick PVDF film. Although the interest in PVDF in this thesis is not as a bulk wave transducer material, it is instructive to examine exactly what occurs when it is used for this purpose before designing inter-digital Lamb wave transducers.

In air, 110  $\mu\text{m}$  thick electroded PVDF exhibits a heavily damped resonance at around 7.5 MHz corresponding to a standing wave, half a wavelength long, through the thickness of the material. When unbacked transducers made from this thickness of PVDF are bonded to a substrate with a high acoustic impedance, they behave as damped quarter or three quarter wavelength resonators, the quarter wavelength resonance being between 3 and 4 MHz. It has been demonstrated that if the substrate impedance is reduced below approximately 7 MRayl, the half wavelength resonance of the PVDF at a frequency of 7.5 MHz again dominates. It is interesting to observe that even on a substrate with a high acoustic impedance, the PVDF can still act as a half wavelength resonator if the bond between it and the substrate is made sufficiently thick. In most applications, this is probably an undesirable effect, as transducers which resonate in such a manner tend to reverberate for a considerable length of time after receiving an impulse of energy.

The effect of backing a PVDF layer bonded to a solid substrate with a medium other than air is a concept which will be shown to be very important in later chapters. In this chapter, only the effect of backing the transducer with a semi-infinite medium of variable acoustic impedance has been investigated. This has been shown to have the effect of deadening the quarter and three quarter wavelength resonances and making the response reasonably broadband from very low frequencies up to around 20 MHz, where there is a full wavelength resonance through the thickness of the film. The pulse-echo response always drops to zero (rather than exhibiting a resonant peak) when there is an integral number of wavelengths across the PVDF, because the net electrical charge generated by the piezoelectric effect is zero. A distinction should be made at this stage between the effects of backing a PVDF transducer with a semi-infinite layer of high acoustic impedance material and finite thickness layer of the same material. If the finite thickness is many times greater than the wavelength in the material, then it will behave in a similar manner to an infinite medium. However, if the thickness of the layer is significantly less than the wavelength, it will appear as a rigid mass which loads the PVDF in much the same way as the thin silver ink electrodes do. In chapters 4 and 6, this effect will be exploited to reduce the resonant frequency of PVDF inter-digital transducers. If the thickness of the backing layer is of the order of a wavelength, then resonances will occur within it, and it must be treated carefully in the model.

### 3. Development and validation of one-dimensional transducer model

Parameter	Symbol	Value	Units	Comments
Thickness	$d$	110	$\mu\text{m}$	including 2 $\mu\text{m}$ thick silver ink electrodes
Density	$\rho$	1780	$\text{kg m}^{-3}$	
Bulk longitudinal velocity	$c_l$	2.2	$\text{mm } \mu\text{s}^{-1}$	through thickness (plane strain conditions)
Dielectric permittivity	$\epsilon_{xx}$	62.7	$\text{pF m}^{-1}$	
Piezoelectric coupling	$k_t$	14	per cent	
Dielectric loss angle	$\delta_e$	15	degrees	quoted at 1 kHz

Table 3.1 Material properties of PVDF from Amp Inc. published data.

Material	Parameter	Symbol	Value	Units	Comments
PVDF	Acoustic impedance	$Z_0$	3.9	MRayl	Calculated from $z_0 = \rho c_l$
	Density	$\rho$	1780	$\text{kg m}^{-3}$	From Amp Inc. Data
	Mechanical loss angle	$\delta_m$	5	degrees	Estimated and assumed frequency independent. Leung and Yung (1979) measured values in the range 4-5° in the frequency range below 20 MHz.
	Permittivity	$\epsilon_{xx}$	62.7	$\text{pF m}^{-1}$	From Amp Inc. Data
	Dielectric loss angle	$\delta_e$	15	degrees	From Amp Inc. data and assumed frequency independent. Leung and Yung (1979), Swartz and Plummer (1980) and Chen (1983) all measured values in the range 10-15° in the frequency range below 10 MHz
	Piezoelectric coupling	$k_t$	14	per cent	From Amp Inc. data
Silver ink	Acoustic impedance	$Z_0$	14.2	MRayl	From $Z_0 = (C_{ink} \rho_{ink})^{1/2}$ , where $\rho_{ink}$ is the measured density of the ink and $C_{ink}$ is its stiffness which is estimated from: $C_{ink} = C_{silver} \times \rho_{ink} / \rho_{silver}$ where $C_{silver} = 11.9 \text{ kN mm}^{-2}$ and $\rho_{silver} = 10500 \text{ kg m}^{-3}$ .
	Density	$\rho$	4190	$\text{kg m}^{-3}$	Measured by weighing known area of film with and without electrodes
	Mechanical loss angle	$\delta_m$	5	degrees	Estimated
Epoxy	Acoustic impedance	$Z_0$	3.6	MRayl	From Krautkramer and Krautkramer (1983)
	Density	$\rho$	1250	$\text{kg m}^{-3}$	
	Mechanical loss angle	$\delta_m$	5	degrees	Estimated
Vacuum	Acoustic impedance	$Z_0$	0	MRayl	From Krautkramer and Krautkramer (1983)
	Density	$\rho$	0	$\text{kg m}^{-3}$	
	Mechanical loss angle	$\delta_m$	0	degrees	
Water	Acoustic impedance	$Z_0$	1.5	MRayl	
	Density	$\rho$	1000	$\text{kg m}^{-3}$	
	Mechanical loss angle	$\delta_m$	0	degrees	
Aluminium	Acoustic impedance	$Z_0$	17.0	MRayl	
	Density	$\rho$	2700	$\text{kg m}^{-3}$	
	Mechanical loss angle	$\delta_m$	0	degrees	
Perspex	Acoustic impedance	$Z_0$	3.2	MRayl	
	Density	$\rho$	1180	$\text{kg m}^{-3}$	
	Mechanical loss angle	$\delta_m$	0	degrees	

Table 3.2 Material properties used in one-dimensional model.

### 3. Development and validation of one-dimensional transducer model

Backing material	Substrate	Bond thickness ( $\mu\text{m}$ )	Results
Air	Perspex	15	figure 3.11
Air	Aluminium	15	figure 3.12
Water	Aluminium	15	figure 3.13
Water	Aluminium	75	figure 3.14

Table 3.3 Pulse-echo tests performed.

Parameter	5 MHz resonant peak				13 MHz resonant peak			
	-10 % change in parameter		+10 % change in parameter		-10 % change in parameter		+10 % change in parameter	
	$\Delta f_1/f_1$ (%)	$\Delta a_1/a_1$ (%)	$\Delta f_1/f_1$ (%)	$\Delta a_1/a_1$ (%)	$\Delta f_2/f_2$ (%)	$\Delta a_2/a_2$ (%)	$\Delta f_2/f_2$ (%)	$\Delta a_2/a_2$ (%)
PVDF thickness	10.0	17.1	-6.7	-13.9	8.6	24.7	-6.2	-18.5
PVDF coupling	0.0	-19.0	0.0	20.9	0.0	-18.7	0.0	20.5
PVDF longitudinal velocity	-10.0	0.5	10.0	-2.4	-7.4	-17.9	7.4	19.8
PVDF permittivity	0.0	-9.7	0.0	9.6	0.0	-9.0	0.0	8.8
Bond longitudinal velocity	-3.3	-8.0	3.3	6.1	-2.5	11.7	2.5	-9.1
PVDF mechanical loss	0.0	3.6	0.0	-3.4	0.0	5.4	0.0	-5.0
Substrate properties (*)	0.0	-4.3	0.0	3.6	0.0	-1.2	1.2	0.8
Electrode density	0.0	-0.2	0.0	-0.1	1.2	2.2	-1.2	-2.2
Bond density	0.0	-4.0	0.0	3.0	-1.2	5.9	1.2	-5.0
Electrode thickness	0.0	0.2	0.0	-0.5	1.2	1.6	-1.2	-1.6
Bond thickness	0.0	3.3	0.0	-3.5	1.2	-4.9	-1.2	4.7
Bond mechanical loss	0.0	0.9	0.0	-0.9	0.0	1.8	0.0	-1.7
PVDF dielectric loss	0.0	-0.9	0.0	1.0	0.0	-0.6	0.0	0.8
PVDF density	0.0	7.7	0.0	-7.1	1.2	-7.0	0.0	6.5
Electrode longitudinal velocity	0.0	-0.5	0.0	0.4	0.0	0.8	0.0	-0.6
Electrode mechanical loss	0.0	0.1	0.0	-0.1	0.0	0.1	0.0	-0.1

(\*) perturbations in either substrate density or longitudinal velocity both have identical effects

Table 3.4 The effect of parametric perturbations on the location of the resonant peaks in the one-dimensional transducer model.

Parameter	$\Delta f/f$ (%)	$\Delta a/a$ (%)	Overall effect (%)
PVDF thickness	7.9	18.5	13.2
PVDF coupling	0.0	19.8	9.9
PVDF longitudinal velocity	8.7	8.7	8.7
PVDF permittivity	0.0	9.3	4.7
Bond longitudinal velocity	2.9	1.7	2.3
PVDF mechanical loss	0.0	4.3	2.2
Substrate properties (*)	0.3	2.5	1.4
Electrode density	0.6	1.1	0.8
Bond density	0.6	1.0	0.8
Electrode thickness	0.6	1.0	0.8
Bond thickness	0.6	0.7	0.7
Bond mechanical loss	0.0	1.3	0.7
PVDF dielectric loss	0.0	0.8	0.4
PVDF density	0.3	0.3	0.3
Electrode longitudinal velocity	0.0	0.1	0.1
Electrode mechanical loss	0.0	0.1	0.0

(\*) perturbations in either substrate density or longitudinal velocity both have identical effects

Table 3.5 Summary of parametric perturbations on one-dimensional model.

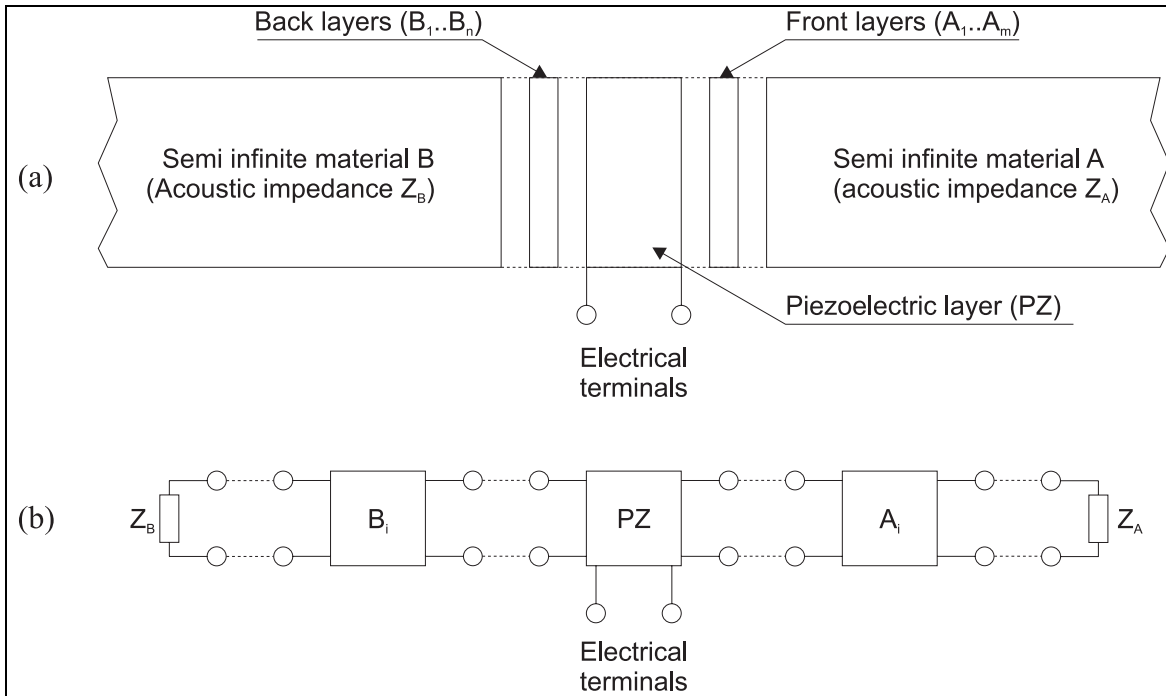


Figure 3.1 (a) Physical transducer configuration and (b) representation as an electrical network.

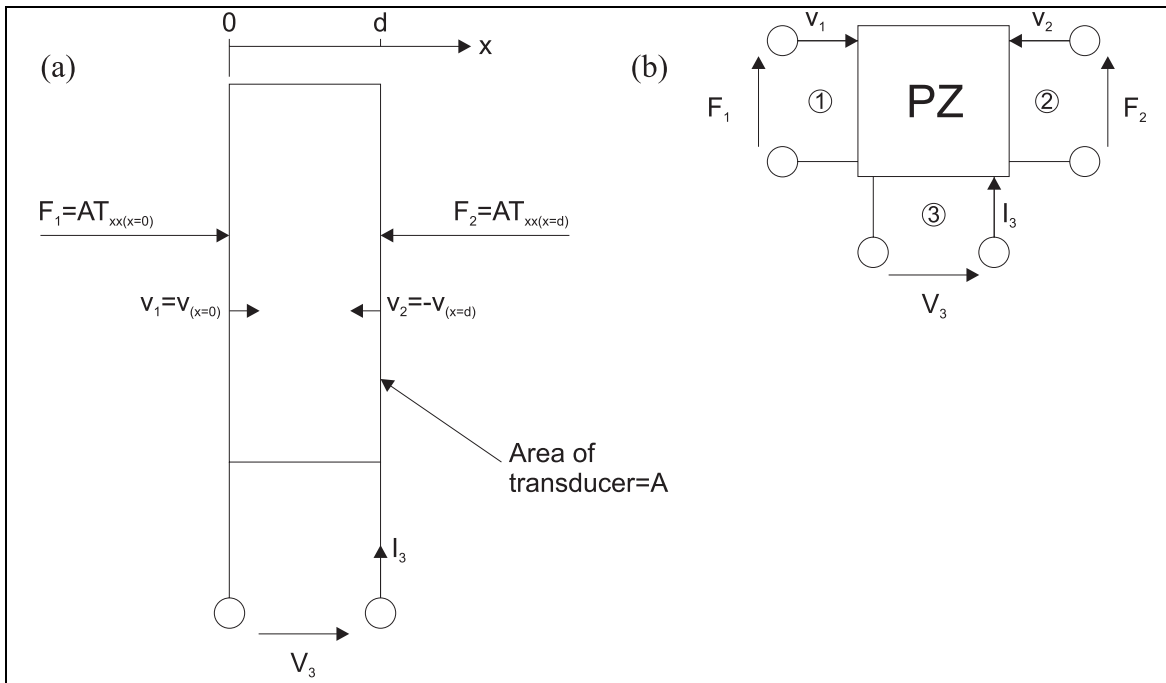


Figure 3.2 (a) Piezoelectric layer and (b) representation of the piezoelectric layer as a three port network.

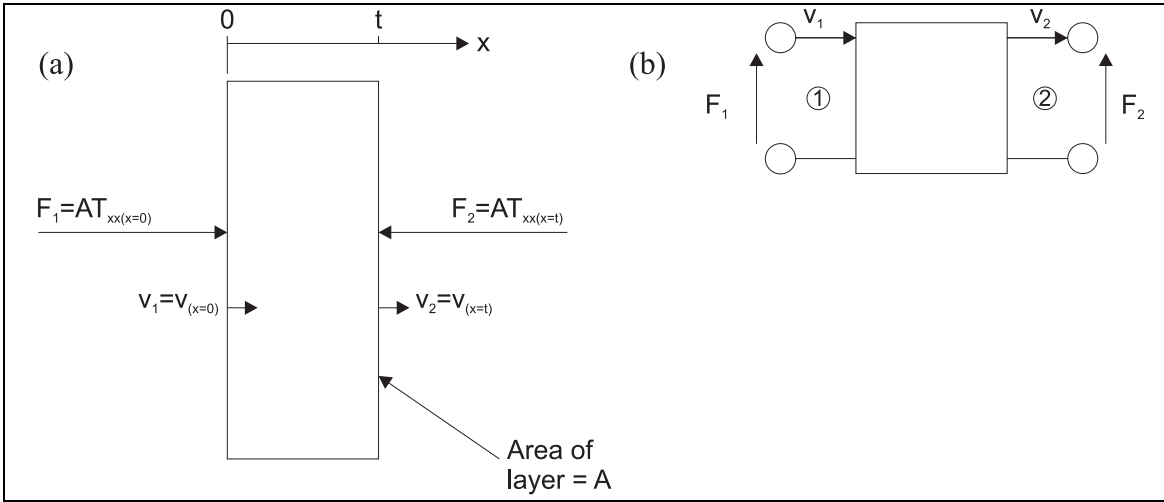


Figure 3.3 Representation of a non-piezoelectric layer as a two port network.

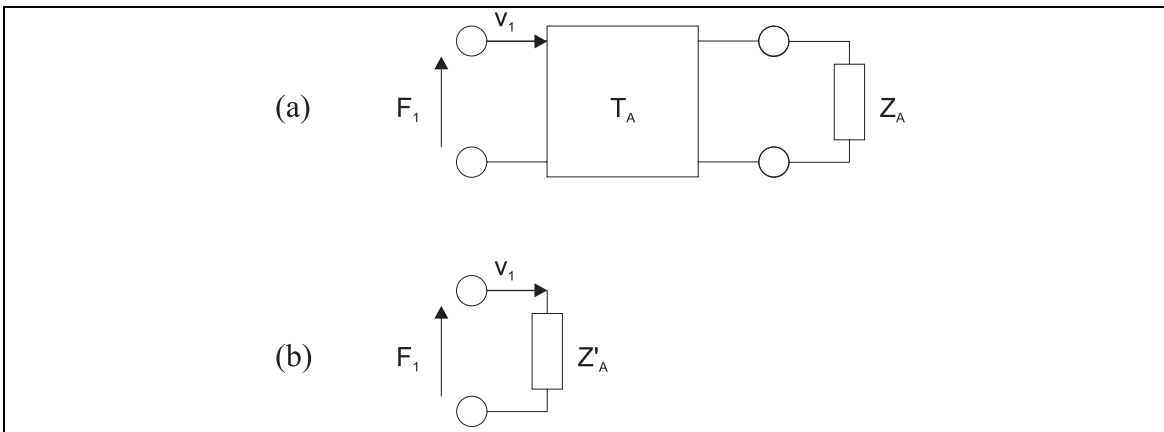


Figure 3.4 (a) Reduction of two port network and impedance to (b) a single impedance.

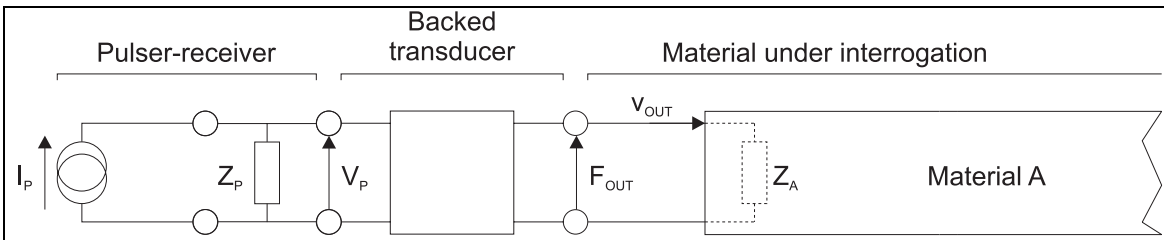


Figure 3.5 Model used to predict acoustic response.  $Z_A$  is the apparent impedance looking into the semi-infinite medium, A.

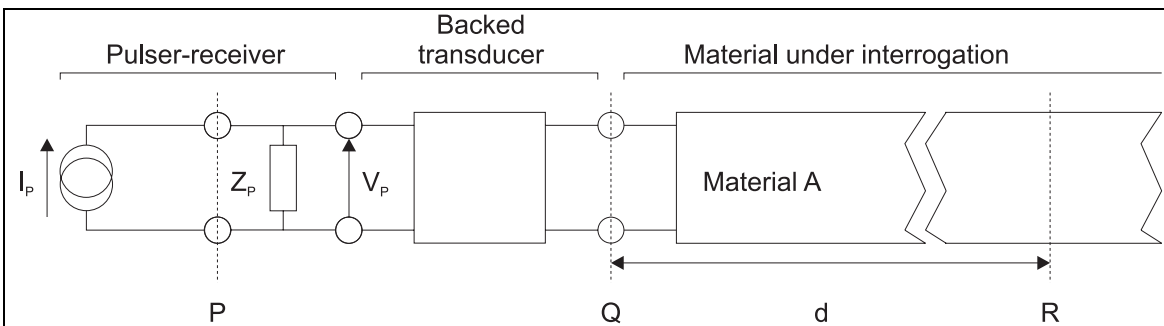


Figure 3.6 Model of the complete system, including the output impedance of the pulser.

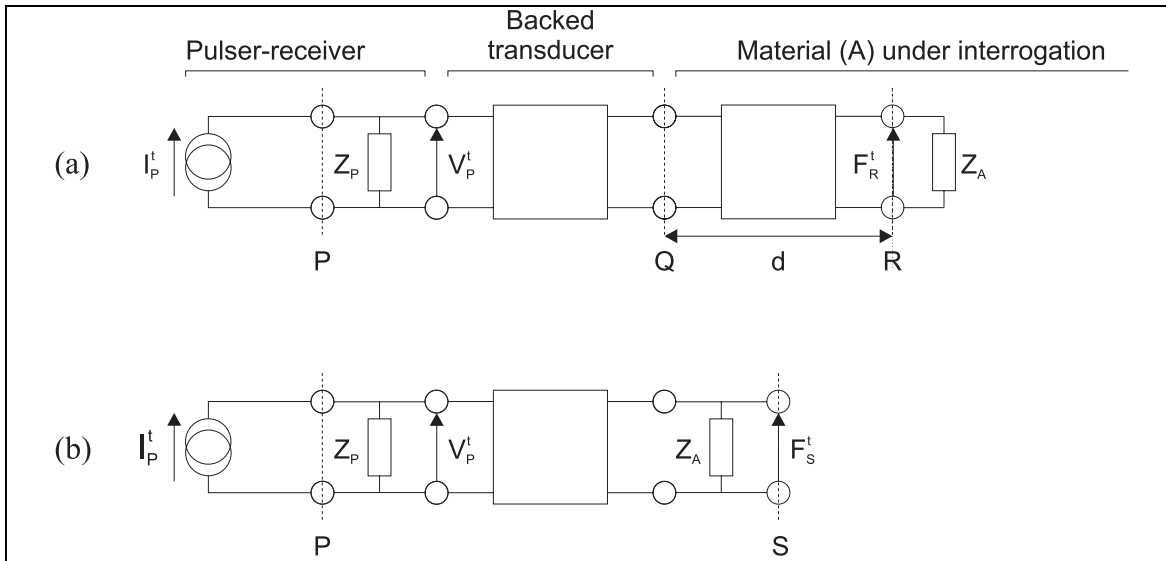


Figure 3.7 (a) The network used in the transmit case and (b) the corresponding network ignoring the time delay in medium A.

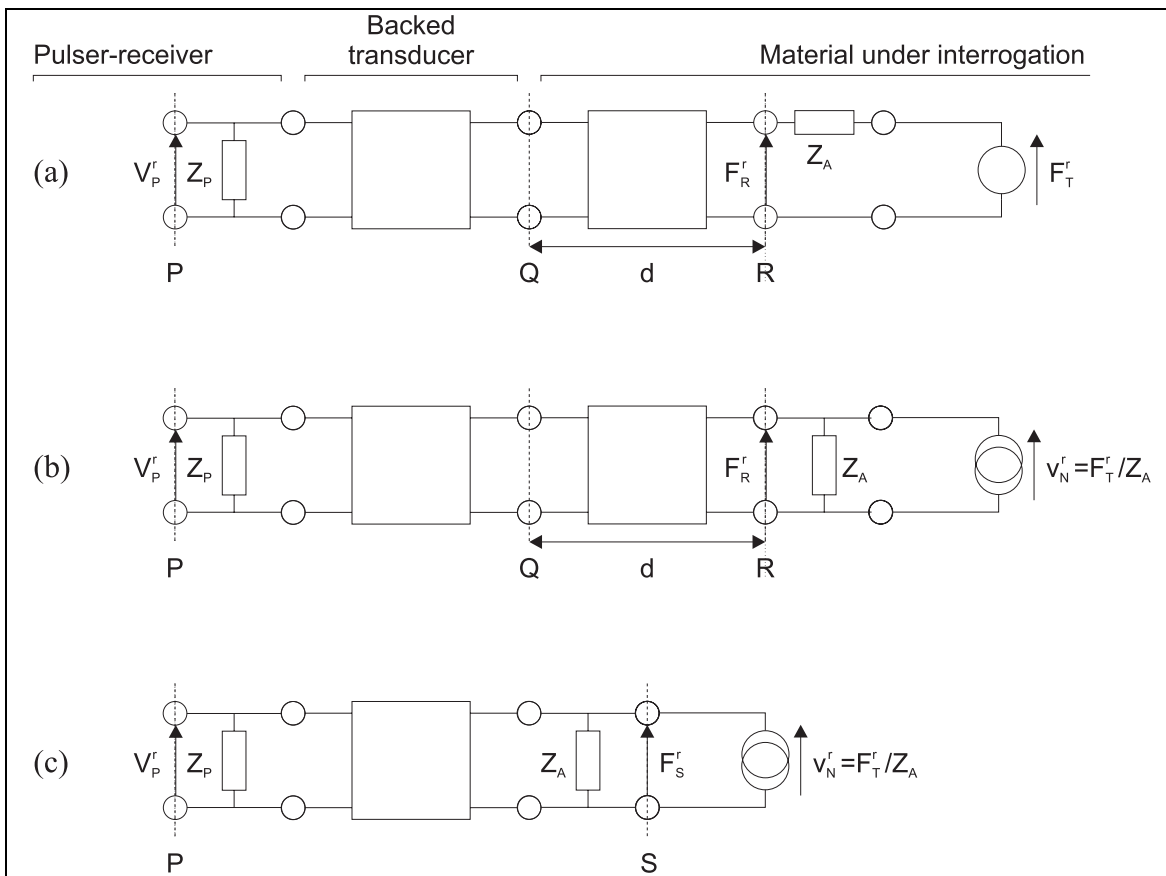


Figure 3.8 (a) The network used in the receive case using a Thévenin driving circuit, (b) using a Norton driving circuit and (c) ignoring the time delay in medium A.

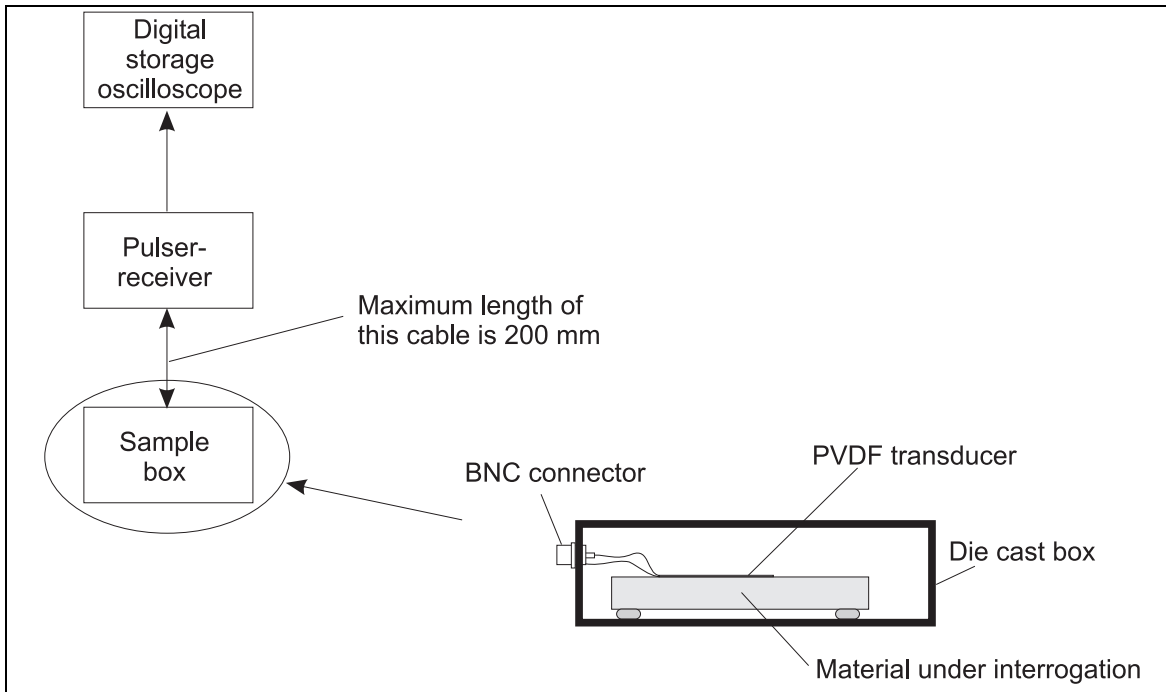


Figure 3.9 Experimental set-up for measuring the pulse-echo response of PVDF transducers bonded to solid substrates.

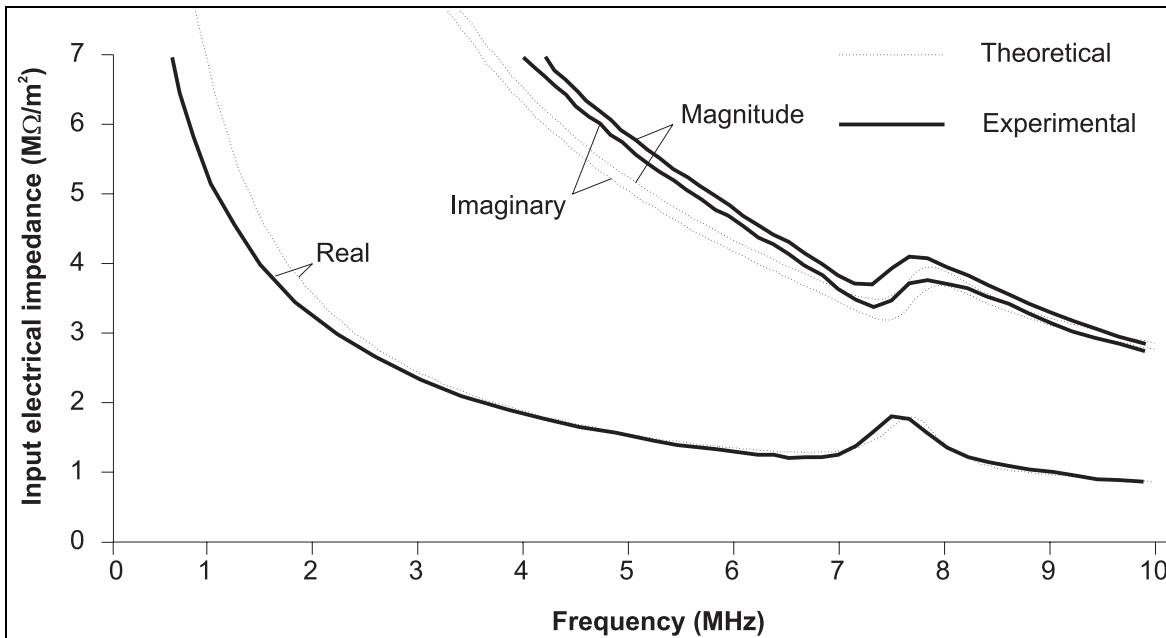


Figure 3.10 Comparison of experimentally measured and predicted input impedance of PVDF film in air.

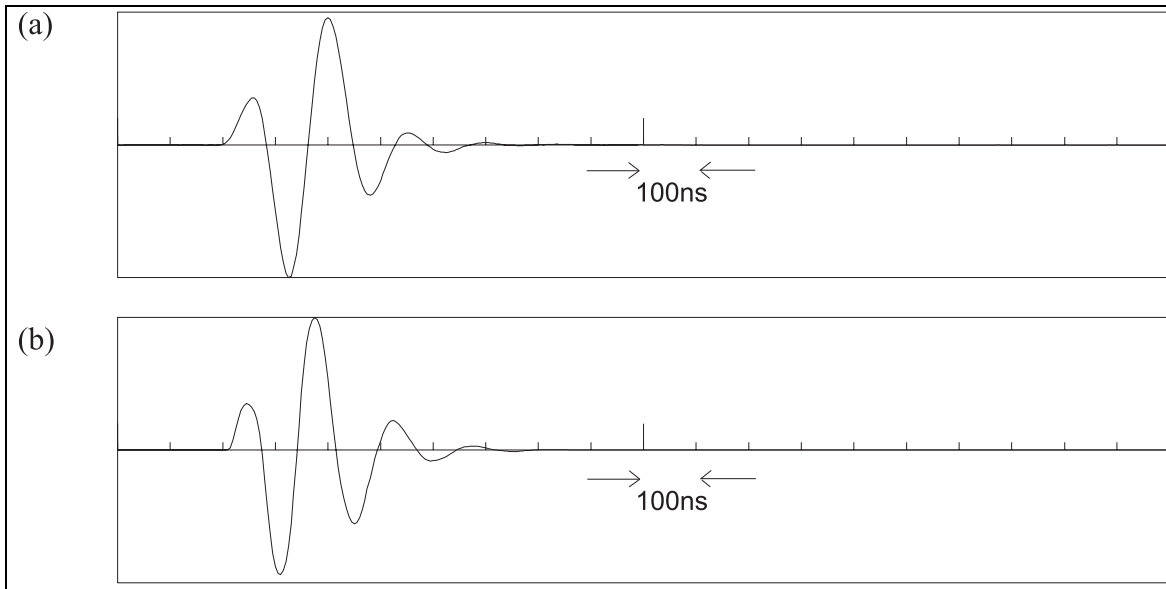


Figure 3.11 (a) Experimentally measured and (b) predicted pulse-echo time-traces for the case of an air-PVDF-perspex transducer configuration.

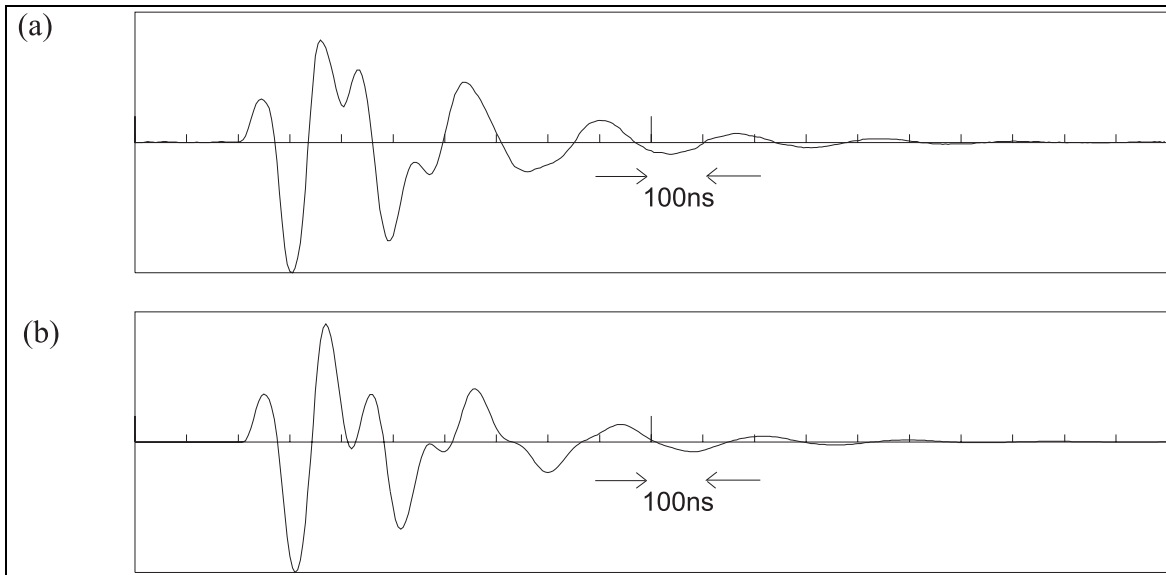


Figure 3.12 (a) Experimentally measured and (b) predicted pulse-echo time-traces for the case of an air-PVDF-aluminium transducer configuration.

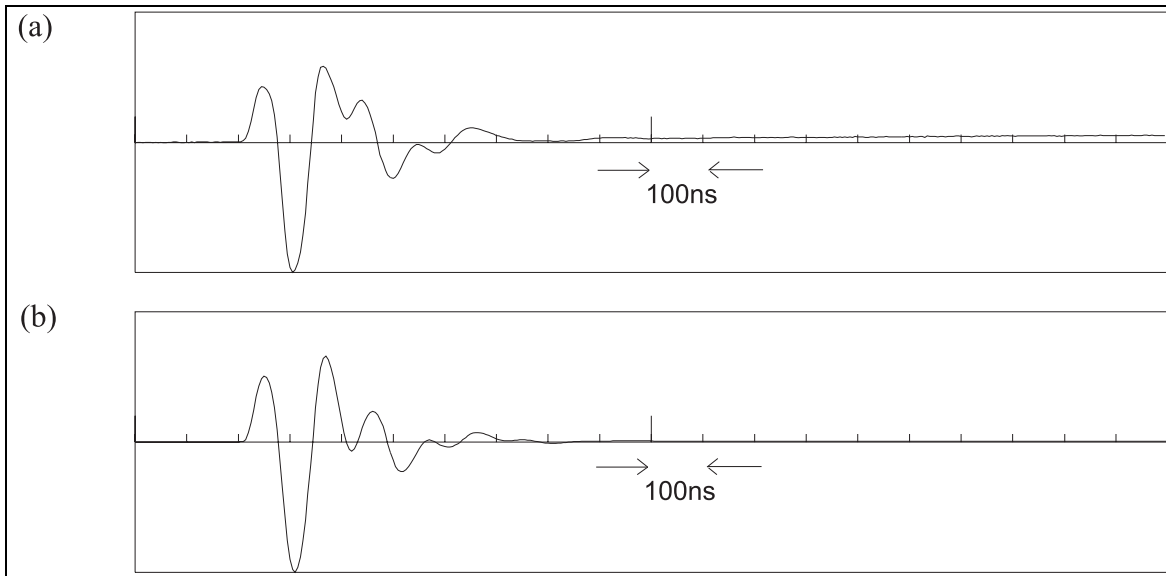


Figure 3.13 (a) Experimentally measured and (b) predicted pulse-echo time-traces for the case of a water-PVDF-aluminium transducer configuration.

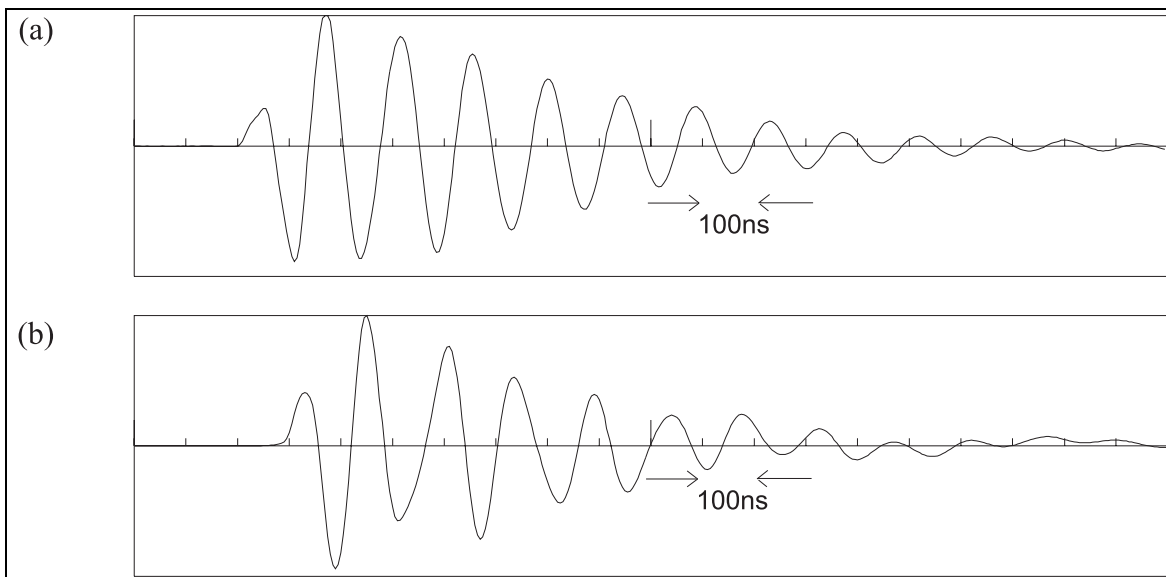


Figure 3.14 (a) Experimentally measured and (b) predicted pulse-echo time-traces for the case of a water-PVDF-aluminium transducer configuration with a thicker (75  $\mu\text{m}$ ) bond layer between the PVDF and the aluminium.

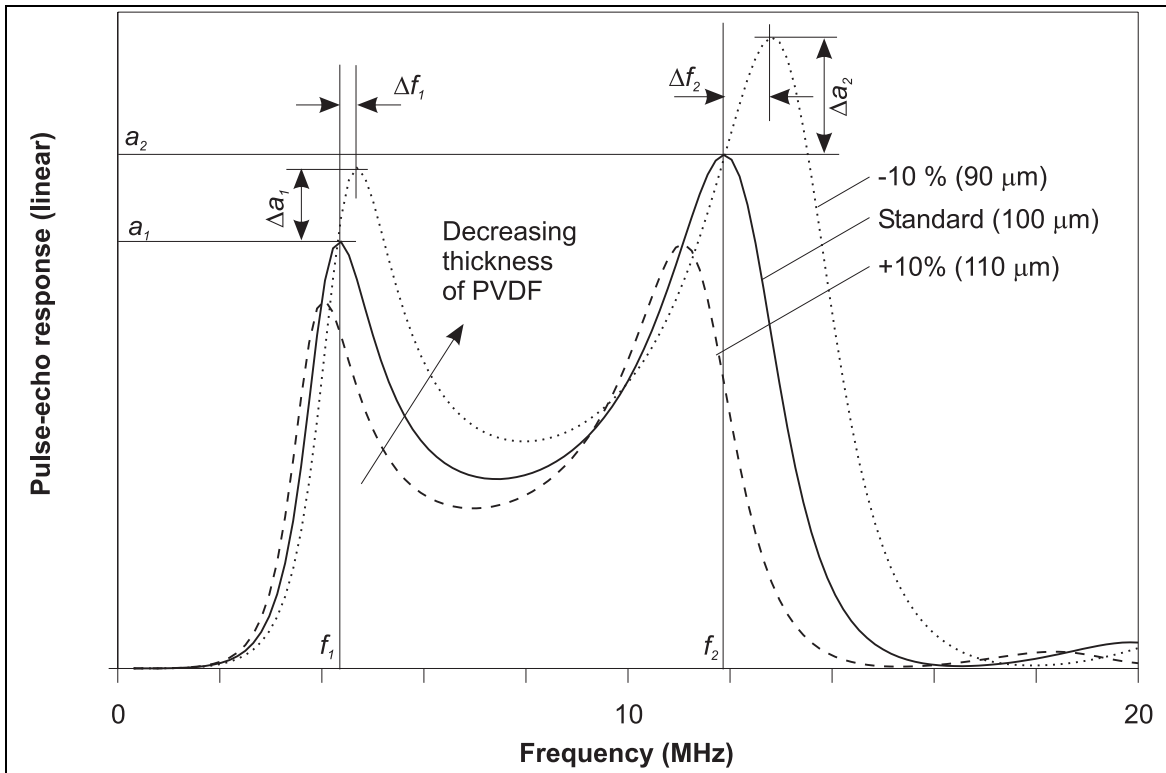


Figure 3.15 Example predicted pulse-echo response vs. frequency graph, showing the effect of perturbing an input parameter (in this case the thickness of the PVDF layer) by  $\pm 10\%$ .

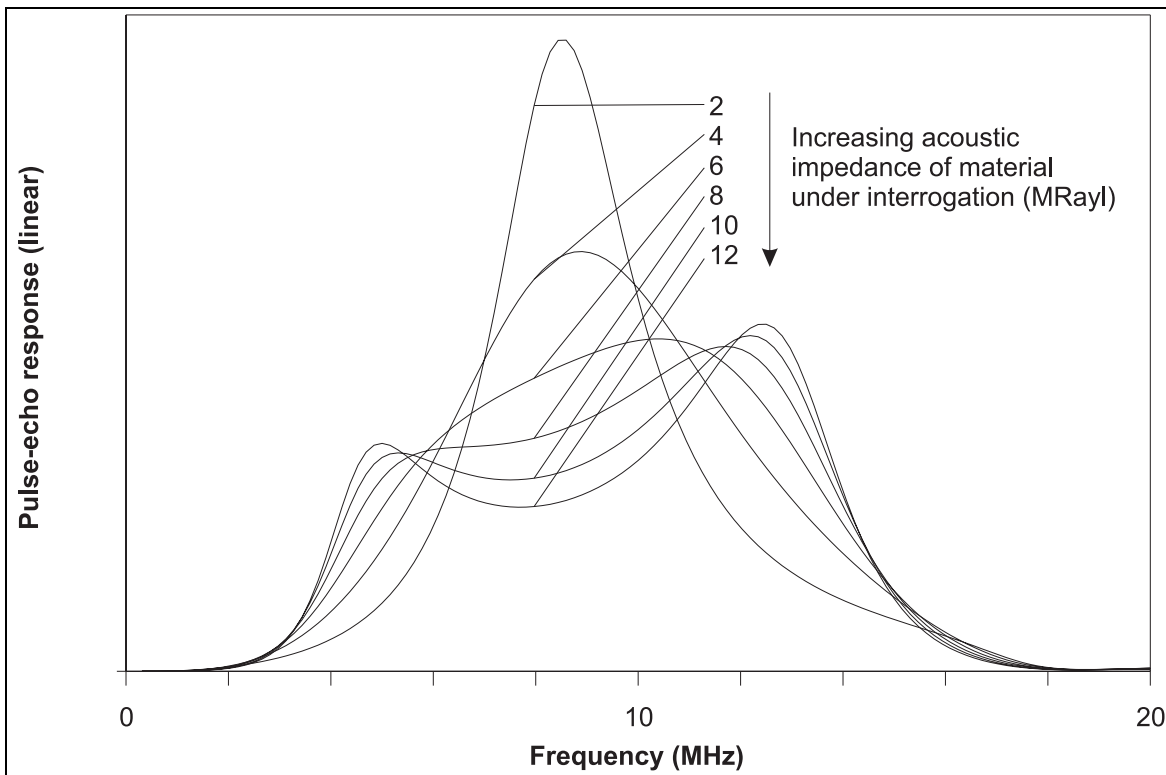


Figure 3.16 Effect of varying the acoustic impedance of the material under interrogation on predicted pulse-echo response.

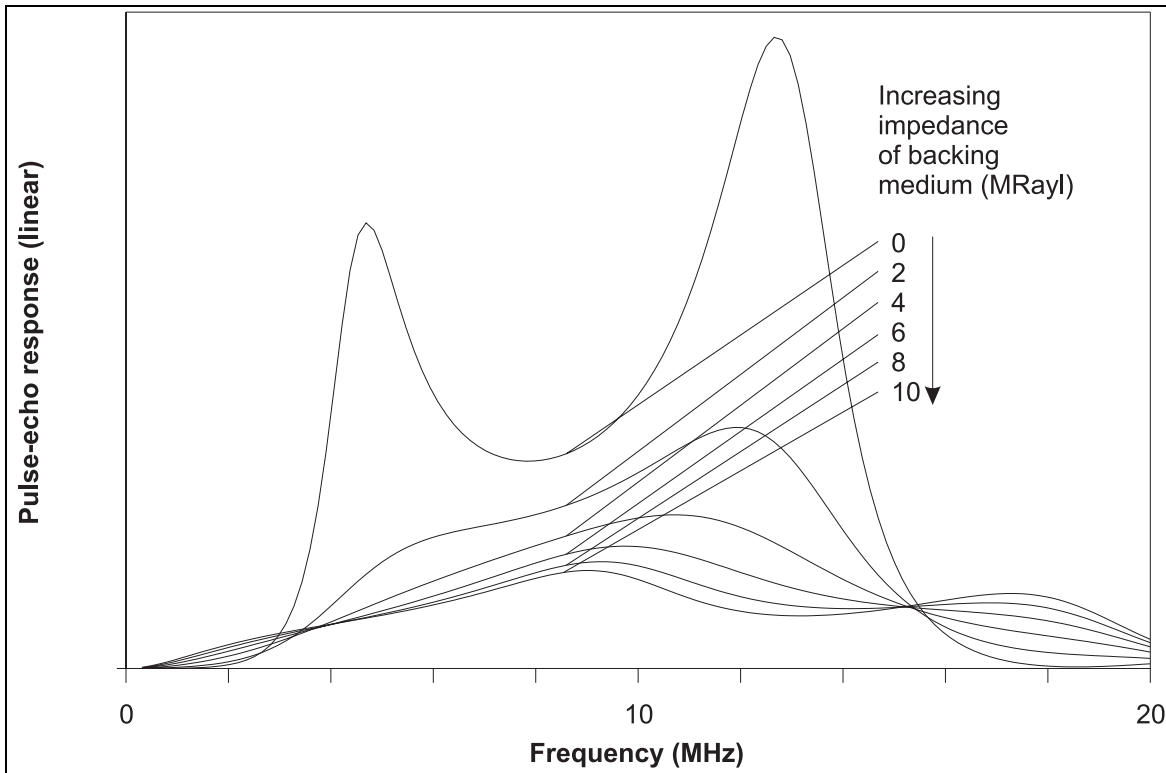


Figure 3.17 Effect of varying the acoustic impedance of the backing material on predicted pulse-echo response.

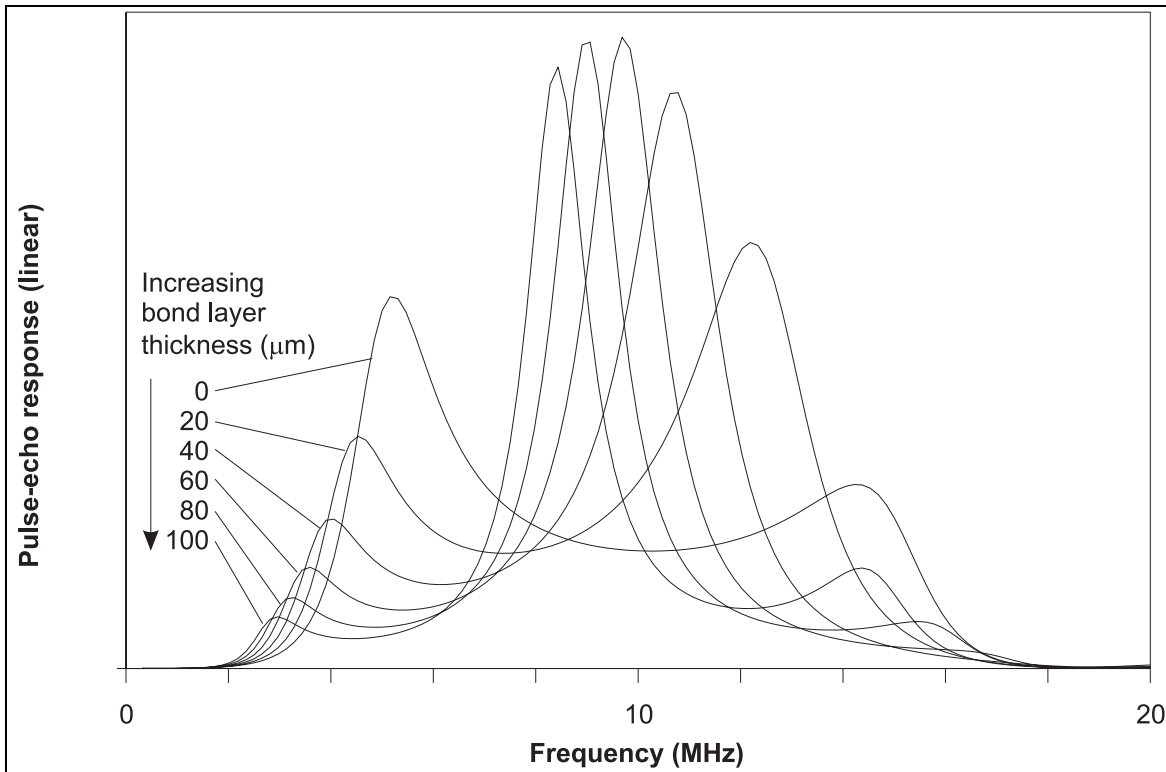


Figure 3.18 Effect of varying the bond layer thickness on predicted pulse-echo response.

## 4. High frequency PVDF inter-digital transducers

---

### 4.1 INTRODUCTION

The previous chapter described the implementation and validation of a one-dimensional transducer model, with particular emphasis on the use of the piezoelectric polymer PVDF (polyvinylidene fluoride) as the piezoelectric material. That model was specifically for transducers which transmit and receive bulk waves into the structure on which they are mounted. However, as noted in chapter 1, the use of permanently attached bulk wave transducers is not a satisfactory method of inspecting an entire structure, as the number of transducers required is very large. Hence, in this chapter, attention is turned to the design and construction of permanently attached transducers, which again use PVDF as the piezoelectric material, but which can transmit Lamb waves into the structure and receive reflections from features in the structure including defects. Potentially, the use of Lamb wave transducers will enable an entire structure to be monitored by a small number of transducers, and the remainder of this thesis will be concerned with investigating the design and behaviour of such transducers.

This chapter begins by discussing the requirements for transducers to transmit and receive Lamb waves, and a brief review of existing methods is presented. This is followed by a description of the design and construction of the first generation of inter-digital PVDF Lamb wave transducers. Experimental data is presented which shows the successful operation of these IDTs on thin plates. It will then be shown that the same IDT technology can be used to transmit and receive higher order Lamb waves in thicker structures, but that this is not an ideal strategy for their inspection.

### 4.2 BACKGROUND

#### 4.2.1 *Requirements for the transmission and reception of Lamb waves*

Lamb waves are excited in plate structures to varying degrees by almost any type of acoustic excitation, whether intentionally or not. The reason why more specialised techniques need to be employed to excite and detect them if useful information is to be obtained from experimental results is due to the need for modal selectivity. More details can be found in the works of Alleyne and Cawley (1992b and 1994b) but the main conclusions are summarised below.

In the next chapter, software will be described which can be used to predict the surface displacement as a function of time that would be received some distance away from an acoustic source. Here, that software is used as a tool to provide the example time-traces shown in figure 4.1 which illustrate the effect of different types of excitation. Exciting a plate with a brief pulse of force, as would be the case if a bulk wave transducer was placed on the surface and connected to a conventional pulser-receiver, imparts energy to the structure over a wide bandwidth of frequencies. Figure 4.1(a) shows a typically confused signal that would be received if this type of excitation was used. Reference to typical Lamb wave dispersion curves such as those shown in figure 2.4 indicates that this broadband excitation will potentially excite a large number of Lamb wave modes which

are generally dispersive. It is the superposition of numerous dispersive modes which causes the received time-trace to be so complicated. This is clearly not an ideal testing scenario. Some improvement can be obtained by constraining the frequency bandwidth of the excitation by using a toneburst rather than a pulse, as shown by the predicted results in figure 4.1(b). But again reference to figure 2.4 shows that this constraint alone is not sufficient to select a single mode, as there are always two or more modes present at any one frequency. Thus, a second constraint is necessary to selectively excite a single mode, and this is achieved in all practical methods of Lamb wave excitation by constraining the wavelength of excitation, which can produce a 'clean' time-trace as shown by the example in figure 4.1(c). (This technique is effectively matching the surface excitation of the plate to the sinusoidal shape of the desired Lamb wave mode in the direction of its propagation - in a finite element model, single mode excitation can also be achieved by imposing displacements through the thickness of the plate and matching the distribution of these to the mode shape of the desired mode - Alleyne and Cawley 1992b) To constrain the wavelength as well as the frequency, excitation is required that applies spatially as well as temporally varying surface tractions to a structure.

#### 4.2.2 Transducers to transmit and receive Lamb waves

##### *Immersion coupling and wedge transducers*

To obtain the required spatial distribution of surface tractions, a commonly used laboratory technique is to immerse a portion of the plate under test in water or other liquid. A conventional plane bulk longitudinal wave transducer is then positioned in the water so that its axis is at some angle  $\theta$  to the normal of the surface of the plate, as shown schematically in figure 4.2(a). When excited at a particular frequency  $f$ , the beam of plane compression waves produced by the transducer in the water impinges on the plate at an angle, and this creates a normal surface stress distribution on the surface of the plate which varies harmonically in space with a wavelength  $\lambda$  given by:

$$\lambda = \frac{c_l}{f \sin \theta} \quad (4.1)$$

where  $c_l$  is the bulk longitudinal wave velocity in water. An obvious drawback of such a system is the need for a coupling fluid, which precludes its use in many practical situations. Air may be used as a coupling fluid (Farlow and Hayward 1994, Safaeinili *et al.* 1995). However, great care is needed as the mismatch in acoustic impedance between air and most solids is large and hence only a small fraction of the incident acoustic energy will be converted into Lamb waves, the majority being reflected back into the air. Also, the angle of incidence for air coupled Lamb wave transducers is much more critical than for fluid coupled Lamb wave transducers.

A further alternative is to use a solid coupling medium such as perspex, and to couple this to the structure using a thin layer of gel couplant. Such a system is typically in the form of a variable angle wedge transducer (fixed angle wedge transducers are also used in some applications) as shown in figure 4.2(b). Again the angle of the incident waves, and hence the wavelength of the tractions imposed on the surface of the structure, can be varied by adjusting the angular position of the bulk wave transducer on the perspex wedge.

The mathematical analysis of immersion coupling and wedge transducers for Lamb wave excitation may be found in Viktorov's work (1965) and a more advanced analysis which takes into account reflections and radiation in the coupling fluid may be found in the work of Jia (1996).

##### *Inter-digital transducers*

A second class of excitation method which enables different Lamb wave modes to be excited selectively may be described as inter-digital transducers (IDTs). In this type of transducer, the spatially varying tractions on the surface of the structure are created within the transducer itself, rather than by the oblique incidence of bulk waves generated in an intervening medium. Certain types of electromagnetic acoustic transducers (EMATs), surface acoustic wave (SAW) devices and piezoelectric comb transducers are all examples of IDTs.

EMATs transmit and receive acoustic waves (including Lamb waves) in electrically conductive materials using the Lorentz principle. A magnetic field is produced in the material beneath the EMAT using either permanent magnets or DC electromagnets which are built into it. Also contained within the EMAT is a conducting wire, usually in the form of a meander or pancake coil. When the EMAT is transmitting, an alternating current is passed through the wire, eddy currents are induced in the material beneath the EMAT. These currents interact with the magnetic field to generate forces within the material which in turn generate acoustic waves. The orientation of the magnetic field and the position of the conducting wires can be configured in different ways in order to produce different types of acoustic waves (see for example Alers and Burns 1987 or Maxfield *et al.* 1987 for discussions of different types of EMAT). For generating Lamb waves, an EMAT with a meander coil as shown in figure 4.3(a) is used. The spacing between the meanders creates the necessary spatial variation of forces in the material. If the magnetic field is arranged as shown in the figure, the directions of the forces introduced into the plate will be normal to the plate surface as indicated. If instead the magnetic field was arranged to pass downwards through the meander coil, the forces generated would be parallel to the plate surface. The latter configuration makes EMATs a very attractive method for the transmission and reception of Lamb wave modes in which the particle motion is predominantly in-plane at the surface of the plate. Such modes cannot be efficiently excited by the immersion or air coupling techniques described above, as the bulk waves in the coupling medium do not couple well to the in-plane motion of the Lamb wave mode in the plate. A further advantage of EMATs is the fact that they do not need to be in physical contact with the surface of the plate and do not need to be used with a coupling fluid, which makes them ideal for measurement of high temperature plate inspection (Whittington 1989 for example). This attribute has also seen EMATs being used on 'pigs' for internal pipe inspection (Thompson *et al.* 1979) and on moving cold-rolled steel sheets (Murayama *et al.* 1996). The major disadvantage of EMATs is their lower sensitivity than piezoelectric devices, which is mainly due to limitations on the strength of magnetic field which can be achieved in a practical device (Alers and Burns 1987). The efficiency of EMATs is also affected by variations in the magnetic properties of materials on which they are used which can be significant.

SAW devices have many applications in signal processing to transmit and receive Rayleigh waves in the 10 MHz to 2 GHz frequency range with wavelengths ranging from a few microns up to around 0.25 mm. The non-dispersive nature of Rayleigh waves and

the fact that they can be readily excited on piezoelectric substrates mean that complicated tapped delay lines can be easily fabricated directly into integrated circuits. The term ‘SAW device’ in a signal processing context usually encompasses an inter-digital transmitter, inter-digital receiver and acoustic delay line. A typical SAW device is shown in figure 4.3(b) and consists of fingered electrode patterns deposited on a piezoelectric substrate such as quartz or lithium niobate. The purpose of the inter-digital finger patterns in an SAW device is to obtain the required signal processing characteristics rather than to select a particular wavelength of acoustic wave, which is not necessary since the devices use Rayleigh waves. Despite this difference, several important aspects of the design of the PVDF inter-digital transducers described here can be traced back to SAW devices, hence their inclusion in this discussion. A general description of some of the many devices of this type may be found in the text by Kino (1987) and considerable literature is available on the electrical characteristics of SAW devices for signal processing applications. However, this is not generally relevant to the initial development of inter-digital transducers for long range testing applications.

Although most SAW devices are concerned with Rayleigh waves, the use of SAW technology to generate Lamb waves has been reported in a few cases. Toda and Ikenohira (1980) demonstrated the use of an inter-digital PVDF Lamb wave device as an infrared temperature sensor. This device transmitted, propagated and received Lamb waves within the PVDF film itself. Jin and Joshi (1991) present a detailed theoretical investigation into an SAW device in which Lamb waves were propagated along a lithium niobate delay line which they propose as a liquid sensing device. Toda and Sawaguchi (1992) report the construction of an ingenious variable focus bulk wave transducer based on a leaky Lamb wave SAW device. The SAW device with concentric fingers generates Lamb waves in a two layer piezoelectric plate. When operated in water, the Lamb waves leak energy into the liquid in the form of bulk waves which are focused due to the circular finger pattern. The angle at which the bulk waves leak, and hence the position of the focal spot, could then be adjusted by altering the frequency. In all these devices, the emphasis was on Lamb wave propagation within the device, but not in an external structure.

Of much greater relevance to the work described here is an inter-digital PVDF transducer to transmit and receive Rayleigh waves in a non-piezoelectric substrate for potential non-destructive testing applications. This was reported by Mattiocco *et al* (1980) who used 25  $\mu\text{m}$  thick PVDF to launch Rayleigh waves on the surface of a silica substrate at a frequency of 8 MHz. Although successful, they were limited by the frequency response of the thin PVDF, and its high internal losses at the high frequency used. This device is very close in the principle of its operation to the PVDF IDTs described in this chapter.

Also highly relevant, albeit in terms of potential application rather than construction, is a device built by Demol *et al.* (1996). This is what might be described as a comb transducer (Viktorov 1967) which uses rectangular strips of PZT to excite Lamb waves in a composite laminate plate for non-destructive testing purposes. The PZT strips are bonded onto a supporting glass layer and the device is placed, PZT side down, onto the plate under inspection. The method of coupling is not specified but the presence of the supporting glass layer renders the transducer completely inflexible and would almost certainly cause coupling problems on anything other than a perfectly flat surface. They also found that the presence of the transducer appeared to significantly perturb the Lamb wave propagation in the structure beneath it - a result that will be observed for some of the transducers described later in chapter 6. The same workers (Blanquet *et al.* 1996) have

attempted to embed a type of inter-digital device within a sheet of perspex, in order to excite Lamb waves in it. Their results from both the embedded transducer and the comb transducer are not particularly good but this is probably due to the practical difficulties of attempting to propagate Lamb waves in a composite plate, rather than the transducer design.

Ditri *et al.* (1993) and Rose *et al.* (1996) have both worked on comb transducers for the transmission and reception of axially propagating guided waves in hollow pipes. Although they do not give exact details of the construction of their comb transducers, it appears that they comprise a monolithic layer of piezoelectric material behind a front wear plate, which is machined into the required comb shape. The fingers of the comb are therefore driven in phase. The transducer is designed to be movable (i.e. not permanently attached) and although the method of coupling is not specified, it is assumed that conventional gel couplant is used.

In collaboration with Imperial College, workers at Strathclyde University have investigated the construction of inter-digital devices of similar design to those which are described here, except using a matrix of piezo-ceramic platelets embedded in soft epoxy rather than PVDF as the piezoelectric material. These IDTs have the potential to be much more sensitive than those made from PVDF, due to the higher piezoelectric coupling in piezo-ceramic material. Although not as flexible as PVDF, the ceramic platelet matrix can still be made to conform to gently curving surfaces, which would not be possible if monolithic piezo-ceramic material was used. The epoxy matrix has the added bonus of deadening any resonances which could be set up along the length of the transducer which could be a major problem if monolithic ceramic material was used. Some prototype piezo-ceramic platelet devices have been tested (Gachagan *et al.* 1996) with very promising results.

### 4.3 PVDF INTER-DIGITAL TRANSDUCER DESIGN AND CONSTRUCTION

From section 4.2.2 and the experiments described in the previous chapter, it would appear that a rudimentary IDT could be fabricated from parallel strips of PVDF bonded to a plate structure, the spacing of the strips corresponding to the wavelength of the desired Lamb wave mode. However, there are several practical considerations which render this type of construction unfeasible, all of which stem from the frequency response of PVDF when bonded to a substrate with a high acoustic impedance. The physical construction of the first generation of PVDF IDTs is described below in section 4.3.1. After this the important features in the design are discussed in more detail.

#### 4.3.1 Construction of PVDF inter-digital transducers

A schematic diagram showing the assembly and construction of a PVDF IDT is shown in figure 4.4. The IDT is assembled from two separate components, the PVDF film itself and the electrode pattern which is printed on thin polyamide film. The PVDF is the same 110  $\mu\text{m}$  thick film as that which was used in the previous chapter, except that the silver ink electrodes with which it is supplied are removed using acetone prior to assembly of the IDT.

The polyamide film is 50  $\mu\text{m}$  thick and is of the type used in flexible printed cable and printed circuit board (PCB) assemblies. Its sole purpose is to provide a substrate onto

which the electrode pattern is printed using conventional PCB technology before the transducer is assembled. The layout of the electrode pattern will be discussed in more detail below. Before assembly of the IDT, the electrode pattern is also copper plated to a total thickness of around  $125\ \mu\text{m}$  (approximately equivalent to a '4 oz ft<sup>-2</sup>' plating) in order to obtain the necessary low frequency response characteristics for the IDT. The reasons for this will also be explained in greater detail below. Thin polyamide film (rather than conventional 1.6 mm thick PCB board) is used for two reasons: firstly to maintain the flexibility of the complete IDT and secondly so that Lamb waves are less likely to be generated within it, which may cause ringing within the transducer. A more attractive solution would be to selectively etch off the silver ink electrodes already on the PVDF film using PCB techniques and then copper-plate the remaining silver ink to the necessary thickness. However, several attempts at this method proved unsuccessful as the silver ink tended to separate from the film when plated.

The electrode pattern consists of equi-spaced parallel lines called fingers. In the simplest form these are configured in the manner shown in figure 4.5(a). It is the spacing of the fingers which determines the wavelength of Lamb waves which the IDT will transmit and receive. In this case the spacing between the fingers is equal to the wavelength of the desired Lamb wave mode. When an electrical signal is applied between an electrode finger and the substrate (i.e. the structure) a localised electrical field is created in the PVDF film in the region below the finger, leading to localised straining of the PVDF induced by the piezoelectric effect, which in turn generates tractions at the interface of the PVDF and the substrate. Applying the same signal to a set of parallel fingers creates the required spatial distribution of surface tractions as shown in figure 4.5(b). In practice, two sets of interleaved parallel fingers are usually used as shown in figure 4.5(c). Both sets of fingers are excited simultaneously but in anti-phase with respect to the substrate. This sets up the spatial variation of surface tractions shown in figure 4.5(d). In this case the spacing between the fingers needs to be equal to half the wavelength of the desired Lamb wave mode. The wavelength selectivity of the IDT will be discussed further in section 4.3.3

The IDT is assembled *in-situ* as follows. First the surface of the structure is smoothed and cleaned at the transducer location. The PVDF sheet is then bonded to the structure using cyano-acrylate adhesive (Loctite 406). Finally, the polyamide is bonded, copper side downwards, onto the PVDF again using cyano-acrylate adhesive. Later IDTs used low viscosity epoxy as the bonding agent as the longer curing time enabled the transducer to be assembled more carefully.

#### 4.3.2 Frequency response

When considering which Lamb wave mode to use for a testing application, frequencies below the cutoff point of the  $A_1$  mode are highly attractive, since only the two fundamental modes,  $A_0$  and  $S_0$ , can propagate. In aluminium, the  $A_1$  cutoff frequency-thickness is 1.57 MHz mm and in steel the value is very similar at 1.63 MHz mm. From the dispersivity considerations given in chapter 2, the ideal operating points in the region below the cutoff frequency-thickness of the  $A_1$  mode are the  $A_0$  mode at 1.343 MHz mm and the  $S_0$  mode at frequency-thicknesses below around 1 MHz mm. In the IDT configuration described here, PVDF generates predominantly out-of-plane surface tractions on the surface to which it is bonded. Examination of the mode shape of  $S_0$  in the low frequency-thickness regime shows that the particle motion at the plate surface is predominantly in-plane and therefore this mode is unlikely to be excited

efficiently by a PVDF IDT. Thus the  $S_0$  mode will be discarded at present and attention concentrated on the  $A_0$  mode at a frequency-thickness of 1.343 MHz mm.

It was shown in chapter 3 that the acoustic response of a single sheet of 110  $\mu\text{m}$  thick PVDF film with silver ink electrodes bonded to an aluminium or steel substrate is poor at frequencies below the quarter wavelength resonance of the film at 3.75 MHz. With this low frequency limit, the  $A_0$  operating point at 1.343 MHz mm can only be achieved on plates less than 0.4 mm thick. This is clearly not an ideal situation since firstly, the range of plate structures below this thickness would severely limit the number of applications and secondly, from an experimental point of view, the wavelength of the  $A_0$  mode in such structures would be 0.36 mm or less, which would make the construction of suitable transducers difficult.

##### *Methods of improving low frequency response*

It is clearly necessary to reduce, or ideally remove completely, the constraint on the lowest operating frequency. It has already been observed in chapter 3 that this can be achieved by increasing the acoustic impedance of the semi-infinite medium behind the PVDF, which also damps out the resonant peaks in the response spectrum. In principle, this is an ideal method of boosting the low frequency response, except that it requires a layer of material with high acoustic impedance behind the transducer, the thickness of which, if not infinite, must at least be many wavelengths long. This is not desirable for two reasons: firstly, the size and weight of the transducer will be significantly increased, which is in diametric opposition to achieving the goal of constructing a low profile transducer which has minimal impact on the structure to which it is attached. Secondly, as the backing layer cannot be made infinitely thick, there are likely to be reverberations of bulk waves from the back of it, which may be confused with other signals in the PVDF. Even if these bulk wave reverberations are minimised by selecting a material with high losses such as tungsten loaded epoxy (Silk 1984), there may also be reverberations of interface waves excited on the interface between the PVDF and the backing material.

Instead of attempting to simulate the presence of a semi-infinite layer behind the PVDF, an alternative means of altering the frequency spectrum of the PVDF is to back it with a layer of high density material which is considerably less than one wavelength thick. This method has been successfully used for the relatively high frequency IDTs described in this chapter using a copper layer around 125  $\mu\text{m}$  thick. In chapter 6, the method will be shown to work at considerably lower frequencies by using a 1.3 mm thick layer of lead plate.

##### *Effect of using thick back electrode*

To investigate the effect of using various thicknesses of backing layer, the one-dimensional model was used in conjunction with results obtained in the experiments described below.

The experimental set-up is shown in figure 4.6. Several transducers were constructed with various thicknesses of brass shim to act as the backing layer. Brass rather than copper was used for the backing layers to suit the available materials, but this is unlikely to have a significant effect on the experimental results due to the similarity of the acoustic properties of brass and copper. The bonds between the layers in each transducer were made using cyano-acrylate adhesive (Loctite 406). All transducers were made from

approximately 30 mm by 25 mm rectangles of PVDF with a 25 mm by 25 mm square being backed and bonded to the structure. The remaining area was used for making the electrical connections which were again made using silver loaded epoxy (supplied by RS, UK). Due to equipment limitations, it was not possible to perform low frequency pulse-echo tests on the transducers. However, by using a conventional unfocused 5 MHz transducer and a pulser-receiver (Panametrics 5052PR) operating in pitch-catch mode, through transmission tests could be performed, as shown in the figure. A through transmission test was first performed using two matched 5 MHz transducers. By measuring the frequency content of the input signal, the frequency response of a single 5 MHz transducer could then be calculated. This was achieved by dividing the frequency spectrum of the received signal by the frequency spectrum of the input signal and then square rooting it in order to obtain the frequency response of a single 5 MHz transducer. Next one 5 MHz transducer was used as a receiver, and a PVDF transducer was used as a transmitter, as shown in figure 4.6. The frequency spectrum of the received signal was then normalised by the frequency response of the 5 MHz transducer and the input signal to give the frequency response of the PVDF transducer alone. The results of these tests are shown in figure 4.7(a).

The one-dimensional model was also used to predict the acoustic response of a 110  $\mu\text{m}$  thick PVDF layer backed with various thicknesses of brass backing. In the model, the bond layers and the silver ink electrode layers were omitted. These results are shown in figure 4.7(b).

From figure 4.7, it can be seen that reasonable agreement is obtained between the experimental and theoretical results, although the position of the peak for a transducer without backing is somewhat different between the two graphs in the figure. The reason for this difference is because the one-dimensional model did not include the silver ink electrodes on the PVDF, but these were present on the PVDF used in the experiment. In the cases where the PVDF is backed, the total mass behind the PVDF is dominated by the mass of the brass and the omission of the silver ink electrode layer does not significantly affect the results.

It is interesting to compare the graph shown in figure 4.7(b) to that shown in figure 3.17, the latter showing the effect of increasing the acoustic impedance of a semi-infinite backing material. In both graphs it can be seen that the response at low frequencies is increased, but there is an important distinction to be made between the two cases. In figure 3.17, the acoustic impedance of a semi-infinite layer behind the transducer is increased thus providing something for the PVDF to ‘push on’, hence improving the low frequency response. However, acoustic energy is also dissipated into this semi-infinite layer and any resonances in the system are almost completely damped out. On the other hand, when a thin layer of a reasonably dense backing material is added to the PVDF as shown in figure 4.7(b) no further means of energy dissipation are introduced, and the system remains resonant although the frequency at which the resonance occurs is reduced. This effect will be discussed further in chapter 6, when the design of lower frequency IDTs is considered.

From both the model and the experimental results described above, it can be seen that the pulse-echo response at low frequencies is substantially improved when even a thin layer of brass backing is added. As the thickness of the backing is increased, the response at low frequencies also increases, albeit at a decreasing rate. For the type of IDTs described

in this chapter, copper rather than brass was used to provide the backing layer as it can be readily electro-plated onto the electrode pattern printed on the polyamide film using conventional printed circuit board technology. As noted previously, any differences between using copper and brass will be negligible, due to their similar densities. The electro-plating process limits the copper backing thickness to maximum value of around 125  $\mu\text{m}$ , although this value can be somewhat lower if the fingers are very closely spaced. The limit on the backing thickness sets the lowest practical operating frequency of this type of PVDF IDT to around 0.75 MHz. As far as using the  $A_0$  mode is concerned, this imposes an upper limit of 1.8 mm on the thickness of plate which can be inspected.

### 4.3.3 Wavelength selectivity

It should be stressed that the diagrams shown in figure 4.5(b) and (d) are estimations of the likely distribution of surface tractions due to the electrode patterns. In practice, the distribution of surface tractions may be significantly more complex due to the interaction of the electric fields from adjacent fingers, and the interaction of the stress fields below the fingers. For the purposes of understanding the wavelength selectivity of an IDT, an even more idealised model will be used where the surface traction distribution is assumed to be a perfect sinusoid over the length of the IDT. Consider a cross section through the plate, which at some section cuts through the IDT perpendicular to its fingers as shown in figure 4.8(a). The assumed spatial distribution of surface tractions along the length of the plate are shown in the graph in figure 4.8(b). It can thus be seen that in space, the IDT appears in much the same way as a toneburst appears in time. By taking a spatial Fourier transform of the surface tractions along the length of plate shown in figure 4.8(b), the wavenumber spectrum of the IDT may be obtained, figure 4.8(c), which is the spatial analogue of the frequency spectrum of a time signal. In much the same way as a finite length toneburst is associated with a finite bandwidth of frequencies, an IDT of finite length is associated with a finite bandwidth of wavenumbers. Similarly, the longer an IDT (in terms of the number of wavelengths it spans), the narrower the wavelength bandwidth.

The effect of the distribution of the actual surface tractions not being a perfect sinusoid is to introduce harmonics into the wavenumber spectrum at multiples of the fundamental wavenumber. In the extreme case where the IDT is assumed to apply only a concentrated line of force under each finger, the distribution of surface tractions appears as a series of impulses at each of the finger locations, and is the spatial analogue of a digitalised temporal signal. Using the temporal analogy, it is not too difficult to see that with only one set of fingers (i.e. one finger per wavelength) aliasing will occur at all multiples of the fundamental wavenumber. Similarly, if two sets of fingers are used, as is the case for all the IDTs described in this chapter, aliasing occurs only at the odd multiples of the fundamental wavenumber.

Lines of constant wavenumber may be plotted on Lamb wave phase velocity dispersion curves, and appear as straight lines which pass through the origin. The gradient of such a line is equal to the reciprocal of the wavenumber, the wavelength. Therefore, an IDT associated with a finite bandwidth of wavenumbers can be represented on phase velocity dispersion curves as the region between two straight lines passing through the origin. Similarly, a toneburst signal is represented by the region between two vertical lines. Hence, an IDT excited with a toneburst is associated with a region on the phase velocity dispersion curves which is the intersection of the regions corresponding to the toneburst and the IDT, as demonstrated in figure 4.9. The intersection of these regions will be

referred to as the operating region, and the point at which the centre frequency of the toneburst and the centre wavenumber of the IDT intersect as the operating point. It should be noted that achieving the operating point is an unobtainable goal, as to do so would require the use of an infinitely long IDT and infinitely long toneburst. It should also be noted that for a particular IDT on a particular plate, the wavenumber boundaries of the operating region are fixed, but the frequency boundaries may be varied by changing the input signal, subject of course to the physical limitations of the IDTs frequency response. The effect of wavenumber aliasing is also indicated in figure 4.9.

An elegant way of representing the above concepts is to plot the phase-velocity dispersion curves for a plate of a particular material on dimensionless logarithmic axes. Such a plot will be referred to as a DLV (Dimensionless Logarithmic phase Velocity) plot. The definitions of dimensionless frequency and dimensionless phase velocity may be found in chapter 2. A DLV plot for aluminium is shown in figure 4.10. Lines of constant wavenumber now appear as parallel diagonal lines of unity gradient. It was noted in chapter 2 that on a logarithmic frequency axis, the bandwidth of a toneburst of  $n$  cycles appears as a vertical band of fixed width, independent of the centre frequency. On a graph with logarithmic frequency and logarithmic phase velocity axes, the wavenumber bandwidth of an IDT which is  $m$  wavelengths long appears as a diagonal band of fixed width, independent of the wavelength of the IDT. Using a DLV diagram enables the proximity of other modes to a particular operating point to be assessed visually. Hence the number of cycles required in an excitation toneburst and the required size of an IDT in wavelengths can be estimated.

#### 4.4 TRANSMISSION AND RECEPTION OF FUNDAMENTAL ANTI-SYMMETRIC MODE IN THIN PLATES

##### 4.4.1 Introduction

A readily obtainable thickness of aluminium and steel plates is 1.2 mm (18 SWG) which is well within the thickness range which can be inspected using the IDT design described above. In fact, several iterations in the design of PVDF IDTs took place on 1.2 mm thick aluminium plates before the final construction was arrived at. The experiment described below in section 4.4.2 documents the first successful use of PVDF IDTs to propagate Lamb waves over a reasonable distance. The second experiment, which is described in section 4.4.3, demonstrates the use of two PVDF IDTs to detect the presence of an artificial defect in a 1.2 mm thick steel plate.

##### 4.4.2 Transmission and reception of $A_0$ mode in 1.2 mm thick aluminium plate

###### *Selection of operating points and transducer geometry*

It was decided to operate at the maximum group velocity of the  $A_0$  mode which occurs at 1.02 MHz in 1.2 mm thick aluminium plate. The wavelength of 2.4 mm associated with this point may be readily obtained from the dispersion curves shown in figure 4.11. The geometry of the IDTs which were constructed is shown in figure 4.12. It will be observed in the figure that the geometry of the IDT is such that the width of the fingers increases towards the centre of the IDT, the spacing between the centres of the fingers remaining constant. This effect is known as apodisation. The objective is to achieve a smooth

window (e.g. Hanning or Gaussian) in the spatial excitation distribution, rather than a rectangular one, the assumption being that the size of the surface traction associated with a finger is proportional to its width. The fabrication of the transducer imposes physical limits on both the minimum finger width (around 0.25 mm) and the minimum spacing between adjacent fingers (also around 0.25 mm) which can be achieved in practice. Fingers which are less than 0.25 mm wide become increasingly prone to breakages and inter-finger spacings less than 0.25 mm make short circuits likely.

##### *Experimental set-up*

The experimental set-up is shown in figure 4.13. At this stage in the project, pulse-echo facilities were not available, hence one IDT was used as a transmitter, and the other as a receiver. The input toneburst was generated by an arbitrary function generator (LeCroy 9101) and passed through a RF power amplifier (ENI 240L) to the IDT. As the power amplifier output is single ended, a 1:1 high frequency toroidal transformer was used to provide two floating signals which were then fed to the two sets of IDT fingers. With this configuration, the two sets of fingers electrically balance themselves with respect to the plate, which may then be earthed. A similar arrangement was used to obtain a single ended output from the two sets of fingers at the receiving IDT. This signal from this IDT was then fed through a low noise pre-amplifier (Macro design custom model) to a digital oscilloscope (LeCroy 9400). The 1.5 k $\Omega$  resistors shown in the figure were necessary to damp out electrical resonances which are set-up between the capacitance of the IDTs and the inductance of the transformers.

##### *Results and comments*

The complete time-trace (after 100 time averages) from the receiving IDT when the transmitting IDT was excited with a 20 cycle toneburst with an amplitude of 200 V (peak-peak) at 1.02 MHz is shown in figure 4.14(a). In all time-traces shown in the figure, the time origin is set at the temporal centre of the transmitted signal. The first arrival is from the wave packet which propagates along the direct path between the IDTs. After this, three further arrivals can be clearly seen, which are associated with waves reflecting off the ends of the plates. The latest of these is associated with a wavepacket reflecting off both ends of the plate and propagating a total distance of 2.56 m.

The effect which varying the number of cycles in the input signal has on the first arrival in the received signal is assessed in figures 4.14(b) to (e). With only 5 cycles, the amplitude of the received signal is  $\sim 3$  mV, and the signal appears untidy which is due to either dispersion effects or the generation of a second mode. When either 10, 20 or 50 cycles are used, the signal is visibly cleaner and the amplitude remains constant at  $\sim 5$  mV. The distance between the IDTs is 338 mm, or in terms of the plate thickness  $d$ ,  $282 d$ . From the work on dispersivity in chapter 2, the optimum number of cycles for propagation over a distance of  $500 d$  is around 10. This is reasonably consistent with these results, since when more than 10 cycles are used, the received signal increases in duration but not amplitude. In all cases, there is a small trailing signal behind the main wave packet in the first arrival. This corresponds to two wave packets which are transmitted obliquely to the direct path between the IDTs and are then reflected off the sides of the plate to the transmitting IDT. This path is of course slightly longer than the direct path between the IDTs and hence results in the later arrival of the signals. This fact can easily be

demonstrated by holding the sides of the plate at the approximate locations where the reflections take place in order to damp these waves and remove the trailing signal from the received time-trace.

An experiment was also performed in which the frequency of excitation was adjusted from 0.5 MHz to 2.7 MHz in increments of 0.05 MHz, in all cases using a 20 cycle toneburst. At each frequency, the received time-trace was captured and stored. These can be plotted in a waterfall or *F-scan* plot as shown in figure 4.15. These plots demonstrate the effect of moving the operating point up the operating line of the IDT on the phase velocity dispersion curves shown in figure 4.11(a). Each time the operating line intersects a mode, a signal will be sent and received. In the figure, signals associated with the  $A_0$ ,  $S_0$  and  $A_1$  modes can be clearly identified. Reference to the group velocity dispersion curves shows that while both the  $A_0$  and  $A_1$  modes are excited at points of low dispersion (i.e. stationary group velocity), the  $S_0$  mode is excited at a point where its group velocity is rapidly changing. This leads to highly dispersive  $S_0$  signals which are of much longer duration than the input signal. The changing group velocity of the  $S_0$  mode is also manifested as a changing arrival time of the  $S_0$  signals as the frequency is varied, whilst the temporal locations of the  $A_0$  and  $A_1$  signals remains fairly constant as the frequency is varied. The inverted group velocity dispersion curves (i.e. group delay) may also be superimposed on the *F-scan* as has been done in the figure, and it can be seen that they coincide with the locations of the received signals.

From figure 4.11(a), it is clear that the operating line of the same IDTs is also close to the point of least dispersivity on the  $A_1$  mode, hence when operated at the correct frequency these IDTs can also be used to transmit and receive this mode. The complete time-trace received when transmitting the  $A_1$  mode using a 20 cycle toneburst at 2.51 MHz is shown in figure 4.14(f). The amplitude of the first arrival is actually higher than the equivalent signal when using the  $A_0$  mode (the input signals being of approximately the same amplitude in both cases). However, in the case of the  $A_1$  mode, there are no signals which correspond to later arrivals of this mode (these would be expected at approximately the same times as when using the  $A_0$  mode due to the similarity in group velocities) although there is a second small signal shortly after the first arrival. From its temporal location, the mode associated with this second arrival is thought to be the first arrival of a slower mode, such as  $S_1$  or  $S_0$  which the IDTs are inadvertently sensitive to. This is exactly the sort of undesired signal which could lead to erroneous conclusions in a practical application where it could be mistaken for an echo from a feature in the plate. The lack of any further signals corresponding to the  $A_1$  mode after the first arrival indicates that the attenuation of this mode is higher than that of the  $A_0$  mode. This type of effect will be discussed further when thick plates are considered.

#### ***4.4.3 Transmission and reception of $A_0$ mode in 1.2 mm thick steel plate with artificial defect***

##### *Selection of operating points and transducer geometry*

On 1.2 mm thick steel plate, the least dispersive point on the  $A_0$  mode is around 1.12 MHz, but in this case, the wavelength is 1.9 mm, as shown by the phase velocity dispersion curves in figure 4.16(a). However, the experiment described in this section was performed using the same geometry of transducers as those used in the previous

experiment (these are shown in figure 4.12) which have a wavelength of 2.4 mm. This means that the actual operating frequency on the  $A_0$  mode is reduced to 1.04 MHz in 1.2 mm thick steel plate and therefore slightly below the ideal frequency. However, the relatively slowly changing group velocity of the  $A_0$  mode in this frequency range (see figure 4.16(b)) means that the increase in dispersion will be negligible.

##### *Experimental set-up*

The experimental set-up is shown in figure 4.17. The salient feature of the steel plate is the quarter thickness notch which is machined across the width of the plate at right angles to the wave propagation direction. The width of the notch was approximately 1 mm. Other than the different plate the experimental set-up is identical to that described for the previous experiment.

##### *Results and comments*

The complete time-trace received at the receiving IDT ( $R_X$ ) when the transmitting IDT ( $T_X$ ) was excited with a 10 cycle toneburst at the operating frequency of 1.04 MHz is shown in figure 4.18(a). Once again, the first arrival (labelled  $T_X R_X$  in the figure) and that with the largest amplitude corresponds to direct transmission between the IDTs. The arrival with the next largest amplitude ( $T_X E_1 R_X$ ) corresponds to waves which have reflected off the end ( $E_1$ ) of the plate before reaching the receiving IDT. In between these two arrivals is a third wave packet which is that reflected from the artificial defect ( $D$ ). After these three arrivals, further arrivals are visible, two of which can be identified as indicated in the figure. However, the reverberation pattern rapidly becomes very complex due to the multiple reflection paths that are provided by the three reflectors,  $E_1$ ,  $E_2$  and  $D$ , and further arrivals cannot be reliably identified.

Again the effect of transmitting signals with different numbers of cycles has been investigated, and these results are shown in figure 4.18(b) to (e). As would be expected, the optimum number of cycles is again around 10. It is interesting to note that when 50 cycles are used, the reflection from the defect can no longer be distinguished from the end reflection, due to the overlap of the two signals. This highlights the need to use the optimum number of cycles to maximise the resolution, as discussed in chapter 2.

As was the case in the previous experiment, the same IDTs can also be operated at a higher frequency to excite the  $A_1$  mode at 2.58 MHz. The received time-trace is shown in figure 4.18(e), and the first three arrivals can again be readily identified. Between the first arrival ( $T_X R_X$ ) and the second arrival ( $T_X D R_X$ ) there is considerably more noise than in the time-trace shown in figure 4.18(f). This can be attributed to the presence of the dispersive  $S_1$  mode, which is being inadvertently transmitted and received by the IDTs due to its proximity in phase velocity-frequency space to the  $A_1$  mode. It is interesting to note that no further arrivals are visible after the first three, which again indicates that the  $A_1$  mode has greater attenuation than the  $A_0$  mode.

#### **4.4.4 Conclusions**

In this section, results have been presented which demonstrate the successful use of PVDF IDTs to transmit and receive pure Lamb wave modes in two thin metallic

structures. In the case of the aluminium plate, propagation was possible over a distance of around 2.5 m when using the  $A_0$  mode. Propagation over a reduced distance was shown to be possible when the same IDTs were used to excite the  $A_1$  mode, although an unwanted mode was also excited. In the case of the steel plate, both the  $A_0$  and  $A_1$  modes were shown to be sensitive to an artificial defect.

These experiments, as well as demonstrating that the transducers operate, have raised several important points, some of which will take on more significance in the following section. The number of fingers on the transducer and the number of cycles in the toneburst have been seen to be important in determining the selectivity of the transducers to a particular mode. It has also been observed that the  $A_1$  mode suffers potentially greater selectivity problems due to the proximity of other modes than the  $A_0$  mode does. Although the materials have been considered lossless, the difference between the  $A_0$  and the  $A_1$  received signals in both experiments has qualitatively demonstrated the large decrease in maximum Lamb wave propagation distance possible when using the  $A_1$  mode.

Since these early experiments, much further work has been undertaken at Imperial College using this type of IDTs on thin plate, some of which has been published (Monkhouse *et al.* 1997a and b). However, the next consideration in this thesis is to determine whether or not this technology can be successfully transferred to thicker plates.

#### 4.5 TRANSMISSION AND RECEPTION OF HIGHER ORDER MODES IN THICKER PLATES

##### 4.5.1 Introduction

The PVDF IDTs described above are clearly highly successful at transmitting and receiving the  $A_0$  and  $A_1$  modes in thin plates. It has already been shown that with this design of IDT, the minimum operating frequency is around 0.75 MHz, which precludes the use of the  $A_0$  mode on plates which are greater than 1.8 mm thick. However, it was hoped that the same type of IDTs could still be used to transmit and receive higher order modes in thicker plates.

To this end, a series of experiments on ductile iron pipe, steel pipe and steel plate were carried out. It should be stated that at the time when these experiments were executed, the work on dispersion effects described in chapter 2 had not been carried out and the effect of the finite wavelength bandwidth of an IDT had been given only limited consideration. Had the extent to which these problems are encountered when using higher order modes been more fully understood, this line of investigation may have been abandoned at an earlier stage. For this reason, only the results of two experiments on ductile iron pipe are reported below.

These experiments were performed on ductile iron pipe with an nominal internal diameter of 6", a mean wall thickness of 6.5 mm and wave propagation in the circumferential direction. The radius to thickness ratio of the pipe is around 11.5:1. According to the phase velocity dispersion curves for curved plates presented in chapter 2, this degree of curvature is sufficiently low for it to be ignored. Hence, for wave propagation purposes, the pipe will be regarded as a flat ductile iron plate of the same thickness.

### 4.5.2 *Transmission and reception of $A_2$ mode in ductile iron pipe with 6.5 mm thick walls*

#### *Selection of operating points and transducer geometry*

In 6.5 mm thick ductile iron plate, the first point of low dispersion on a mode above the minimum IDT operating frequency of 0.75 MHz is at 0.99 MHz on the  $A_2$  mode, as shown in figure 4.19(a). It can be seen from the figure that this operating point is very close to the  $S_1$  and  $S_2$  modes, and by examining the group velocity dispersion curves shown in figure 4.19(b), it can be seen that the three modes all have similar group velocities. This is not an ideal situation, as firstly, the proximity of the adjacent modes in phase velocity space means that it will be hard to avoid exciting them, and secondly, their proximity in group velocity space means that if they are excited, it will be hard to separate them from the desired mode in time. Nonetheless, a pair of IDTs with 6.0 mm wavelength to transmit and receive the  $A_2$  mode was constructed, the geometry of which is shown in figure 4.20.

#### *Experimental set-up*

Again, pulse-echo facilities for IDTs were not available at the time when these experiments were performed, hence two transducers were used in a pitch-catch configuration, using the same electrical apparatus as described in section 4.4.2. The transducers were arranged as shown in figure 4.21. The detailed electrical connections have been omitted for clarity in the figure. It should be noted that there are two possible direct paths between the transducers which are intentionally chosen to be different lengths so that the signals associated with both paths may be resolved in time.

#### *Results and comments*

An example of a received time-trace is shown in figure 4.22(a), when the input signal was a 20 cycle toneburst at 1.05 MHz. The amplitude of the signals received at this frequency was higher than at the analytically predicted operating frequency of 0.99 MHz. Two distinct signals can be identified in the figure, and these are associated with waves propagating in each of the two directions around the pipe. In each signal, the wave packet with the larger amplitude can be identified as the desired  $A_2$  mode, by measuring the group velocity. The slightly slower wave packet of lower amplitude, which is visible more clearly in the second arrival signals, may likewise be identified as belonging to the dispersive  $A_1$  mode. From the dispersion curves, it is likely that there may also be a signal associated with the highly dispersive  $S_2$  mode, which propagates at a similar or slightly faster speed than the  $A_2$  mode.

Figures 4.22(b) to (d) show how the received signal associated with waves travelling around the shorter path between the IDTs changes as the number of cycles is varied. When 5 or 10 cycles are used in the input signal, as shown in figures 4.22(b) and (c) respectively, the presence of the faster  $S_2$  mode is clearly visible ahead of the  $A_2$  mode. When the number of cycles in the input signal is increased to 20 as shown in figure 4.22(d), the signal from the  $S_2$  mode overlaps the signal from the  $A_2$  mode so much that it is impossible to comment on whether or not the relative amplitudes of the two modes have changed. Comparison of figures 4.22(c) and (d) may indicate that the tail

behind the main signal has been slightly reduced in amplitude by increasing the number of cycles to 20, but the overlap and interference of the modes again make it hard to be certain.

The earlier work on dispersivity described in chapter 2 indicates that for a propagation distance of  $100d$  ( $d =$  plate thickness) the optimum number of cycles to use for the  $A_2$  mode is around 30. The shorter propagation path around the pipe is around  $20d$ , hence it would be expected that the 20 cycle toneburst used experimentally is reasonably close to the optimum from a dispersion point of view. Unfortunately this does not take any account of the number of cycles necessary to achieve single mode excitation and from the experiment described above, it can be seen that even with 20 cycles extraneous modes are still being excited. With hindsight, the wavelength selectivity of the IDT itself is not adequate and it should have been made a greater number of wavelengths long. However, reference to the DLV plot in figure 4.10 (for this purpose the DLV plots for aluminium and iron can be assumed to be the same) indicates that the proximity of the adjacent modes is such that single mode operation could probably never be achieved at this point on the  $A_2$  mode in practice.

#### ***4.5.3 Transmission and reception of $S_4$ mode in ductile iron pipe with 6.5 mm thick walls***

##### *Selection of operating points and transducer geometry*

An examination of the dispersion curves shown in figures 4.19(a) and (b) shows that the maxima in group velocity (i.e. where the minima in dispersivity occur) of all the higher order modes whether symmetric or anti-symmetric, correspond to locations on the phase velocity dispersion curves where adjacent modes are in close proximity. With this in mind, it is hard to see how pure mode excitation can ever be achieved when using a higher order mode. However, if the maximum group velocity of one of the symmetric modes is used as an operating point, the group velocity will always be considerably higher than the group velocity of any of the surrounding modes. Hence, even if other modes are excited, the faster symmetric mode will be the first arrival, and should be resolvable in time from the unwanted modes. This cannot be achieved if the maximum group velocity of one of the anti-symmetric modes is used as an operating point since the group velocities of the surrounding modes are all of a similar magnitude. With this in mind, it was decided to attempt to transmit and receive a symmetric mode.

The mode shapes at each of the symmetric mode maxima in the iron plate were examined using *Disperse* (Pavlakovic *et al.* 1997). Unfortunately, for the first four symmetric modes (i.e.  $S_0$  to  $S_3$ ) in ductile iron plate, the ratio of the out-of-plane to the in-plane displacement at the surface of the plate is less than 1:10, compared to around 2:1 at the maximum group velocity of the  $A_0$  mode. For the  $S_4$  mode, the ratio rises to around 1:5 and for the  $S_5$  mode the ratio rises further to around 1:4. On this basis, it was thought that it would be exceedingly difficult to efficiently excite any symmetric mode below  $S_4$  using PVDF IDTs. Hence a pair of IDTs with 2.7 mm wavelength was constructed to transmit and receive the  $S_4$  mode at 2.21 MHz. The geometry of these IDTs is shown in figure 4.23.

##### *Experimental set-up*

The transducers were arranged as shown in figure 4.24. The remaining electrical apparatus is the same as that described in section 4.4.2.

##### *Results and comments*

The received time-trace when transmitting a 20 cycle toneburst at 2.21 MHz is shown in figure 4.25(a). It is interesting to compare this to the corresponding signal when using the  $A_2$  mode (figure 4.22(a)) obtained previously. Although in both cases the amplitude of the input signal was approximately the same, the amplitude of the first arrival is an order of magnitude lower in the case of the  $S_4$  mode. Also, in the case of the  $S_4$  transducers, there is no evidence of a second arrival, which is surprising, even taking into account the lower amplitude of the first arrival. This suggests that there is significant attenuation in the pipe, which affects the  $S_4$  mode to a greater extent than the  $A_2$  mode. The nature of this attenuation has not been identified but contributions may be expected from three sources. Firstly, there is likely to be 'true' attenuation due to material damping in the iron itself which converts some fraction of the acoustic energy into heat. It is commonly assumed that this type of attenuation increases with frequency when expressed per unit distance of wave propagation. This would be consistent with the lower frequency  $A_2$  mode being less attenuated over a fixed distance of propagation than the  $S_4$  mode, as the wavelength of the latter is smaller. A second cause of attenuation is due to scattering of the propagating waves. In the manufacturing process (spin casting), the outer surface of the ductile iron pipe acquires a dimpled appearance, the diameter of the dimples being of a similar magnitude to wavelength of the  $S_4$  mode. This is thought to lead to an increase in the scattering attenuation of this mode. Although detailed investigations into this effect have not been made here, the scattering theory recently developed by Chimenti and Lobkis (1997) for propagating Lamb waves in plates with rough surfaces may well be applicable. A third cause of the reduction in signal amplitude is due to geometric attenuation caused by beam spreading. However, the work on IDT beam divergence which is described later in chapter 6 has subsequently been used to show that, for an IDT of a given width, the beam spreading of short wavelength Lamb waves should be less than that of longer wavelength Lamb waves. As the IDTs for the  $A_2$  mode and the  $S_4$  mode are of equal width and the  $S_4$  mode has a considerably shorter wavelength, it can be concluded that geometric attenuation does not contribute to the lower amplitude of the  $S_4$  mode.

At the time when these experiments were performed the group velocity dispersion curves for curved plates had not been obtained. However, reference to figure 2.7 shows that the group velocity dispersion curves are significantly distorted at certain points even when the curvature is not severe. One such point is close to the maximum group velocity of the  $S_4$  mode which is used here. Whether or not this has affected the results here is hard to say, due to the problems of obtaining single mode propagation.

Before moving on from this topic, it is again interesting to observe the effect which the number of cycles in the input signal has on the received signal which is shown in figures 4.25(b) to (d). It can be clearly seen that as the number of cycles is increased from 10 to 50, the received signal becomes cleaner and more like the input signal. Furthermore, the overall duration of the received signal is, if anything, reduced by increasing the number of cycles. This is of course partly due to the dispersivity effects discussed in chapter 2 and also partly to do with the improved modal selectivity. Reference to

figure 2.17 indicates that the optimum number of cycles is around 50 at the least dispersive point of the  $S_4$  mode in aluminium when the propagation distance is  $100d$  ( $d$  is the plate thickness). In this experiment the propagation distance is only around  $20d$ , hence it would be expected that the optimum number of cycles would be less than 50. This is consistent with the experimental measurements shown in figure 4.25(b-d), which were made before the dispersivity work was carried out.

#### 4.5.4 Conclusions

From the results in this section, it is clear that operating on higher order Lamb wave modes is considerably more complex than on the fundamental modes. The combination of the wavenumber and frequency of the transmitting IDT must be exactly correct in order to excite the correct mode at the correct point on the dispersion curves. The tolerance on the operating frequency is much tighter on higher modes than lower modes, because of the need to operate at exactly the peak group velocity to avoid dispersion effects. Since the frequency cannot be changed significantly, so the wavelength of the IDT must be exactly correct for efficient operation. This is in contrast to operation on the  $A_0$  mode for instance, where the operating frequency is less critical and the wavelength of the mode can be matched to the wavelength of the IDT by tuning the frequency of excitation.

The work described in chapter 2, has shown that, in theory, the minimum resolvable distance which may be attained when using a pure higher order mode is of similar magnitude to that which may be attained when using the fundamental modes. Unfortunately, it has also become clear that the point on a higher order mode where the potential minimum resolvable distance can be achieved (i.e. the maximum in group velocity) is always in very close proximity to adjacent modes in wavenumber space. Hence it is hard, if not impossible, to build an IDT of reasonable dimensions which will select a pure mode. Furthermore, the scattering and absorption effect which the fingers of an IDT have on waves passing underneath them has been assumed negligible. Although, experimental work has suggested that this is a justifiable assumption for the IDTs constructed so far, it cannot remain the case as the number of fingers is increased indefinitely. At some point, the effect of adding more fingers must become negligible, as waves generated by fingers at the back of the IDT will not be able to propagate under it and will therefore not contribute to the field in front of the IDT. This imposes a physical limit on the wavenumber resolution which can be obtained by an IDT, regardless of its size. If a pure mode cannot be selected, the minimum resolvable distance which is predicted for the higher order modes is irrelevant.

The tendency for attenuation per unit distance to increase as the order of the mode (and therefore the frequency) is increased is another factor against using a higher order mode in preference to a lower one for long range testing.

Taking these factors into consideration, it was decided to abandon trying to excite higher order modes, and instead try to reduce the operating frequency of the IDTs so that the fundamental modes could be excited in thicker structures.

## 4.6 CONCLUSIONS

This chapter has explained the basic operation of inter-digital transducers (IDTs) for transmission and reception of Lamb waves. The development of a first generation of IDTs

which use PVDF as the active piezoelectric material have been described and their successful use as transmitters and receivers of the fundamental  $A_0$  Lamb wave mode in 1.2 mm thick plate has been demonstrated. The success of this work has stimulated further investigation into practical applications on similar structures by other workers in the group. In particular, Mr. R. Dalton is currently investigating the use of rosette arrays of high frequency IDTs for monitoring areas of aircraft fuselages (some measurements from this work may be found in the Wilcox *et al.* 1998 paper) and Mr. P. Marty is investigating the use of normal mode theory for predicting the efficiency of such IDTs. As noted earlier in this chapter, the use of alternative piezoelectric materials with superior performance to PVDF in similar IDTs is also being investigated. Initial results using piezo-ceramic platelets in an epoxy matrix manufactured at Strathclyde University have been extremely encouraging (Gachagan *et al.* 1996).

It was hoped that the same type of IDT technology could be transferred directly to structures with thicknesses between 5 and 15 mm, where the IDTs would be used to transmit and receive higher order Lamb wave modes. However, inspection of the dispersion curves has indicated that excitation of a pure higher order mode is difficult and experimental results on thick pipe have confirmed this. The experiments have also highlighted several other effects which indicate that the use of higher order modes is impractical. On this basis, chapter 6 will examine methods of reducing the frequency response of PVDF IDTs further so that they can be used to transmit and receive the fundamental Lamb wave modes on thicker structures. First however, the next chapter will describe the development of a model based on Huygens' principle of superposition which enables the acoustic field from an IDT to be predicted.

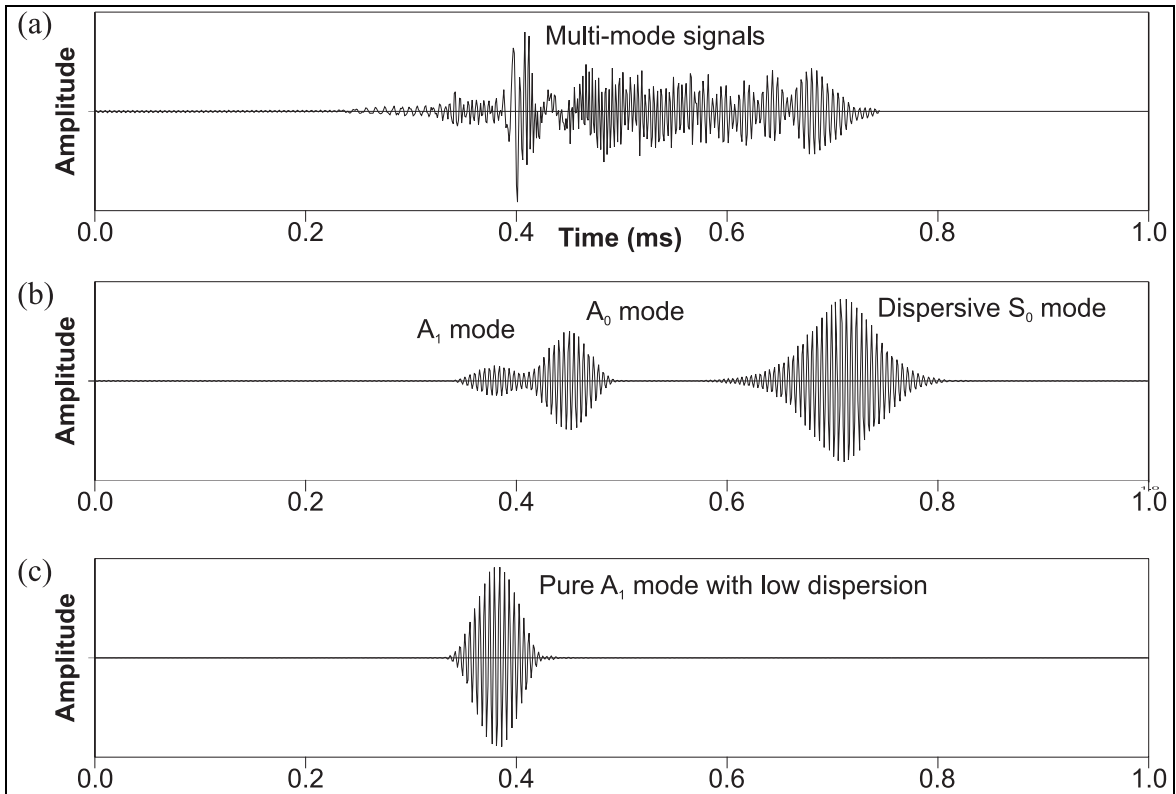


Figure 4.1 Example predictions of time-traces that would be measured 100 mm away from a source on a 1 mm thick aluminium plate, if (a) the source was a broadband pulse (b) the source was a 20 cycle toneburst and (c) the source was a 20 cycle toneburst and only excited a single mode, in this case  $A_1$ .

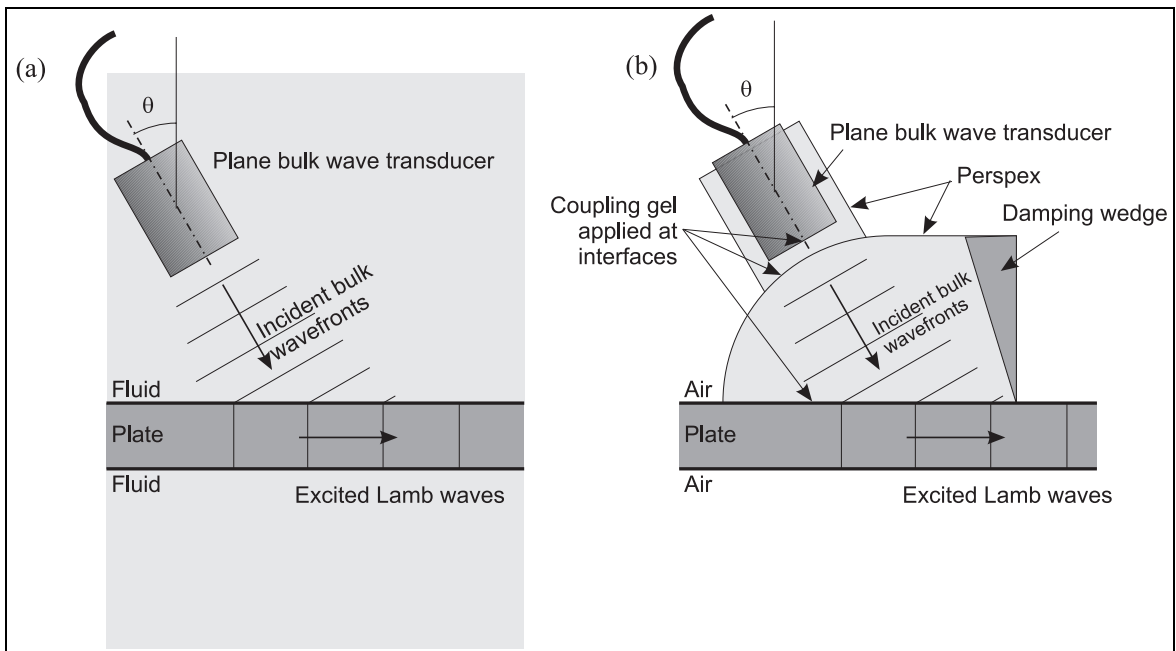


Figure 4.2 Excitation of Lamb waves by (a) immersion coupling and (b) variable angle wedge transducer.

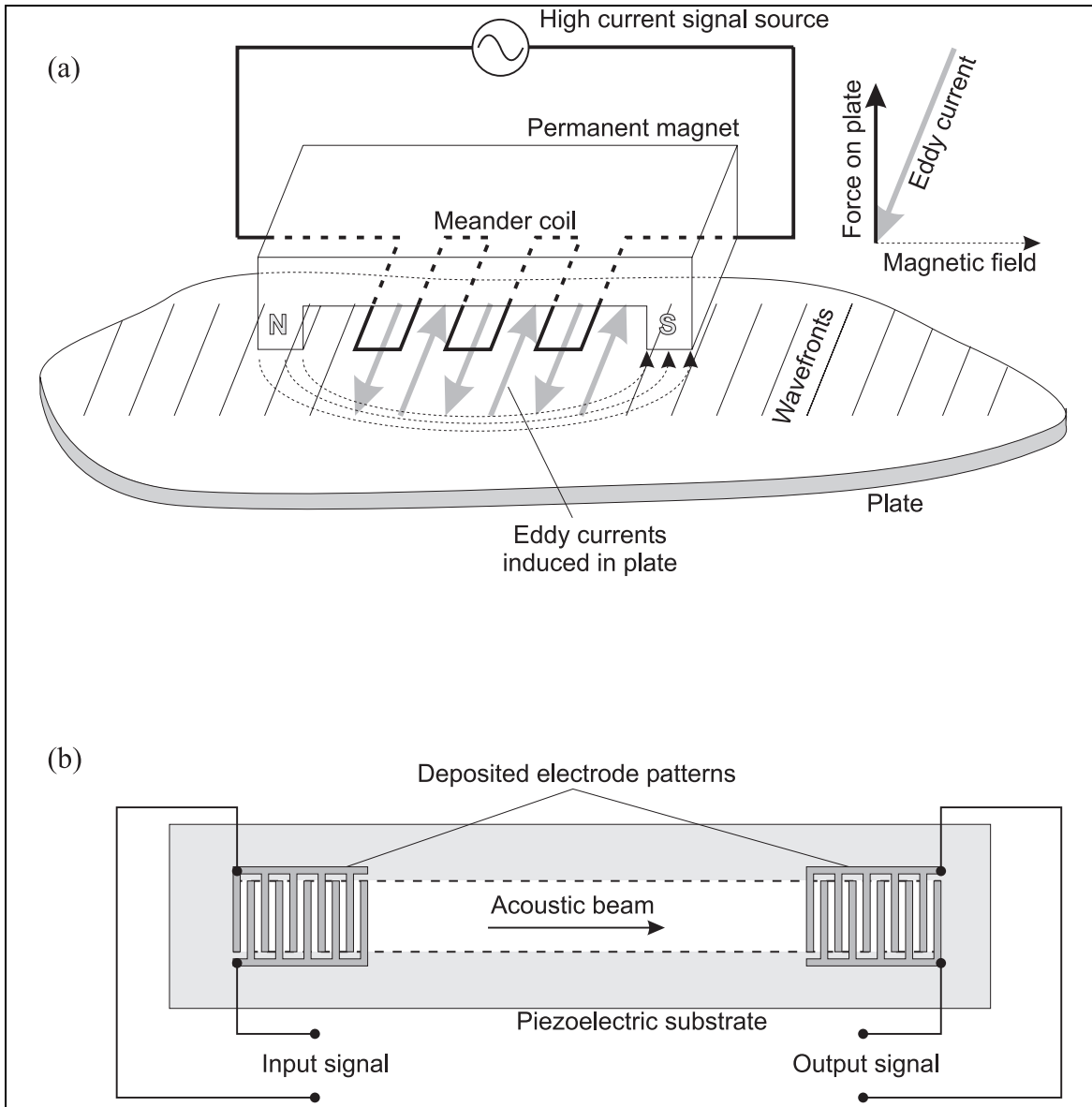


Figure 4.3 (a) Excitation of Lamb waves by electromagnetic acoustic transducer. (b) A surface acoustic wave device generating Rayleigh waves in a piezoelectric substrate (after Kino 1987).

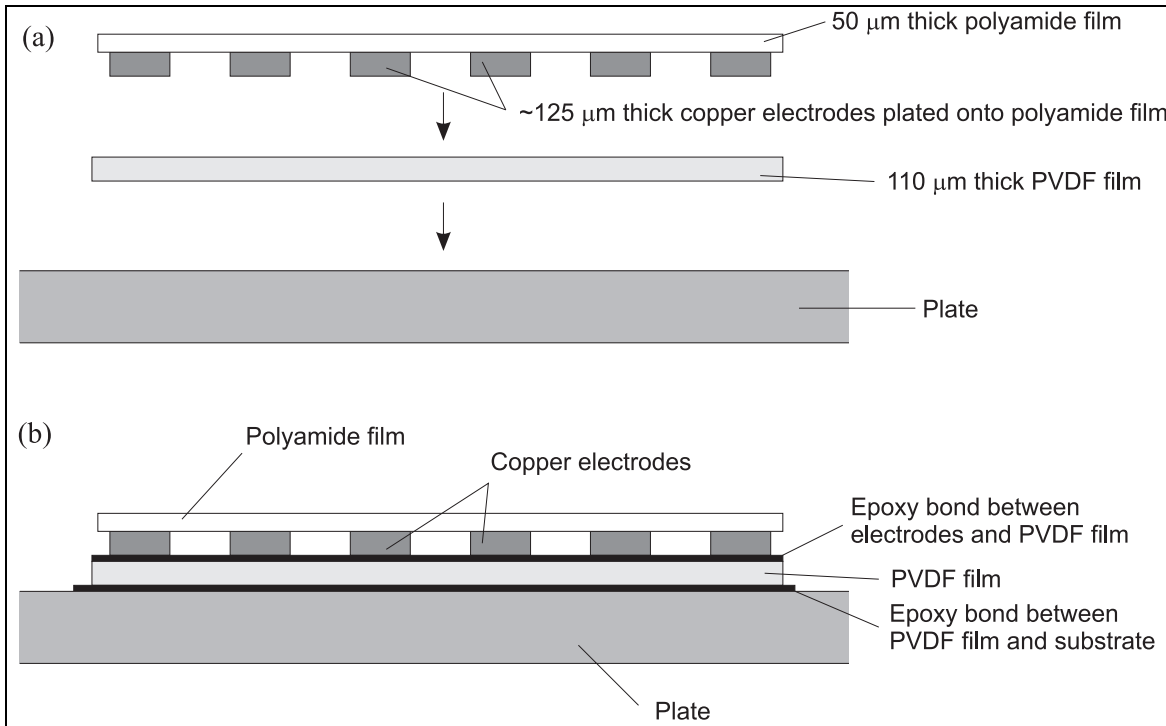


Figure 4.4 Schematic cross section, showing the construction of a high frequency PVDF IDT (a) before and (b) after assembly.

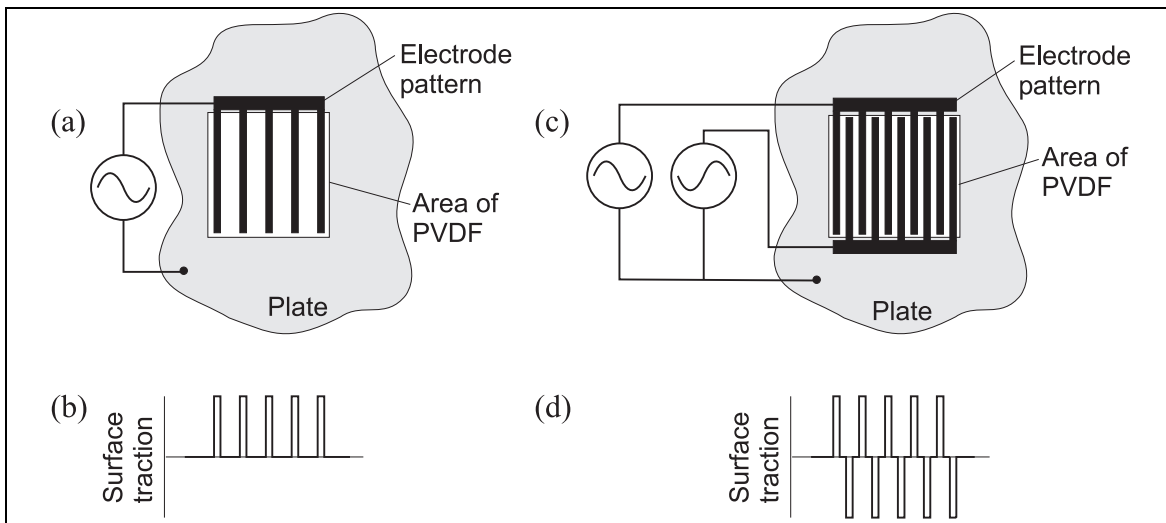


Figure 4.5 (a) Example electrode pattern for a single phase IDT and (b) the associated distribution of surface tractions. (c) Example electrode pattern for a two phase IDT and (d) the associated distribution of surface tractions.

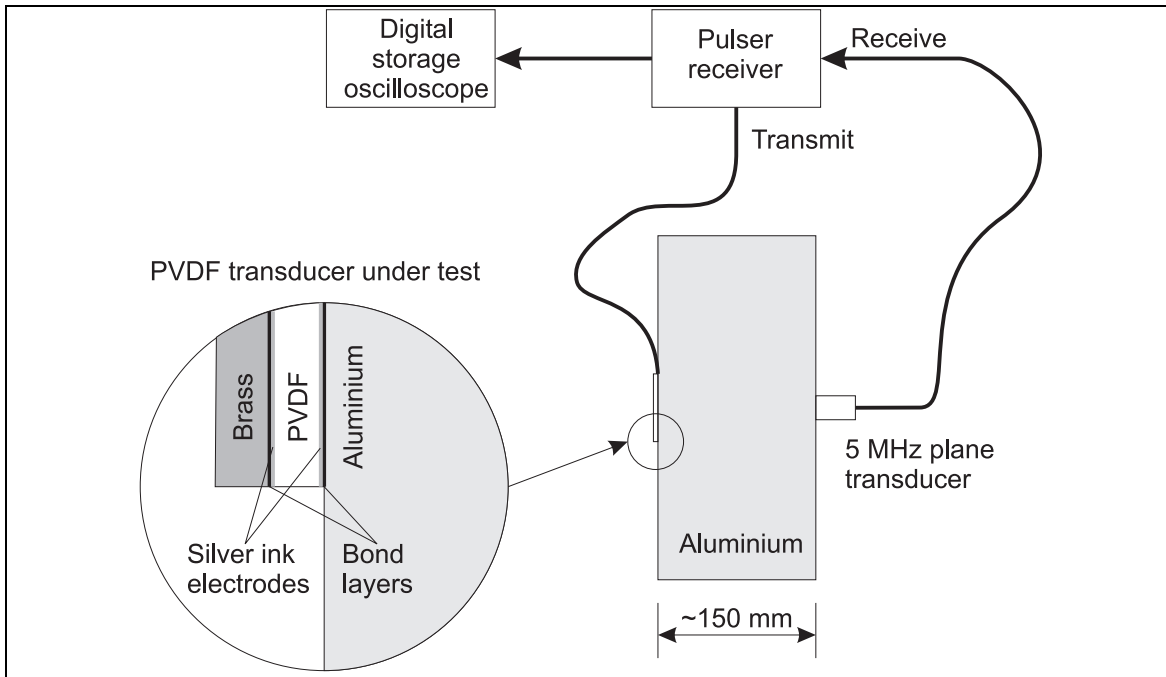


Figure 4.6 Experimental set-up to investigate effect of backing layer thickness on bulk wave transducer response.

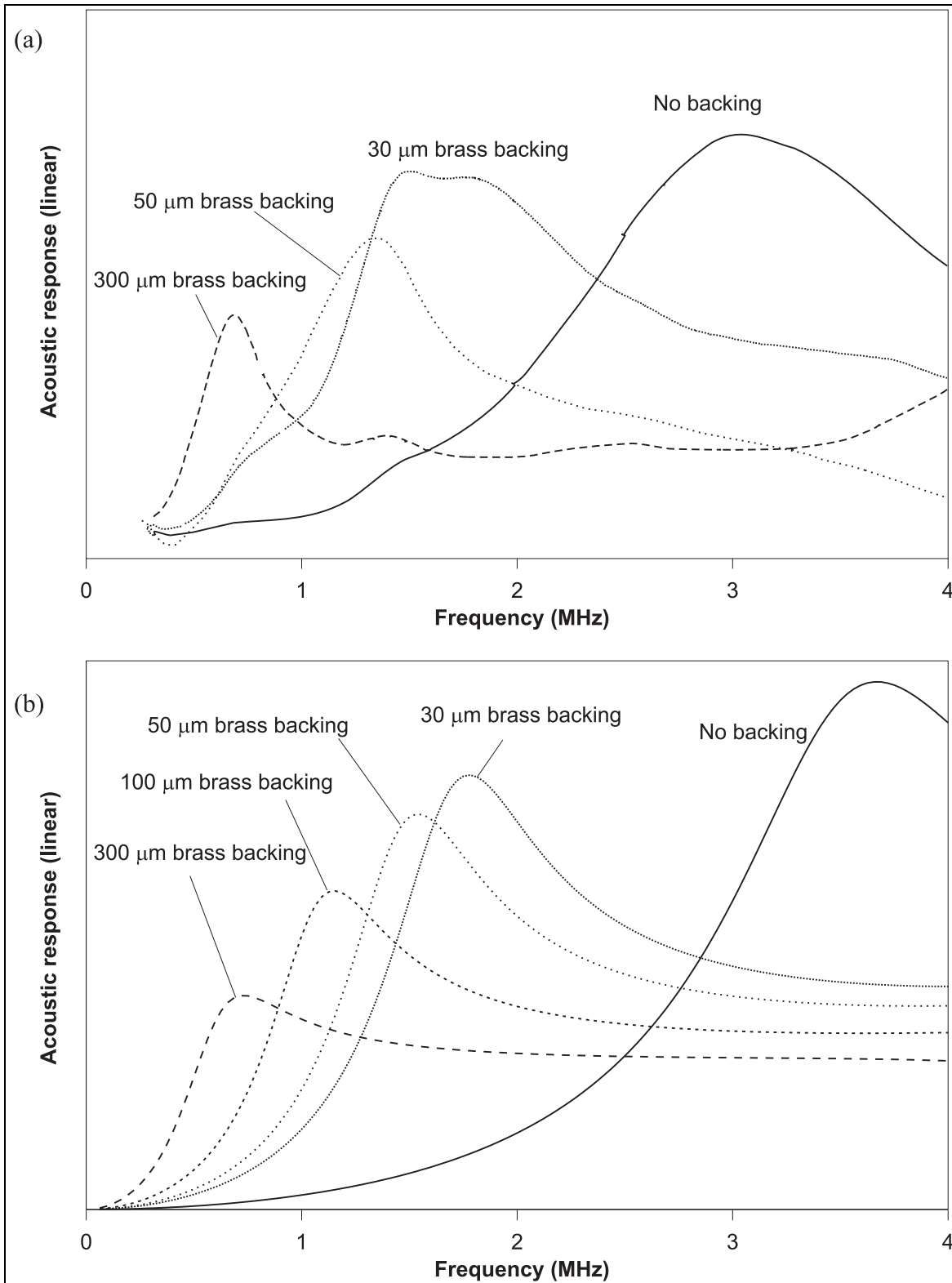


Figure 4.7 (a) Experimentally measured and (b) predicted effect of increasing the thickness of backing layer on acoustic response of the PVDF bulk wave transducer system shown in figure 4.6.

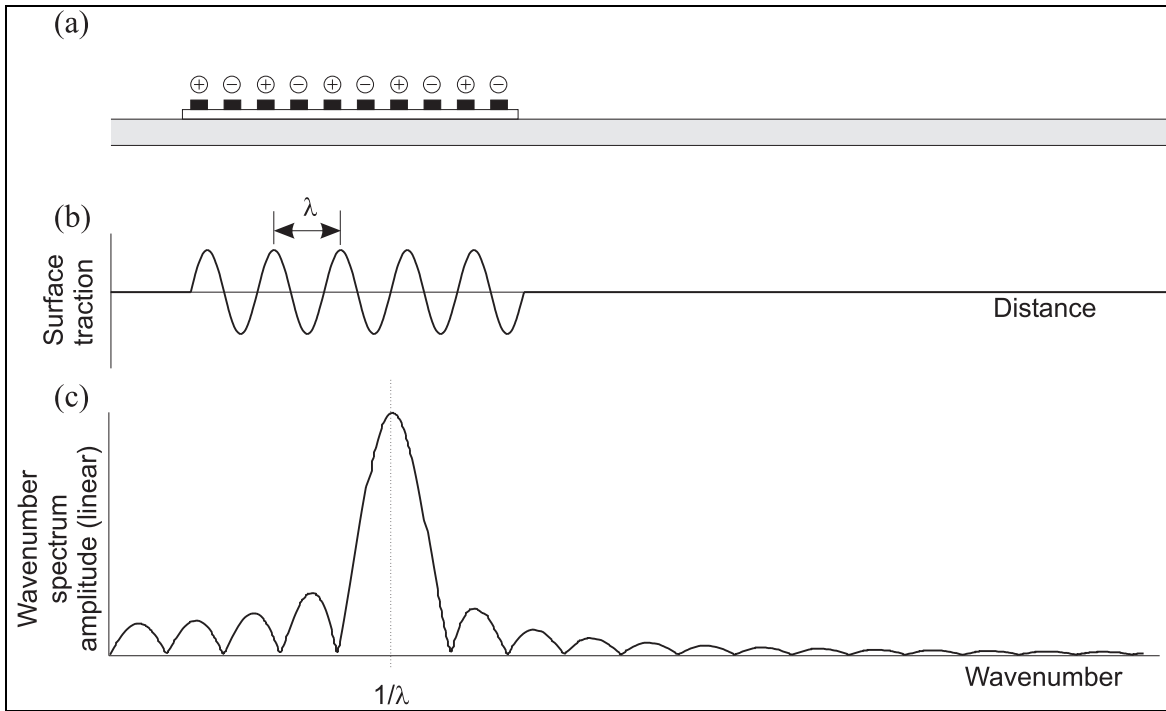


Figure 4.8 (a) Cross section through an IDT and plate and (b) the idealised distribution of surface tractions associated with the IDT. (c) Shows the wavenumber spectrum of the IDT.

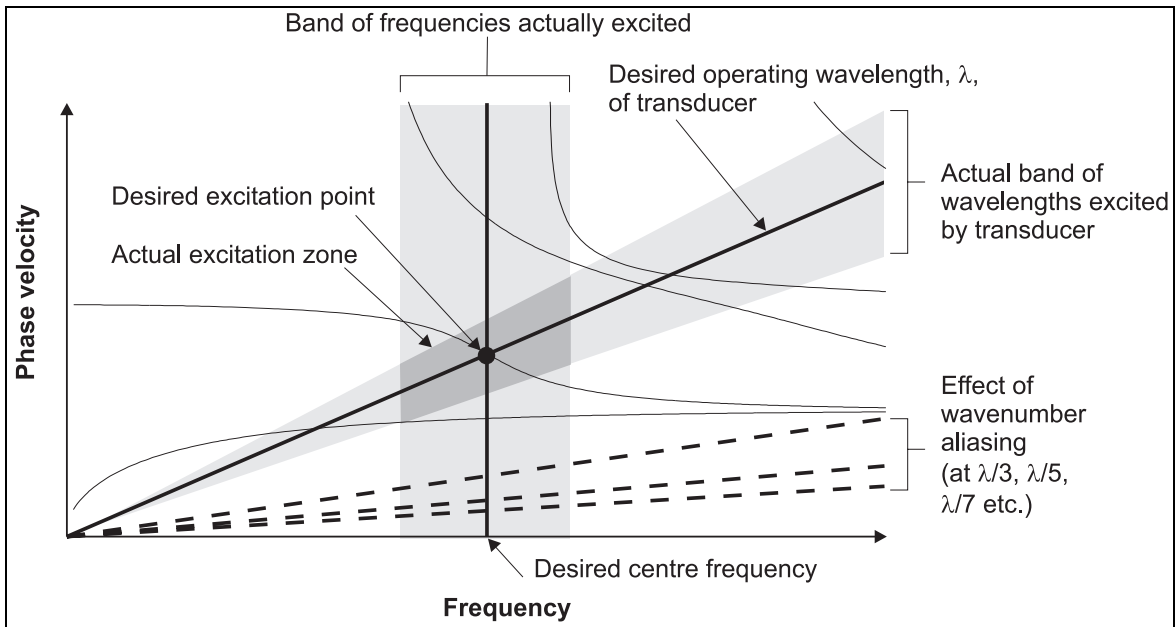


Figure 4.9 Example dispersion curves showing operating lines and regions associated with both an IDT and a toneburst.

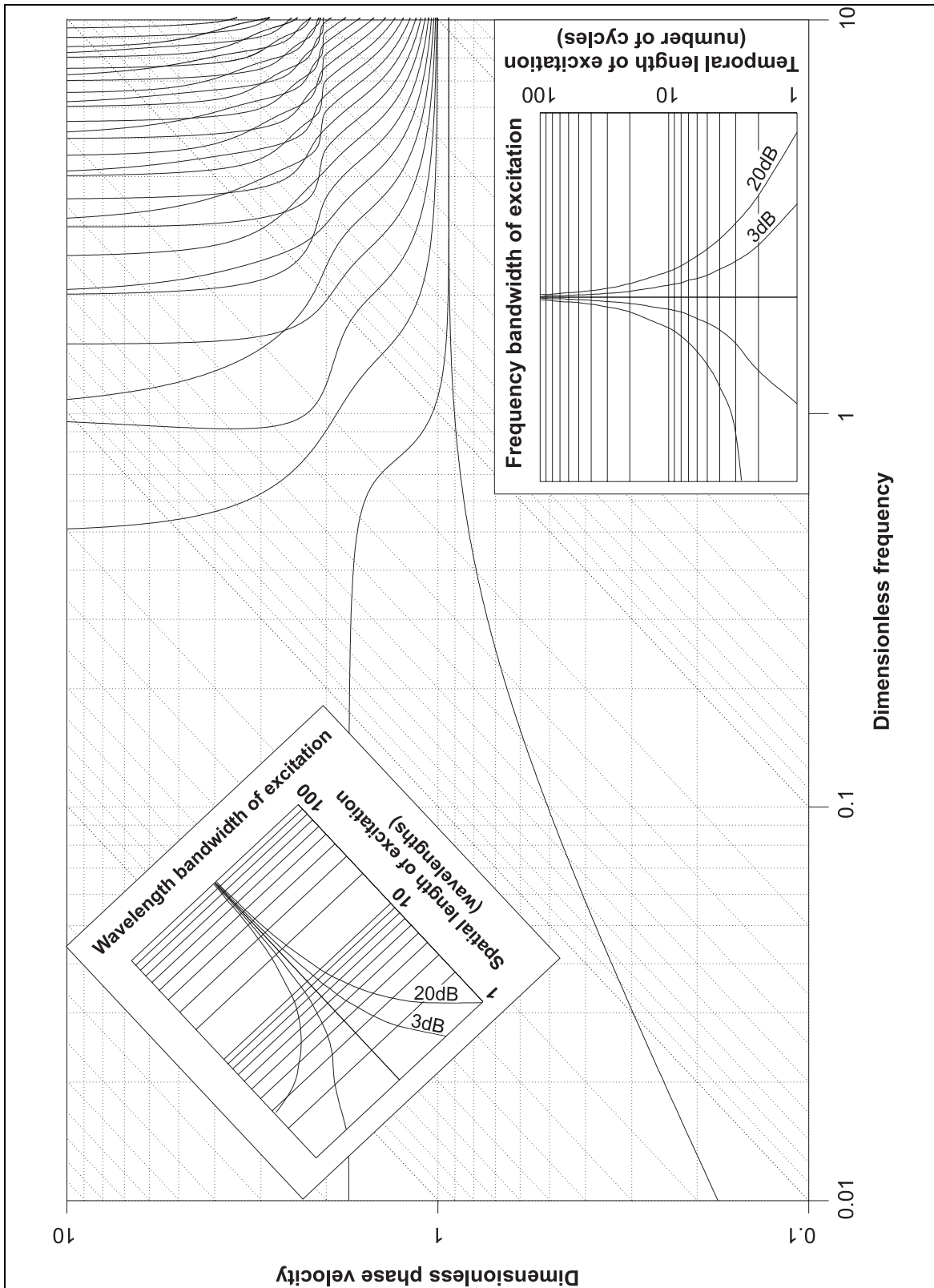


Figure 4.10 DLV plot for aluminium plate. The inset graphs indicate the temporal and spatial bandwidths on the main graph which are associated with different lengths of toneburst and different lengths of IDT respectively.

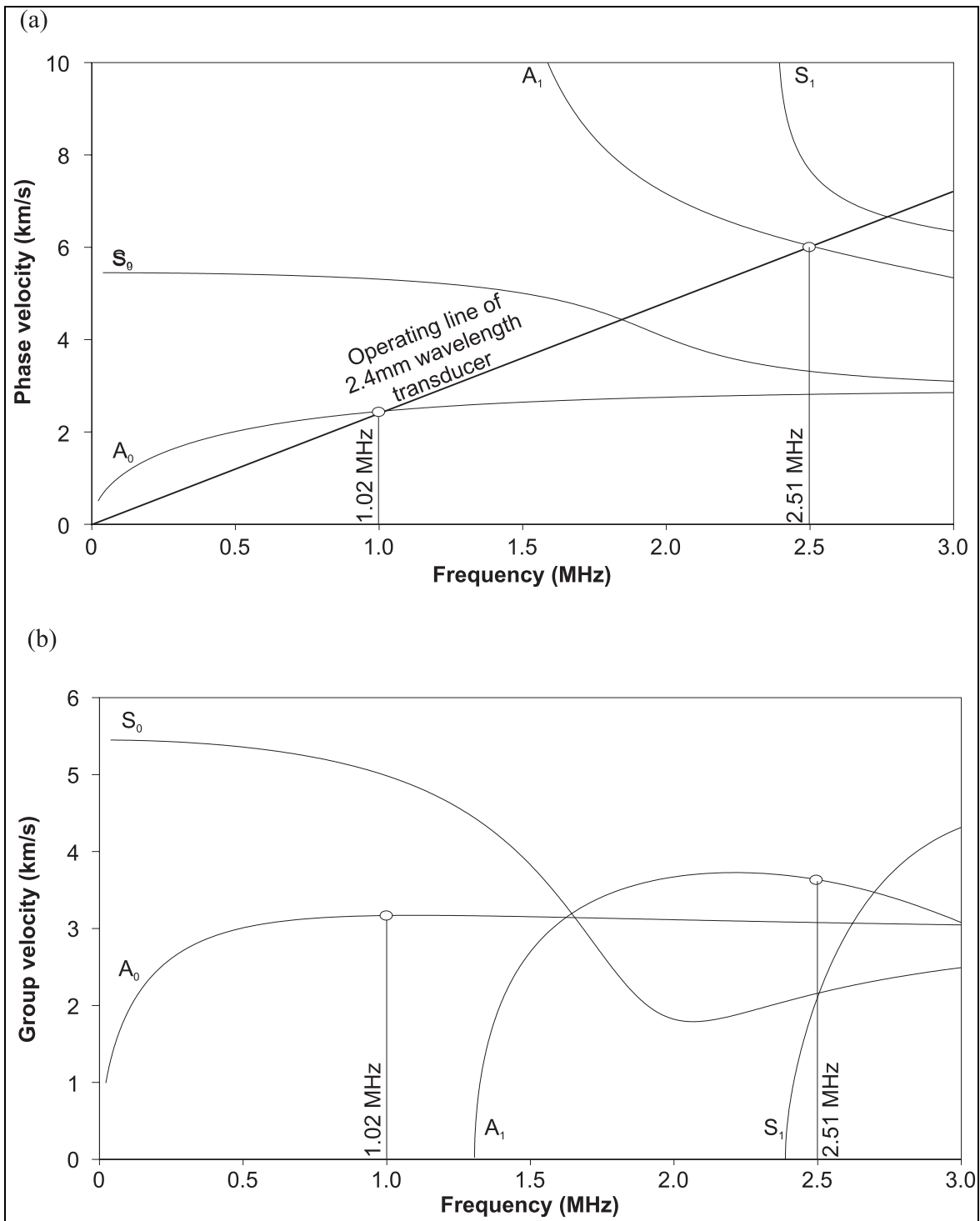


Figure 4.11 (a) Phase and (b) group velocity dispersion curves for 1.2 mm thick aluminium plate, showing the operating line of a 2.4 mm wavelength IDT.

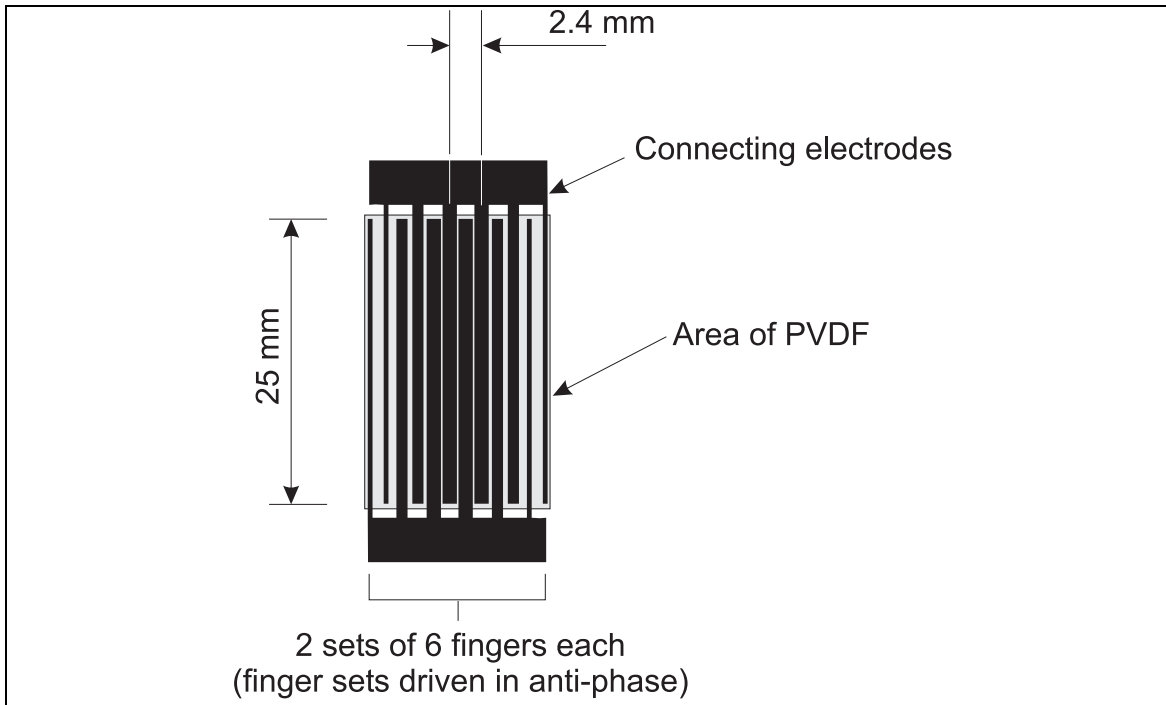


Figure 4.12 Geometry of 2.4 mm wavelength IDT.

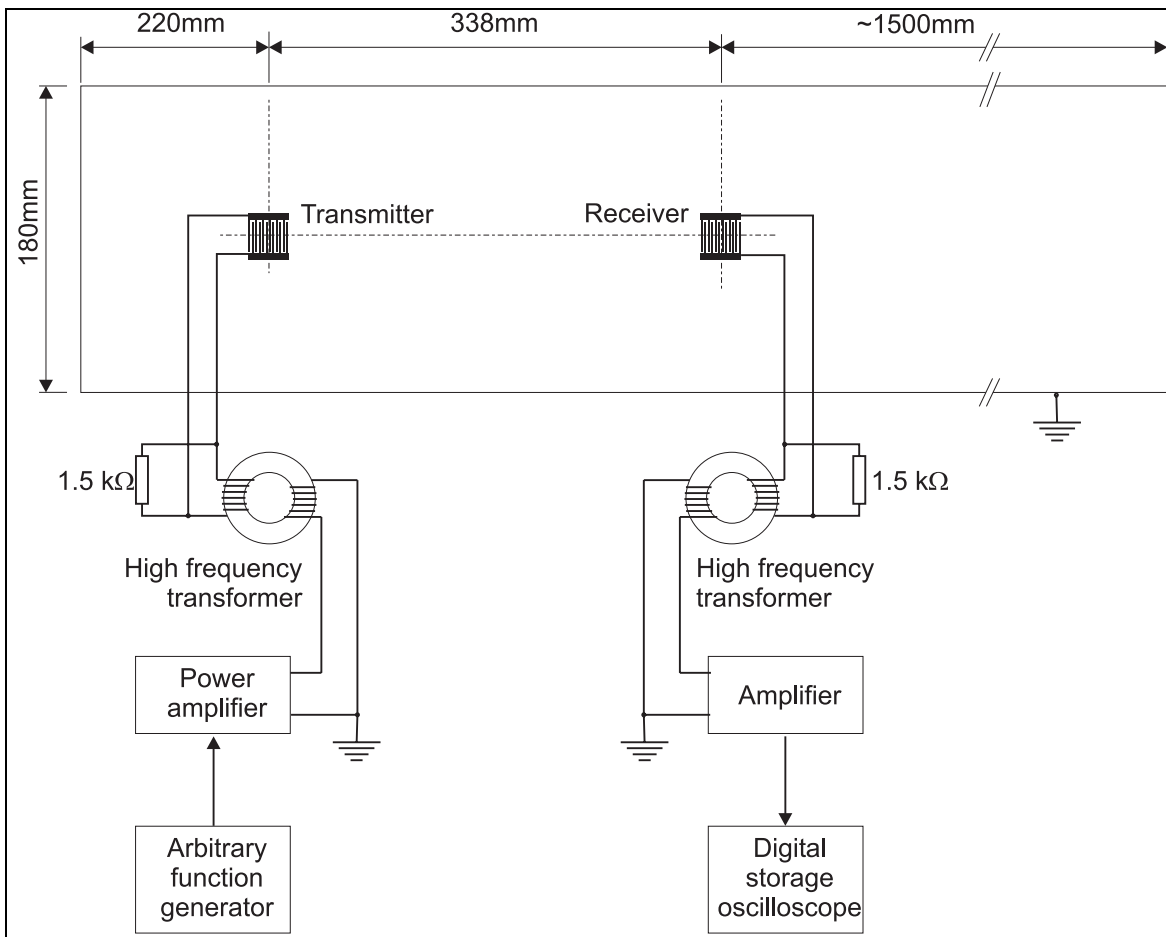


Figure 4.13 Experimental set-up of 2.4 mm wavelength IDTs operating in pitch-catch mode on 1.2 mm thick aluminium plate.

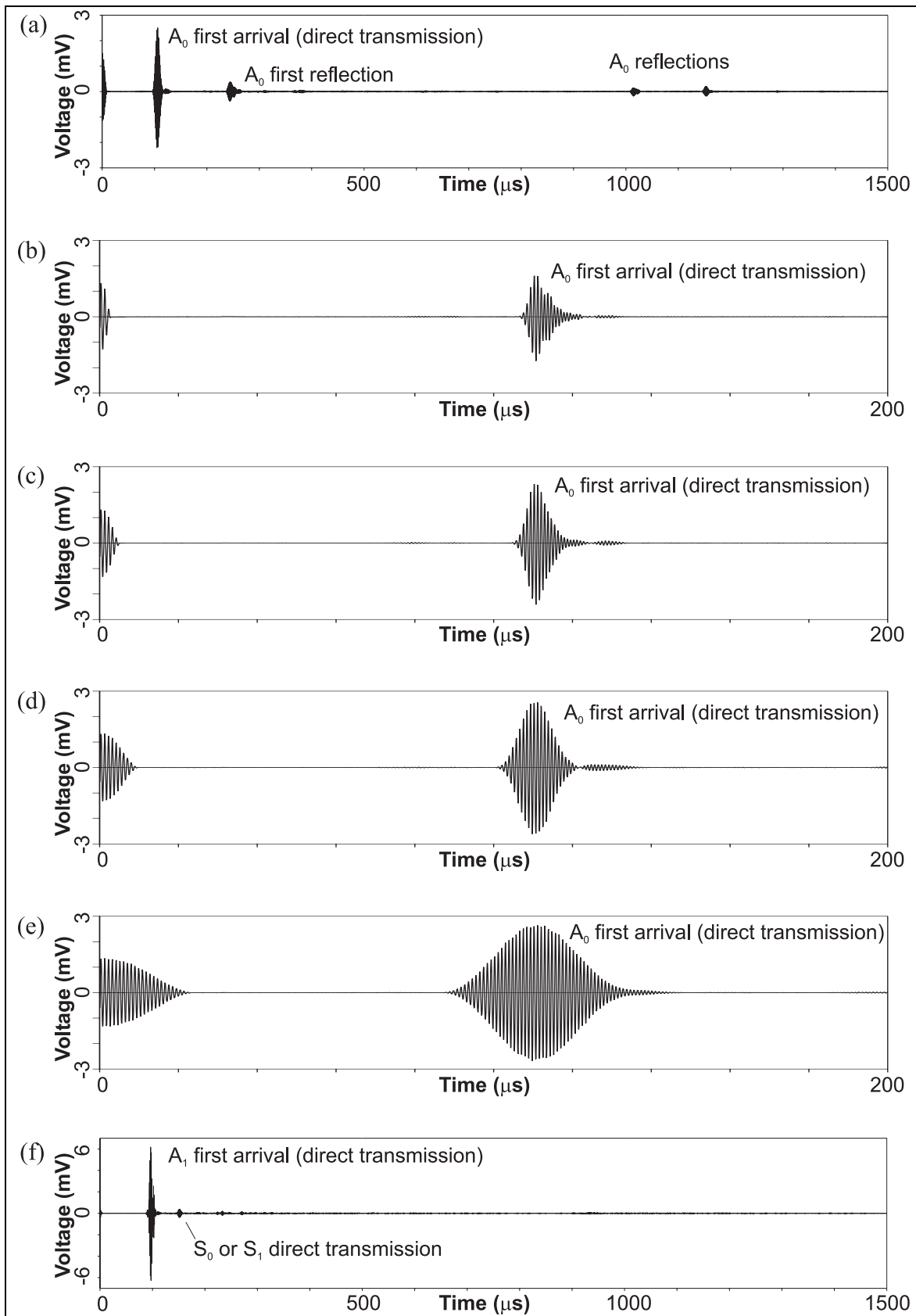


Figure 4.14 Received time-traces from experiment shown in figure 4.13. The complete received signal when using a 20 cycle toneburst at 1.02 MHz is shown in (a). The effects of using 5, 10, 20 and 50 cycles are shown in (b), (c), (d) and (e) respectively. The complete time-trace obtained using a 20 cycle toneburst at 2.51 MHz is shown in (f).

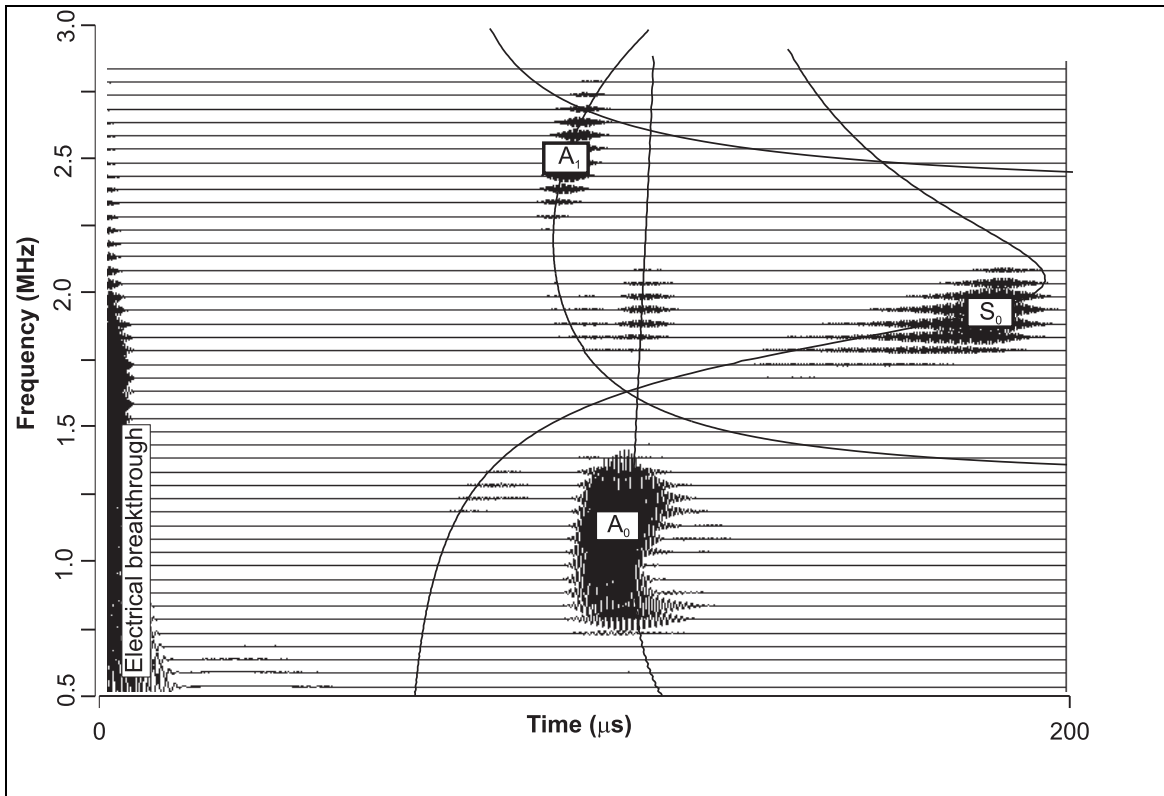


Figure 4.15 *F-scan* plot of the received signals from the experiment shown in figure 4.13. The analytically predicted group velocity dispersion curves are also superimposed after being mapped into group delay space and scaled appropriately.

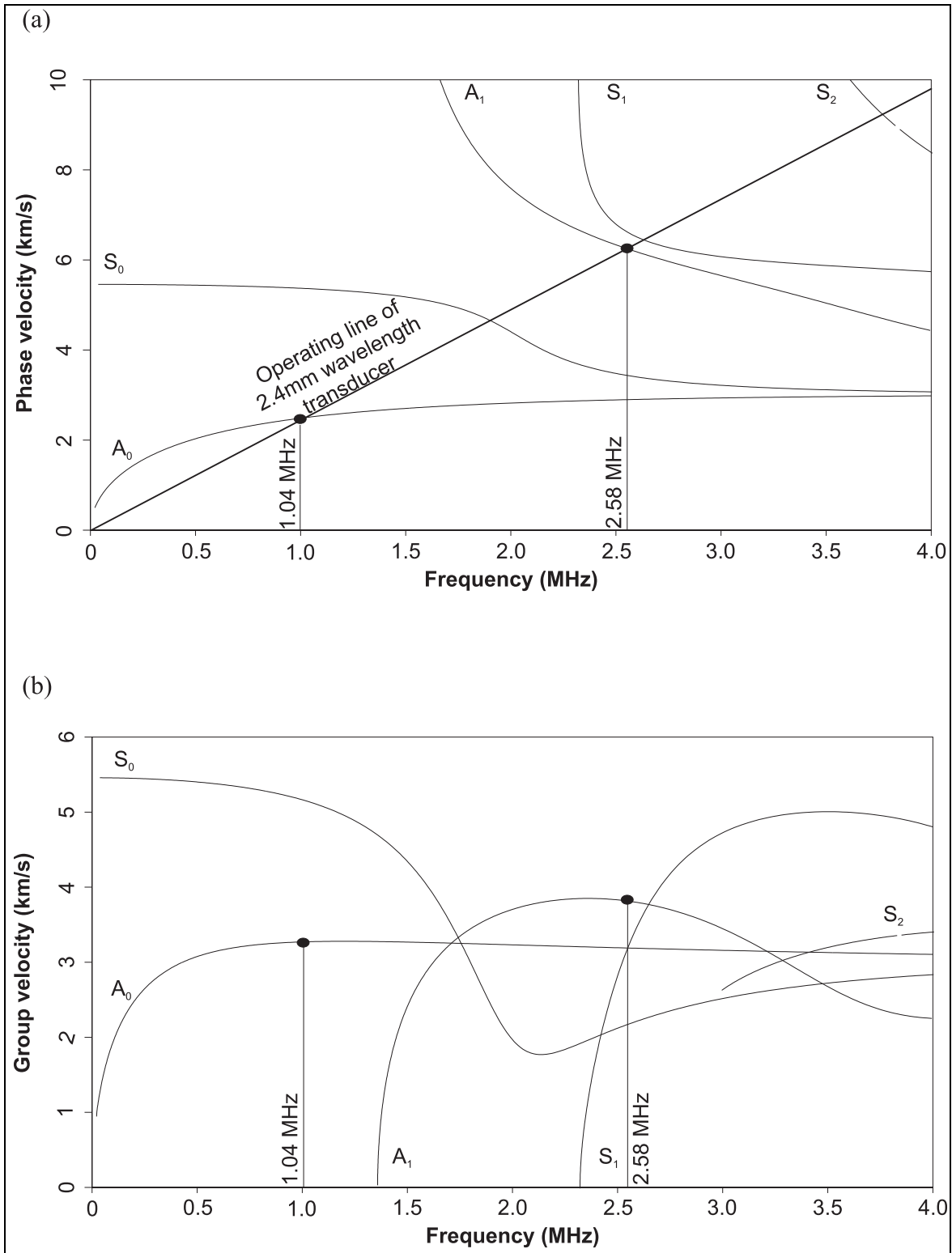


Figure 4.16 (a) Phase and (b) group velocity dispersion curves for 1.2 mm thick steel plate, showing the operating line of a 2.4 mm wavelength IDT.

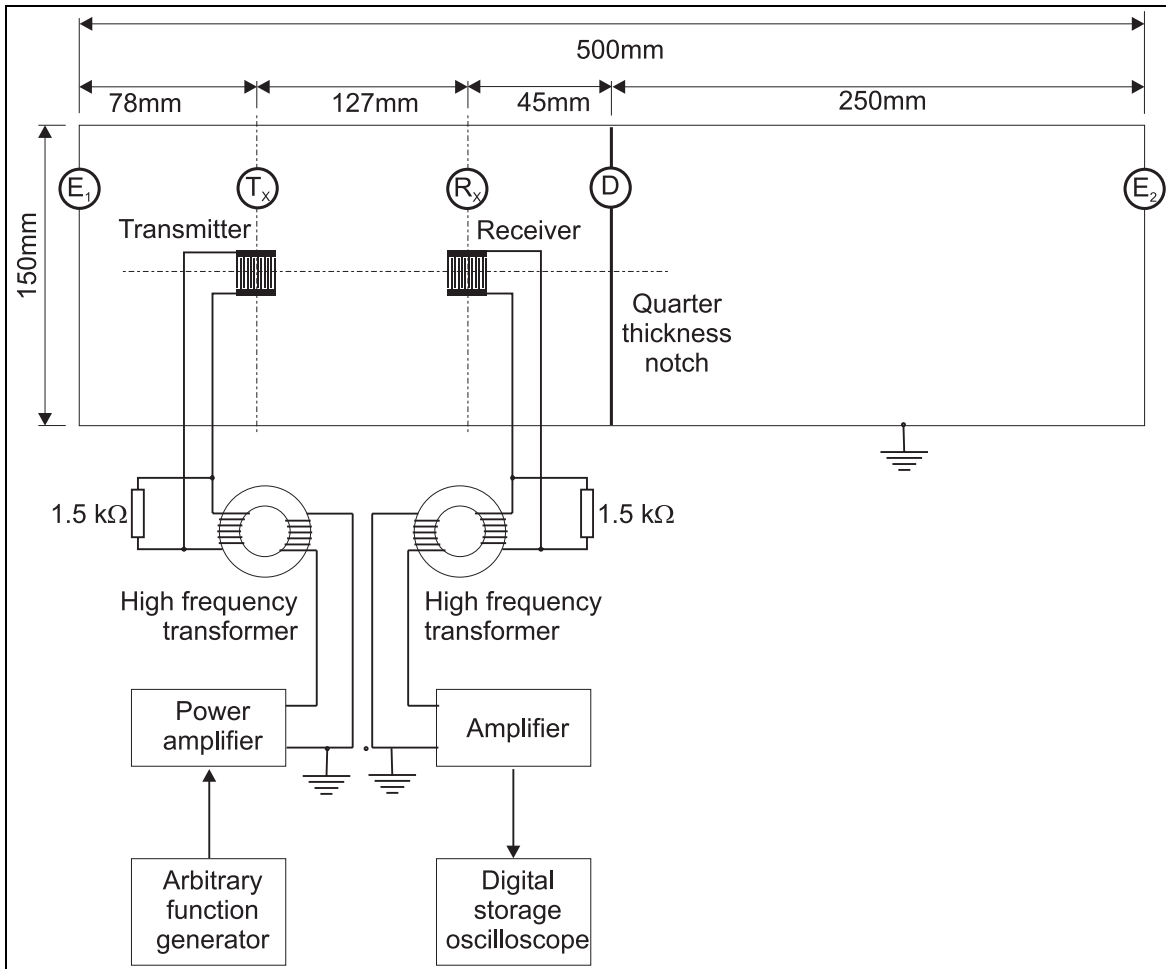


Figure 4.17 Experimental set-up of 2.4 mm wavelength IDTs operating in pitch-catch mode on 1.2 mm thick steel plate with an artificial defect.

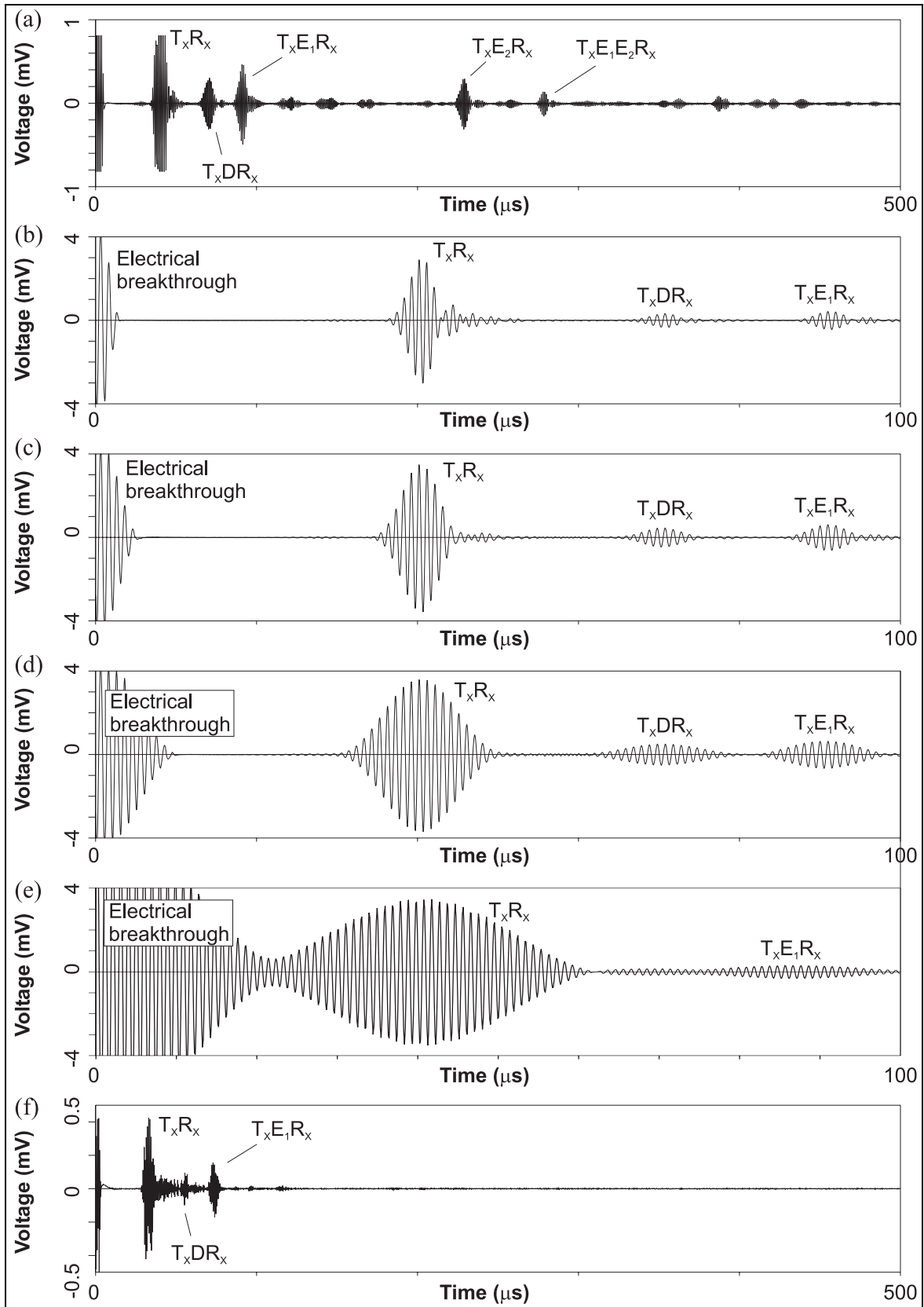


Figure 4.18 Received time-traces from experiment shown in figure 4.17. The complete received signal when using a 20 cycle toneburst at 1.04 MHz is shown in (a). The effects of using 5, 10, 20 and 50 cycles are shown in (b), (c), (d) and (e) respectively. The complete time-trace obtained using 20 cycles at 2.58 MHz is shown in (f).

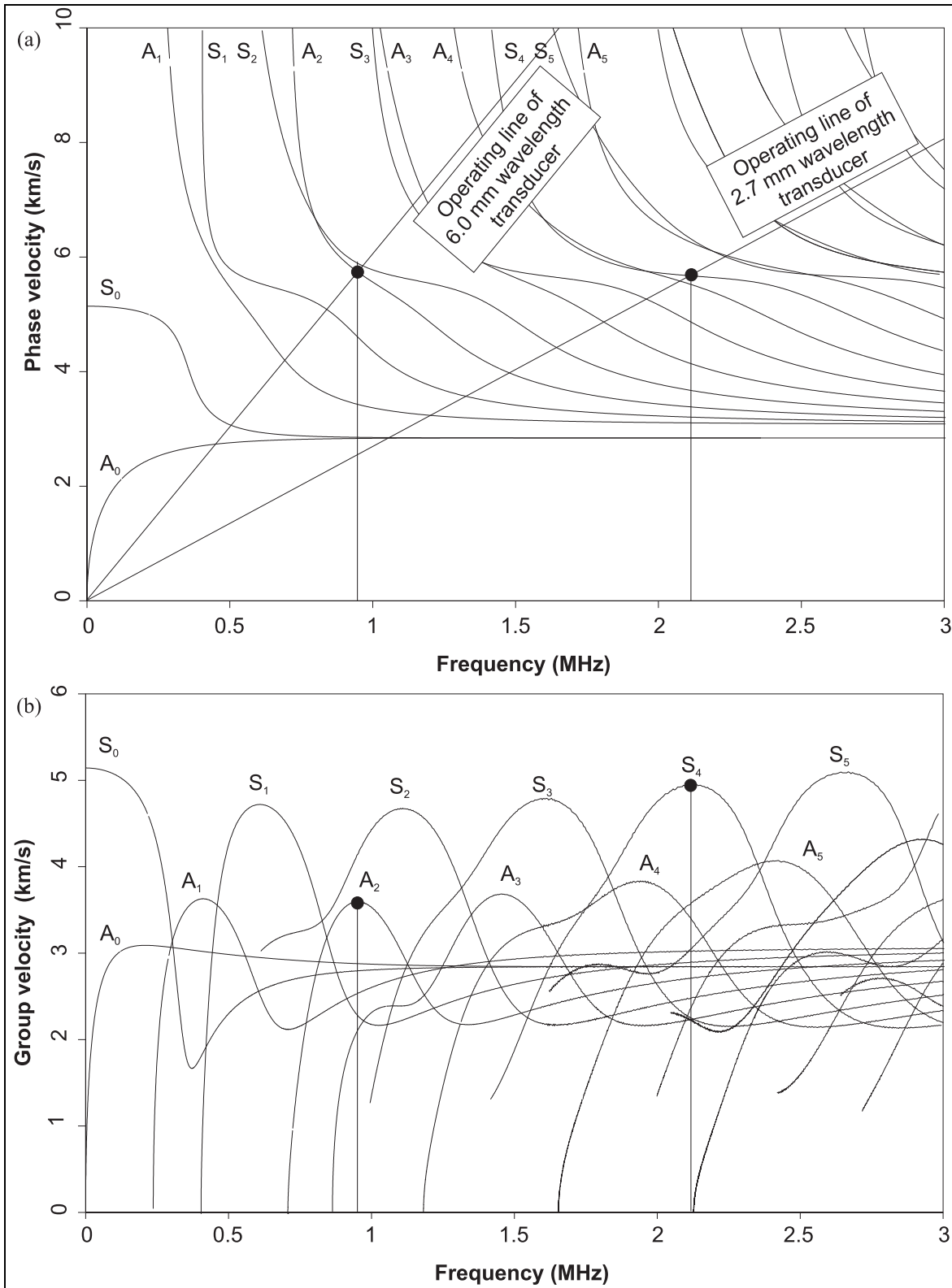


Figure 4.19 (a) Phase and (b) group velocity dispersion curves for 6.5 mm thick ductile iron plate, showing the operating lines of a 6.0 mm and 2.7 mm wavelength IDTs.

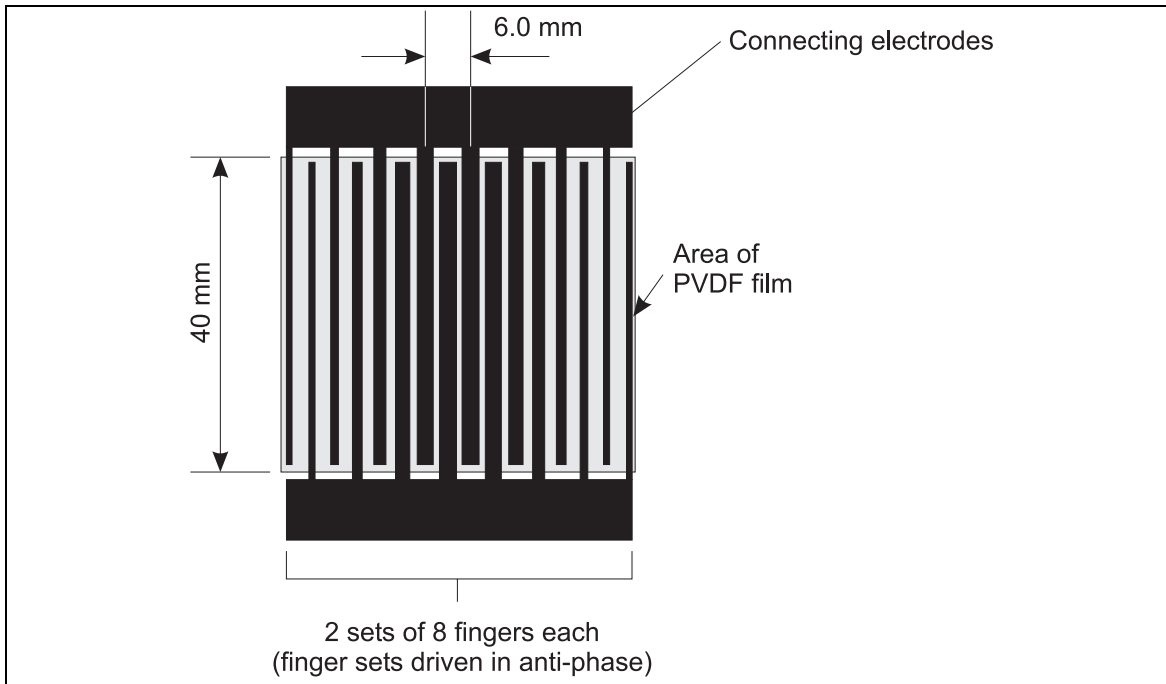


Figure 4.20 Geometry of 6.0 mm wavelength IDT.

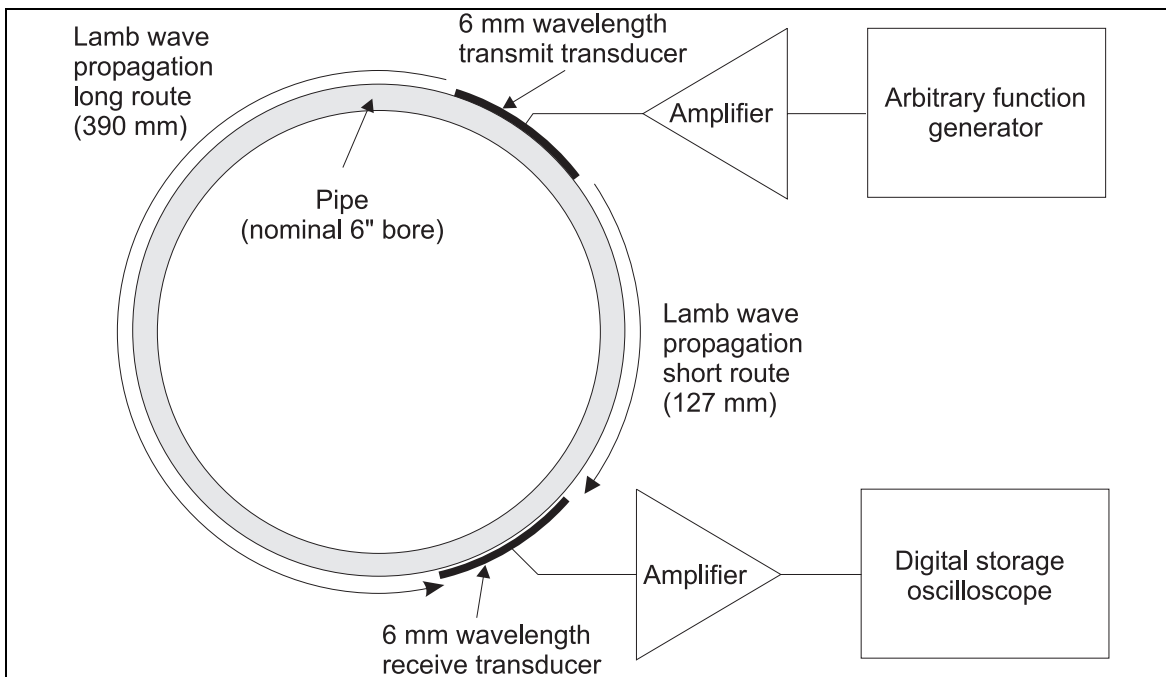


Figure 4.21 Experimental set-up of 6.0 mm wavelength IDTs operating in pitch-catch mode around circumference of ductile iron pipe. The details of the electrical connections to the IDTs are omitted for clarity.

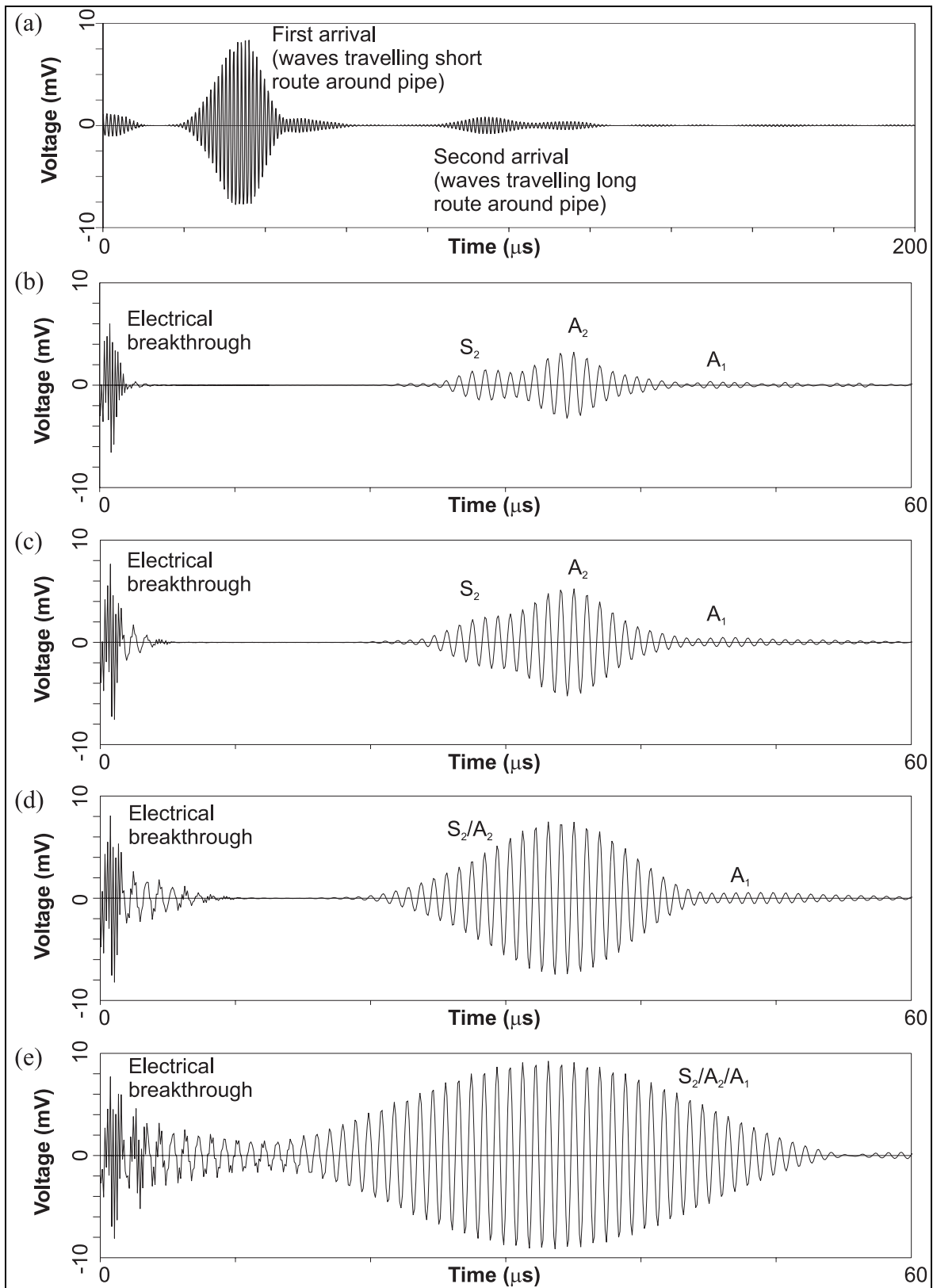


Figure 4.22 Received time-traces from experiment shown in figure 4.21. (a) is the complete received signal when the excitation was a 20 cycle toneburst at 1.05 MHz. The effects of using 5, 10, 20 and 50 cycles are shown in (b), (c), (d) and (e) respectively.

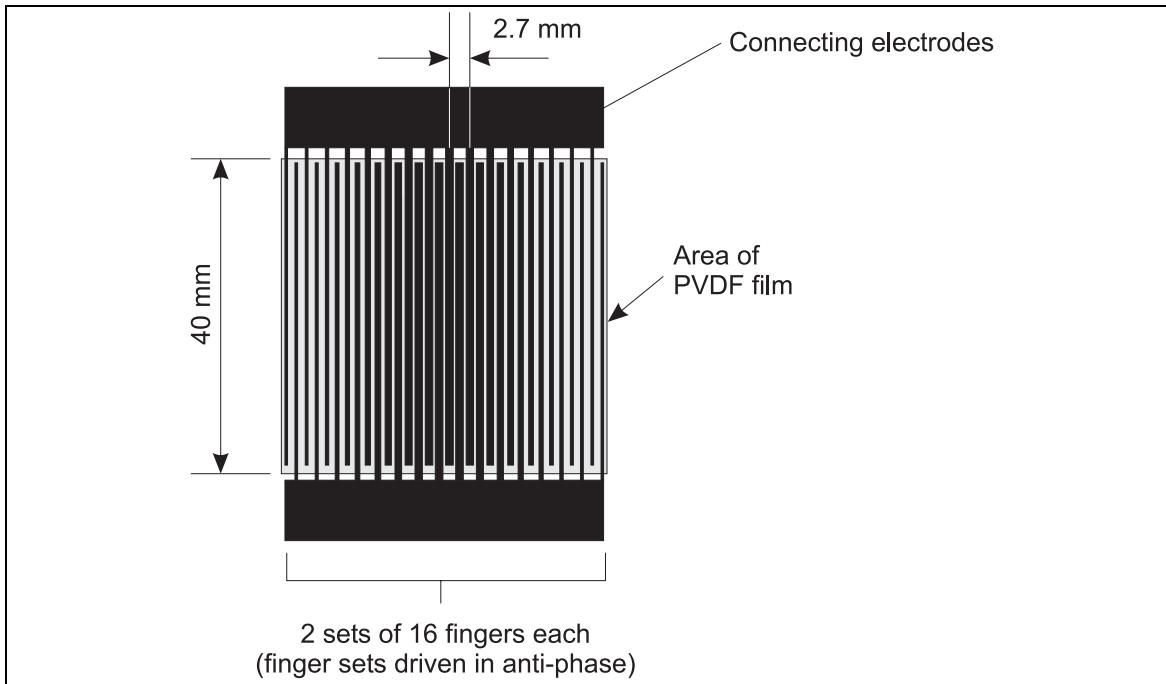


Figure 4.23 Geometry of 2.7 mm wavelength IDT.

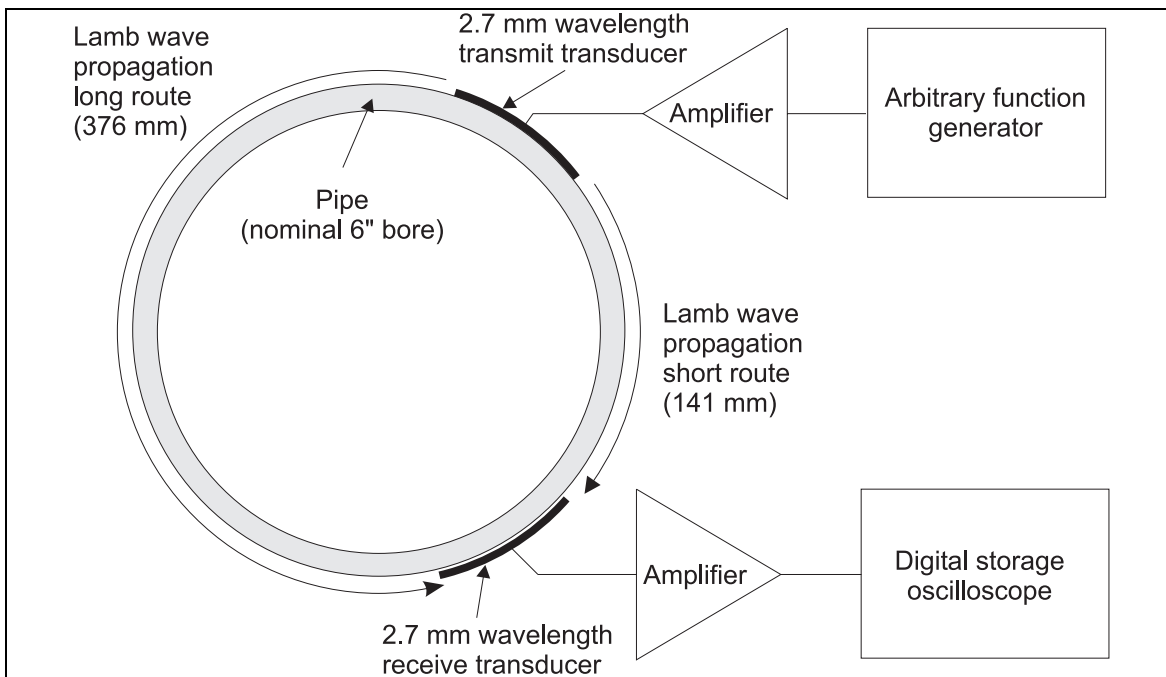


Figure 4.24 Experimental set-up of 2.7 mm wavelength IDTs operating in pitch-catch mode around circumference of ductile iron pipe. The details of the electrical connections to the IDTs are omitted for clarity.

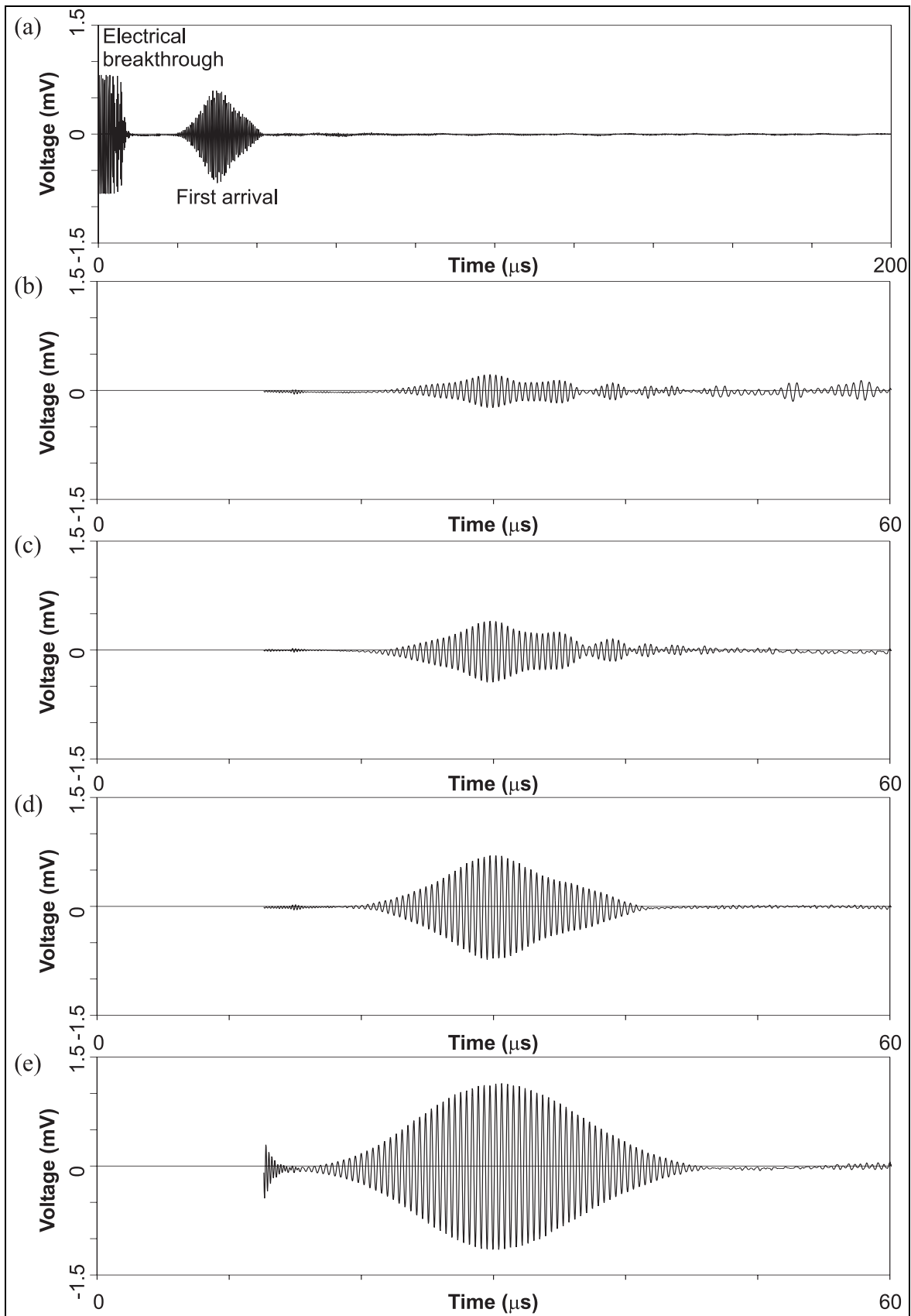


Figure 4.25 Received time-traces from experiment shown in figure 4.24. (a) is the complete received signal when the excitation was a 20 cycle toneburst at 2.21 MHz. The effects of using 5, 10, 20 and 50 cycles are shown in (b), (c), (d) and (e) respectively.

## 5. Use of Huygens' principle to predict acoustic fields generated by inter-digital transducers

---

### 5.1 INTRODUCTION

This chapter describes a model based on Huygens' principle of superposition, which was developed to predict the Lamb wave field which is generated in a plate structure when excited with an inter-digital transducer (IDT). After assessing the suitability of two alternative methods to predict the field from an IDT, section 5.2 describes the theory of the Huygens' model. The implementation of the model in software is briefly described in section 5.3, and its validation against finite element results and experimental data is presented in section 5.4. In the following chapter, predictions from the Huygens' model will be used in conjunction with further experimental data to elucidate general trends in the design of two particular types of IDT.

#### 5.1.1 Strategies for IDT modelling

Before describing the Huygens' model in detail, two alternative methods which have been (or could potentially be) employed for predicting the fields generated by IDTs should be mentioned briefly. The first of these, using finite element modelling, makes exactly the same assumptions about transducer-structure interaction as Huygens' model and, as will be shown later, gives results which are extremely close to the Huygens' model. The second method, using normal mode theory, means in principle that transducer-structure interaction can be modelled much more accurately, and a brief appraisal of this technique is given below.

##### *Finite element techniques*

One method of predicting the field generated by an IDT is to use time marching 3-dimensional finite element (FE) modelling of the plate which the IDT is acting on. This is described in two previous publications (Monkhouse *et al.* 1997a and Wilcox *et al.* 1998b) in which the FE package *Finel* (Hitchings, 1997) was used. In general, the plate is represented by a 3-dimensional mesh composed of brick elements, which, depending on the exact element type, may have nodes in the centre of each edge as well as at the corners. The size of the elements must be sufficiently small for there to be eight or more nodes per wavelength for the shortest wavelength of waves which can propagate in the system. An explicit time integration scheme is used. The time step is chosen to be typically 80% shorter than the time taken for the fastest wave in the system (the bulk longitudinal wave) to propagate between adjacent nodes. These limits on the element size and time step are necessary for accurate results and stability.

The physical IDT itself is not currently included in the FE model, but its effect on the structure is modelled as an array of time dependent forces acting at nodes on the surface of the mesh. The amplitude of each force is scaled according to the area of IDT which it represents. The output from the FE model can be examined in numerous different ways,

but generally, the out-of-plane surface displacement is monitored with respect to time at a number of nodes on the surface of the mesh.

The total time interval modelled must obviously be sufficiently long for waves to propagate over the monitoring area. The overall size of the mesh in the plane of the plate must be large enough for reflections of waves from the mesh boundaries not to interfere with outgoing waves in the monitoring region during the time interval being modelled. This is a particular problem when more than two or more modes are propagating with different group velocities, as the total mesh size must always be based on the wave mode with the fastest group velocity which may not necessarily be the mode of interest.

For making simple predictions of the acoustic field generated by an IDT, the FE model is many times slower than the Huygens' model, but it is also much more flexible. For example, the FE model can be used to predict how the waves generated by a transducer interact with defects, or how in an actual system, reflections from natural boundaries may affect the area which an IDT can interrogate.

### *Perturbation method and normal mode expansion*

An alternative method for the analysis of IDTs based on perturbation theory and normal mode expansions is currently being developed by a colleague, Mr. P. Marty. Potentially, this method will enable full account to be taken of the mechanical interaction between the IDT and the substrate and in addition it could be readily extended to include a complete model of the electro-mechanical transduction process taking place within the IDT. This model is based on assuming that the effect of an IDT on a plate is to perturb the Lamb wave modes which may propagate within it. The perturbations caused by the IDT are added to the model in stages, firstly by adding the layers, then the electrodes and then the electro-mechanical coupling. At each perturbation stage, advantage is taken of the orthogonality (Auld 1990, volume 2) of the un-perturbed Lamb wave modes in order to calculate the distribution of energy between them. In theory, a relationship can ultimately be obtained between the input electrical voltage and the output mechanical displacements in the plate. Some elements of this model have already been completed for a two dimensional (plane strain) case, but the complete model is still some way off. In terms of predicting the complete acoustic field from an IDT with an arbitrary finger pattern, this approach is not likely to be practically viable, due to the enormous difficulties of extending the theory to anything more complicated than an axi-symmetric three-dimensional case.

### *Huygens' model*

The work of Christiaan Huygens was the foundation of the wave theory of light. Using mostly geometric arguments, he showed how the future position of a wavefront of light could be deduced from the current position of the wavefront. This was done by considering the current wavefront as being composed of numerous coherent light sources, each emitting a spherical wavefront. The position of the total wavefront at some later point in time was a surface tangential to all of the spherical wavefronts. Using this method, Huygens deduced the laws governing reflection and refraction of light. It was not until long after the death of Huygens that his principle was completely justified mathematically. A description of Huygens' life and work may be found in the proceedings

of a recent conference in which the contributions which he made to science were reviewed (Wolf 1990).

In the context used here, Huygens' principle is simply the concept that a wave source of complex shape can be modelled as a number of point sources which is applied to an acoustic problem.

## **5.2 THEORY**

Huygens' principle itself is nothing more than a linear superposition of vector fields from a number of point sources to obtain the total vector field. This principle of superposition may be applied to any vector field property for which the superposition principle is valid, such as stress or particle displacement in a particular direction. It may not be applied directly to scalar quantities such as energy density, which are not superposable.

The problem in the application of Huygens' principle to IDTs is in calculating the acoustic field in a plate due to a single point source. In optics, or acoustic calculations in an unbounded isotropic medium, the field due to a point excitation source is straightforward to calculate, since wave propagation is usually non-dispersive and at most, only two modes can propagate. In the case of a plate, multiple Lamb wave modes can be excited and these are generally dispersive. Section 5.2.1 describes how the acoustic field in a plate due to a single frequency harmonic point source is calculated, and section 5.2.2 describes how this is extended to predict the acoustic field when a point source excites a plate with an arbitrary time dependent function. Section 5.2.3 shows how the superposition principle is applied to calculate the acoustic field due to multiple point sources and section 5.2.4 shows how an IDT is modelled using this technique.

### ***5.2.1 Calculation of displacements resulting from continuous excitation of a plate at a point***

Before being able to calculate the acoustic field in a plate due to a point source, it is necessary to make two decisions, firstly on which vector field quantity will be used to describe the acoustic field, and secondly on the nature of the point source.

For the acoustic field, either the displacement or the stress at some point within the thickness of the plate would be a suitable vector field quantity, and depending on the application either of these could be used. For delamination detection, for example, a useful measure of the acoustic field would be the amount of shear stress at the depth of interest. In practice, the easiest quantity to measure experimentally is the out-of-plane displacement at the plate surface, and from here on that is what will be considered, and referred to as the acoustic field.

The point source needs to be of a type which will be suitable to represent a small element of an IDT. The IDTs described in this thesis may be generally regarded as applying only normal stresses on the surface of the structure to which they are bonded. For this reason, the point source considered from here onwards will be a time dependent normal force of finite amplitude applied at an infinitely small point on the surface of the plate. Again, this should not be considered a limiting case; if the acoustic field due to say an in-plane force

acting at a point on the plate surface could be calculated, then Huygens' principle could still be applied, and the acoustic field due to a shear IDT could be modelled.

An advantage of taking the point source as being an out-of-plane force is that the problem then becomes axi-symmetric and much easier to solve analytically. The acoustic field at a particular point in a plate due to a point source is therefore only a function of the distance of that point from the point source. This would clearly not be the case if the point source was an in-plane force applied in a particular direction at the plate surface. In this case, the acoustic field in the plate would exhibit both an angular and a radial variation.

Viktorov (1965) published expressions for the displacements associated with wedge transducer excitation of a plate to generate straight crested waves. The relevant calculations are summarised below; even though they are not directly applicable to the Huygens' model, the method of calculation follows a similar pattern to that for axi-symmetric excitation performed by Ditri *et al.* (1994a and b) and the results of the two calculations exhibit some interesting similarities. Both calculations are outlined, and their extensions to the limiting cases of a line force in the plane strain calculation and a point force in the axi-symmetric calculation are presented.

*Application of Viktorov's technique to line excitation of a plate*

The initial stages of calculating the excitability of 2-dimensional Lamb waves in a plate by a line source begin in the same manner as the modal solution of 2-dimensional Lamb waves described in chapter 2. Equation 5.1 below, which was derived in chapter 2, relates the stresses at the plate surfaces to the four arbitrary constants in the wave equations.

$$\begin{bmatrix} \sigma_{zz}|_{z=d/2} \\ \sigma_{zz}|_{z=-d/2} \\ \sigma_{xz}|_{z=d/2} \\ \sigma_{xz}|_{z=-d/2} \end{bmatrix} = \mu \begin{bmatrix} (k^2 + q_i^2) \cosh q_i d / 2 & (k^2 + q_i^2) \sinh q_i d / 2 & 2ikq_i \sinh q_i d / 2 & 2ikq_i \cosh q_i d / 2 \\ (k^2 + q_i^2) \cosh q_i d / 2 & -(k^2 + q_i^2) \sinh q_i d / 2 & -2ikq_i \sinh q_i d / 2 & 2ikq_i \cosh q_i d / 2 \\ 2ikq_i \sinh q_i d / 2 & 2ikq_i \cosh q_i d / 2 & -(k^2 + q_i^2) \cosh q_i d / 2 & -(k^2 + q_i^2) \sinh q_i d / 2 \\ -2ikq_i \sinh q_i d / 2 & 2ikq_i \cosh q_i d / 2 & -(k^2 + q_i^2) \cosh q_i d / 2 & (k^2 + q_i^2) \sinh q_i d / 2 \end{bmatrix} \begin{bmatrix} S_i \\ A_i \\ A_i \\ S_i \end{bmatrix} \quad (5.1)$$

For the modal solutions, there is no external input of energy and these stresses are all set to zero, but for this calculation it is the forced response which is of interest. To investigate the response of a plate to surface excitation, Viktorov considers a region between  $x = -b$  and  $x = b$  on the surface  $z = d/2$ , over which a harmonic normal stress is applied at a frequency  $\omega$ . As this analysis was intended to model excitation by a wedge transducer, the stress also has a spatial variation of  $\exp(ik_0 x)$  over this region. Its peak amplitude at the surface is  $\sigma_0 |\Phi|$  (again this format results from the wedge transducer analysis, where  $\sigma_0$  is the peak normal stress in the direction of bulk wave propagation in the transducer, and  $\Phi$  is the ratio of this to the normal stress on the plate surface). All other surface stresses are zero. Hence the boundary conditions may be written as:

$$\begin{aligned}
 \sigma_{zz} \Big|_{z=d/2} &= \begin{cases} \sigma_0 |\Phi| \exp i(k_0 x - \omega t) & \text{for } |x| \leq b \\ 0 & \text{for } |x| > b \end{cases} \\
 \sigma_{zz} \Big|_{z=-d/2} &= 0 \\
 \sigma_{xz} \Big|_{z=\pm d/2} &= 0
 \end{aligned} \tag{5.2}$$

By writing the potential functions (given by equation 2.12 in chapter 2) as Fourier integrals:

$$\begin{aligned}
 \phi &= \int_{-\infty}^{+\infty} S_l(k) \cosh q_l z \exp(ikx) dk + \int_{-\infty}^{+\infty} A_l(k) \sinh q_l z \exp(ikx) dk \\
 \psi_y &= \int_{-\infty}^{+\infty} S_t(k) \sinh q_t z \exp(ikx) dk + \int_{-\infty}^{+\infty} A_t(k) \cosh q_t z \exp(ikx) dk
 \end{aligned} \tag{5.3}$$

and using these functions to calculate surface stresses which satisfy the boundary conditions specified in equation 5.2, the functions  $S_l(k)$ ,  $A_l(k)$ ,  $S_t(k)$  and  $A_t(k)$  may be found. To calculate the displacement field, the integrals in equation 5.3 are evaluated using residual calculus. It is then possible to obtain an expression for the out-of-plane displacement,  $u_z$ , at the surface of the plate:

$$u_z = \frac{i\sigma_0}{\mu k_t} |\Phi| \left\{ \begin{aligned} &\sum_{k(\text{symmetric})} \left( \frac{k_t \sin(k_0 - k)b}{k_0 - k} \cdot \frac{q_t(q_t^2 - k^2) \sinh q_t d/2 \sinh q_t d/2}{\partial \Delta_s / \partial k} \cdot \exp(ikx) \right) \\ &+ \\ &\sum_{k(\text{anti-symmetric})} \left( \frac{k_t \sin(k_0 - k)b}{k_0 - k} \cdot \frac{q_t(q_t^2 - k^2) \cosh q_t d/2 \cosh q_t d/2}{\partial \Delta_a / \partial k} \cdot \exp(ikx) \right) \end{aligned} \right\} \exp(-i\omega t) \tag{5.4}$$

The  $\sum_{k(\text{symmetric})}$  and  $\sum_{k(\text{anti-symmetric})}$  symbols denote a summation over all the possible symmetric and anti-symmetric Lamb wave modes which exist in the plate at the frequency  $\omega$ , and the terms  $\Delta_a$  and  $\Delta_s$  are again the factors in the determinant of the Lamb wave matrix as given by equations 2.15 in chapter 2. The values of  $k(\text{symmetric})$  and  $k(\text{anti-symmetric})$  which exist at the frequency  $\omega$  must be calculated by solving the dispersion equation 2.15 in chapter 2. The displacement amplitude at the surface of the plate is a weighted sum of the displacements associated with each of the possible modes, the weighting factor being the product of the two dimensionless fractions after each summation sign. The first of these fractions is associated with the spatial distribution of the excitation stress. In this analysis, the source of interest is an infinitely narrow line source, exerting a harmonic force,  $F = F_0 \exp(i\omega t)$ , per unit distance. To incorporate this in the calculation, the limit of the first fraction after each summation sign is taken as the distance  $b$  is reduced to zero:

$$\begin{aligned}
 \lim_{b \rightarrow 0} \frac{k_t \sin(k_0 - k)b}{k_0 - k} &= b k_t \lim_{b \rightarrow 0} \frac{\sin(k_0 - k)b}{(k_0 - k)b} \\
 &= b k_t
 \end{aligned} \tag{5.5}$$

and then making use of the fact that the total force  $F_0$  per unit length is equal to  $2b\sigma_0|\Phi|$  enables equation 5.4 to be written:

$$u_z = F_0 \frac{i}{2\mu} \left\{ \begin{array}{l} \sum_{k(\text{symmetric})} \left( \frac{q_l(q_l^2 - k^2) \sinh q_l d/2 \sinh q_l d/2}{\partial \Delta_s / \partial k} \cdot \exp ikx \right) \\ + \\ \sum_{k(\text{anti-symmetric})} \left( \frac{q_l(q_l^2 - k^2) \cosh q_l d/2 \cosh q_l d/2}{\partial \Delta_a / \partial k} \cdot \exp ikx \right) \end{array} \right\} \exp(-i\omega t) \quad (5.6)$$

The surface displacement amplitude,  $u_z$ , associated with each mode at a particular frequency is proportional to the normal excitation force,  $F_0$ . The constant of proportionality may be loosely termed the *excitability* of the mode, and is a function of frequency. It is more elegant to rearrange equation 5.6 into dimensionless form, using the following substitutions:

$$\begin{aligned} \bar{u}_z &= \frac{u_z}{d} & \bar{F}_0 &= \frac{F_0}{\mu d} \\ \bar{q}_l &= q_l d & \bar{q}_t &= q_t d & \bar{k} &= kd & \bar{\omega} &= \frac{\omega d}{v_t} \\ \bar{\Delta}_s &= \Delta_s d^4 & \bar{\Delta}_a &= \Delta_a d^4 \\ \bar{x} &= \frac{x}{d} & \bar{t} &= \frac{tv_t}{d} \end{aligned} \quad (5.7)$$

where  $v_t$  is the bulk transverse wave velocity. Thus equation 5.6 becomes:

$$\bar{u}_z = \bar{F}_0 \left\{ \begin{array}{l} \sum_{\bar{k}(\text{symmetric})} \left( \frac{i \bar{q}_l (\bar{q}_l^2 - \bar{k}^2) \sinh \bar{q}_l / 2 \sinh \bar{q}_l / 2}{2 \partial \bar{\Delta}_s / \partial \bar{k}} \cdot \exp i \bar{k} \bar{x} \right) \\ + \\ \sum_{\bar{k}(\text{anti-symmetric})} \left( \frac{i \bar{q}_l (\bar{q}_l^2 - \bar{k}^2) \cosh \bar{q}_l / 2 \cosh \bar{q}_l / 2}{2 \partial \bar{\Delta}_a / \partial \bar{k}} \cdot \exp i \bar{k} \bar{x} \right) \end{array} \right\} \exp(-i \bar{\omega} \bar{t}) \quad (5.8)$$

or more simply:

$$\bar{u}_z(\bar{x}, \bar{t}, \bar{\omega}) = \bar{F}_0 \sum_k \left( \bar{E}_s(\bar{k}, \bar{\omega}) \exp i \bar{k} \bar{x} \right) \exp(-i \bar{\omega} \bar{t}) \quad (5.9)$$

where  $\sum_{\bar{k}}$  denotes a summation over each of the modes present at the dimensionless frequency  $\bar{\omega}$ , and  $\bar{E}_s(\bar{k}, \bar{\omega})$  is the excitability function for each mode (which is of one of two forms depending on whether the mode is symmetric or anti-symmetric).

In chapter 2, the dimensionless wavenumber,  $\bar{k}$ , was shown to be a function of dimensionless frequency,  $\bar{\omega}$ , and the ratio of the bulk wave velocities of the material,  $\bar{v}_l$ .

Hence it follows that the excitability function,  $\overline{E}_s$ , is also a function of  $\overline{\omega}$  and  $\overline{v}_l$  only. In chapter 2,  $\overline{v}_l$  was shown to be a function of the Poisson's ratio of the material, thus the dimensionless excitability curves are also only dependent on the Poisson's ratio of the material.

Figure 5.1(a) shows the plane strain excitability of Lamb wave modes for an aluminium plate in vacuum. It is very interesting to note the similarity between these excitability curves and the attenuation curves for an identical plate immersed in a non-viscous fluid (i.e. water for example) as shown in Figure 5.1(b). A qualitative explanation for this similarity is to observe that it is only the out-of-plane surface displacement of Lamb waves which couples to a surrounding fluid and causes energy leakage. Hence modes with large amounts of out-of-plane surface displacement will have high attenuation when a plate is immersed in fluid. Conversely, applying an out-of-plane force to the surface of a plate in vacuum will tend to couple best to modes with large amounts of out-of-plane surface displacement. Thus one would expect that the more highly attenuating modes of a plate in liquid would correspond to the more highly excitable modes of the same plate in vacuum and *vice versa*.

The excitability is of key importance in the development of the Huygens' model, but equation 5.9 is for excitation of straight crested waves by a line source, and the Huygens' model requires a corresponding function relating the amplitudes of circular crested waves to the amplitude of a point force. As will be demonstrated, the results are very similar, but exhibit certain key differences.

#### *Application of Ditri's technique to point excitation of a plate*

For the point normal force exciting circular crested waves in an isotropic plate, the problem is axi-symmetric about the location of the force. Hence cylindrical co-ordinates are used, the  $z$  direction being normal to the plate, and the  $r$  and  $\theta$  directions being in the plane of the plate. Following the method of Ditri *et al.* (1994a), Hankel transforms are used to solve the problem. The wave equations (equation 2.11 in chapter 2) become:

$$\begin{aligned} \frac{d^2 \Phi_0}{dt^2} - (\xi^2 - k_r^2) &= 0 \\ \frac{d^2 \Psi_1}{dt^2} - (\xi^2 - k_l^2) &= 0 \end{aligned} \tag{5.10}$$

where  $\Phi_0$  and  $\Psi_1$  represent the zeroth and first order Hankel transforms of the scalar and vector potential fields,  $\xi$  is the transform variable and  $k_r$  and  $k_l$  are again the wavenumbers of the transverse and longitudinal bulk waves. Solution of the transformed wave equations yields:

$$\begin{aligned} \Phi_0(\xi, z) &= S_l \cosh(q_l z) + A_l \sinh(q_l z) \\ \Psi_1(\xi, z) &= A_r \cosh(q_r z) + S_r \sinh(q_r z) \end{aligned} \tag{5.11}$$

where  $S_i$ ,  $A_i$ ,  $A_t$  and  $S_t$  are arbitrary constants, and  $q_i = \sqrt{\xi^2 - k_i^2}$  and  $q_t = \sqrt{\xi^2 - k_t^2}$ . Using an exactly analogous method to that for straight crested waves, expressions for the stresses at the surfaces of the plate are written in terms of the potential fields:

$$\begin{aligned}\sigma_{zz} &= \lambda \left[ \frac{\partial^2 \phi}{\partial r^2} + \frac{1}{r} \frac{\partial \phi}{\partial r} + \frac{\partial^2 \phi}{\partial z^2} \right] + 2\mu \left[ \frac{\partial^2 \phi}{\partial z^2} + \frac{1}{r} \frac{\partial}{\partial r} \left( r \frac{\partial \psi}{\partial z} \right) \right] \\ &= -\lambda k_i^2 \phi + 2\mu \frac{\partial^2 \phi}{\partial z^2} + \frac{2\mu}{r} \frac{\partial}{\partial r} \left( r \frac{\partial \psi}{\partial z} \right) \\ \sigma_{rz} &= \mu \left[ 2 \frac{\partial^2 \phi}{\partial r \partial z} + \frac{\partial^2 \psi}{\partial r^2} + \frac{1}{r} \frac{\partial \psi}{\partial r} - \frac{\psi}{r^2} - \frac{\partial^2 \psi}{\partial z^2} \right]\end{aligned}\quad (5.12)$$

and by applying the appropriate Hankel transforms to these expressions, the transformed boundary conditions ( $\Sigma_{zz}$  and  $\Sigma_{rz}$ ) may be written in terms of the arbitrary constants:

$$\begin{bmatrix} \Sigma_{zz}|_{z=d/2} \\ \Sigma_{zz}|_{z=-d/2} \\ \Sigma_{rz}|_{z=d/2} \\ \Sigma_{rz}|_{z=-d/2} \end{bmatrix} = \mu \begin{bmatrix} (\xi^2 + q_i^2) \cosh q_i d/2 & (\xi^2 + q_i^2) \sinh q_i d/2 & 2i\xi q_i \sinh q_i d/2 & 2i\xi q_i \cosh q_i d/2 \\ (\xi^2 + q_i^2) \cosh q_i d/2 & -(\xi^2 + q_i^2) \sinh q_i d/2 & -2i\xi q_i \sinh q_i d/2 & 2i\xi q_i \cosh q_i d/2 \\ 2i\xi q_i \sinh q_i d/2 & 2i\xi q_i \cosh q_i d/2 & -(\xi^2 + q_i^2) \cosh q_i d/2 & -(\xi^2 + q_i^2) \sinh q_i d/2 \\ -2i\xi q_i \sinh q_i d/2 & 2i\xi q_i \cosh q_i d/2 & -(\xi^2 + q_i^2) \cosh q_i d/2 & (\xi^2 + q_i^2) \sinh q_i d/2 \end{bmatrix} \begin{bmatrix} S_i \\ A_i \\ A_t \\ S_t \end{bmatrix}\quad (5.13)$$

which is identical to the matrix equation 5.1 for the straight crested wave case, except that the boundary conditions have been transformed and the transform variable,  $\xi$ , replaces  $k$ . Clearly in the free plate case, when the surface stresses and their transforms are all zero, exactly the same dispersion relations are found between  $k$  (or  $\xi$ ) and  $\omega$  in both cases.

The next step is to specify the excitation. In principle, the problem can be solved for any harmonic axi-symmetric distribution of stresses, but in this instance, a uniform stress of amplitude  $\sigma_0$  applied over a circular area of radius  $a$ , on the upper surface of the plate, is sufficient. Hence, the boundary conditions are:

$$\begin{aligned}\sigma_{zz}|_{z=d/2} &= \begin{cases} \sigma_0 \exp(-i\alpha r) & \text{for } |r| \leq a \\ 0 & \text{for } |r| > a \end{cases} \\ \sigma_{zz}|_{z=-d/2} &= 0 \\ \sigma_{rz}|_{z=\pm d/2} &= 0\end{aligned}\quad (5.14)$$

After subjecting these boundary conditions to the appropriate Hankel transforms, the method of Fourier integrals is again used (as in the case of straight crested waves) to obtain the transformed potential functions. Application of the appropriate inverse Hankel transforms yields the actual potential functions from which the displacement field may be calculated. Hence, an expression for the out-of-plane surface displacement at the plate surface is obtained:

$$u_z = -\frac{\pi\sigma_0}{2\mu} \left\{ \begin{array}{l} \sum_{k(\text{symmetric})} \left( \frac{aJ_1(ka)}{k} \cdot k \cdot \frac{q_t [(q_t^2 - k^2) \sinh q_t d/2 \sinh q_t d/2]}{\partial \Delta_s / \partial k} \cdot H_0^{(1)}(kr) \right) \\ + \\ \sum_{k(\text{anti-symmetric})} \left( \frac{aJ_1(ka)}{k} \cdot k \cdot \frac{q_t [(q_t^2 - k^2) \cosh q_t d/2 \cosh q_t d/2]}{\partial \Delta_a / \partial k} \cdot H_0^{(1)}(kr) \right) \end{array} \right\} \exp(-i\alpha x) \quad (5.15)$$

where  $\xi$  has been replaced by  $k$  for comparison with equation 5.4. Again the first fraction after each summation sign is associated with the geometry of the source, which in this calculation is not of interest. Hence, the limiting case is taken as the radius of the source is reduced to zero, while the total amplitude of the applied force,  $F_0$ , is held constant.

$$\begin{aligned} \lim_{a \rightarrow 0} \frac{aJ_1(ka)}{k} &= a^2 \lim_{a \rightarrow 0} \frac{J_1(ka)}{ka} \\ &= \frac{a^2}{2} \end{aligned} \quad (5.16)$$

and using the fact that the total force,  $F_0$ , is equal to  $\pi a^2 \sigma_0$  enables equation 5.15 to be written as:

$$u_z = -F_0 \cdot \frac{1}{4\mu} \left\{ \begin{array}{l} \sum_{k(\text{symmetric})} \left( k \cdot \frac{q_t [(q_t^2 - k^2) \sinh q_t d/2 \sinh q_t d/2]}{\partial \Delta_s / \partial k} \cdot H_0^{(1)}(kr) \right) \\ + \\ \sum_{k(\text{anti-symmetric})} \left( k \cdot \frac{q_t [(q_t^2 - k^2) \cosh q_t d/2 \cosh q_t d/2]}{\partial \Delta_a / \partial k} \cdot H_0^{(1)}(kr) \right) \end{array} \right\} \exp(-i\alpha x) \quad (5.17)$$

This is the analogous expression to equation 5.6, relating the amplitude of the out-of-plane surface displacements for a particular mode to the amplitude of a normal excitation force acting at a single point. Once again, it is instructive to re-write equation 5.17 in dimensionless form, using the same substitutions as given in equation 5.7 but with the important difference that dimensionless force is now written as  $\bar{F}_0 = F_0 / \mu d^2$  since the force is no longer a force per unit distance. This yields:

$$\bar{u}_z = -\bar{F}_0 \left\{ \begin{array}{l} \sum_{\bar{k}(\text{symmetric})} \left( \frac{\bar{k}}{4} \cdot \frac{\bar{q}_t [(\bar{q}_t^2 - \bar{k}^2) \sinh \bar{q}_t /2 \sinh \bar{q}_t /2]}{\partial \bar{\Delta}_s / \partial \bar{k}} \cdot H_0^{(1)}(\bar{k}r) \right) \\ + \\ \sum_{\bar{k}(\text{anti-symmetric})} \left( \frac{\bar{k}}{4} \cdot \frac{\bar{q}_t [(\bar{q}_t^2 - \bar{k}^2) \cosh \bar{q}_t /2 \cosh \bar{q}_t /2]}{\partial \bar{\Delta}_a / \partial \bar{k}} \cdot H_0^{(1)}(\bar{k}r) \right) \end{array} \right\} \exp(-i\bar{\omega}t) \quad (5.18)$$

The similarities between equation 5.8 and equation 5.18 are obvious, but there is an extra occurrence of the wavenumber,  $\bar{k}$ , in the latter case.

Simplifying equation 5.18 gives:

$$\bar{u}_z(\bar{r}, \bar{t}, \bar{\omega}) = \bar{F}_0 \sum_{\bar{k}} \left( \bar{E}_c(\bar{k}, \bar{\omega}) H_0^{(1)}(\bar{k}\bar{r}) \right) \exp(-i\bar{\omega}\bar{t}) \quad (5.19)$$

where  $\sum_{\bar{k}}$  denotes a summation over each of the modes present at the frequency  $\bar{\omega}$ , and  $\bar{E}_c(\bar{k}, \bar{\omega})$  is again the excitability function for each mode, except this is not the same excitability function as in equation 5.9, as this is for circular crested waves. Comparison of equations 5.8 and 5.18 shows that the two excitability functions are related by:

$$\bar{E}_c(\bar{k}, \bar{\omega}) = \frac{i\bar{k}}{2} \bar{E}_s(\bar{k}, \bar{\omega}) \quad (5.20)$$

Figure 5.2 shows the excitability curves for circular crested Lamb waves excited by a point source on an aluminium plate in vacuum. It is interesting to note that there is a significant difference between figures 5.1(a) and 5.2 caused by the extra wavenumber term. Degerketin and Khuri-Yakub (1996) appear to use, incorrectly in the opinion of the current author, the straight crested analysis for their work on Lamb wave excitation by Hertzian contacts, and as a result do not obtain particularly good agreement with their experimental measurements.

Physically, the difference between the straight crested case and the circular crested case means that at a particular distance from a source, the relative amplitudes of modes with different wavenumbers depend on whether the source is an infinite line and the waves are straight crested, or a point source and the waves are circular crested. It has also been verified that the two solutions are consistent, this being achieved by numerically integrating the fields from a series of point sources arranged in a long straight line to obtain the solution for a line source.

Equation 5.19 is the foundation of the Huygens' model for IDTs. It enables a graph of out-of-plane surface displacement versus distance from source to be plotted, when a plate is excited at a particular frequency. Such a graph will henceforward be referred to as a displacement-distance curve.

Attention should be drawn to the fact that, in the preceding analysis, because the harmonic force is expressed as  $F_0 \exp i\omega t$ , it contains both a real component,  $F_0 \cos \omega t$ , and an imaginary component,  $iF_0 \sin \omega t$ , which are  $90^\circ$  out phase with each other. The presence of the factor  $F_0 \exp i\omega t$  in equation 5.17 means that the surface displacement can also be separated into the sum of two components, one associated with the real part of the input force,  $F_0 \cos \omega t$ , and one associated with the imaginary part of the input force,  $iF_0 \sin \omega t$ . Examination of equation 5.17 reveals that for point excitation of circular crested waves, the surface displacement associated with the real part of the input force is  $Re(u_z)$ . However, it should be noted that in the case of line excitation of straight crested waves (equation 5.6) the surface displacement associated with the real part of the input force is actually  $Im(u_z)$  due to the presence of an extra  $i$  in equation 5.6. For subsequent

computations, the imaginary component of the surface displacement is always retained as well as the real part. The reason for this is that the spatial envelope of the surface displacement at a particular instant in time is then simply  $|u_z|$ .

As an example, figure 5.3 shows the displacement-distance curve for the case of an aluminium sheet being excited at a dimensionless frequency of 0.4287 (the frequency at which the  $A_0$  mode is at its maximum group velocity which is a commonly used centre frequency in Lamb wave NDT applications), by a harmonic force of peak dimensionless amplitude 1.0. This figure shows the real part and modulus of the displacement. Although both  $A_0$  and  $S_0$  modes are being excited,  $S_0$  is not readily apparent due to it having considerably lower excitability than  $A_0$  at this frequency. However, examination of the modulus envelope reveals it to have a rippled appearance, this being the effect of the presence of the lower amplitude  $S_0$  wave.

### 5.2.2 Use of model to predict acoustic fields due to inputs of finite duration

So far the calculation has been concerned with continuous excitation at a single frequency. In an NDT testing application, the excitation is likely to be a toneburst with finite duration and a finite bandwidth. It is not generally the case that over a particular frequency range, the propagation characteristics (i.e. excitability, phase velocity and group velocity) of a Lamb wave mode are constant. Although viewing the acoustic field pattern produced by a transducer at its designed centre frequency is useful, the ability to examine the acoustic field at different points in time after the transducer has been excited with an input signal of finite duration is also valuable. The latter approach enables modes with different group velocities to be separated in distance, which is obviously not possible if continuous excitation is used.

To model the displacements associated with an input of finite duration,  $f(t)$ , a Fourier transform is used to decompose the input signal into its different frequency components,  $f(\omega)$ . The displacement distance curves for each frequency component may be calculated using equation 5.19, where the time,  $t$ , has its origin at the start of the input signal. The total surface displacement as a function of time and distance from the source is then given by:

$$u_z(r, t) = \int f(\omega) \sum_k E(k, \omega) H_0^{(1)}(kr) \exp(-i\omega t) d\omega \quad (5.21)$$

This equation enables the surface displacement to be plotted as a function of both distance and time, when a plate is excited by a finite duration input at a point. A plot of displacement vs. distance vs. time will be referred to as a displacement-distance-time diagram. These are usually in the form of greyscale maps, where the  $x$  and  $y$  axes represent distance and time respectively and the grey level indicates the magnitude of either the real part of the displacement or the modulus. Figures 2.8 and 2.9 in chapter 2 are examples of such plots, and a further example is shown in figure 5.4. This is for the excitation of an aluminium plate at a dimensionless centre frequency of 0.4287 and with a 10 cycle Hanning windowed toneburst. The  $A_0$  and  $S_0$  modes are clearly visible and distinguishable by their different group velocities (the group velocity of a mode is manifested on a displacement-distance-time plot as the gradient at which the wave packet crosses the plot). Obviously, a cross section through the displacement-distance-time plot

parallel to the distance axis yields a displacement-distance plot, an example of which is shown in figure 5.5. For comparison with figure 5.3, figure 5.5 shows the real part and modulus of the displacement.

### 5.2.3 Calculation of acoustic field due to multiple sources

For the purposes of the Huygens' model, the acoustic field due to multiple point sources is required. All the sources are assumed to be excited simultaneously by the same input signal, but they may be scaled by different amplitudes. As the amplitudes may be complex, different sources can have mutual phase differences of anything between  $-180^\circ$  and  $180^\circ$ . To predict the total acoustic field,  $U_z$ , at a point with coordinates  $(x,y)$  in a plate when  $n$  point sources at locations  $(x_1,y_1) \dots (x_n,y_n)$  with amplitudes  $F_1 \dots F_n$  are excited with an input signal,  $f(t)$ , the contributions from each point source are calculated using the displacement versus distance curve given in equation 5.21 and the results summed:

$$U_z(x, y, t) = \sum_{i=1}^n u_z \left( \sqrt{(x-x_i)^2 + (y-y_i)^2}, t \right) \quad (5.22)$$

It should be noted that in this case the acoustic field is the out-of-plane displacement and the summation is trivial, since the contributions from all the sources are all in the  $z$  direction. If instead the acoustic field was defined as being the in-plane displacement at the surface, then the acoustic field would have components in both the  $x$  and  $y$  directions and these would have to be considered separately.

Equation 5.22 gives the total acoustic field at a particular point on a plate surface. The point  $(x,y)$  will be referred to as a monitoring point. Clearly, the acoustic field over an array of monitoring points arranged in a raster pattern can be calculated and used to provide a field map of the spatial distribution of acoustic energy at a point in time. Alternatively, the acoustic field can be calculated along a line or arc of monitoring points to provide a cross section through the overall acoustic field. It is the fact that the acoustic field can be calculated independently at any location that gives the Huygens' model a major advantage over FE techniques, where the entire acoustic field must always be calculated.

Equation 5.22 represents the actual implementation of Huygens' principle. It also encapsulates the assumption implicit in the Huygens' model, which is that the field from a single point source in a plate is unaffected by the presence of other point sources. In practice, the acoustic waves from a single source are affected to some degree when passing under the rest of the transducer. In the point source model of an IDT, this effect could be regarded as point sources having point impedances (i.e. they apply a resisting surface force proportional to the surface displacement of waves passing under them, in addition to their own excitation force). The validity of the assumption that this effect is minimal for the PVDF IDTs considered here will be demonstrated later in the validation section.

The next issue which must be addressed is how to discretise an IDT into a number of finite point sources.

### 5.2.4 Application of Huygens' principle to IDTs generating Lamb waves

The time taken to perform a Huygens' calculation for a given number of monitoring points is directly proportional to the number of sources, as indicated by the summation sign in equation 5.22. Hence, for minimum computation time, the transducer should be discretised into as few sources as possible. The rules that have been used in order to minimise the number of sources needed to model an IDT are explained below.

#### *Modelling a small area of an IDT*

Consider an area from a single finger of an IDT bonded onto a structure as shown in figure 5.6. Over the total area shown, the spatial distribution of stress exerted on the structure is assumed to be either slowly varying or uniform. Therefore, a small area,  $\delta A$ , can be assumed to exert a constant stress,  $\sigma_{zz}$ , on the structure, as shown. The Huygens' model assumes that this distributed stress can be represented as a point force,  $\delta F$ , applied to the structure at the centroid of the area,  $\delta A$ , the amplitude of  $\delta F$  being equal to  $\sigma_{zz}\delta A$ . As long as the dimensions of the area are small compared to the shortest wavelength of Lamb waves that will be excited the precise shape of the area is assumed to be unimportant. In practice, a rectangular element is used rather than the circular element shown in figure 5.6, since rectangular elements tessellate and obviously lend themselves to modelling rectangular IDT fingers.

#### *Discretisation of an IDT*

In this section, an imaginary plate is considered, which can only support a single, non-dispersive Lamb wave mode which has a wavelength of  $\lambda$  at some frequency  $\omega$ . For generality, all dimensions are given in terms of this wavelength, and the IDTs are assumed to be excited continuously and only at the frequency  $\omega$ .

The width of a finger in the physical IDTs considered here is always less than half a wavelength of the Lamb wave mode which the IDT is designed to excite. Therefore, it must be decided how many sources are required across the width of a finger. Consider a single finger of an IDT,  $5\lambda$  long by  $0.5\lambda$  wide, generating continuous non-dispersive waves of a single mode, with wavelength  $\lambda$ , as shown in figure 5.7. Figure 5.8 shows the amplitude of the predicted acoustic fields when 1, 2, 3, 4 or 5 point sources are used across the width of the finger (these correspond to 2, 4, 6, 8 and 10 sources per wavelength). In all cases, 50 sources (i.e. 10 sources per wavelength) are used along the length of the finger. To see the variations more clearly, figure 5.9 shows angular sections through these acoustic fields taken at a radius of  $100\lambda$  (this distance being measured from the geometric centre of the finger) on the same axes. Due to the symmetry of the fields, it is only necessary to consider the sections from  $0$  to  $90^\circ$ . It can be seen that as soon as more than one source across the width of the finger (i.e. more than two sources per wavelength) is used, the amplitude of the field in front of the transducer (at  $0^\circ$ ) decreases quite sharply. This is to be expected as although the sum of the amplitudes from all the sources is always a constant, the presence of multiple sources at different locations causes interference which reduces the total amplitude in front of the finger.

It would appear from these results that at least two sources should be used across the width of each finger (i.e. four sources per wavelength) in an IDT. However, two reasons can be suggested as to why this is an unnecessary complication. Firstly, although the use of multiple sources causes a significant reduction in amplitude, the effect on the actual shape of the field is minimal. As the practical application of Huygens' model is not usually concerned with absolute amplitudes, the loss of absolute accuracy is of little importance. Secondly, it is not yet known whether modelling the stress across the transducer finger as being uniform is any more accurate than assuming the stress is concentrated along a line. For these reasons it is assumed that, for the time being at least, a finger of an IDT may be modelled as single line of point sources. It may be that later, a better model of the stress distribution will be established, in which case more sources could be used with justification, but it seems unlikely based on the previous study that this will have any significant effect on the field pattern.

The next consideration is the number of sources required along the length of a finger in an IDT. Again a single finger  $5\lambda$  long is modelled, this time using a single line of point sources as shown in figure 5.10. Figure 5.11 shows the effect on the acoustic field of using 1, 2, 3, 4 and 10 sources per wavelength, along the length of the finger. It can be seen that when only one source per wavelength is used, the fundamental shape of the field pattern changes dramatically, due to constructive interference taking place along the length of the finger. However, with more than three sources per wavelength the changes to the field pattern reduce. Again this can be seen more clearly if angular sections of the fields at  $100\lambda$  are compared as shown in Figure 5.12. On the basis of Figure 5.12 and taking into account the other assumptions made in the Huygens' model, it seems that taking a minimum of four sources per wavelength along the length of a finger, is a reasonable compromise between accuracy and computation time.

The guidelines for using Huygens' principle to model IDTs may therefore be summarised as follows:

- Only one row of sources is needed to model each finger of the IDT.
- Along the length of the row, the spacing of the sources should be such that there are at least four per wavelength. If the transducer is being operated at a frequency where multiple modes are being generated with different wavelengths, then the shortest of these wavelengths should be used when calculating the spacing of the sources, even if this is not the wavelength of the mode which the transducer is designed to excite.

### 5.3 SOFTWARE IMPLEMENTATION

The software to implement the Huygens' model was written in two parts, the first to predict the acoustic field due to a point source and the second to perform the Huygens' superposition. Both parts were written in Pascal (Borland Delphi version 2.0) with graphical user interfaces for use with the Microsoft Windows 95/NT operating system on a PC.

### ***5.3.1 Program for calculating acoustic field due to a point source***

A screen shot of the input screen for the program for calculating the acoustic field due to a point source is shown in figure 5.13. The main inputs to this part of the program are the input signal and the wave propagation data. The output is a text file containing a matrix of complex surface displacements. Each row in the matrix represents displacement vs. time data and each column represents displacement vs. distance data. The output may also be viewed visually as a displacement-distance-time plot as shown in figure 5.14.

The top section of the screen in figure 5.13 is concerned with the nature of the input that will be applied at the point source, and options for either continuous harmonic excitation, toneburst excitation or arbitrary file input are possible. The Fourier transform of the input signal is shown in the top right of the screen.

The middle section of the screen governs the propagation model which is used to predict the displacement field. Both axi-symmetric (circular crested waves) and 2-dimensional (straight crested waves) models are possible, although in practice, only the former is used in the Huygens' model. The phase velocity and excitability of the propagating waves may be specified manually in which case both quantities are assumed to be frequency independent. This idealised model was used for many of the general studies described in this chapter. Alternatively, the phase velocity may be read from a file generated by *Disperse* (Pavlakovic *et al.* 1997) and the excitability calculated using the method described in section 5.2.1, this being illustrated in the screenshot shown in figure 5.13. In either case, individual modes may be switched on or off so that effects particular to individual modes may be isolated. To completely model the physics of point source excitation of a plate, the propagation data must come from *Disperse* and all modes which exist over the bandwidth of the input signal must be switched on.

The bottom portion of this screen shows the limits and step sizes of the calculation in distance and time. The button marked 'Execute' begins the main calculation of the displacement-distance-time matrix. When completed the displacement-distance-time matrix is displayed as a displacement-distance-time plot in a new window as shown in the screen shot in figure 5.14. Cross sections through the displacement-distance-time plot may be viewed and the matrix may be saved for use in the Huygens' superposition program.

### ***5.3.2 Program for performing Huygens' superposition***

A screen shot of the second part of the program which actually performs the Huygens' calculation is shown in figure 5.15. The inputs to this part of the program are a text file of the displacement-distance-time matrix and a second text file of the excitation points representing the IDT being modelled. Several outputs are possible, including angular and radial field cross sections as well as complete field maps.

The top left portion of the screen allows a displacement-distance-time file to be chosen and a displacement-distance curve at a particular instant in time to be selected from it. The displacement-distance curve which has been selected is plotted in this portion of the screen.

In the portion below, a transducer file is selected. Transducer files consist of a list of excitation points, their  $x$  and  $y$  coordinates and their complex amplitudes. When a transducer file is selected, a plot of the location of the excitation points is shown.

In the top right of the screen is space for the model output of acoustic field predictions. The size and resolution of the field to be calculated may be selected and, when completed, the output may be saved as either a text file of the actual complex surface displacements or as a bitmap. Below is the output of angular or radial cross sections through the field. These may also be saved as text files for analysis in other software.

### 5.4 VALIDATION

#### 5.4.1 Validation of displacements resulting from point excitation of a plate

##### *Comparison of displacement-distance curves with FE model*

The displacement versus distance curves for several finite duration inputs predicted by the analytic model described in section 5.2.1 have been compared with FE predictions, the latter being performed by a colleague, Mr. P. Marty.

Taking advantage of the axi-symmetric nature of the problem, the FE model uses a two dimensional mesh to represent a cross section through a length of plate, but with an axi-symmetric geometry specified, the axis passing vertically through one end of the plate as shown in figure 5.16. Ideally, the input force should be applied normal to the plate at the node at a corner on the axis. Unfortunately, due to the way the condition of axi-symmetry is implemented in FE models, this is not possible. Instead, the force must be applied at the next node away from the axis, as shown in figure 5.16, which in fact represents force applied around a small ring in the three dimensional case. However, the node spacing is only 0.1 mm (considerably less than a wavelength); hence, it is assumed that the ring of force is still sufficiently small to be regarded as a point source. Applying a force of 1.0 N/radian to the node indicated in the FE model is therefore equivalent to applying a point force of  $2\pi$  N in the analytical model.

The first case which was modelled was the input of a 10 cycle Hanning windowed toneburst with a centre frequency of 1.0 MHz at a point on the surface of a 1.0 mm thick steel plate. The resulting displacement versus distance curves 15  $\mu$ s after the start of the excitation signal from the analytical and FE models are shown in figure 5.17(a) and (b) respectively. As can be seen, excellent agreement between the two models is obtained. In particular, attention should be drawn to the amplitudes of the  $A_0$  and  $S_0$  modes, which are predicted very accurately, thus validating the excitability calculations described previously. The root-mean-square (RMS) discrepancy between the analytic and FE models over the distance shown in figure 5.17 is 1.45 pm (pm = picometre), which is approximately 1 % of the peak to peak amplitude of the  $A_0$  mode.

The second case which was examined was when the excitation was again a 10 cycle Hanning windowed toneburst applied to a 1.0 mm thick steel plate, but this time with a centre frequency of 2.5 MHz. Reference to the relevant dispersion curves (chapter 2 figure 2.3) show that this frequency is very close to the cut off frequency of the  $A_1$  mode.

Figure 5.18(a) and (b) show the resulting displacement versus distance curves 10  $\mu\text{s}$  after the start of the excitation signal from the analytic model and the FE model respectively. It is immediately apparent that the correlation between the analytic model and the FE model is not as good as at 1.0 MHz. More surprisingly, the analytic model appears to be predicting displacements ahead of the main signal, which would have to have propagated faster than the bulk longitudinal wave speed in the material, and hence cannot exist in reality. This anomaly can be explained by the presence of the  $A_1$  mode which has a group velocity tending to zero and a phase velocity tending to infinity in this frequency range. As such, it is thought that the Fourier decomposition technique described in section 5.2.2 is inaccurate in this case as it is not possible to obtain sufficient frequency points in the high phase velocity region of  $A_1$  to accurately represent the behaviour of this mode. This problem also explains the discrepancies in the region close to the source. As the  $A_1$  mode is being excited at its cut off frequency, it exists as non-propagating reverberation through the plate thickness in the region close to the source, as predicted by the FE model in the region below 10 mm in figure 5.18(b). Modes at their cut off frequencies have few if any practical applications in long range Lamb wave inspection, and hence their presence is at best a distraction from the propagating Lamb wave modes and at worst they may cause misleading results. For the purposes of the Huygens' model, it is desirable to remove the erroneous effects which cut off modes have on the calculation of displacement distance curves. To do this, it is easy to discount any modes with a phase velocity in excess of some value from the calculations. This method has been used to predict the displacement distance curve in figure 5.18(c), which can be seen to now show only the propagating modes, and these agree well with the FE predictions. It would seem that this is a justifiable approach for the purposes of this calculation, although it should be borne in mind that even if the cut off modes are not modelled, they will still exist in a physical application.

### *Comparison of displacement-time curves with experiment*

From equation 5.19, it can be seen that the analytical model can also produce predictions of the variation of out-of-plane surface displacement with time (displacement-time curves or time-traces) that would be measured at a particular distance from a point source. These traces can be compared directly with experimentally obtained time-traces.

To do this two conical point contact transducers were used, one as a point source and the other as a receiver. These transducers were developed by a colleague, Dr. M. Evans, for the original purpose of making acoustic emission measurements and are of a similar design to the NBS conical transducer (Greenspan 1987). A schematic diagram showing the construction of one of these transducers is shown in figure 5.20. Due to the bandwidth of these transducers and available material, the comparison had to be performed at lower frequencies than in the comparison with the FE model, using a 5 mm thick aluminium rather than steel plate. The experimental set-up is shown in figure 5.19. Although the frequency response of the acoustic emission transducers is not flat, it was assumed to be constant over the narrow bandwidth used in the experiments.

Figure 5.21 shows the predicted and measured time-traces when the excitation was a 5 cycle toneburst at a frequency of 0.2 MHz, this frequency being chosen such that operating point on the dispersion curves for the system corresponded approximately to

that used in the FE validation at 1.0 MHz for steel plate. As can be seen from figure 5.21 there is excellent correlation between the predicted and measured time-traces.

Figure 5.22 shows the predicted and measured time-traces when the excitation was a 5 cycle toneburst at 0.5 MHz, the frequency this time corresponding to that used in the FE validation at 2.5MHz. Reasonable agreement is obtained, although some difficulty was experienced in preventing echoes from the edges of the plate overlapping the signal of interest when making the experimental measurements.

### 5.4.2 Validation of displacement field associated with an IDT

An IDT designed to excite the  $A_0$  mode in a 1.2 mm thick steel plate was modelled using both a 3 dimensional FE model, and the Huygens' model. The construction of the transducer is of the type described in the previous chapter and the geometry is shown in figure 5.23. Point measurements of the surface displacement were made experimentally using the same point transducers described above by a colleague, Mr. R. Dalton. The major source of experimental inaccuracy when making this type of measurement is the coupling inconsistency between the point transducer and the plate. In the next chapter, an improved technique developed by the present author will be described, but at the time when these measurements were made, only a crude and somewhat subjective averaging technique was used. The procedure is to place the point transducer at the desired location, and then by rotating and fractionally adjusting its position, maximise the received signal. Similar measurements at all the locations of interest are made and the entire procedure is then repeated, usually four or five times. The final value of the acoustic field strength at a particular location is taken as the average of all the measurements made at that location.

The complete field predicted by the Huygens' model for this transducer is shown in figure 5.24(a). Also shown in this figure are comparisons between theoretical, experimental and FE measurements of field cross sections taken at distances of 50 mm, 100 mm and 150 mm in front of the transducer. The prediction of the complete map of the acoustic field using Huygens' model took around 5 minutes, and the computation of the cross sections took around 5 seconds each. The FE model on the other hand took approximately 3 days to run.

As can be seen from figure 5.24(b), (c) and (d), excellent agreement is obtained between the two models, and reasonable agreement is obtained with the experimental measurements. The results of this validation experiment indicated two things. Firstly they showed that the Huygens' model was far superior to FE modelling in terms of computation speed for predicting the field due to an IDT. Secondly, the good agreement with experimental results demonstrated that the assumptions inherent in the Huygens' model were justified for the transducers in question. On this basis, the Huygens' model became the main design tool for IDTs.

## 5.5 CONCLUSIONS

This chapter has described the theoretical background and implementation of a model based on Huygens' principle for predicting the acoustic fields generated by IDTs.

Beam cross sections predicted by the Huygens' model for a typical IDT configuration and the results predicted by an FE model for the same system have been shown to be almost identical. However, the Huygens' model took a few seconds to predict the beam cross sections, whereas the FE model took around three days. The reason why the FE model is so slow compared to the Huygens' model is that in order to calculate the data of interest, such as a beam profile at a certain point in time, the FE model must also calculate a vast quantity of superfluous data including the stresses and displacements at every node in the mesh at every time step. The Huygens' model uses analytical techniques to provide independent predictions of either displacement or stress at any point in time and at any point in the structure without having to calculate the global displacement or stress field and without having to iterate through time steps.

The correlation between the Huygens' model and experimental measurements is very good, especially considering that the Huygens' model does not take any account of second order interactions between the transducer and the structure. The speed with which the Huygens' model can be used has enabled detailed parametric studies of IDT design to be made, which would have been impossible using existing FE techniques, due to the computation time involved. These will be described in the following chapter.

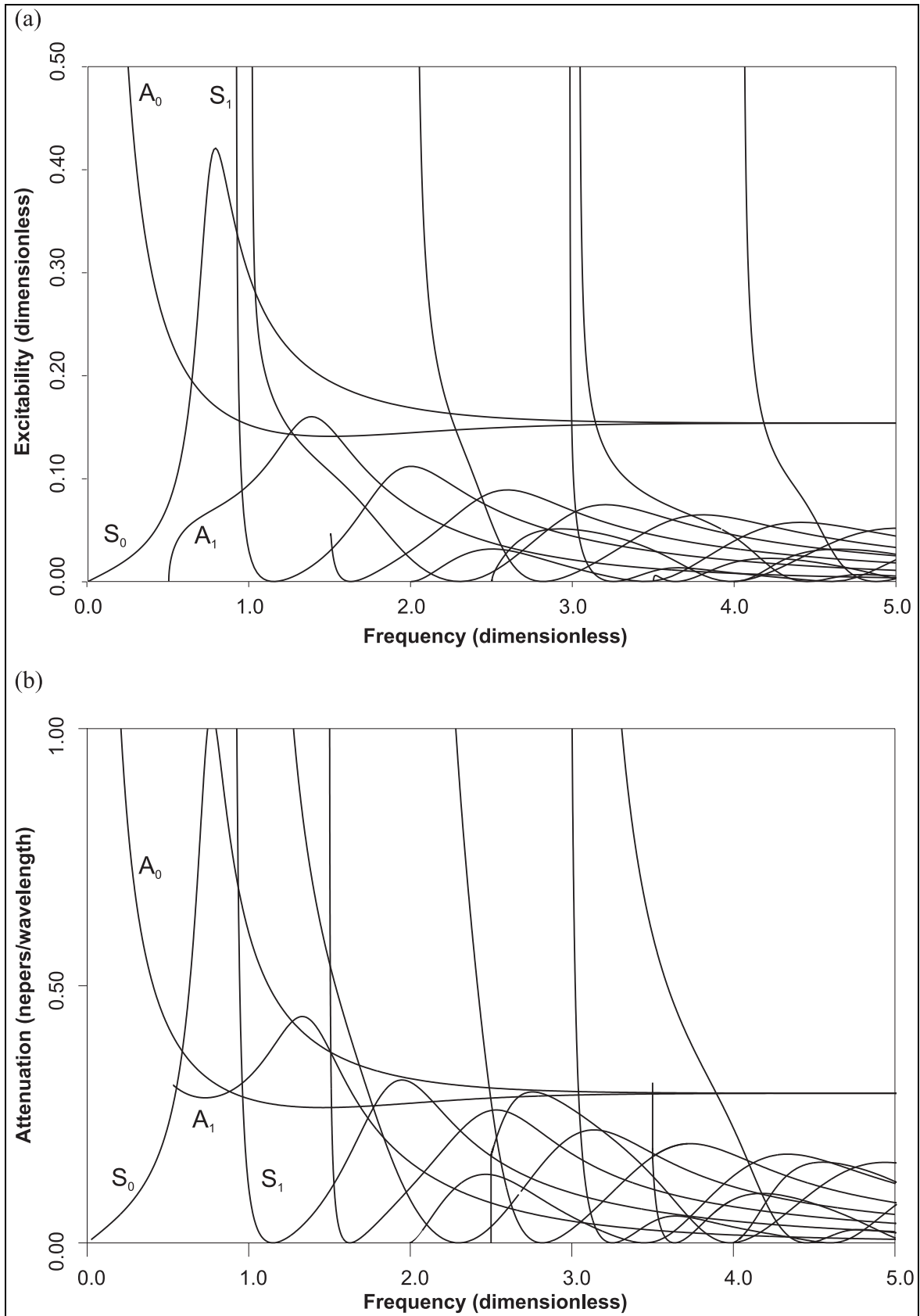


Figure 5.1 (a) Excitability of straight crested Lamb wave modes in aluminium plate when the excitation is by an infinitely long line source. In (b) the attenuation curves for the same plate immersed in water are shown for comparison.

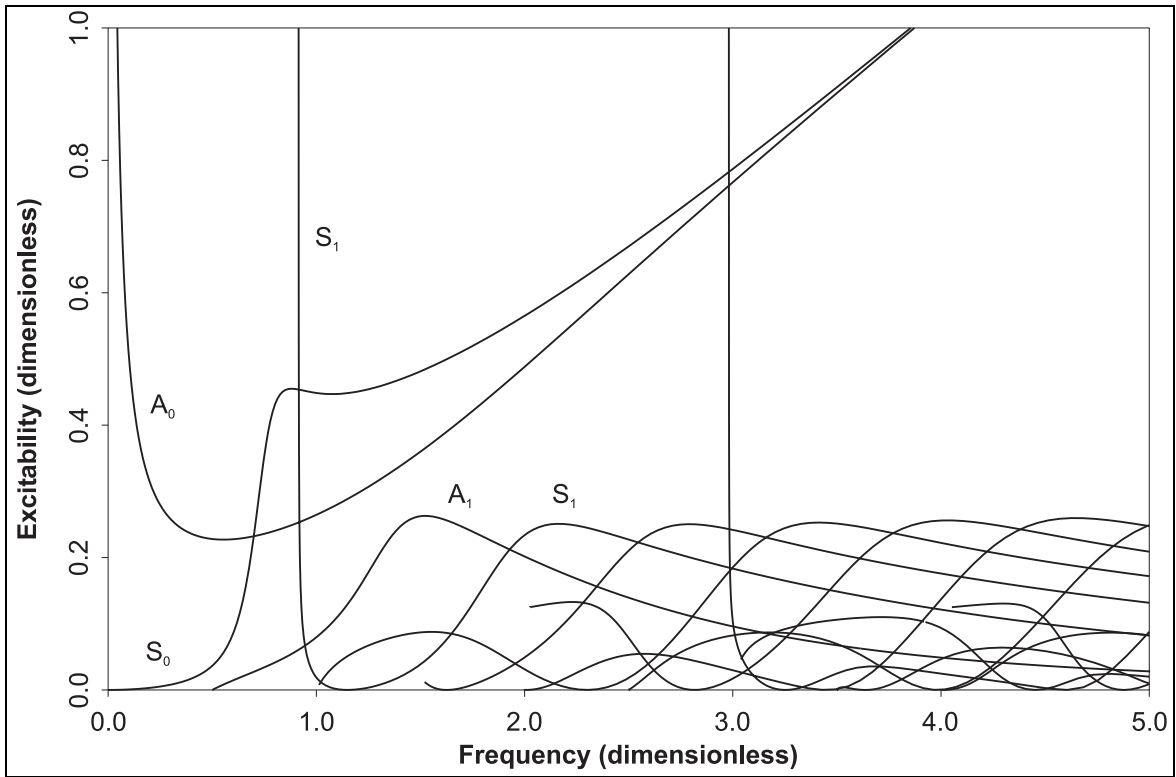


Figure 5.2 Excitability of circular crested Lamb wave modes in aluminium plate when the excitation is by a point source.

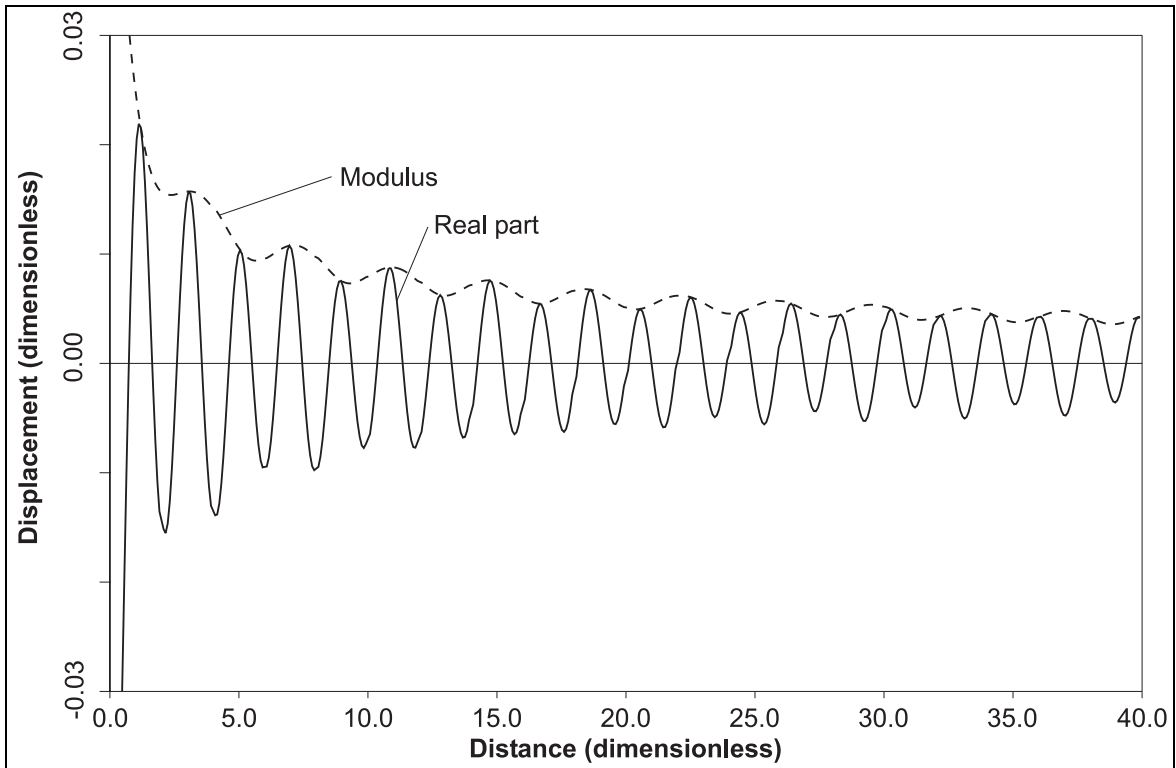


Figure 5.3 An example displacement-distance curve for the case of an aluminium plate being excited at a dimensionless frequency of 0.4287, by a harmonic force of dimensionless amplitude 1.0.

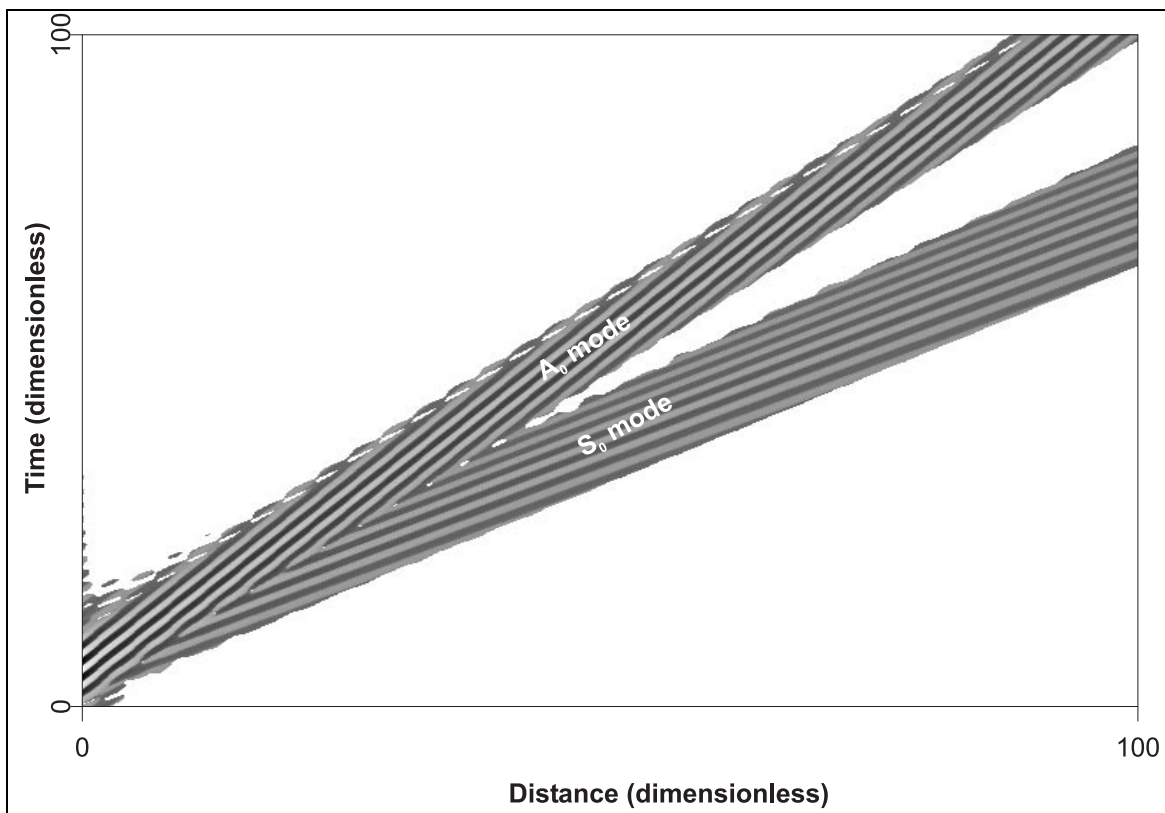


Figure 5.4 An example displacement-distance-time plot for the case of an aluminium plate being excited at a dimensionless frequency of 0.4287, by a harmonic force of dimensionless amplitude 1.0.

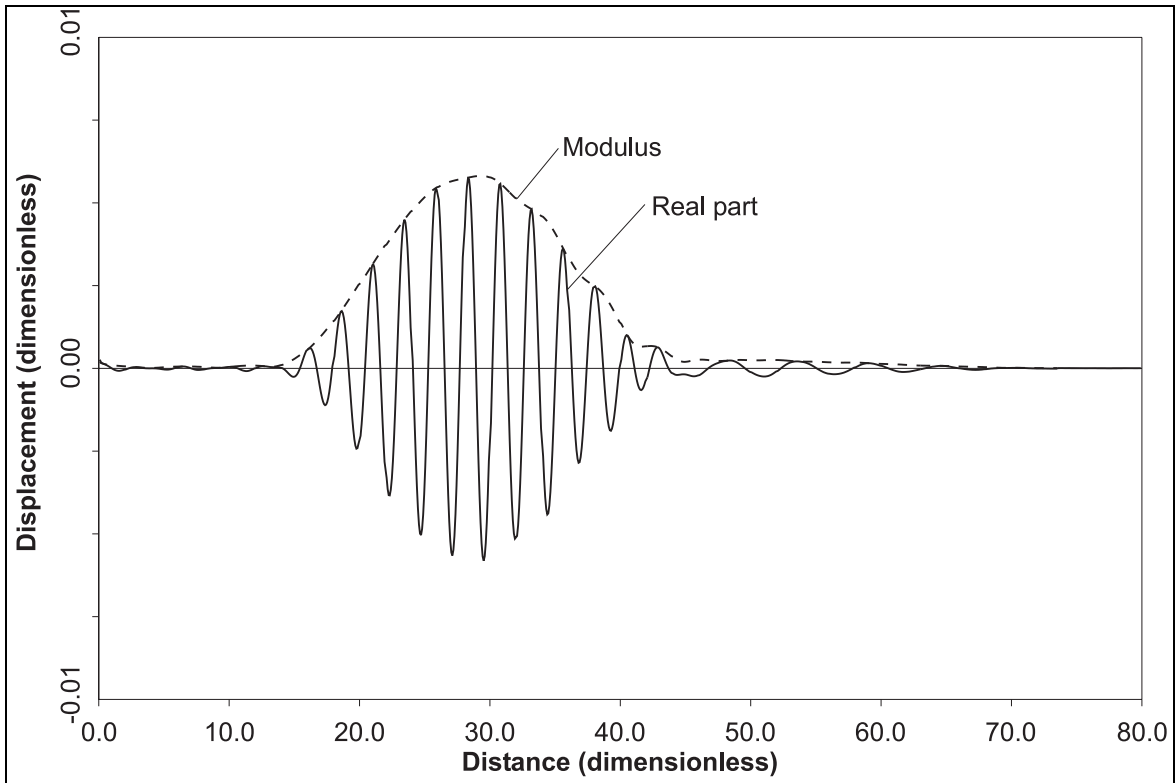


Figure 5.5 An example displacement-distance curve for the case of an aluminium plate  $14\mu\text{s}$  after excitation by a 10 cycle, Hanning windowed toneburst at a dimensionless centre frequency of 0.4287 and a dimensionless peak amplitude 1.0.

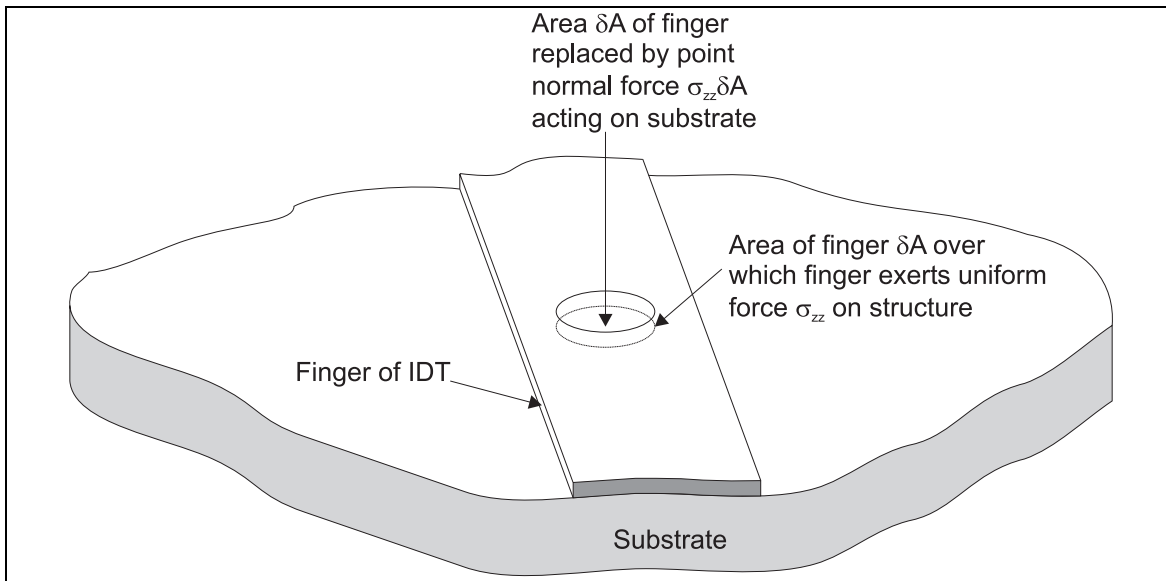


Figure 5.6 Representation of a small area of an IDT by a point source.

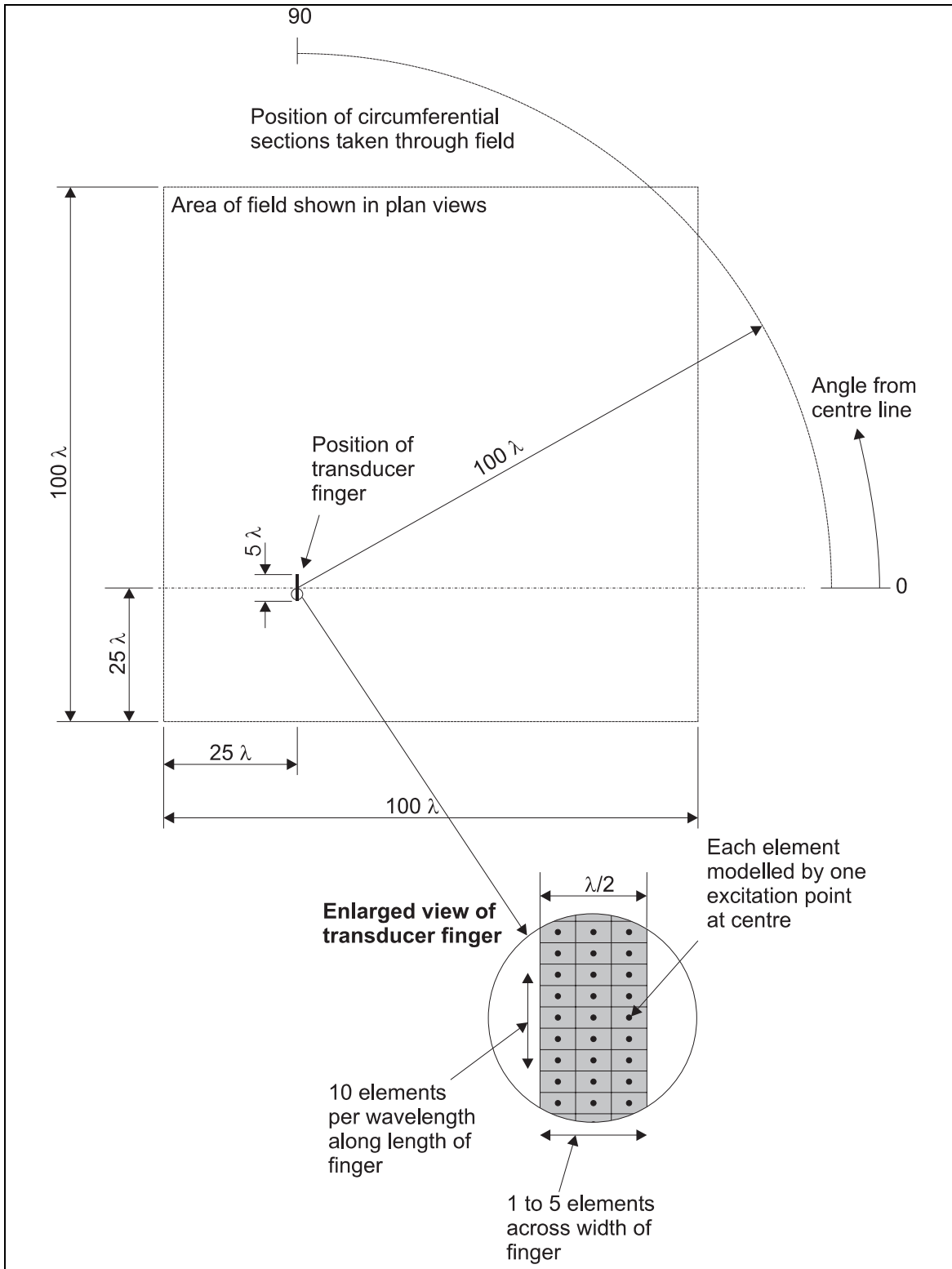


Figure 5.7 Geometry of single finger of an IDT being modelled with varying numbers of sources across its width.

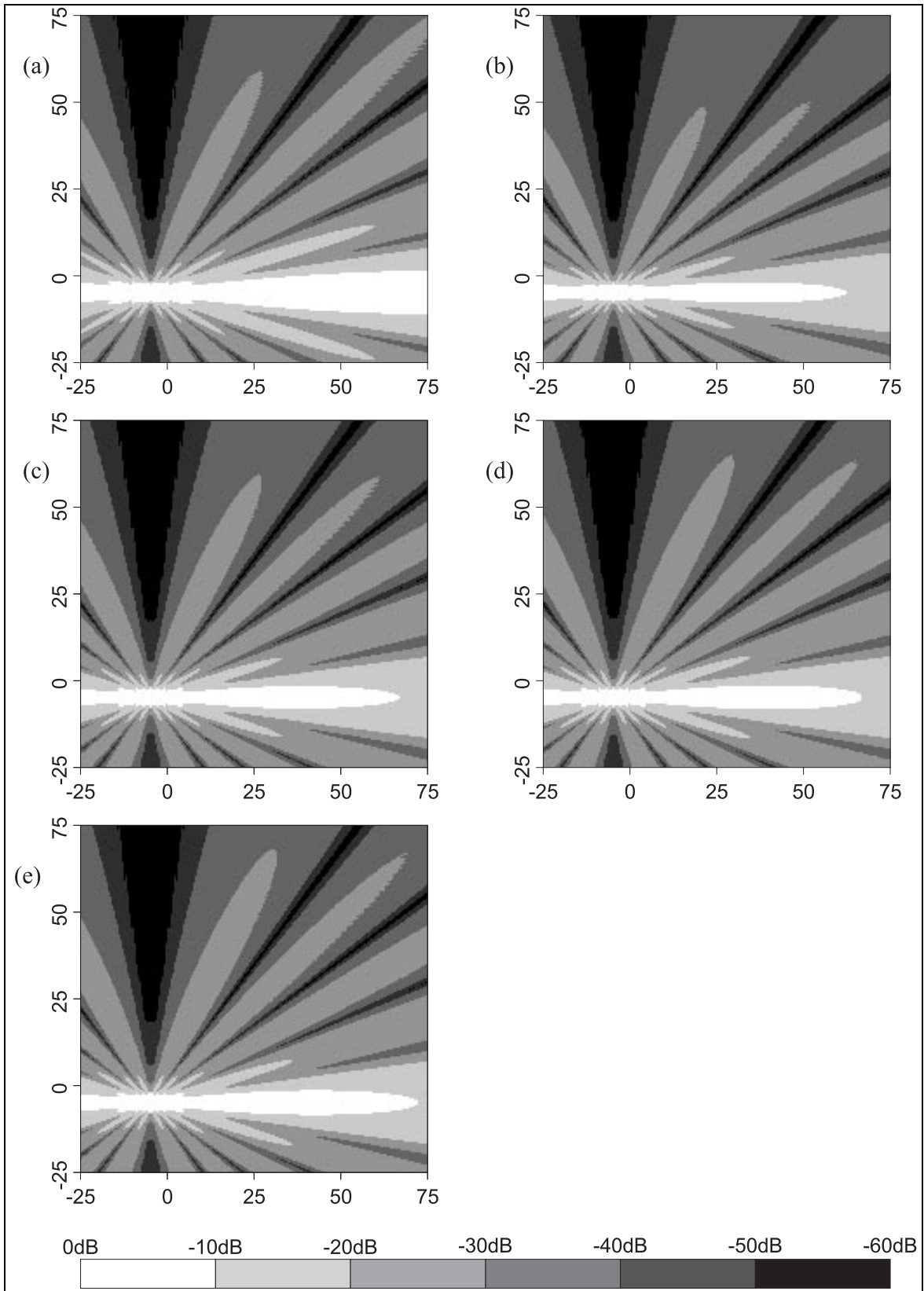


Figure 5.8 Effect of using (a) 2, (b) 4, (c) 6, (d) 8 and (e) 10 sources per wavelength across the width of a finger of an IDT in Huygens' model.

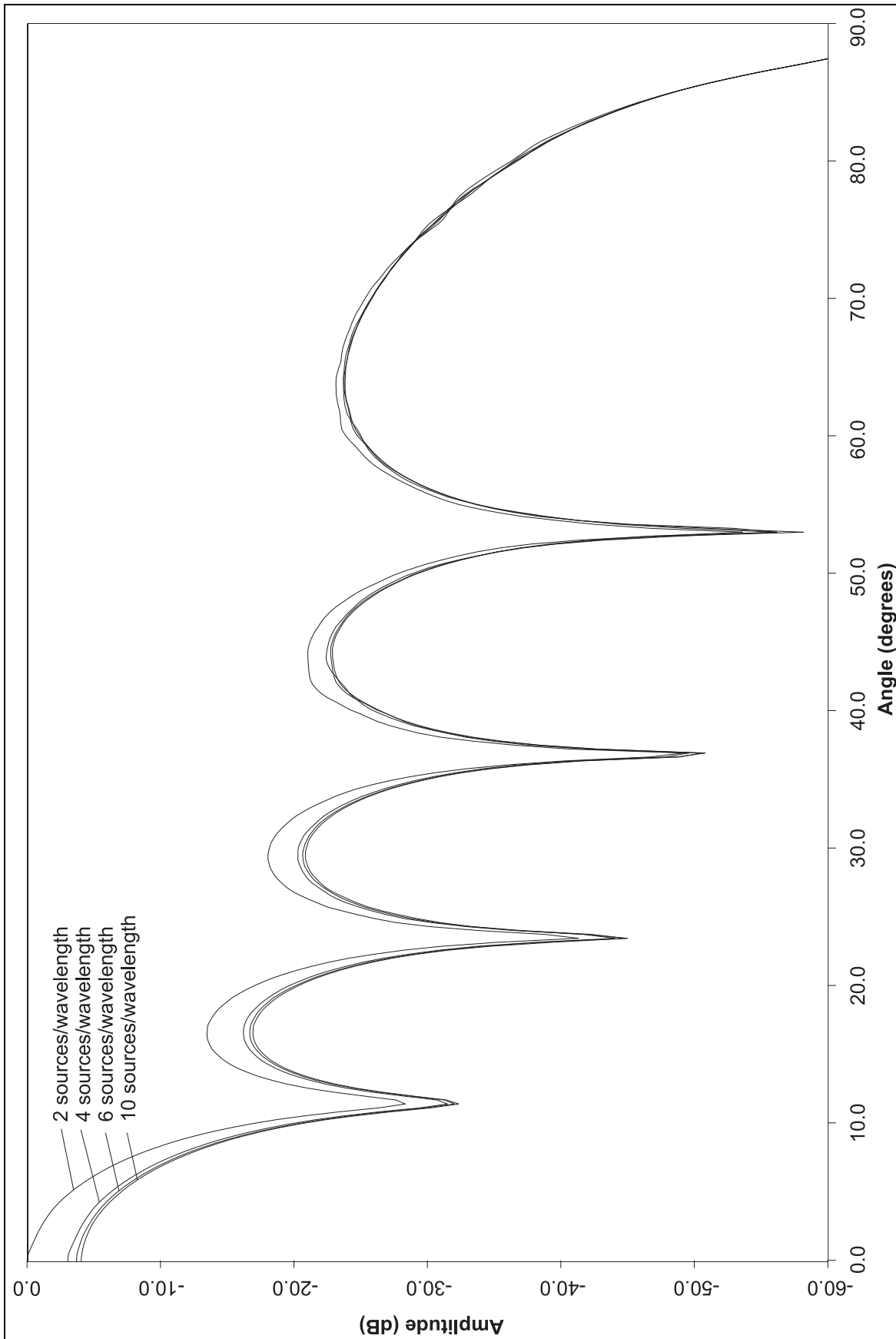


Figure 5.9 Angular sections at a distance of  $100 \lambda$  through the acoustic fields in figure 5.9.

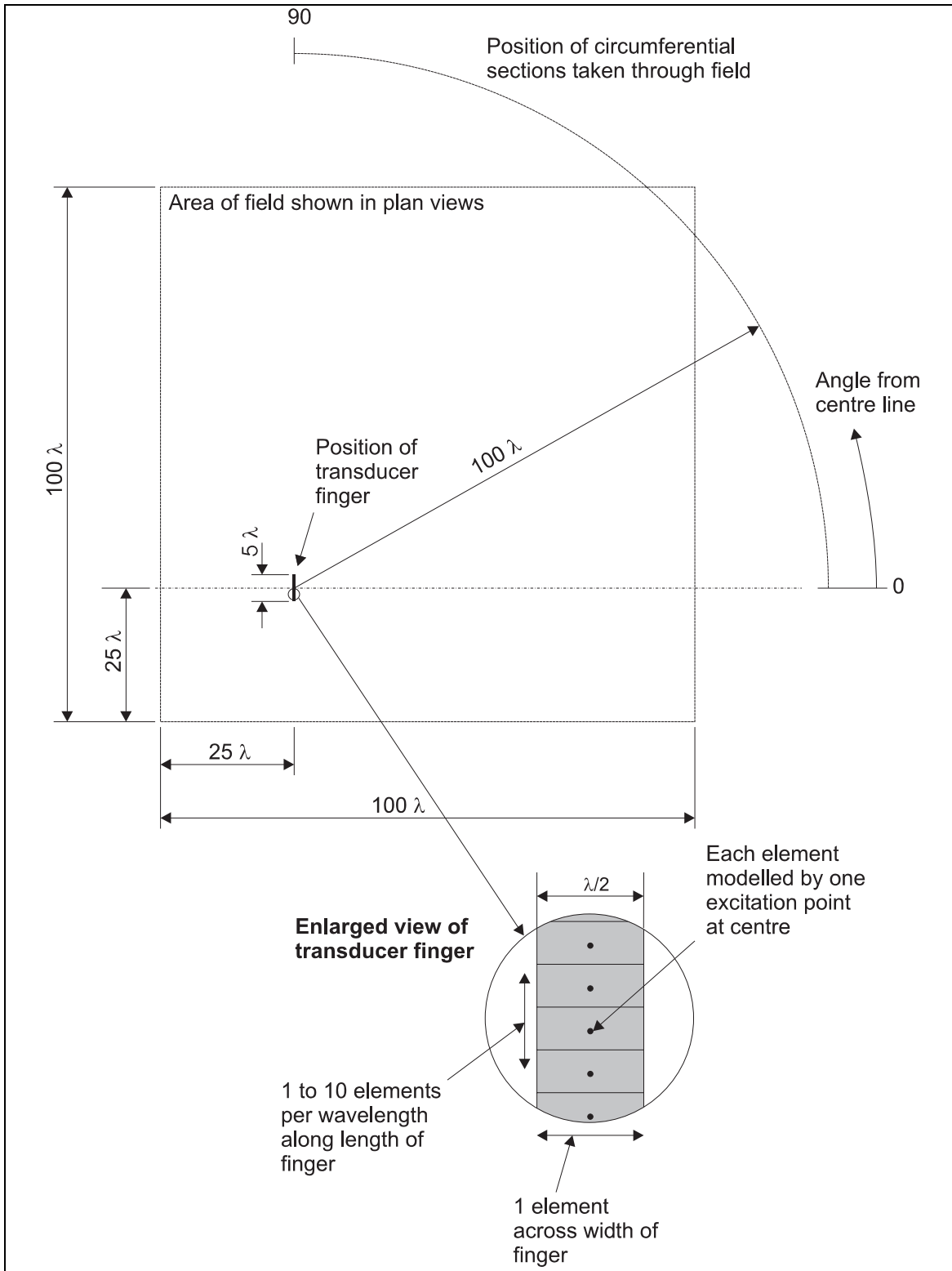


Figure 5.10 Geometry of single finger of an IDT being modelled with varying numbers of sources along its length.

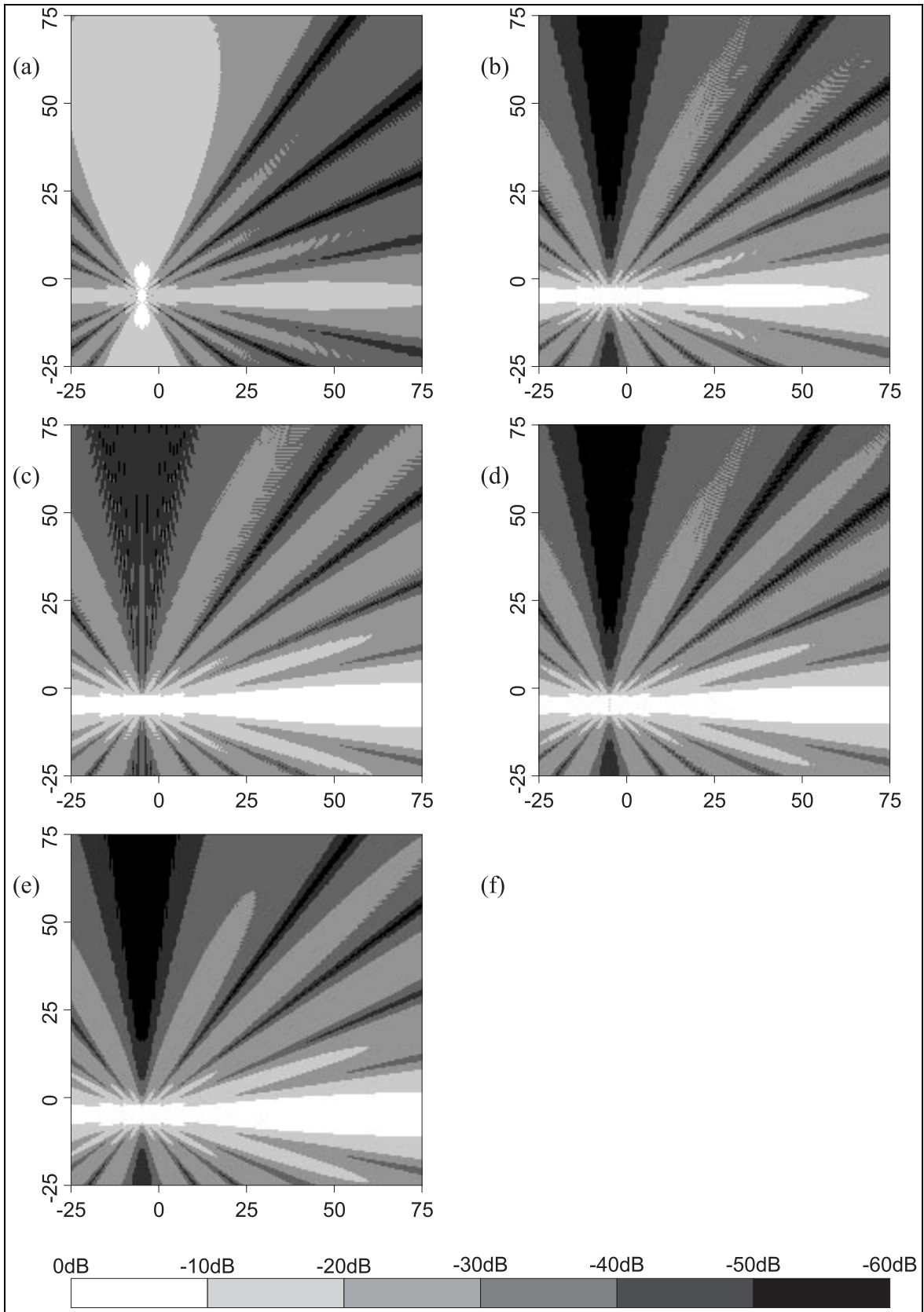


Figure 5.11 Effect of using (a) 1, (b) 2, (c) 3, (d) 4 and (e) 10 sources per wavelength along the length of a finger of an IDT in Huygens' model.

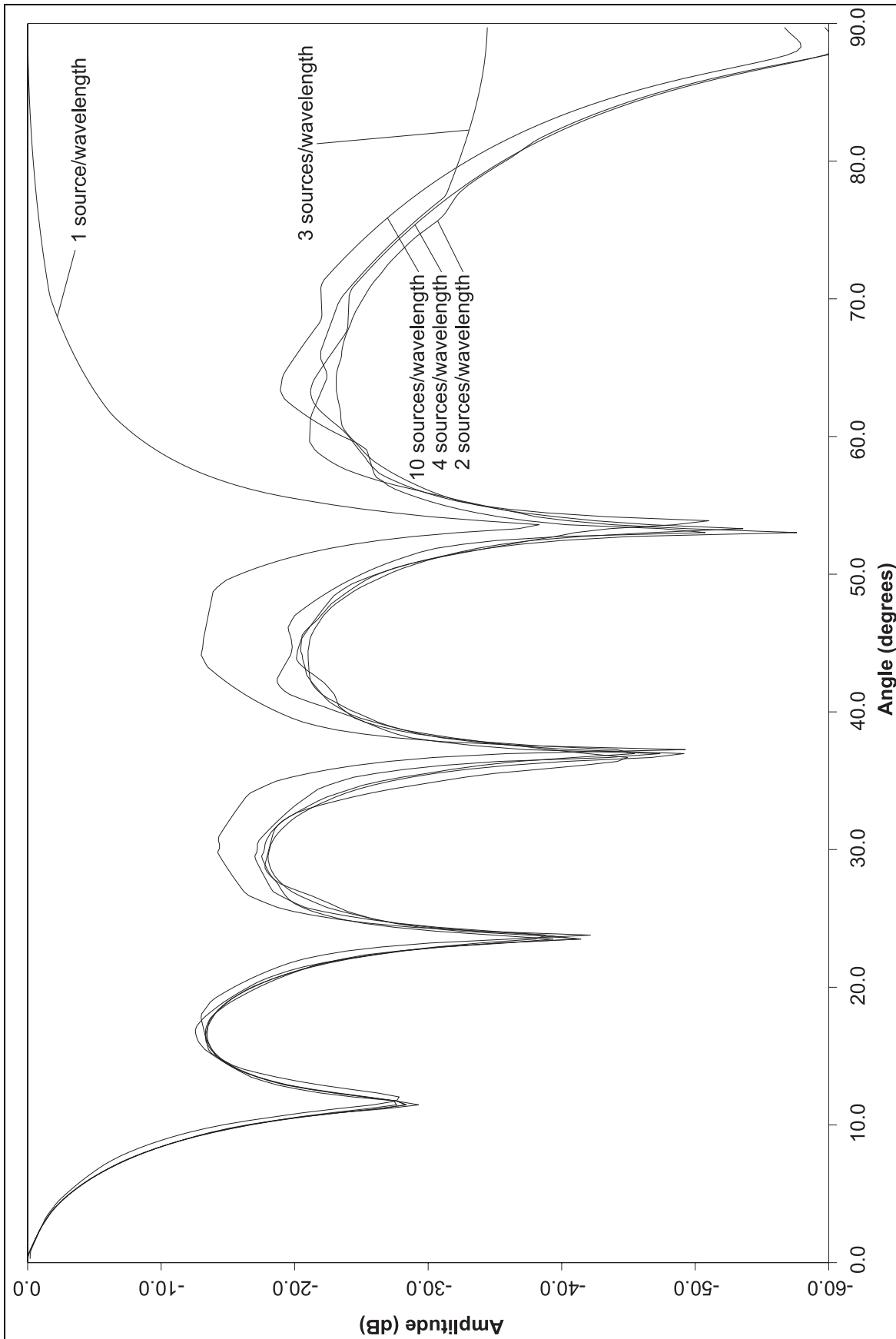


Figure 5.12 Angular sections at a distance of  $100 \lambda$  through the acoustic fields in figure 5.11.

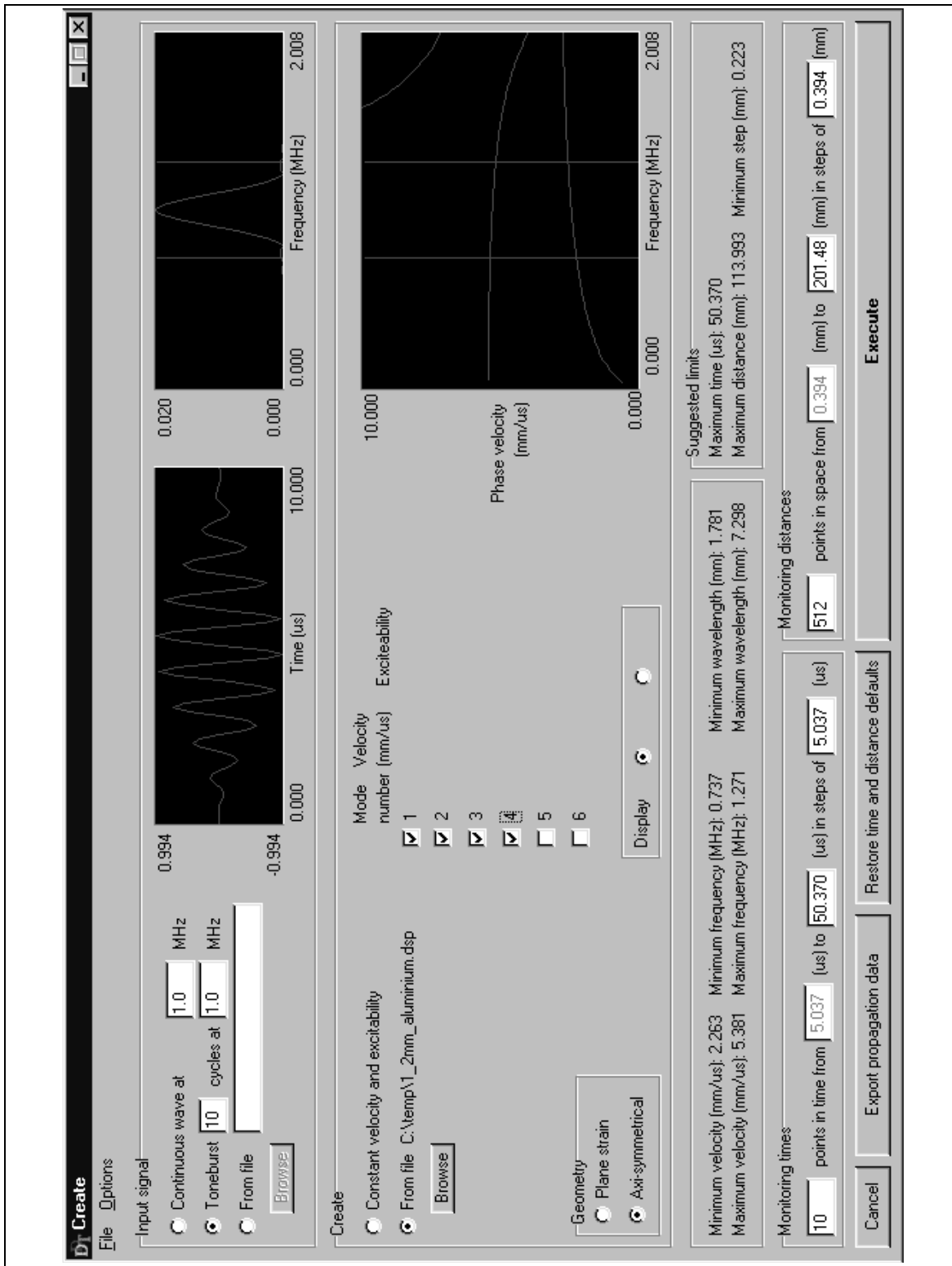


Figure 5.13 Screen shot of the input screen for the software written to calculate displacement-distance-time matrices.

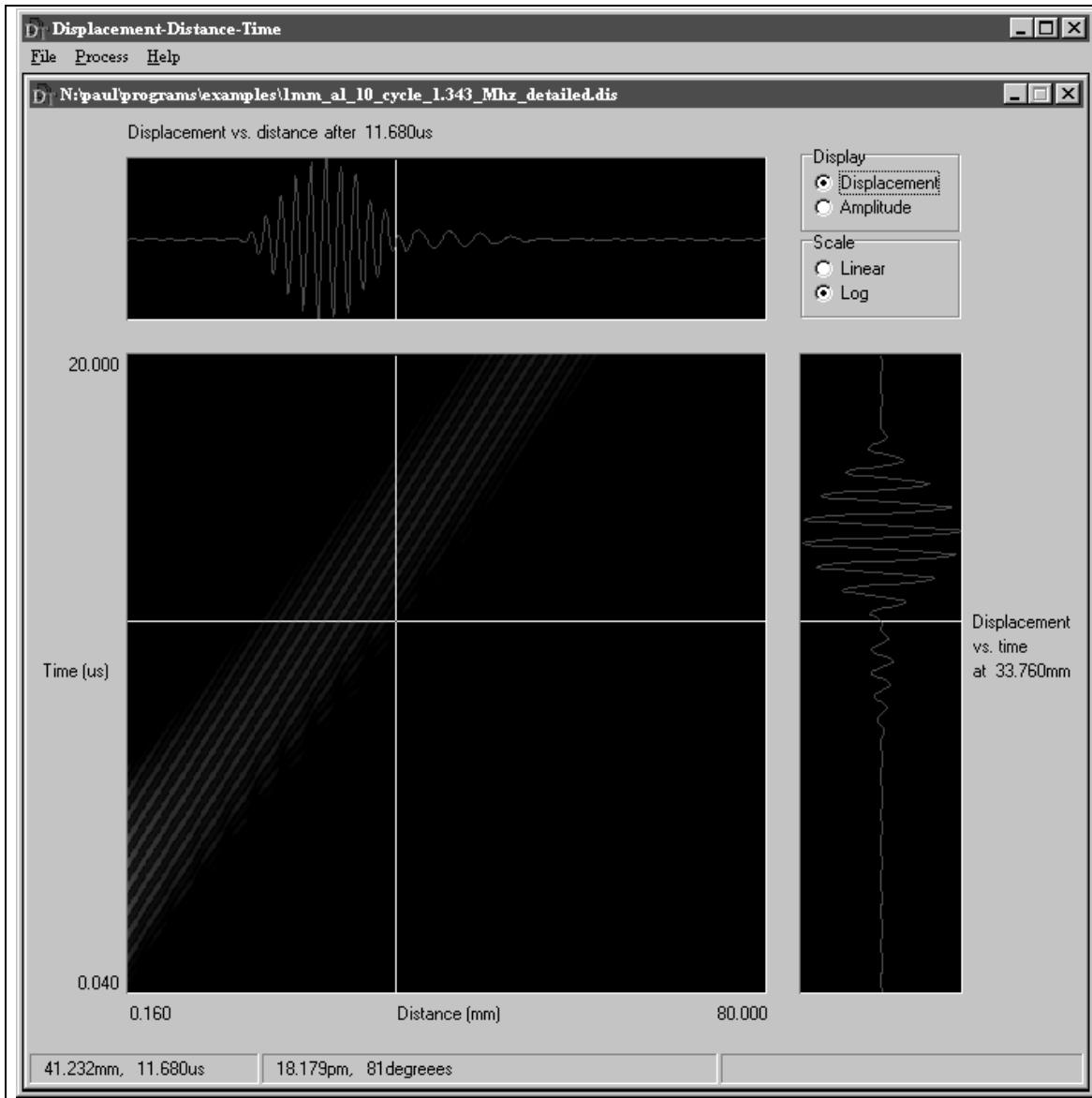


Figure 5.14 Screen shot of the output screen for the software written to calculate displacement-distance-time matrices.

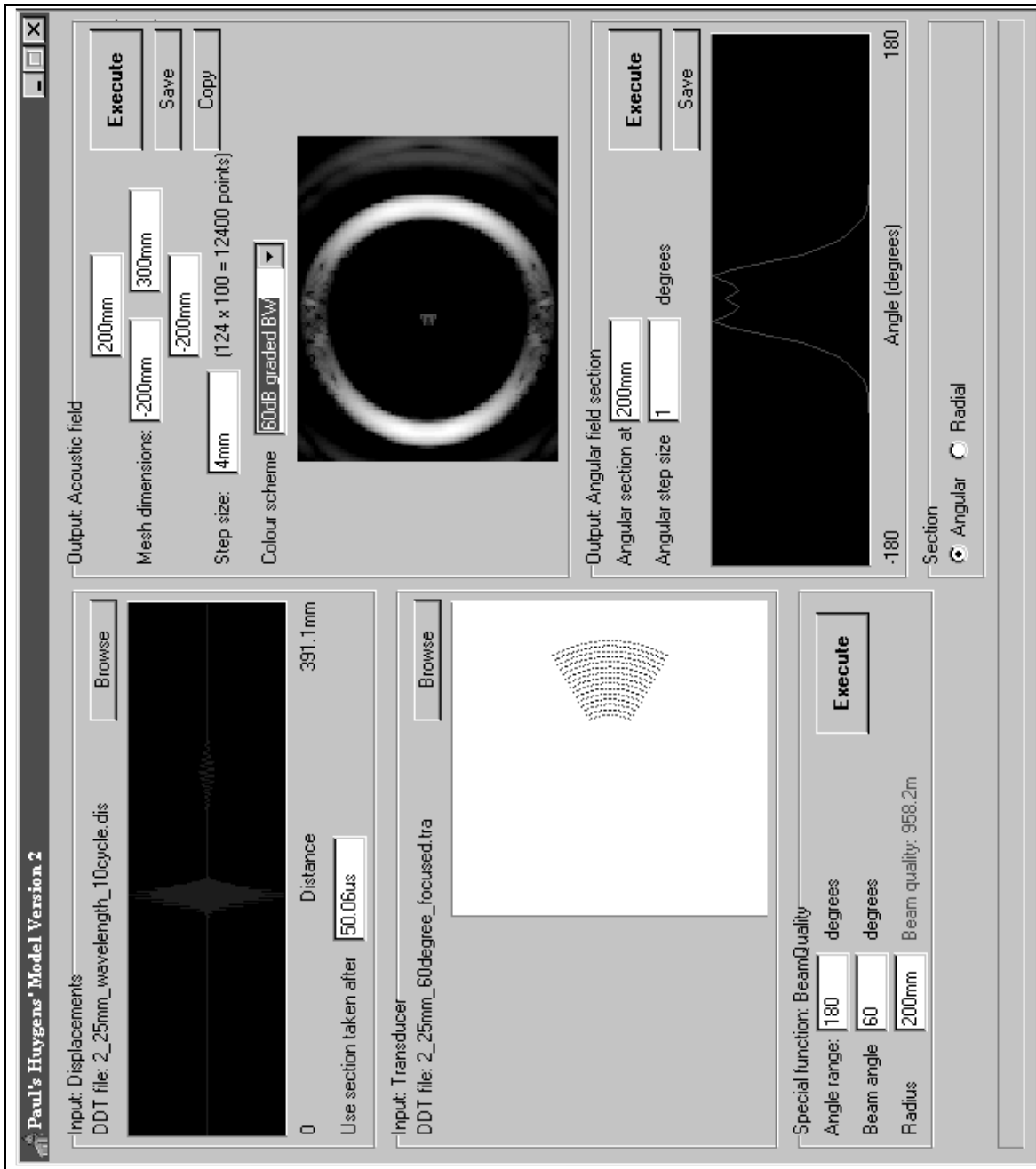


Figure 5.15 Screen shot of the software written to perform the Huygens' calculations.

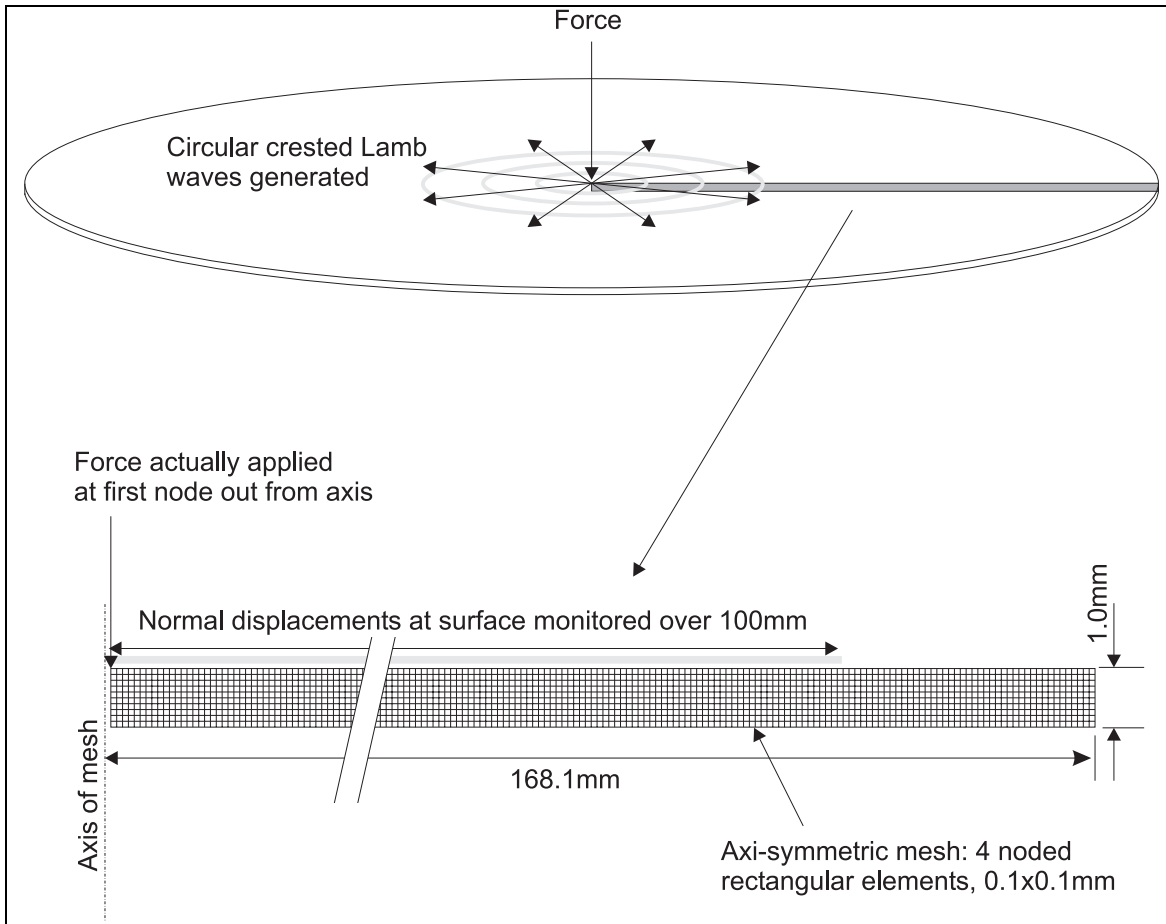


Figure 5.16 Geometry of the FE model used to validate analytic predictions of the acoustic field due to a point source.

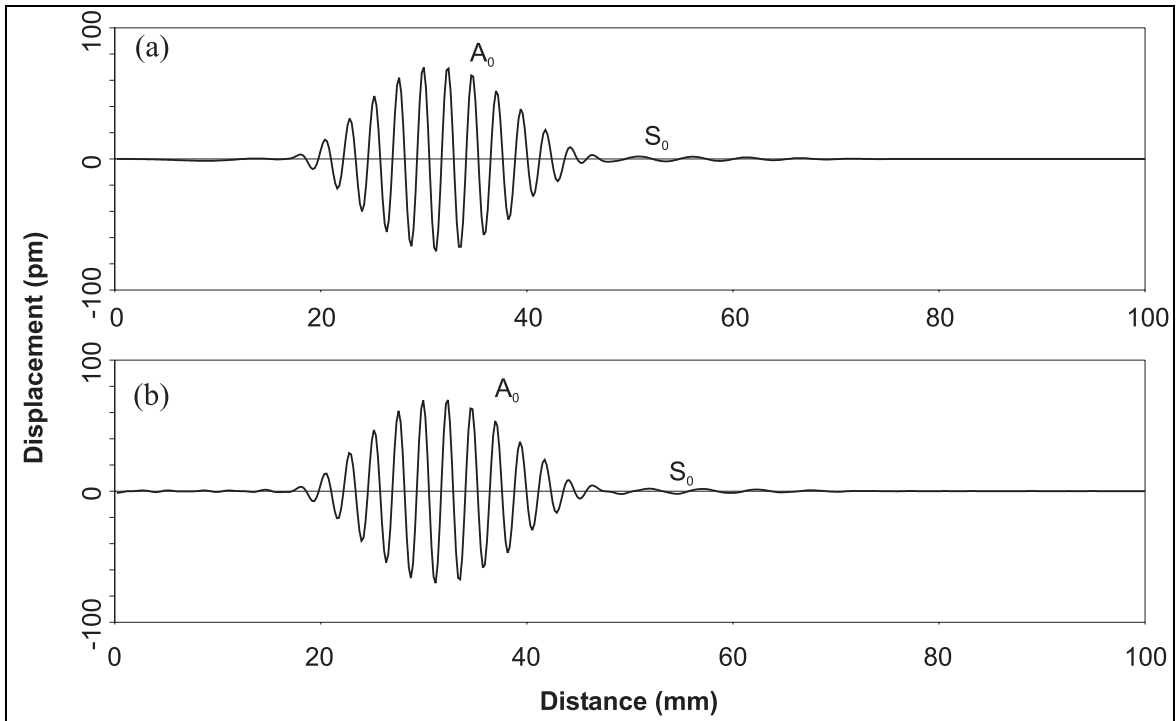


Figure 5.17 Out-of-plane surface displacement vs. distance for a 1.0 mm thick steel plate 15  $\mu$ s after excitation with a 10 cycle toneburst at 1.0 MHz predicted by (a) analytic and (b) FE model.

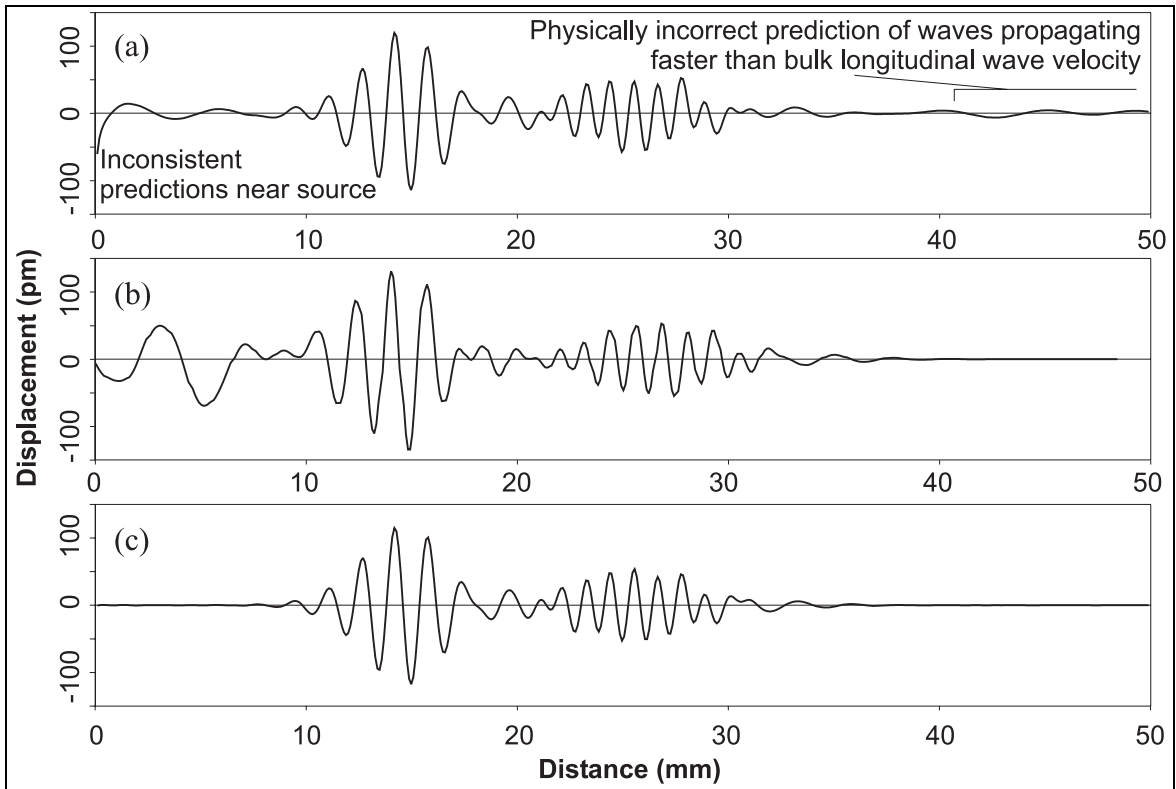


Figure 5.18 Out-of-plane surface displacement vs. distance for a 1.0 mm thick steel plate 10  $\mu$ s after excitation with a 10 cycle toneburst at 2.5 MHz predicted by (a) analytic and (b) FE models. (c) Shows the results from analytic model, but ignoring modes with phase velocities exceeding 10 mm/ $\mu$ s.

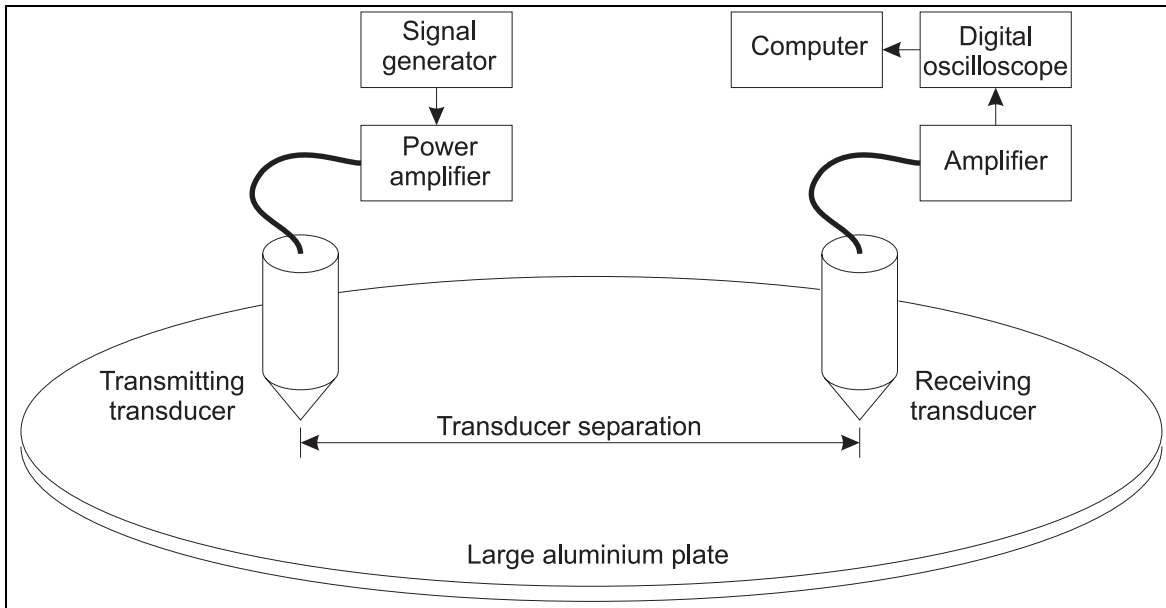


Figure 5.19 Experimental set-up for measuring displacement-time curves.

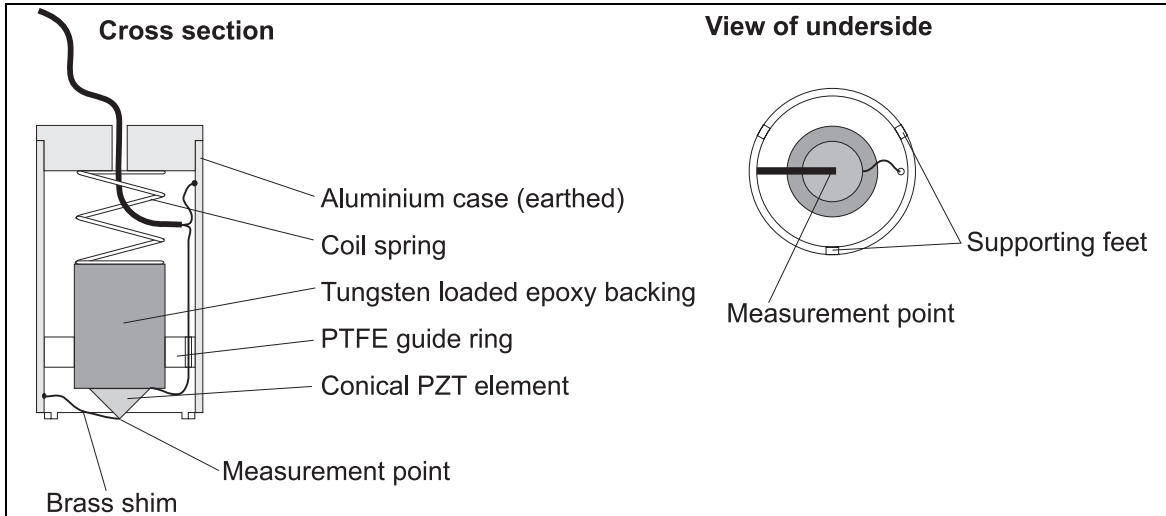


Figure 5.20 Schematic diagram showing the construction of conical point contact transducers used for making surface displacement measurements, after Evans (1997).

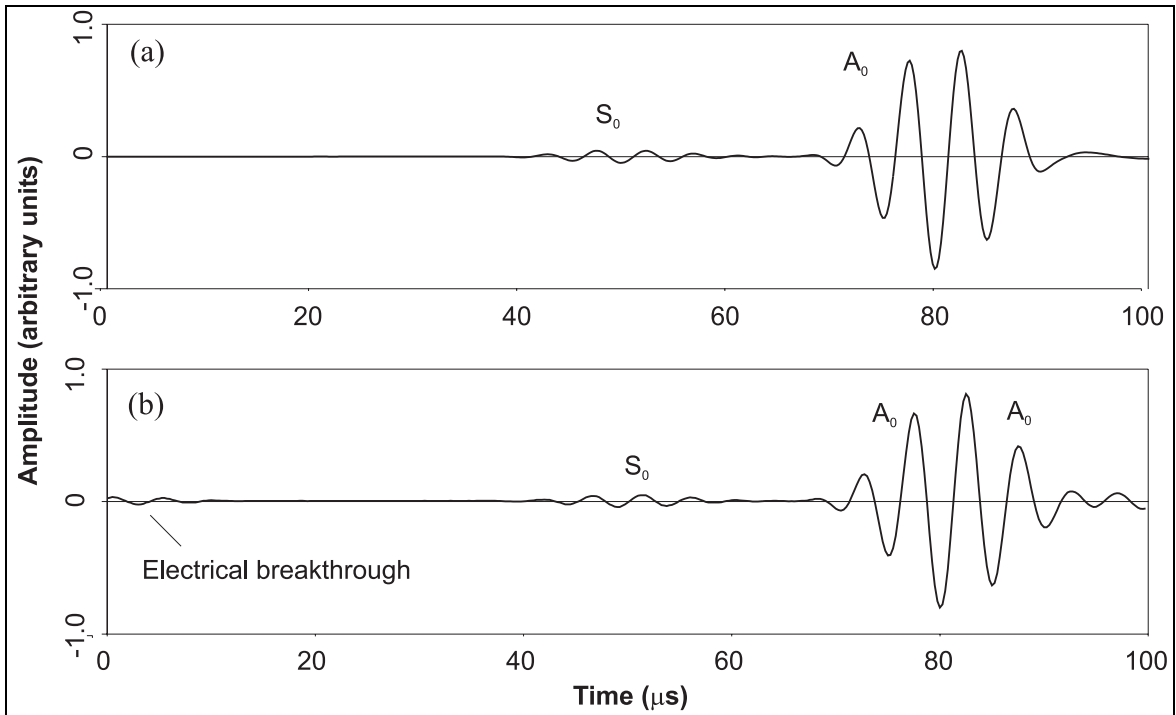


Figure 5.21 Time-traces (a) predicted using the analytic model and (b) measured experimentally when a 5 mm thick aluminium plate was excited with a 5 cycle toneburst at 0.2 MHz, 250 mm away from the monitoring point.

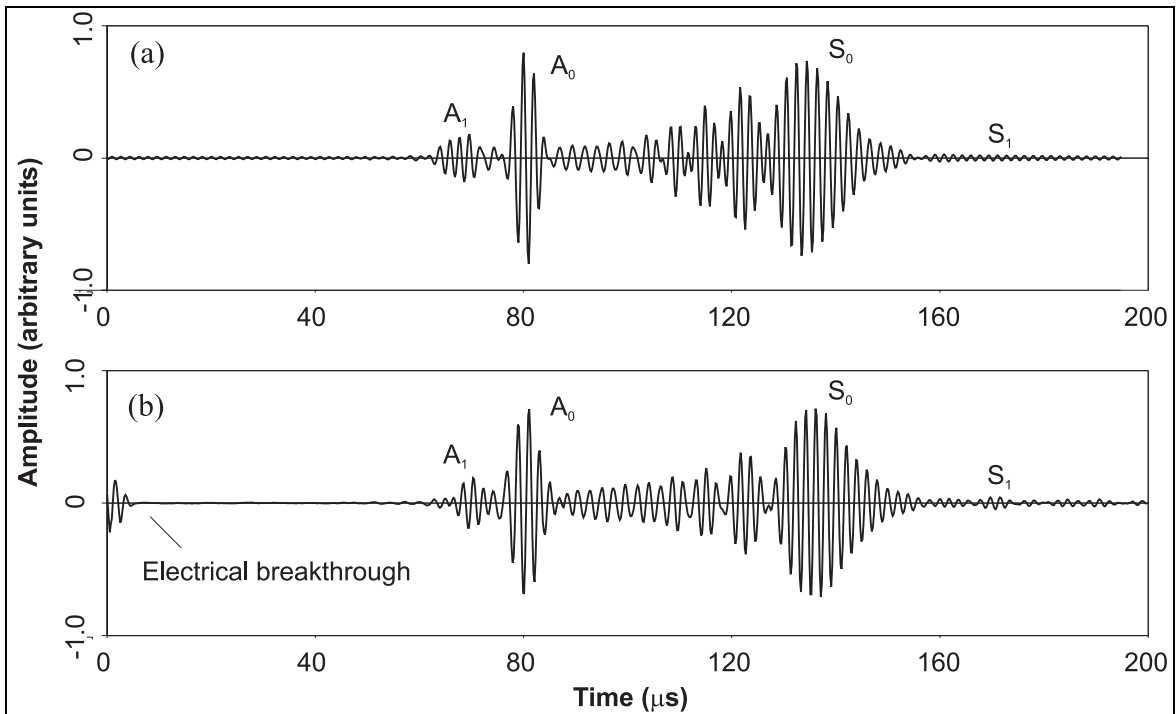


Figure 5.22 Time-traces (a) predicted using the analytic model and (b) measured experimentally when a 5 mm thick aluminium plate was excited with a 5 cycle toneburst at 0.5 MHz, 250 mm away from the monitoring point.

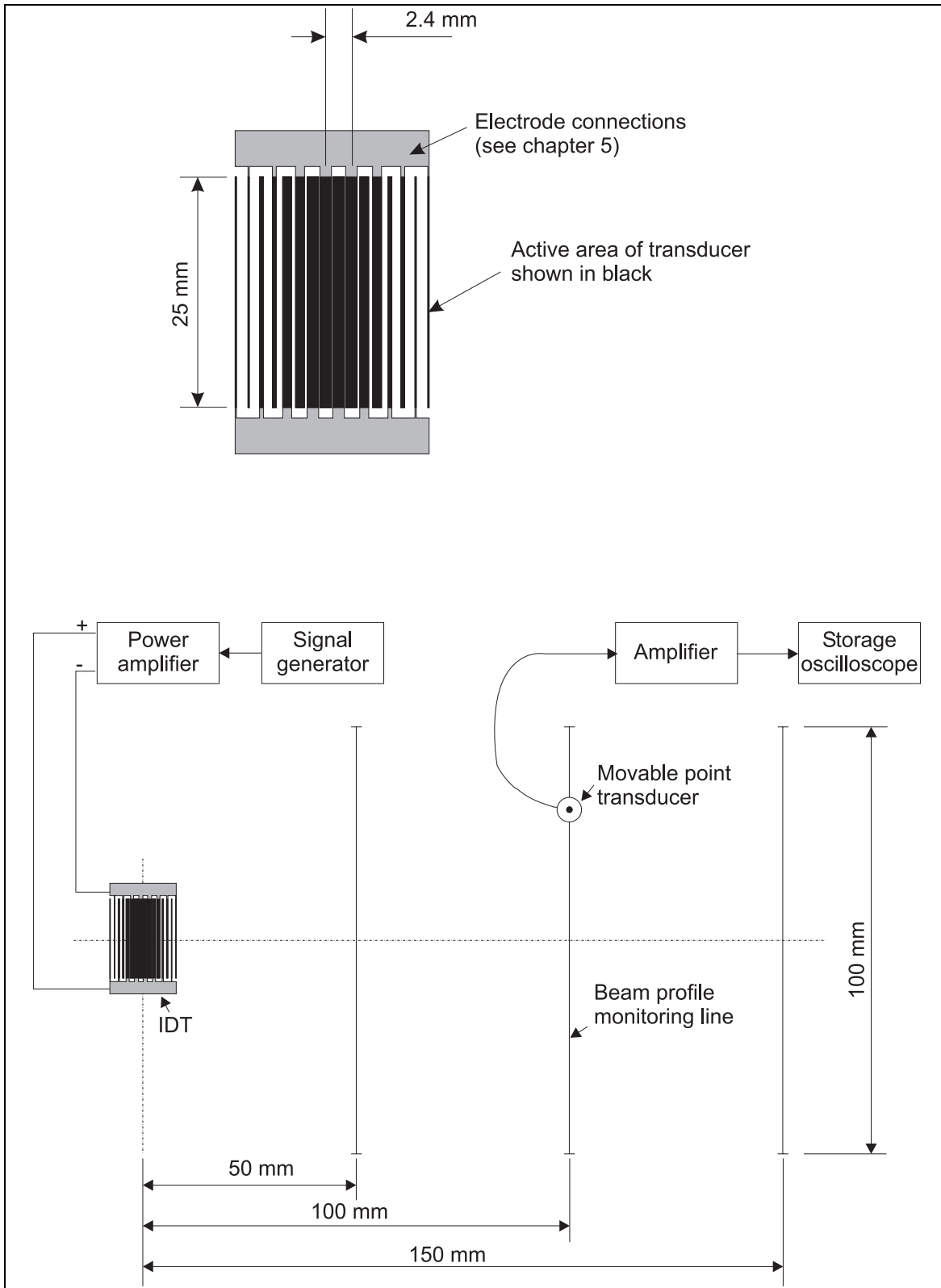


Figure 5.23 Geometry of transducer used in validation, and experimental set-up.

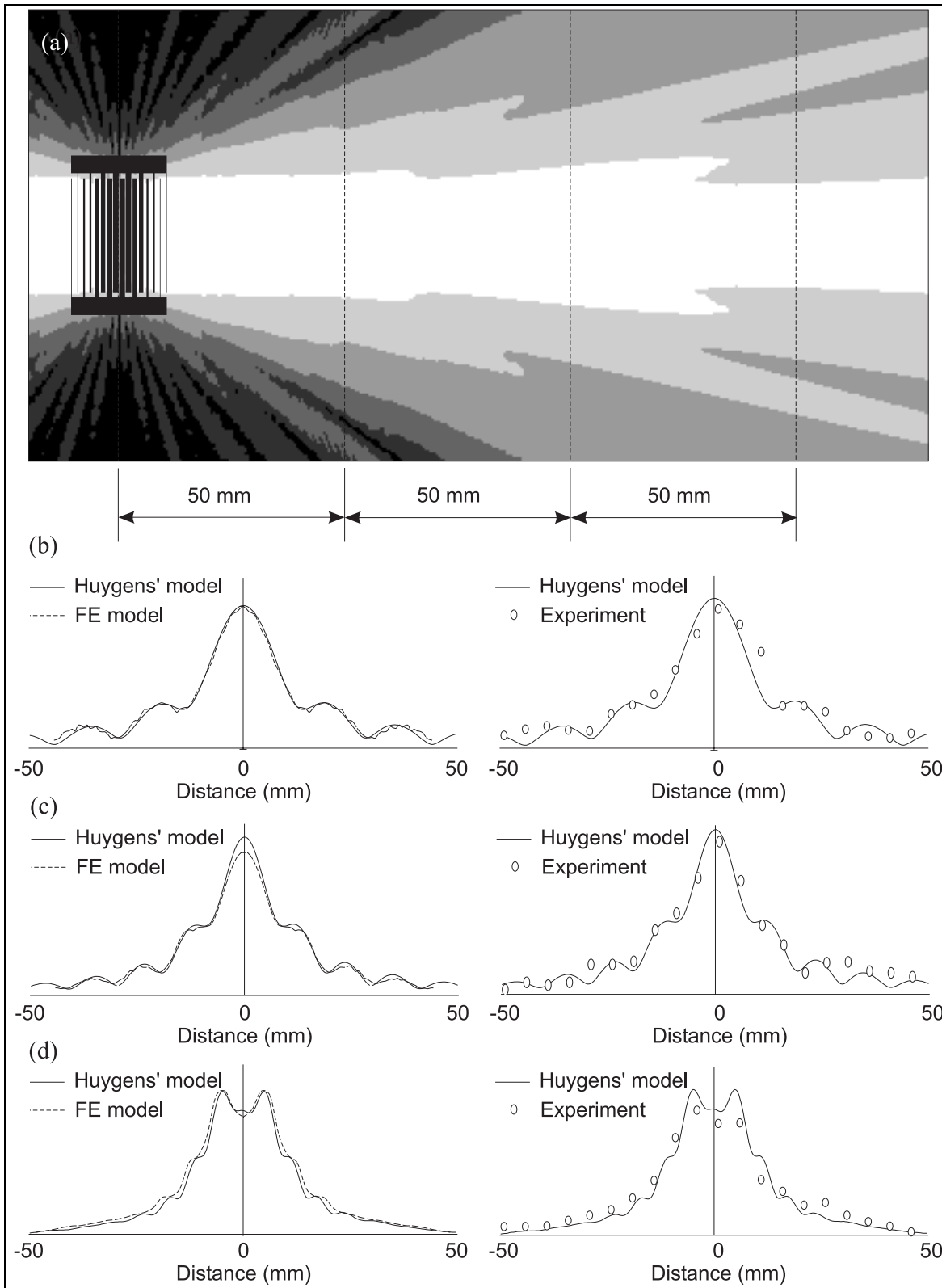


Figure 5.24 (a) Acoustic field predicted by the Huygens' model. Comparison of field cross sections at (b) 50 mm, (c) 100 mm and (d) 150 mm between Huygens' model, experimental point measurements and FE model.

## 6. Low frequency inter-digital transducers

---

### 6.1 INTRODUCTION

This chapter contains three topics involving low frequency inter-digital transducers (IDTs) starting with a description of their development, design and construction in section 6.2. Because of their larger size and simpler construction compared to the high frequency IDTs described previously, low frequency IDTs make an ideal experimental tool for studying general aspects of IDT behaviour. An improved experimental method for measuring the acoustic field from an IDT has been developed and this is described in section 6.3. The use of this experimental technique in parallel with the Huygens' model to elucidate general guidelines for IDT design is discussed in section 6.4.

### 6.2 DESIGN AND TESTING OF LOW FREQUENCY INTER-DIGITAL TRANSDUCERS

Chapter 4 described the successful design, construction and testing of IDTs made from the piezoelectric polymer PVDF (polyvinylidene fluoride) operating in the 0.75-2.5 MHz range. Such IDTs were shown to work most satisfactorily when generating the  $A_0$  mode at a frequency-thickness of around 1.34 MHz mm. Although their use to transmit and receive certain higher order modes in a 6.5 mm thick structure was partially successful, the problems of modal selectivity and dispersion associated with using these modes would preclude their use in most practical long range testing applications. In order to operate PVDF IDTs on thicker structures using lower order modes, the lower limit of their operating frequency must be reduced. A typical operating frequency to aim for is around 100 kHz, which is around ten times lower than the high frequency IDTs described in chapter 4, and would thus enable the inspection of structures up to around 13 mm thick.

In this section, the fundamental construction of PVDF IDTs is re-assessed from the perspective of the one-dimensional transducer model described in chapter 3. Studies will be presented which investigate how the operating frequency may be reduced, and the construction and testing of monolithic transducers will be described. The results of these experimental tests do not agree particularly well with the one-dimensional model predictions, due to reasonable sized low frequency transducers failing to satisfy the required assumptions. However, initial tests of low frequency IDTs of a similar construction on 12.65 mm thick aluminium bar will show that the transducers successfully transmit and receive the  $A_0$  mode at around 100 kHz. This section concludes with a description of the most sophisticated IDT fabricated thus far, which incorporates several of the features which have been discussed. This curved finger low frequency IDT uses a quadrature drive system to produce a divergent acoustic field on one side of the transducer only. An IDT of this type could potentially be used to inspect a  $90^\circ$  sector of a structure.

#### 6.2.1 *Initial considerations using one-dimensional model*

The basic construction of the high frequency IDTs described in chapter 4 consisted of a  $110\ \mu\text{m}$  thick layer of PVDF backed by a  $125\ \mu\text{m}$  thick layer of copper and these

transducers were shown to operate most successfully at frequencies around 1 MHz. In order to gain a greater insight into the frequency behaviour of a layered transducer system, it is instructive at first to consider a simpler model than the complete one-dimensional model.

*Mass-spring model of the mechanical system*

At low frequencies, where the wavelength of bulk waves in the backing layer is long compared to its thickness, the transducer may be regarded as a mass-spring system for the purpose of understanding its frequency response characteristics. In this model, the copper layer is the mass, and the PVDF is a light spring connecting the copper to a substrate (the aluminium) which is assumed to be rigid. In reality the aluminium is not rigid, but its stiffness is sufficiently high compared to the combined stiffness of the PVDF and copper layers for it to make little difference to the resonant frequency of the complete system.

Considering a unit area of the system, the spring stiffness,  $k_{PZ}$  (i.e. the stiffness of the PVDF layer or layers), is calculated as:

$$k_{PZ} = \frac{c_{zz}}{d_{PZ}} = \frac{Z_{PZ}^2}{d_{PZ}\rho_{PZ}} \quad (6.1)$$

where  $c_{zz}$  is the material stiffness of the PVDF in the thickness direction,  $d_{PZ}$  is its thickness,  $\rho_{PZ}$  is its density and  $Z_{PZ}$  is its characteristic acoustic impedance. The mass,  $m_{Cu}$  (i.e. the mass of the copper layer) per unit area, is given by:

$$m_{Cu} = \rho_{Cu}d_{Cu} \quad (6.2)$$

where  $\rho_{Cu}$  is the density and  $d_{Cu}$  is the thickness of the copper layer. The resonant frequency of the mass-spring system may be easily calculated to be:

$$f = \frac{1}{2\pi} \sqrt{\frac{k_{PZ}}{m_{Cu}}} = \frac{Z_{PZ}}{2\pi} \sqrt{\frac{1}{d_{PZ}d_{Cu}\rho_{PZ}\rho_{Cu}}} \quad (6.3)$$

For the case of 110  $\mu\text{m}$  thick layer of PVDF backed with a 125  $\mu\text{m}$  thick layer of copper, the resonant frequency may be calculated using this method to be 1.38 MHz. The complete one-dimensional model predicts that the first peak in pulse-echo response will occur at around 1.5 MHz. For the purposes of this argument, this small discrepancy may be ignored.

Equation 6.3 indicates three options to reduce the resonant frequency of the mass-spring system and therefore, hopefully, to improve the low frequency response of the actual transducer system. The options are either to increase the mass,  $m_{Cu}$ , decrease the stiffness,  $k_{PZ}$ , or both.

From equation 6.3, it can be seen that the mass of the backing layer needs to be increased by a factor of 100 in order to reduce the resonant frequency by a factor of 10. Increasing the mass could be achieved either by increasing the density or the thickness of the backing layer. There is obviously no possibility of finding a material 100 times denser than copper, and increasing the thickness of the backing layer by a factor of 100 would result in a backing layer 12.5 mm thick which is undesirable for a low profile transducer.

Similarly, it can be seen from equation 6.3, that the stiffness of the spring also needs to be reduced by a factor of 100 in order to reduce the resonant frequency by a factor of 10. Clearly the material stiffness of PVDF could not be altered sufficiently to achieve this. Increasing the thickness of the PVDF by a factor of 100 would cause a proportionate decrease in the resonant frequency of the mass-spring system. Unfortunately, this would require an 11 mm thick layer of PVDF, which is not readily obtainable and again would make the transducer very thick.

The third option, which is perhaps the most intuitively obvious, is to increase the thickness of both layers, thereby simultaneously decreasing the spring stiffness and increasing the mass. In this case, only a factor of 10 increase in the thickness of both layers is required in order to obtain a factor of 10 decrease in the resonant frequency. This would require a 1.1 mm thick layer of PVDF and a 1.25 mm thick layer of copper to give a total transducer thickness of 2.35 mm, which is a more reasonable dimension than that suggested by the first two options.

Thus, in principle, this is an ideal way to proceed, as the thickness of plates which can be inspected will also increase in proportion to the thickness dimension of the transducer. Unfortunately, a supplier of 1.1 mm thick poled PVDF was not located. Hence the first idea considered was to use two passive 0.5 mm thick layers of un-poled PVDF on either side of the active poled 110  $\mu\text{m}$  thick PVDF in order to obtain the required thickness.

### *Passive layers design*

In figure 6.1, the complete one-dimensional model has been used to compare the response of two systems: the first being a 1.1 mm thick layer of active PVDF backed with a 1.25 mm thick layer of copper. The second system is identical to the first except that the single layer of PVDF has been replaced by a 0.1 mm thick layer of active PVDF sandwiched between two layers of passive 0.5 mm thick PVDF. In the model, the passive PVDF layers are treated in the same manner as other non-piezoelectric layers and are assigned the same mechanical properties as the active PVDF. It can be seen from the figure that the pulse-echo responses of the two systems are almost identical, in terms of both frequency and amplitude. The similarity in frequency response would be expected from the mass-spring model, but the similarity in amplitude is somewhat surprising. A partial and somewhat simplified explanation for this similarity in amplitude can be obtained by considering piezoelectric film suspended in free space, and observing that for a given applied voltage, the electric field strength in a thin piezoelectric film will be greater than in a thicker film. This increases the amount of piezoelectric induced strain in thinner film, but the net change in displacement between the edges of thick and thin films will be similar since the displacement is obtained by integrating the strain over the thickness. However, a thicker active piezoelectric layer does have the advantage that it can be driven with a higher voltage before electrical breakdown occurs, and hence the maximum output is potentially higher than for a thinner layer.

### *Single layer design*

While performing the experimental tests on monolithic transducers which will be described shortly, a simpler transducer design was observed to produce a similar amplitude of response at low frequencies to the passive layers design. In this design, the

passive layers were simply omitted. The only difference between this design and the design of the transducers in chapter 4 is a tenfold increase in the mass per unit area of the backing layer. From the mass-spring model, this would only be expected to produce a  $\sqrt{10}$  decrease in the resonant frequency of the system. However, the mass-spring model does not predict the amplitude of the transducer response but the one-dimensional model does do so. The predicted pulse-echo response of transducers with and without the passive layers is shown in figure 6.2. It can be seen that although the device without passive layers does have a resonance at higher frequency, its response is nonetheless of reasonable amplitude around the resonant frequency of the passive layered device.

### 6.2.2 *Initial experimental tests using bulk wave transducers*

The two designs described above were investigated by constructing monolithic bulk wave transducers and testing them in a similar manner to that already discussed in section 4.3.2. Only sample results are presented in this section, as these tests were not particularly conclusive and ultimately it was decided that a better test of the theory would be to construct inter-digital transducers.

The reasons for the inconclusive nature of the experimental results from bulk wave transducers mostly stem from problems of scaling up the experiments described in section 4.3.2. Ideally, the planar dimensions of a bulk wave transducer to operate at low frequencies should be around 300 mm (i.e. ten times larger than those used for the transducers in section 4.3.2), which would be a somewhat wasteful use of PVDF. Instead, similar sized transducers to those used in section 4.3.2 were again used. This leads to several problems. Firstly, it becomes increasingly hard to resolve different echoes in the received time-traces, even when using an aluminium substrate approximately 100 mm thick. Secondly, the ratio of the transducer size to the wavelength of the waves transmitted into the substrate begins to decrease significantly as the frequency is reduced. This effect causes increased beam spreading and is manifested as an apparent roll-off in the measured low frequency response, which of course is the frequency range of interest.

In these experiments, various materials for the passive layers were investigated including 0.5 mm thick un-poled PVDF (supplied by Goodfellow, UK) and 0.4 mm thick plastic shim (supplied by RS, UK). As would be expected, within reason the exact choice and thickness of material had little if any effect on results. 1.3 mm thick lead sheet (supplied by a builder's merchant as roofing lead flashing) was used as the backing material, as it is less expensive and more dense than copper.

An example graph showing the experimentally measured pulse-echo response of a passive layers design transducer with and without lead backing is shown in figure 6.3. The effect of the lead layer appears to provide an extra peak in the response at around 125 kHz, which is in reasonable agreement with the resonant frequency predicted using the mass-spring model of 118 kHz. The low frequency roll-off which was mentioned above is apparent, and the curves in the graph also exhibit smaller fluctuations. The latter can be reasonably attributed to both the effect of resonances across the width of the PVDF and the effect of overlapping signals in the time domain.

As would be expected, the effect of the bond layer thickness is not significant at low frequencies, and it was observed experimentally that equally good results could be

obtained by using double sided adhesive tape (supplied by RS, UK) instead of cyanoacrylate adhesive to bond the transducer layers together.

### 6.2.3 Initial experimental tests using inter-digital transducers

The bulk wave transducer designs with and without passive layers were both used as the basis for trial low frequency IDTs to generate the  $A_0$  mode in thick aluminium bar.

#### *Transducer construction*

A 12.65 mm thick rectangular section aluminium bar was obtained. In this thickness of material, the frequency thickness of 1.343 MHz mm occurs at a frequency of 106 kHz and a wavelength of 23.1 mm on the  $A_0$  mode. For wavelengths as large as this, the IDT finger pattern can be cut out by hand from a sheet of PVDF using a sharp knife or scissors. The finger patterns for a two phase 4 finger IDT are shown in figure 6.4(a). The two sets of fingers are cut from the PVDF in such a way that one set must be reversed (i.e. the PVDF sheet must be turned upside down) for the IDT to be assembled as indicated in figure 6.4(b). This means that the IDT can actually be driven from a single phase supply, and still have the substrate earthed since the anti-phasing is achieved by the opposite poling orientation of the two sets of fingers.

In the passive layers device (which will be referred to as  $T_1$ ), the passive layers were cut from 0.5 mm thick un-poled PVDF and the lead backing was cut from 1.3 mm thick lead sheet. The transducer was assembled as shown in figure 6.4(c) using double sided adhesive tape to bond the layers together. The construction of the single layer device (referred to as  $T_2$ ) was identical except for the omission of the passive layers. In both these designs, it would be reasonable to be concerned about flexural resonances being set up across the width of the monolithic backing layer. However, no such effects have been observed experimentally, and this is thought to be due to the high internal losses of lead which damp out any ringing. It should be noted that these losses within the lead should not significantly affect the output of the transducer, since in the thickness direction the lead is essentially moving as a rigid mass.

#### *Experimental set-up*

The transducers,  $T_1$  and  $T_2$  were bonded to the aluminium bar as shown in figure 6.5, using double sided adhesive tape. The operating frequency was sufficiently low to enable an existing switching device (a custom device built for another project) to be used, and the IDTs tested in pulse-echo mode. The operating frequency was adjusted to maximise the amplitude of the signal from the first end reflection. By this stage in the project, a second custom device referred to as a 'Wavemaker' had been specified and commissioned. The Wavemaker fulfils the roles taken by the arbitrary function generator, controlling computer and power amplifier in the experiments described previously. The wavemaker provides a high voltage (200 V p-p) output of various sizes of Hanning windowed toneburst (5, 10, 20 and 50 cycles) over a continuously variable range of frequencies from 50 kHz to 3.5 MHz.

The electrical connections to the PVDF film were made using specially constructed 'crocodile' clips, with one of the two electrically separated jaws wired to the core (live)

and the other to the shield (earth) of the connecting coaxial cable. This alleviated the need to make the connections with silver loaded epoxy (as used for the transducers in chapter 3).

### *Results and comments*

The received time-trace when  $T_1$  was operated in pulse-echo mode at 94 kHz is shown in figure 6.6(a). The arrivals can be correlated to different lengths of paths in the beam as indicated by the labels in figure 6.5. The first arrival corresponds to a reflection from the near end,  $E_1$ , of the bar. The second smaller arrival corresponds to a double echo between  $T_1$  and the near end of the bar,  $E_1$ . The next arrival is a reflection from  $T_2$  and the third reflection is from the further end,  $E_2$ , of the bar. After this, the reflections become too numerous to identify accurately.

It is interesting to observe the effect of connecting either of the two sets of fingers individually as shown in figures 6.6(b) and (c). The time-traces obtained in both cases are almost identical in shape and approximately half the amplitude of that shown in figures 6.6(a).

The same procedure was used to test  $T_2$  and the corresponding results are shown in figure 6.7 - note the different vertical scales to the previous figure. Again the optimum operating frequency was found to be 94 kHz. The first point to observe is that the amplitude of the first arrival is almost twice (i.e. 6 dB greater than) the amplitude of the first arrival observed with  $T_1$ . In neither case is the first arrival affected by the presence of the other transducer, hence it can be concluded that the frequency response of  $T_2$  is around 3 dB (since the difference in amplitude of 6 dB was measured in pulse-echo mode) greater than  $T_1$  at this frequency. Next the ratio of the amplitude of the third arrival (the reflection from the second IDT) to that of the first arrival (the reflection from the near end of the bar) should be compared to the corresponding ratio when  $T_1$  was tested. It is clear that  $T_2$  is a bigger reflector than  $T_1$  which suggests that  $T_2$  has a greater perturbation effect on the waves in the bar than  $T_1$ .

The effect of connecting either of the two sets of fingers individually is shown in figure 6.7(b) and (c). In this case, the time-traces are markedly different. In particular, the reflection from the near end of the bar (first arrival) is mostly in the signal from the set of fingers shown in (c), whereas the reflection from the second end of the bar is mostly in the signal from the other set of fingers shown in (b). Investigation has shown that, unsurprisingly, the signal shown in (c) is from the set of fingers which are nearer to the near end of the bar and that in (b) is from the set of fingers nearer to the far end of the bar. This 'directionality' effect was not observed with  $T_1$ , which is again consistent with  $T_1$  perturbing the Lamb waves in the structure less than  $T_2$ .

It is interesting to note that the optimum experimental operating frequency is 94 kHz, somewhat lower than the predicted operating frequency of 106 kHz, and is the same for both IDTs. This observation will be discussed later in section 6.2.4.

It was hoped that at the low frequencies at which these IDTs operate, it would be possible to use gel to couple the transducers to the structure rather than a bonding agent. This possibility was investigated, but proved unsatisfactory for two reasons. Firstly, the gel was found to have significant electrical conductivity which precluded its use with the

single layer device, as the two sets of fingers were shorted out. Even when used with the passive layers device, in which the lower passive layer acted as an insulator, the coupling was found to be very poor unless weights were used to apply a significant downwards pressure to the transducer. This was not a satisfactory approach, as the weights affect the backing and frequency response characteristics of the IDT.

### *Conclusion*

Due to its simpler construction and greater sensitivity, it was decided that the single layer design of  $T_2$  was superior and this design was used as the basis for several more prototype low-frequency IDTs, the most complex of which is described below.

#### **6.2.4 Example of a four phase IDT**

The final example of a low frequency IDT which is described in this section, embodies many of the concepts previously discussed. It was designed to produce a uniformly divergent beam over a  $90^\circ$  sector of plate on one side of the transducer only. This effect was achieved by using a four phase supply as will be described below.

### *Design*

To suit the availability of materials, the transducer was again designed to operate on 5 mm thick aluminium plate. In this plate, the wavelength of the  $A_0$  mode at its least dispersive point at 269 kHz (a frequency thickness of 1.343 MHz mm) is 10 mm. However, to drive an IDT from a four phase supply, requires the IDT to have four fingers per wavelength, which at this frequency would mean that the fingers would have to be less than 2.5 mm wide. Instead, it was decided to operate at a lower frequency of 91 kHz and longer wavelength of 20 mm. Although, this frequency is below the frequency of least dispersion, the dispersivity is still reasonably low as noted in chapter 2.

With a wavelength of 20 mm, the size of the IDT could easily become very large without careful design. The number of fingers was limited to eight due to the physical difficulty of constructing a four phase transducer. Several iterations using Huygens' model yielded a reasonably compact eight finger design which was predicted to produce a fairly uniform uni-directional field over a  $90^\circ$  sector in front of the IDT. The geometry used is shown in figure 6.8. The acoustic field predicted by Huygens' model and the angular cross section through it at a radius of 150 mm are shown in figure 6.9. It can be seen that the predicted ratio of the amplitude of the field in front of the IDT to that behind is of the order of 20:1 (~25 dB).

### *Construction*

The construction of the four phase IDT required considerable care. The eight fingers were cut from a single PVDF sheet in pairs, the fingers in each pair being driven in phase in the final IDT. For convenience the original PVDF sheet will be referred to as having an anode side and a cathode side, and the final IDT as having a topside and an underside, the underside being that bonded to the plate. The pairs of fingers driven at  $0^\circ$  and  $180^\circ$  were cut so that, when the IDT was assembled, one pair was anode side up and the second pair was cathode side up as shown in figure 6.10(a). A similar arrangement was made for the

pairs of fingers at  $90^\circ$  and  $270^\circ$ . The fingers at  $0^\circ$  and  $180^\circ$  both had their undersides connected to the earth and their topsides to the output of a single ended power amplifier as shown in figure 6.10(b), the anti-phasing between the two pairs of fingers again arising by virtue of their opposing poling directions. The fingers at  $90^\circ$  and  $270^\circ$  were connected in a similar manner to the single-ended output of a second power amplifier. The first power amplifier was then driven with a toneburst at the desired centre frequency and the second power amplifier was driven with a  $90^\circ$  phase shifted copy of the signal to the first amplifier. The transducer was assembled *in-situ* on a 5 mm thick aluminium plate as shown in figure 6.10(c), the bond to the plate being made with double sided adhesive tape. Finally, after confirming that there were no short circuits between the fingers, a 1.3 mm thick lead plate was bonded onto the back of the IDT, again using double sided adhesive tape.

### *Experimental optimisation of four phase drive*

There are four parameters in the drive of the IDT which can be varied: the centre frequency of the excitation, the output level of either power amplifier and the exact phase difference between the signals supplied to the two power amplifiers. Finding the optimal driving conditions for the IDT was achieved by simultaneously monitoring the signals measured by two conical point transducers of the type described in chapter 4, one of which is located in front of the IDT at the point P in figure 6.10(c) and the other at point Q behind the IDT. At the ideal driving condition, the ratio of the amplitude of the signal at P to that received at Q should be a maximum. The associated time-traces measured at the design frequency of 91 kHz at the points P, Q and a third point R to the side of the IDT are shown in figure 6.11.

It is apparent from the figure that the degree of uni-directionality which the transducer achieved at this frequency was poor. However, further experimentation revealed that at the considerably lower frequency of 65 kHz, much better uni-directionality was achieved. The corresponding time-traces received at this frequency are shown in figure 6.12.

Initially, this was thought to be because the wavelength had been incorrectly calculated from the dispersion curves shown in figure 6.13, but a measurement of the phase velocity using two conical point contact transducers revealed the wavelength in the plate to be almost exactly 20 mm at 91 kHz as was expected. However, the thickness and mass of the lead in IDTs of this type is significant and may perturb the wavelength. If the dispersion curves are re-calculated for the case of a 5 mm thick layer of aluminium in perfect contact with a 1.3 mm thick layer of lead as shown in figure 6.13, the wavelength of the  $A_0$  mode (or to be more precise, the fundamental flexural mode in the layered system) at 91 kHz is 15.5 mm. This is significantly lower than the 20 mm which the spacing of the IDT fingers was designed for and hence demonstrates why the uni-directionality achieved at 91 kHz was so poor. However, at 65 kHz, the wavelength of the first flexural mode in the lead-aluminium system is almost exactly 20 mm, while in 5 mm thick aluminium plate alone the wavelength is 25 mm at this frequency, as can be seen in figure 6.13. When they reach the boundary of the IDT, the waves propagating as the flexural mode in the lead-aluminium system will be mode converted into the  $A_0$  mode in the aluminium plate. Although the efficiency of this mode conversion is thought to be reasonably high, it will not be unity. Some of the energy will be reflected back into the IDT as flexural mode

waves propagating in the opposite direction and other modes may be generated in both systems. This has not yet been investigated in detail.

This is a very interesting result, the consequences of which will be discussed below. For the purposes of measuring the acoustic field from the IDT, it was decided to operate at 65 kHz rather than 91 kHz.

### *Experimental measurement of acoustic field*

The experimental set-up is shown in figure 6.10(c). For measuring the acoustic field, the excitation was a 10 cycle toneburst at 65 kHz. The angular cross section was measured at 36 points around a circle of radius 155 mm, centred on the focal point of the transducer using the technique described in the previous chapter. The experimentally measured points are plotted on figure 6.9(b), and it can be seen that excellent agreement with the predicted cross section is obtained.

### *Comments*

The construction of this IDT marks a significant stage in the development of IDTs for monitoring large structures. A reasonably compact transducer has been built which can efficiently excite low frequency Lamb waves in thick aluminium plate. The use of a four phase drive to produce a divergent beam on one side of the transducer only has been shown to be effective. In principle this IDT could be used to monitor one 90° sector of structure.

The testing of this IDT has also exposed the limitations of Huygens' model when it is used to model transducers which cause a significant increase in the mass loading of a structure. This discrepancy between the design frequency (91 kHz) and the operating frequency (65 kHz) is definitely significant, but it was only observed because the acoustic field behind the IDT could not be satisfactorily minimised at 91 kHz. Had the IDT not been a uni-directional one, this situation would not have arisen and the IDT would probably have been operated at its design frequency. A similar effect is likely to have been the reason why a larger signal was also obtained at frequencies below the design frequency in the case of  $T_1$  and  $T_2$  described previously.

### **6.3 IMPROVED EXPERIMENTAL METHODS FOR MEASURING THE ACOUSTIC FIELD FROM INTER-DIGITAL TRANSDUCERS**

The large size of low frequency, large wavelength IDTs makes them an ideal experimental tool for investigating general effects of IDT geometry. To this end, it is necessary to measure the spatial variations in the acoustic field strength from an IDT at numerous locations. As described in chapter 5 this can be achieved by using a single conical point contact transducer and recording the maximum amplitude of the signal it receives when placed at various locations on a plate into which an IDT is transmitting Lamb waves. This technique for measuring the strength of a Lamb wave acoustic field will be referred to as **technique 1**.

The major problem in using point transducers to measure the acoustic field is that the coupling between the point transducer and the plate is not consistent and is very sensitive to numerous factors including the local surface condition of the plate and the exact

manner in which the transducer was placed. Furthermore, the coupling has been observed to exhibit a ‘creeping’ effect, whereby the coupling actually improves if the transducer is left in one location for extended periods. Typically, this might result in a doubling of the amplitude of the received signal over a period of around 30 minutes. **Technique 1** thus requires considerable skill and patience on the part of the operator and is not ideal for performing large numbers of measurements.

### 6.3.1 Methods which correct for coupling inconsistencies

From the previous paragraph it is clear that some means of measuring the coupling of the point transducer when it is placed at any location is necessary. A possible method which has been investigated (Evans 1997) is to modify the point transducer so that a second piezoelectric element is embedded in the transducer behind the backing material. This can be used to detect the shift in resonant frequency of the system when the transducer is coupled to a structure, and the magnitude of the shift can be used to estimate the degree of coupling. This technique was developed for applications where the absolute degree of coupling for the transducer must be measured.

However, for measuring the acoustic field from an IDT, only relative measurements of acoustic field strength are needed at various locations on the same structure. Hence, only the relative coupling as the point transducer is moved from one location to the next needs to be found and this can be achieved more directly by either of the two methods described below. In both cases, a series of measurements,  $M_1, M_2, \dots$  is obtained, which specify the relative strength of the acoustic field at different locations in the structure.

#### *Improved method - technique 2*

A second point transducer is placed at a fixed location to provide a reference signal of constant amplitude. The movable point transducer with which the IDT field will be mapped is placed at some location and the amplitude of the signal,  $B$ , from the reference transducer which the movable transducer receives is measured. From this the coupling,  $C$ , of the movable transducer is calculated from:

$$C \propto B\sqrt{d} \quad (6.4)$$

where  $d$  is the separation of the transducers. The constant of proportionality is dependent on the amplitude of the signal supplied to the reference transducer, the coupling of the reference transducer and the transduction process within the movable transducer, all of which are assumed to remain constant throughout the experiment. The square root of the distance between the reference and the measurement transducers must be included, as the amplitude of the signals generated by the reference transducer are circular crested Lamb waves and therefore decrease in amplitude with the square root of distance from the source, as discussed in the previous chapter.

A typical experimental layout is shown in figure 6.14. The details of the experimental procedure using this technique (**technique 2**) are outlined below:

**Technique 2**

1. The IDT under test is bonded at a suitable location on the plate which is usually taken as being at the origin  $(0,0)$  of a Cartesian coordinate system.
2. The reference point transducer is placed at a suitable location  $(x_r, y_r)$ .
3. The movable point transducer is moved to a measurement location  $(x_i, y_i)$ , and the separation  $d = \sqrt{(x_r^2 - x_i^2) + (y_r^2 - y_i^2)}$  calculated. The movable transducer remains connected to the receiving amplifier throughout the experiment.
4. The reference transducer is connected to the transmitting amplifier, from which it is excited with the same signal as will be used to excite the IDT (typically a 10 cycle toneburst at the required centre frequency).
5. The peak to peak amplitude of the first arrival of the  $A_0$  mode,  $B_1$ , at the movable transducer is measured, typically after 100-200 time averages. The coupling,  $C_1$ , of the movable transducer at this instant is calculated using equation 6.4.
6. The reference transducer is disconnected (but not moved), and the IDT under test is connected to the transmit amplifier.
7. The amplitude of the first arrival of the  $A_0$  mode,  $B_2$ , at the movable transducer is measured, again after 100-200 time averages.
8. The IDT is disconnected and the reference transducer is reconnected to the transmit amplifier.
9. Step 5 is repeated, to gain a second measure of the amplitude,  $B_3$ , of the signal received from the reference transducer and hence a second measure,  $C_3$ , of the coupling may be obtained, using equation 6.4.
10. The measurement from the IDT is now scaled by the mean coupling,  $C_2$ , of the measurement transducer, to give a corrected measure of the acoustic field strength,  $M_i$ :

$$M_i = \frac{B_2}{C_2} = \frac{B_2}{\frac{1}{2}(C_1 + C_3)} \quad (6.5)$$

Steps 3 to 10 are now repeated for each of the required measurement locations.

Several further points need consideration when performing this type of experiment: firstly, since the plate has finite dimensions, the location of both the reference transducer and the IDT should be such that reflections from edges of the plate can be clearly resolved in time, and do not confuse results. Secondly, if the received signal is complicated by other the presence of other modes and reflections, it may be necessary to use the distance between the reference transducer and the movable transducer to predict the time at which the signal for the correct mode should arrive. Knowledge of the correct time of arrival of a particular mode is a necessity if an automatic peak to peak amplitude measurement

system is being used, so that only the correct portion of the signal is examined and reflections (which may be of greater amplitude) are ignored.

In an ideal situation,  $C_1 = C_3$ , but in practice due to the creeping effect in the coupling  $C_3 > C_1$ . However, as the measurement from the IDT is made between the two measurements from the reference transducer, it is reasonable to assume that the coupling for the IDT measurement,  $C_2$ , is bracketed by the coupling from the two measurements made with the reference transducer, so  $C_1 < C_2 < C_3$ . If the three measurements have been made with similar time intervals between, it is furthermore reasonable to assume that  $C_2 = (C_1 + C_3)/2$ , as used in equation 6.5.

The measurement procedure described above is still reasonably slow, as three measurements are required at each location, and for each of these the digital oscilloscope needs a finite time to perform the required number of averages. An elegant way of reducing the delay by almost a factor of three is described below.

### *Improved method - technique 3*

**Technique 2** measures the acoustic field from an IDT transmitting Lamb waves. However, reciprocity dictates that when acting as a receiver, the sensitivity of an IDT to incoming waves originating at some point in the plate must follow the same pattern. Hence, the acoustic field from an IDT can also be mapped by using the IDT as a receiver and measuring its sensitivity to a movable point source of constant amplitude. Again, the practical success of this approach is largely dependent on being able to provide a point source of constant, or at least known, amplitude. However, this can be readily achieved by slight modifications to the experimental set-up described above and these are shown in figure 6.15.

In this case, the movable transducer acts as the point source and is always connected to the output from a power amplifier supplying a toneburst at the desired centre frequency. Two pre-amplifiers are required, one to measure the signal from the reference transducer and one to measure the signal from the IDT. The experimental procedure (**technique 3**) is described below:

### **Technique 3**

1. The IDT under test is bonded at a suitable location on the plate as before. It is connected to the first receiving amplifier.
2. The reference point transducer is again placed at a suitable location  $(x_r, y_r)$ , and connected to the second receiving amplifier.
3. The movable point transducer is moved to a measurement location  $(x_i, y_i)$ , and the separation  $d = \sqrt{(x_r^2 - x_i^2) + (y_r^2 - y_i^2)}$  calculated. This transducer remains connected to the transmitting amplifier throughout the experiment.
4. Time averaged signals from the IDT and the reference transducer are now collected simultaneously by the oscilloscope. The peak to peak amplitude,  $B_r$ , of the desired mode in the signal from the reference transducer and the corresponding amplitude,  $B$ , in the signal from the IDT is measured.

5. The coupling factor,  $C$  is calculated from the amplitude  $B_r$ , using equation 6.4 and the corrected signal,  $M_i$ , from the IDT is calculated:

$$M_i = \frac{B}{C} \quad (6.6)$$

The major advantage of this technique over **technique 2** is that, in this case, the reference signal is measured simultaneously with the signal from the IDT, so there is no concern over the coupling variability with time. Furthermore, the time taken for each measurement is considerably reduced since the oscilloscope can average both signals simultaneously, and all transducers remain connected throughout the experiment.

In both experimental set-ups, there were initial problems with very poor repeatability and apparently random scattering of results. In some cases, the scatter on the corrected results was greater than that which was obtained using only a single point transducer optimised to give the largest signal. Further investigation suggests that these errors resulted from the interference caused by the three supporting feet on the conical point contact transducers (these are shown in figure 5.20). These problems of repeatability were completely alleviated by constructing gantries which spanned the plate onto which the point transducers were mounted, so that their only point of contact with the plate was the measurement point at the apex of the cone.

### *Experimental demonstration of consistency of improved method*

The field around a third conical point contact transducer was mapped using **technique 3** described above. The geometry of the experimental set-up is shown in figure 6.16. The field was mapped at 37 locations on a 180° arc, the separation between measurements being 5°. Due to the axi-symmetric nature of the source, it is expected that the amplitude of the acoustic field along such an arc will be constant

The measurement transducer was excited with a 10 cycle toneburst at 0.328 MHz, and the field was mapped in the manner described above. Three passes were made around the arc, the order in which the measurements were taken being changed with each pass. At each location, 200 time-traces were sampled and averaged before the amplitude of the signal was measured. Both these procedures were performed using functions built into the oscilloscope (LeCroy 9310A). The measurements before the coupling correction was applied are plotted in figure 6.17, and the results after the coupling correction has been applied are plotted in figure 6.18. The results in the second figure have been normalised so that their mean amplitude is the same as the mean amplitude in the first figure.

The standard deviation of the readings before correction is around 40 % of their mean value. After the correction has been applied, this figure falls to around 5 %. The time required to make a measurement at a single location is around 30 seconds, the majority of which is the time taken for the oscilloscope to process the data.

## 6.4 FURTHER USE OF HUYGENS' MODEL FOR INTER-DIGITAL TRANSDUCER DESIGN

In this chapter it has been shown that, with appropriate backing, PVDF can be used as an inter-digital transducer material to transmit and receive Lamb waves at frequencies as low as 100 kHz. Without backing, PVDF IDTs will still function at such frequencies and even

though their sensitivity is significantly reduced, their acoustic fields may still be measured using the technique described above. This means that very simple IDTs can be readily manufactured by cutting out the appropriate shape from a sheet of PVDF and bonding it to a structure using double sided adhesive tape. Although probably not sensitive enough for most practical applications, such IDTs can be constructed very consistently and are an excellent experimental tool for examining IDT behaviour.

In the following sections, unbacked PVDF IDTs are used in conjunction with the Huygens' model described in chapter 5 to investigate the effect of the geometry of an IDT on the acoustic field which it produces. Several basic trends have been elucidated for the cases of straight-finger IDTs producing collimated beams for line inspection and curved finger IDTs producing divergent beams for sector inspection.

### 6.4.1 Design of straight-finger inter-digital transducers

It will be assumed in this section that the main use for straight-finger IDTs is to generate collimated beams, which will propagate over reasonable distances with minimal divergence. It is therefore desirable to obtain an expression for the beam divergence angle for a straight-finger IDT, in much the same way as one can be found for a plane bulk wave transducer (as given in the text by Silk 1984 for example). For simplicity, a single finger IDT is considered first; the effect of adding multiple fingers will be addressed later.

Experimental measurements were performed using the  $A_0$  mode at 328 kHz on a 5 mm thick aluminium plate using **technique 3** described above. At this frequency thickness the wavelength of the  $A_0$  mode is 8 mm. Single 4 mm wide fingers with lengths of 8 mm (2 wavelengths), 40 mm (5 wavelengths) and 80 mm (10 wavelengths) were cut from PVDF sheet and bonded to the aluminium sheet using double sided adhesive tape. Cross sections through the acoustic field were measured on a straight line at a perpendicular distance of 320 mm from each finger. These are shown in figure 6.19(a), (b) and (c) for the three finger lengths, together with the Huygens' model predictions. As can be seen, the agreement between the experimental measurements and the predictions is good, particularly when looking at the width of the main lobe of the beam.

The beam divergence angle is defined in the same way as for a bulk wave transducer, i.e. the angle at which the first minima in the amplitude of the field on either side of the main lobe of the beam diverge (such minima are marked by diamonds in figure 6.19(a),(b) and (c)).

By using Huygens' model to calculate the exact locations of the first minima on either side of the main lobe of the beam (which are marked by diamonds in figures 6.19(a), (b) and (c)) on cross sections at two different distances in front of a transducer, the beam divergence angle,  $\gamma$ , can be calculated. These calculated divergence angles are plotted as a function of finger length in figure 6.20. On the same figure two curves are also plotted. The dashed line is the function  $\sin^{-1}(1.2\lambda/l)$ , where  $\lambda$  is the wavelength and  $l$  is the finger length. This is the function used to calculate the beam divergence angle for a circular bulk wave transducer of diameter  $l$ . As can be seen from the figure, this curve does not fit the measured data very well, although its basic shape is correct. By fitting a better curve to the data, the following equation for the beam divergence angle of a single straight finger was elucidated:

$$\gamma = \sin^{-1}\left(\frac{\lambda}{l}\right) \quad (6.7)$$

This function is also plotted in the figure. The difference between this function and the function describing the divergence angle of a circular bulk wave transducer is thought to arise from the IDT system being for two-dimensional wave propagation whereas the bulk wave transducer system is three-dimensional. From figure 6.20, it can be seen that for a reasonably non-divergent beam, the finger length should be ten or more wavelengths.

The effect of adding more fingers to an IDT was investigated using Huygens' model and the results are shown in figure 6.21(a). This shows straight cross sections, taken at a distance of 40 wavelengths, through the acoustic field of a straight-finger IDT (with a finger length of 10 wavelengths) with different numbers of fingers. It can be seen that the peak amplitude of the main lobe of the beam is approximately proportional to the number of fingers in the IDT, and this is verified in figure 6.21(b), in which the cross sections are normalised by the number of fingers in the IDT and re-plotted.

It can be seen from the figure that, perhaps surprisingly, the number of fingers makes little or no difference to the width of the main lobe of the field and only starts to have noticeable effects at the sides where the amplitude is some 20 dB below the peak amplitude of the field. From this it can be concluded that the number of fingers in a straight-finger IDT does not affect the relationship between the finger length and the beam divergence angle given in equation 6.7. The advantages of using multiple fingers are to increase the overall acoustic power entering the structure and to improve the wavelength selectivity of the IDT.

#### **6.4.2 Design of curved-finger inter-digital transducers**

For a curved-finger IDT, general trends are more complicated to determine as there are more design parameters than for a straight-finger IDT. Furthermore, the definition of a measurable quantity with which to compare different acoustic fields is somewhat difficult. The nomenclature which is used to describe curved finger IDTs is shown in figure 6.22. As a starting point, it will be assumed that the goal when designing a curved-finger IDT is to produce one which generates a field which diverges at the same angle as that subtended by the fingers (hereafter referred to as the angle of the IDT). This ideal field will, at a particular distance from the geometric centre of the IDT, have a constant amplitude within the angle of the IDT and zero amplitude elsewhere. In the studies presented here, only IDTs with concentric fingers, which all subtend the same angle about their common centre, will be considered. This reduces the number of design parameters to be investigated to three: the angle subtended by the fingers (the angle of the IDT), the radius (which is taken as the mean of the innermost and outermost radii for IDTs with more than one finger) and the number of fingers. The effect of radius and angle on the beam from an IDT with a single curved finger are described below. The effect of the number of fingers remains to be investigated.

Consider an IDT with a single curved finger of angle  $90^\circ$ . Angular beam cross sections predicted using Huygens' model are plotted for several different radii of finger in figure 6.23, all cross sections being taken at a radius of 30 wavelengths. The energy at a point in the acoustic field is proportional to the square of the amplitude of the acoustic field at that point. Integrating the energy in the acoustic field over a  $180^\circ$  cross section,

enables the total energy to be found. The amplitude of an ideal beam containing the same total energy can then be calculated. The ideal beams are plotted with lighter lines in the figure. It can be seen that the general trend is that the actual beam becomes closer to the ideal beam as the radius is increased. As this occurs, the cut-offs on either side of the main beam become sharper and the fluctuations within the main beam become shallower and more numerous.

Figure 6.24 shows some of the results from a similar study on an IDT with a single curved finger, except that in this case, the radius of the finger was kept constant (and equal to ten wavelengths) while its angle was varied. From these graphs it can be seen that the field is closest to the ideal field when the angle is large, and deteriorates as the angle is reduced.

For a selection of the IDT geometries shown in figures 6.23 and 6.24, experimental measurements have been made using **technique 3** described previously, and the results plotted on the figures. Once again, good agreement is achieved between experimental measurements and predictions made using Huygens' model.

### *Beam quality*

By integrating the magnitude of the discrepancy between the energy in the beam profile predicted by Huygens' model and the ideal beam profile over the angular range of each cross section, and dividing this by the total energy in the beam, a numerical measure of the beam quality can be obtained for any IDT. The beam quality enables a quantitative comparison to be made between the acoustic fields of any curved-finger IDTs. This concept is shown schematically in figure 6.25.

For a given angle of transducer with a single finger, the beam quality is a function of the radius of the finger. The beam quality for various angles of finger is plotted as a function of radius in figure 6.26. For all angles of transducer, it can be seen that if the radius of the finger is large, the beam quality increases approximately monotonically with radius, as the first study suggested. However, if the radius is small, the beam quality fluctuates both up and down, the amplitude of the fluctuations increasing as the radius is reduced.

### *Critical radius*

The minimum radius of a curved-finger IDT that is necessary to inspect a sector of a structure over a particular angle is of considerable interest, since the radius determines the overall size of the IDT. It can be seen from the inset graph in figure 6.26 that at some critical radius, the beam quality reaches a final peak, before continuously decreasing as the radius is reduced to zero. These peaks are marked by circles on the graph. This critical radius has been found to occur when the distance between the centre of a chord joining the ends of the finger and the centre of the finger equals half a wavelength as shown in figure 6.27. From geometrical considerations, the critical radius,  $r_c$ , is then given by:

$$r_c = \frac{\lambda}{2(1 - \cos\theta/2)} \quad (6.8)$$

where  $\theta$  is the angle of the IDT and  $\lambda$  is the wavelength. Below this radius, a curved finger IDT behaves more like a straight finger one. This critical radius gives the absolute

minimum size of a curved-finger IDT which is necessary to produce a divergent beam. Even in the region just above the critical radius, it can be seen from figure 6.26 that the beam quality still fluctuates rapidly up and down. Hence in practice, it would be desirable to design curved finger IDTs whose radii were several times greater than the critical radius.

Plotting contours of constant beam quality on a graph of radius vs. angle for an IDT with a single curved finger enables the general trends from the above studies to be visualised, and this is shown in figure 6.28. The critical radius is also plotted as a function of angle in this figure, and the region where the beam quality is a rapidly fluctuating function of radius is also indicated, the upper bound of this region being set, somewhat arbitrarily, at four times the critical radius.

### 6.5 CONCLUSIONS

In this chapter, the development of lead backed low frequency PVDF IDTs has been demonstrated. Successful use of such IDTs at frequencies as low as 65 kHz has been described, including the development of a four phase IDT to produce a divergent beam on one side of the transducer only.

The construction of low-frequency lead backed IDTs has also exposed the possible shortcomings of Huygens' model. The effect of bonding such a transducer to a structure is twofold. Firstly, the increased mass loading modifies the wavelength of Lamb waves in the structure immediately beneath the IDT which is indicated by a significant discrepancy between the optimum experimental operating frequency and that predicted theoretically for an unloaded plate. Secondly, the presence of the IDT attenuates the waves passing under it. It is also interesting to observe that these two effects may not be directly coupled as indicated by the results from the IDTs,  $T_1$  and  $T_2$ . In both cases, the optimum experimental operating frequencies were approximately 10 % lower than the theoretical operating frequency, indicating that both IDTs caused a similar perturbation to the wavelength of Lamb waves in the bar. However,  $T_2$  (with a single layer) was shown to be have a much greater attenuating effect than  $T_1$  (with passive layers) and also appeared as a bigger reflector of incident lamb waves. In this respect, the passive layered design of  $T_2$  may be beneficial. There is both the need and scope for considerably more work to be done to investigate these phenomena, as they are important for any type of inter-digital transducer.

In the case of Huygens' model, neither of the above effects can be readily included, and it is surprising that the agreement between predictions and measurements is so good, particularly in the case of the 4 phase IDT, as shown in figure 6.9(b). This is almost certainly due to the fact that the IDT has 8 fingers, and hence the sensitivity of the beam quality to small changes in other parameters such as either the wavelength or mean radius is small. It is possible to envisage a modified version of Huygens' model which does take into account the change in wavelength of waves under an IDT, but the development of such a model is beyond the scope of this thesis. Nevertheless, the existing Huygens' model is the only practical design tool for IDTs at present, and can certainly be used to give a first approximation to the acoustic field from an IDT, as long as its limitations are understood.

An improved experimental technique for measuring the acoustic field strength at different locations on a plate structure using conical point contact transducers has been developed, which eliminates the coupling inconsistencies from the calculation. The use of this technique to accurately measure the relatively weak signals generated by un-backed PVDF has enabled the acoustic fields from a variety of simple IDT configurations to be measured experimentally. In conjunction with the Huygens' model described in the previous chapter these results have enabled several guidelines for the design of straight and curved finger IDTs to be deduced. In the case of a straight finger IDT, a relationship between the beam divergence angle, finger length and wavelength has been found to exist which is similar to that for plane bulk wave transducers. It has been shown that the number of fingers does not affect this result, although it does increase the amplitude of the signal generated by the IDT. Although not considered in this chapter, it should be remembered that the number of fingers in an IDT also affects modal selectivity as previously discussed in chapter 4.

In the case of curved finger IDTs designed to produce uniformly divergent beams of a given angle, it has been shown that, for a single finger, the uniformity of the beam improves as the radius of the finger is increased. The concept of beam quality has been introduced, which enables the beams from different geometries of IDT to be quantitatively compared to each other and to ideal beams. This has been used to show that as the angle of the required divergent beam is decreased, the radius of the IDT must be increased in order to maintain the beam quality. Furthermore, in order to produce a particular angle of divergent beam, there is a definite minimum radius of IDT which is required.

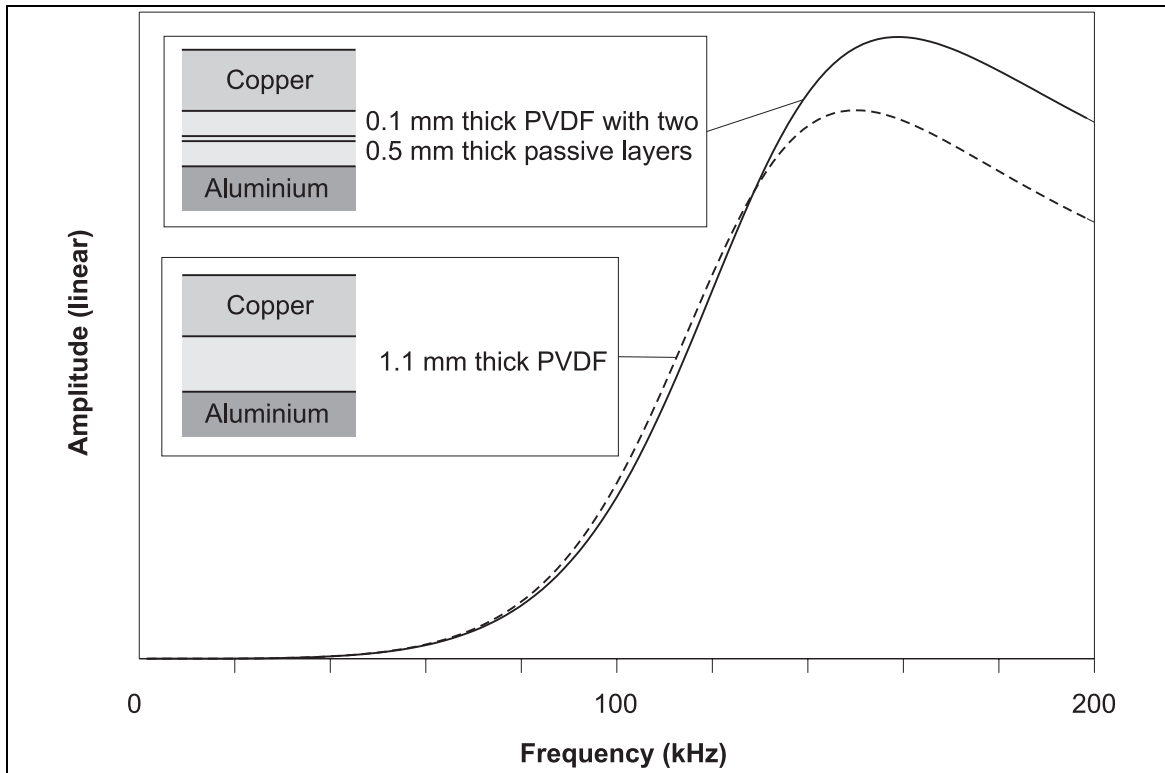


Figure 6.1 Predicted pulse-echo response of a single 1.1 mm thick active PVDF layer and a 0.1 mm thick layer of active PVDF sandwiched between two layers of 0.5 mm thick passive PVDF. Both systems are backed by 1.25 mm thick copper and mounted on an aluminium substrate. No bond layers are included in the model.

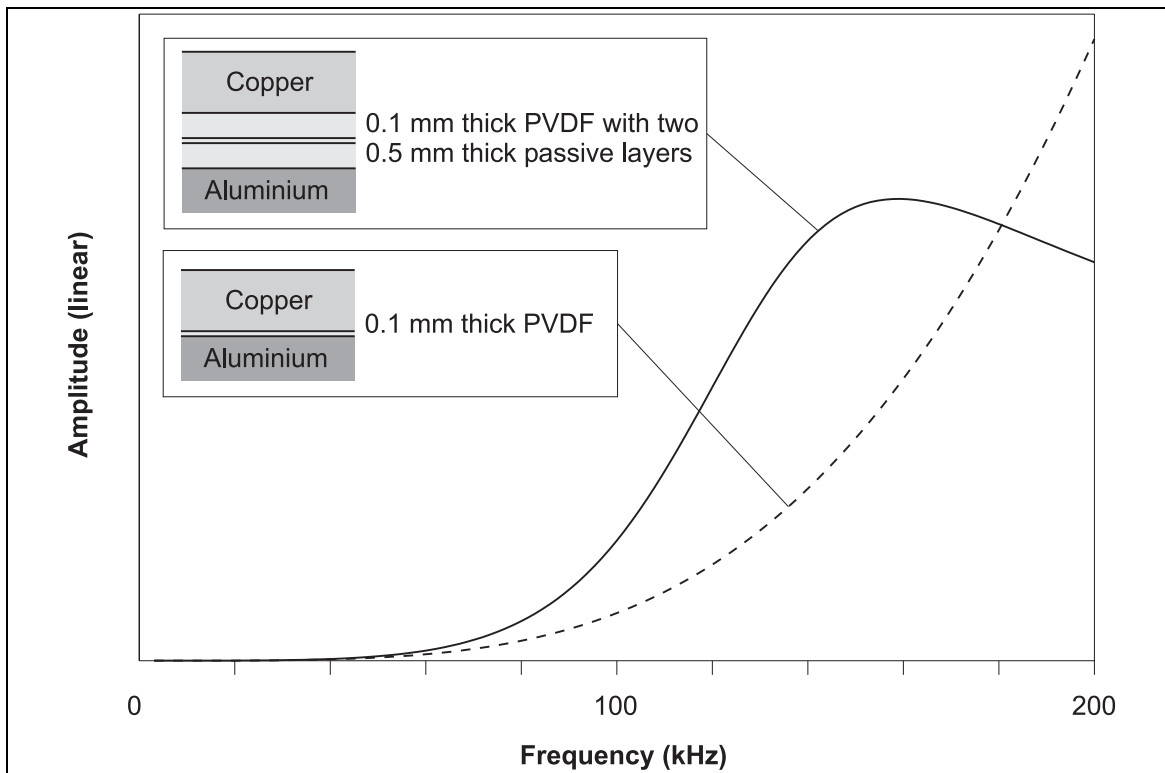


Figure 6.2 Predicted pulse-echo response of a 0.1 mm thick PVDF layer and a 0.1 mm thick PVDF layer sandwiched between two 0.5 mm thick passive layers of PVDF. In both cases, the systems are backed by 1.25 mm thick copper layers and bonded to aluminium substrates.

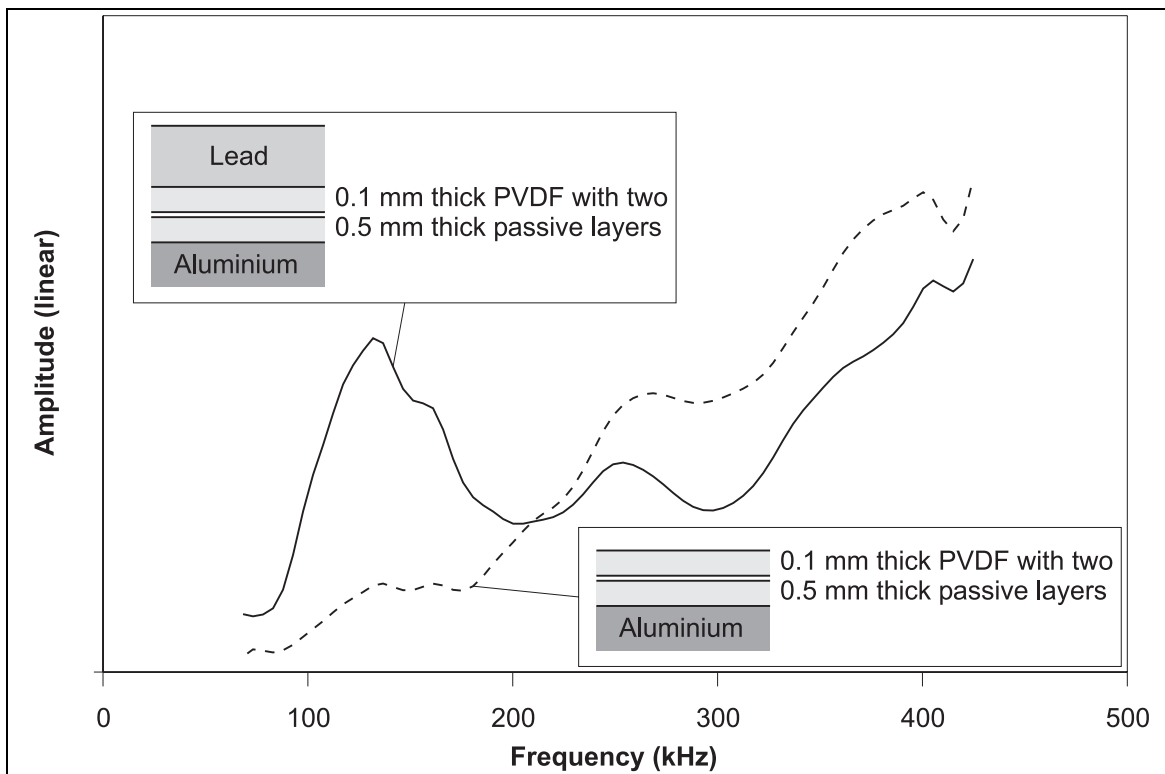


Figure 6.3 Typical measured pulse-echo response of a monolithic bulk wave transducer, in this case showing a device with passive layers, with and without lead backing.

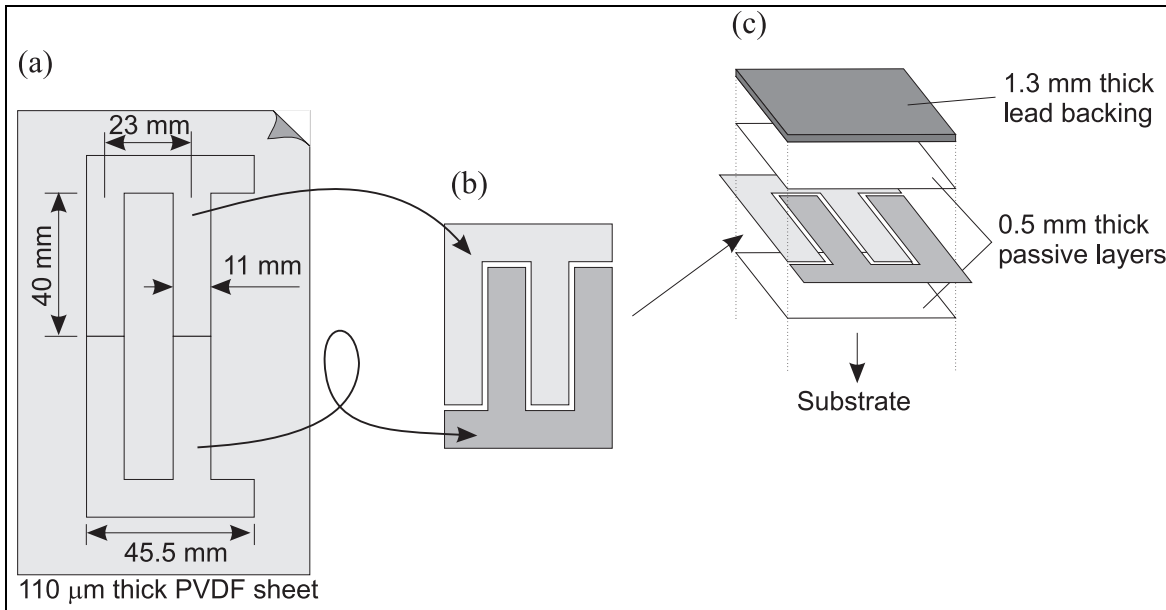


Figure 6.4 Construction of first low frequency IDTs. The fingers are (a) cut from PVDF sheet and configured as shown in (b). The layered assembly of the IDT is shown in (c), in this case for a passive layers design.

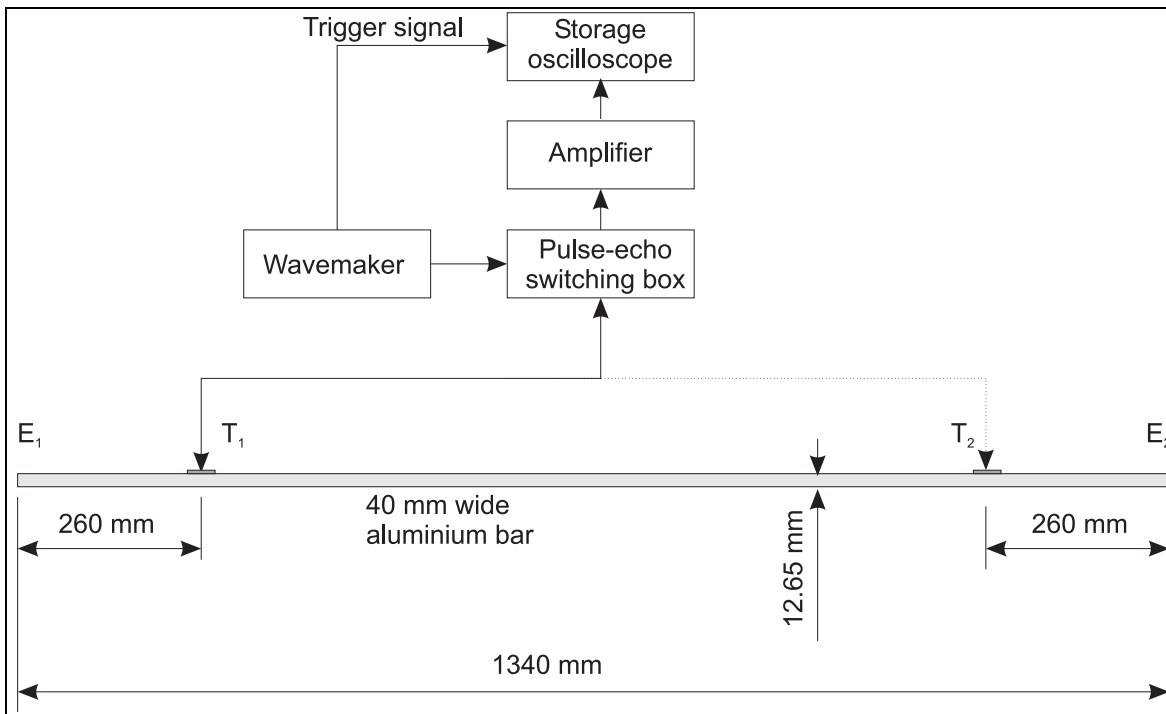


Figure 6.5 Experimental set-up for testing low frequency IDTs.

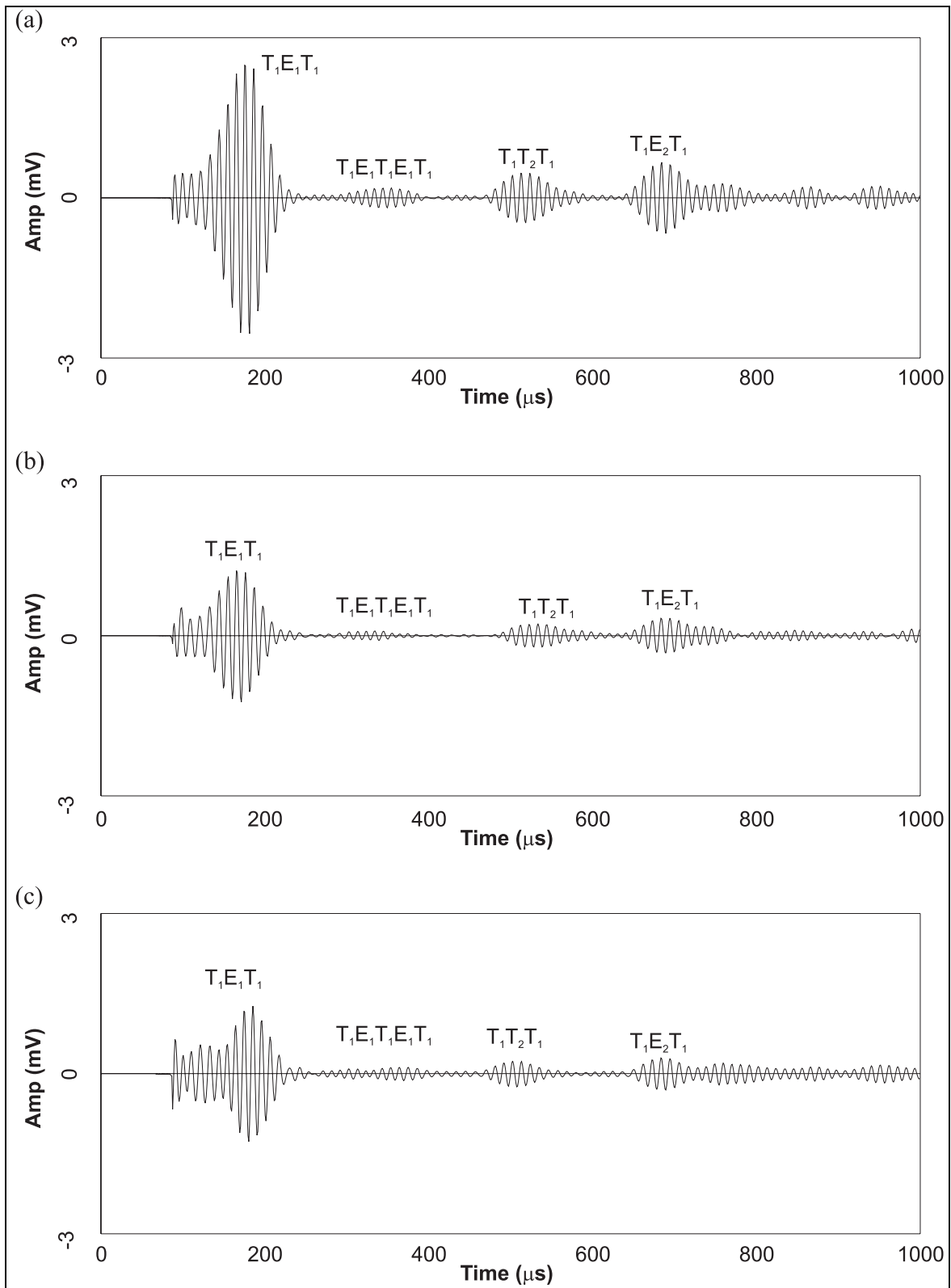


Figure 6.6 Received time-traces obtained from  $T_1$  (passive layer device). The time-trace shown in (a) is with both sets of fingers connected, and the time-traces in (b) and (c) show the effect of connecting each set individually.

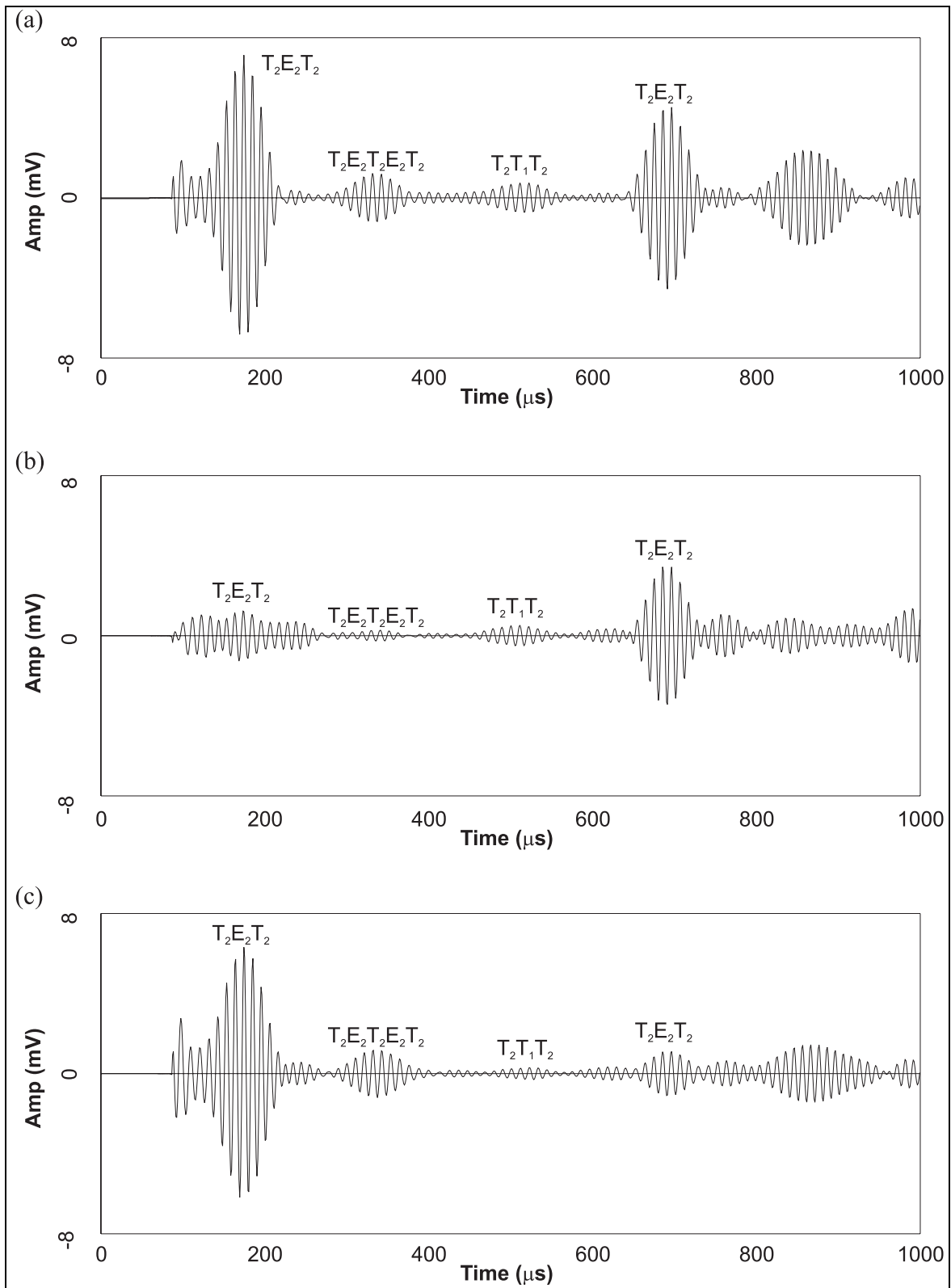


Figure 6.7 Received time-traces obtained from  $T_2$  (single layer device). The time-trace shown in (a) is with both sets of fingers connected, and the time-traces in (b) and (c) show the effect of connecting each set individually.

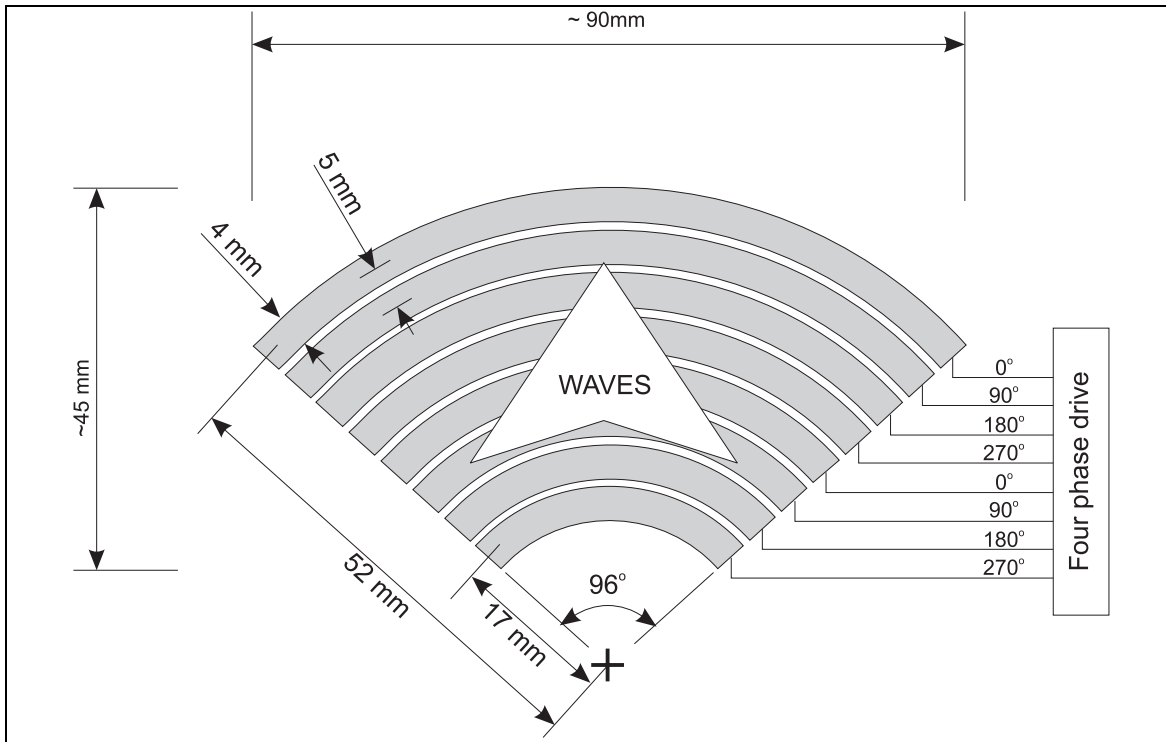


Figure 6.8 Geometry of a four phase IDT designed to produce a uni-directional divergent beam over a  $90^\circ$  sector.

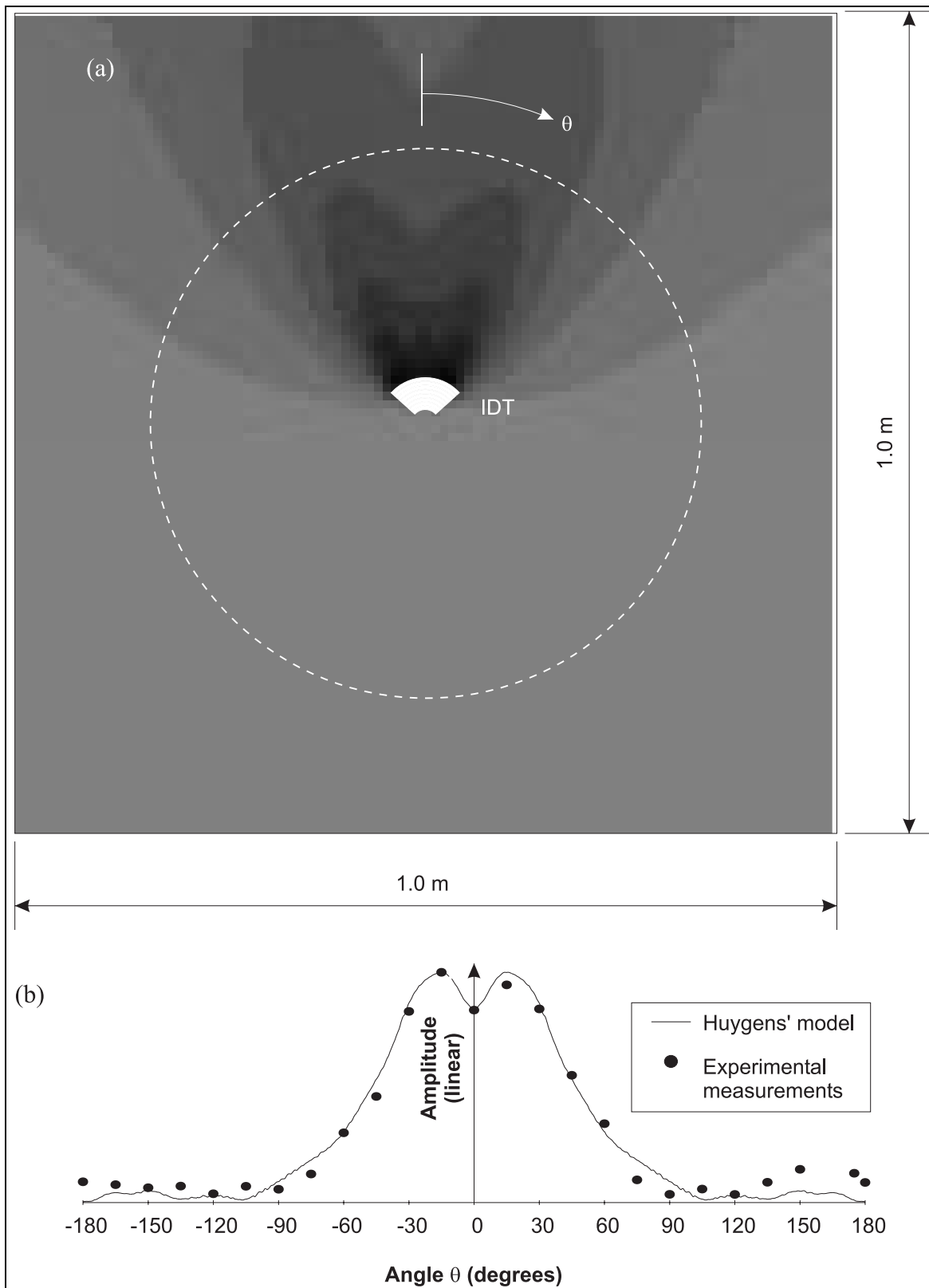


Figure 6.9 (a) Predicted acoustic field from the four phase IDT shown in figure 6.8 and (b) angular cross section along the dotted line in (a). The experimentally measured values are also plotted in (b).

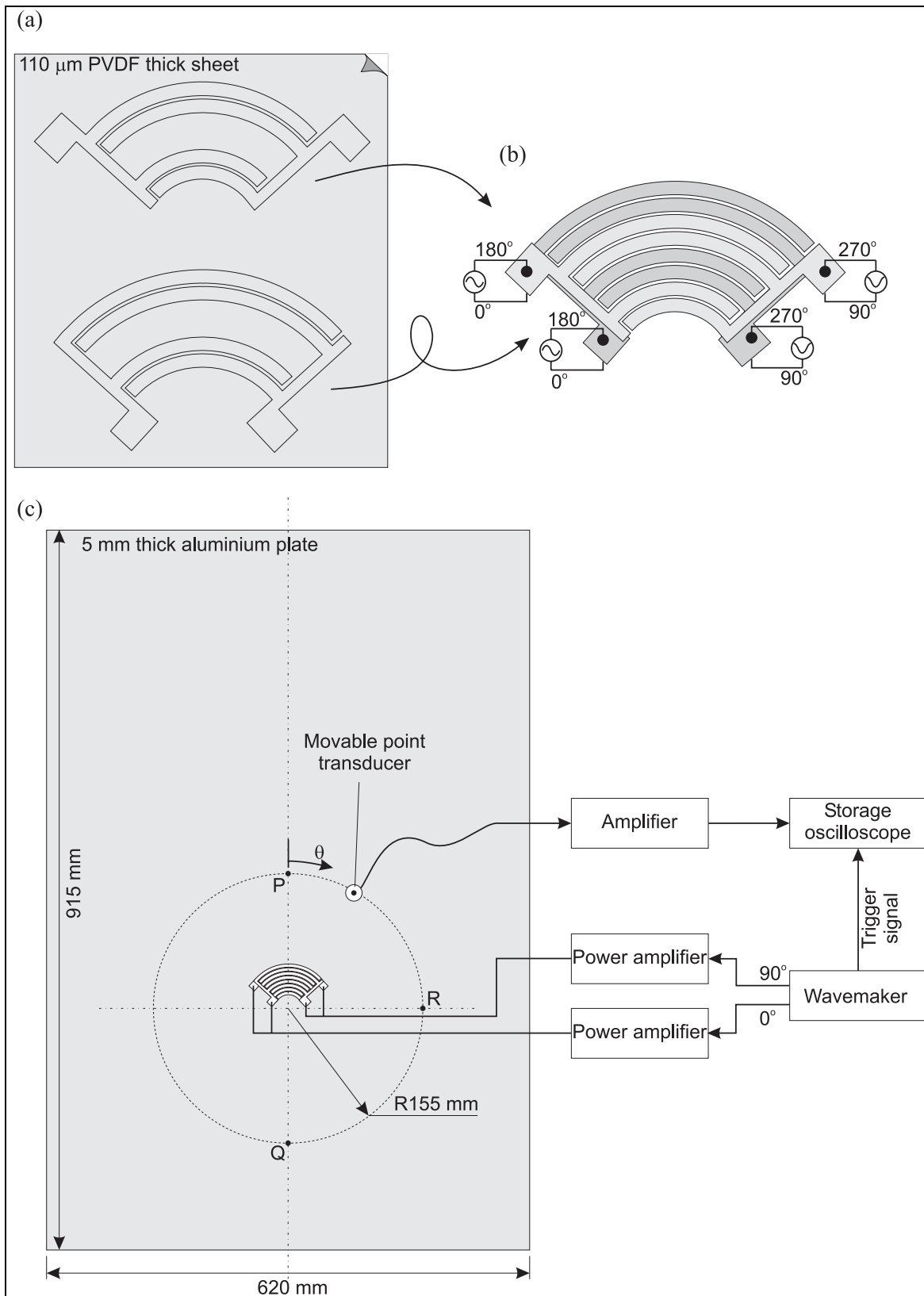


Figure 6.10 Construction of four phase IDT showing (a) the electrode shapes and polarity and (b) the electrical connections. The experimental set-up for measuring the acoustic field from the IDT is shown in (c).

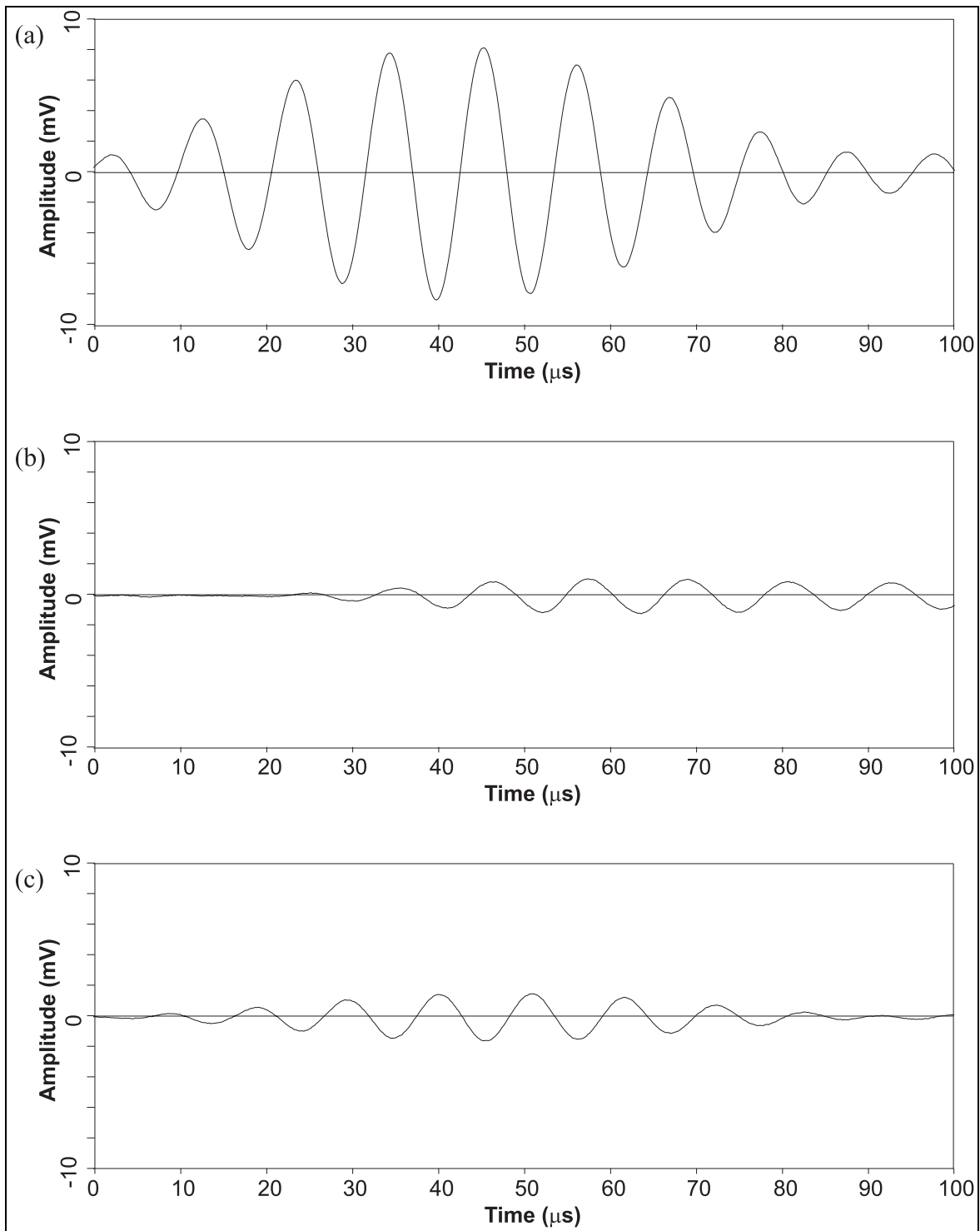


Figure 6.11 Time-traces measured at the locations (a) P, (b) Q and (c) R from the IDT in figure 6.10 when the IDT was driven at 91 kHz.

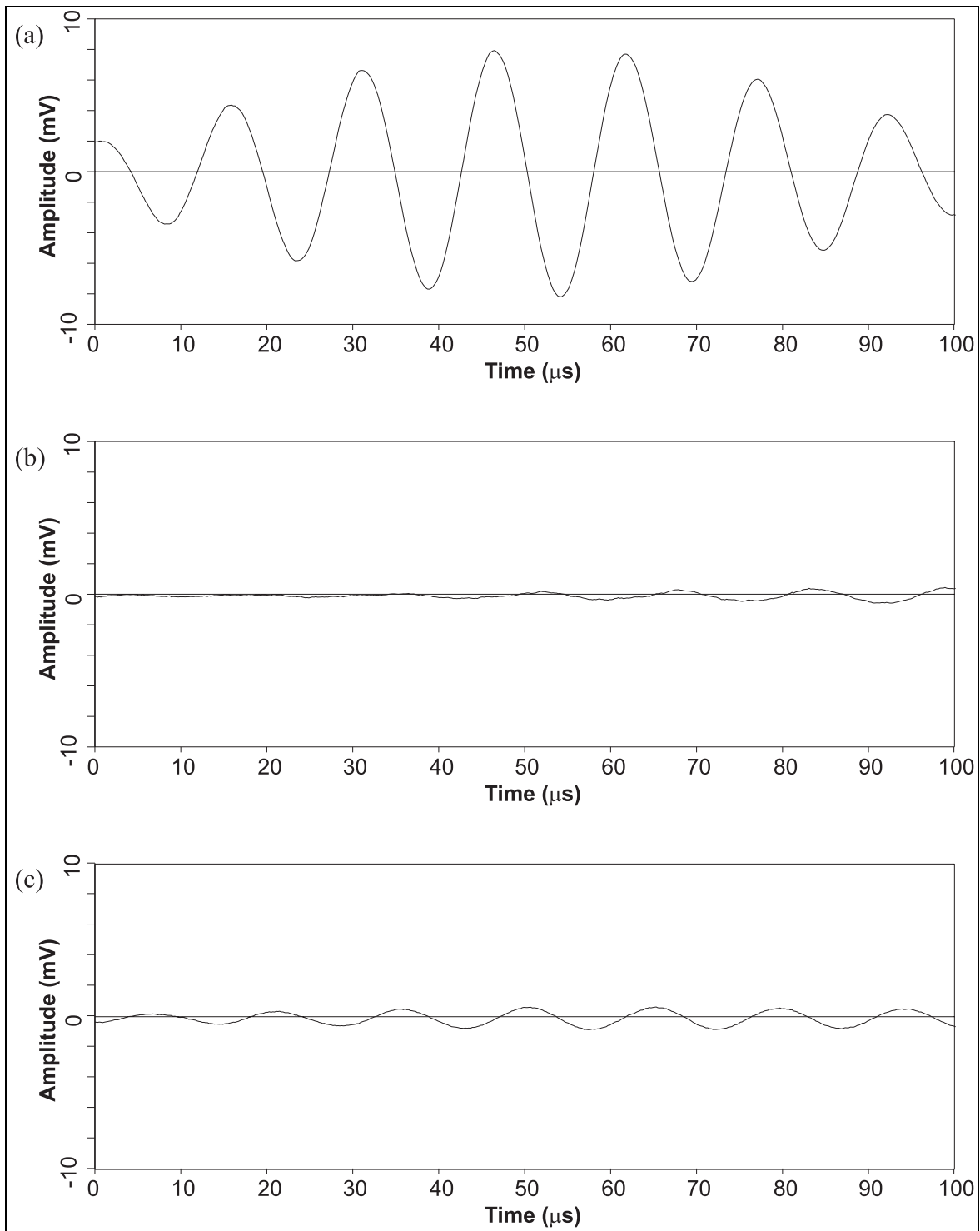


Figure 6.12 Time-traces measured at the locations (a) P, (b) Q and (c) R from the IDT in figure 6.10 when the IDT was driven at 65 kHz.

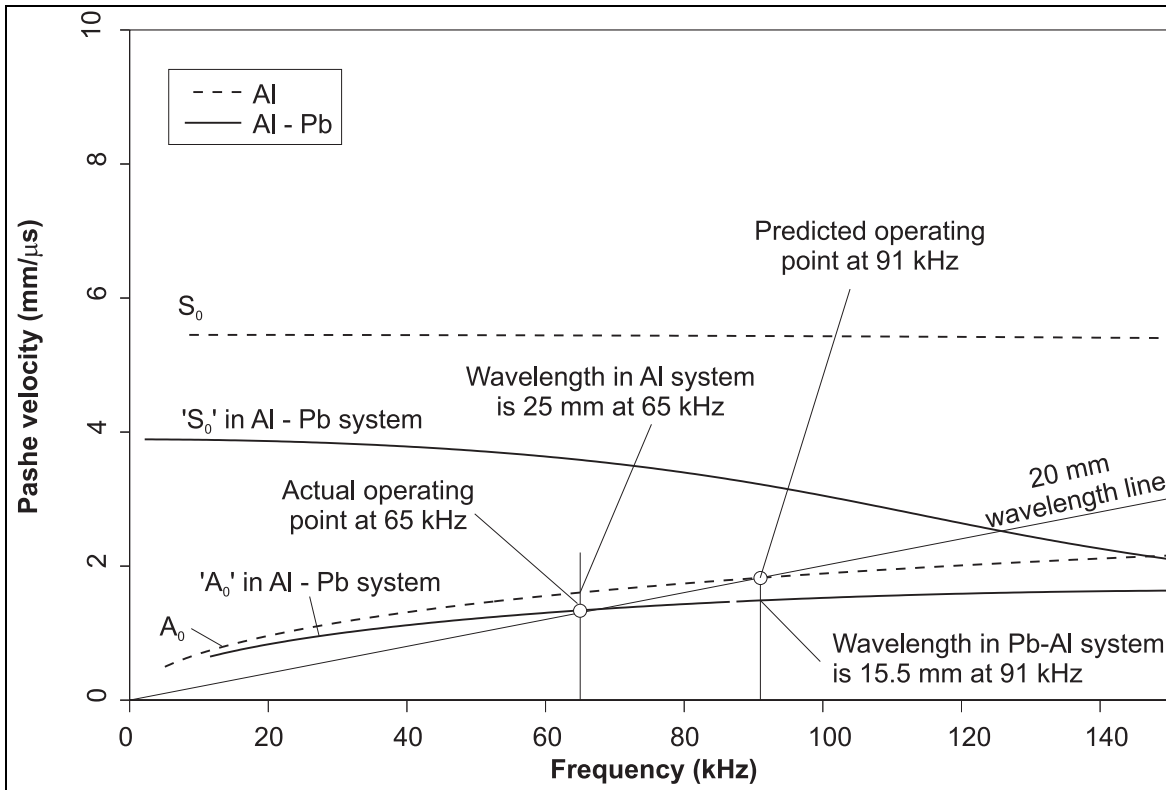


Figure 6.13 Phase velocity dispersion curves for 5 mm thick aluminium plate (Al) and 5 mm thick aluminium plate (Al) in perfect 'welded' contact with 1.3 mm thick lead plate (Pb).

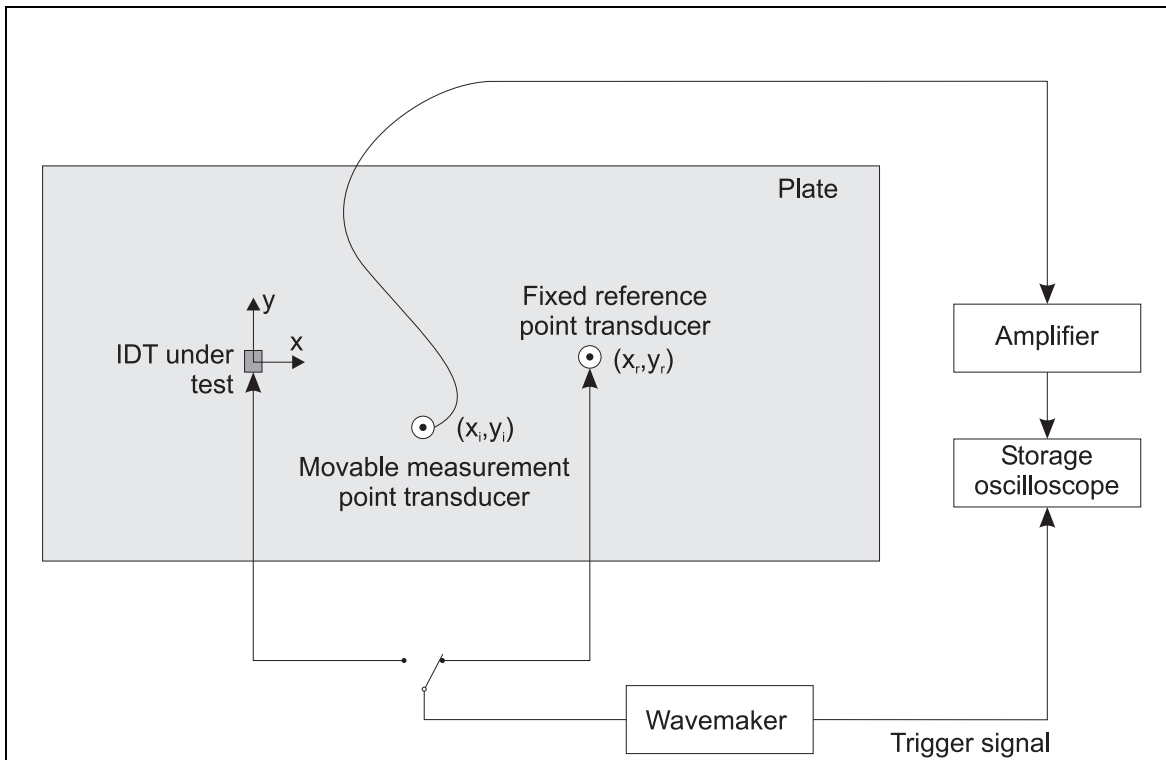


Figure 6.14 **Technique 2** for measuring the acoustic field from an IDT, using two conical transducers and the IDT as the transmitter.

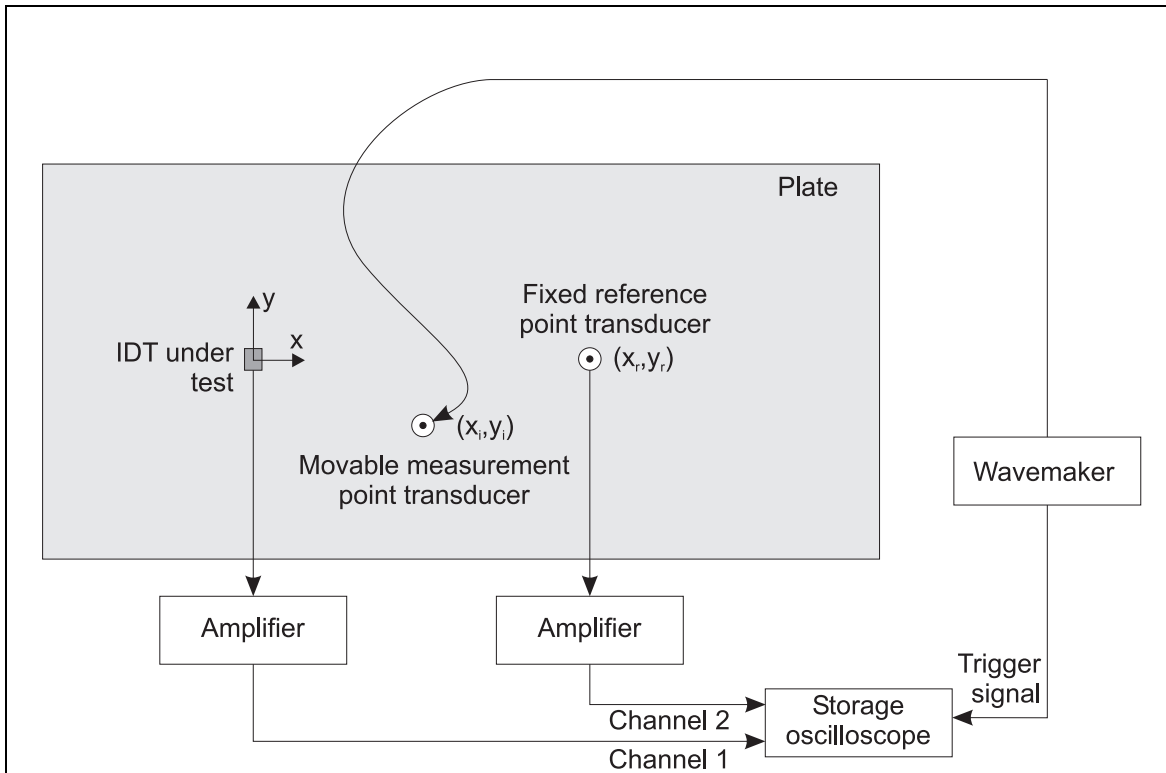


Figure 6.15 **Technique 3** for measuring the acoustic field from an IDT, using two conical transducers and the IDT as a receiver.

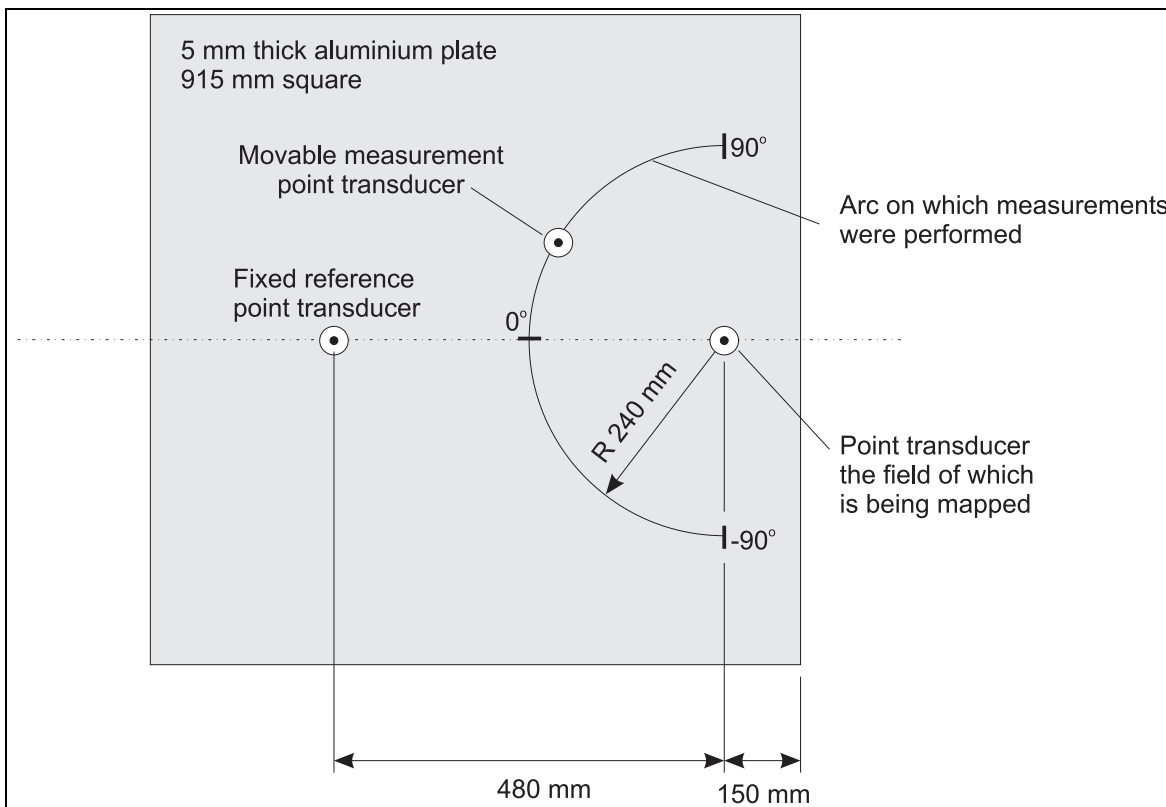


Figure 6.16 Geometry of experimental set-up to measure the acoustic field around a point source by various methods.

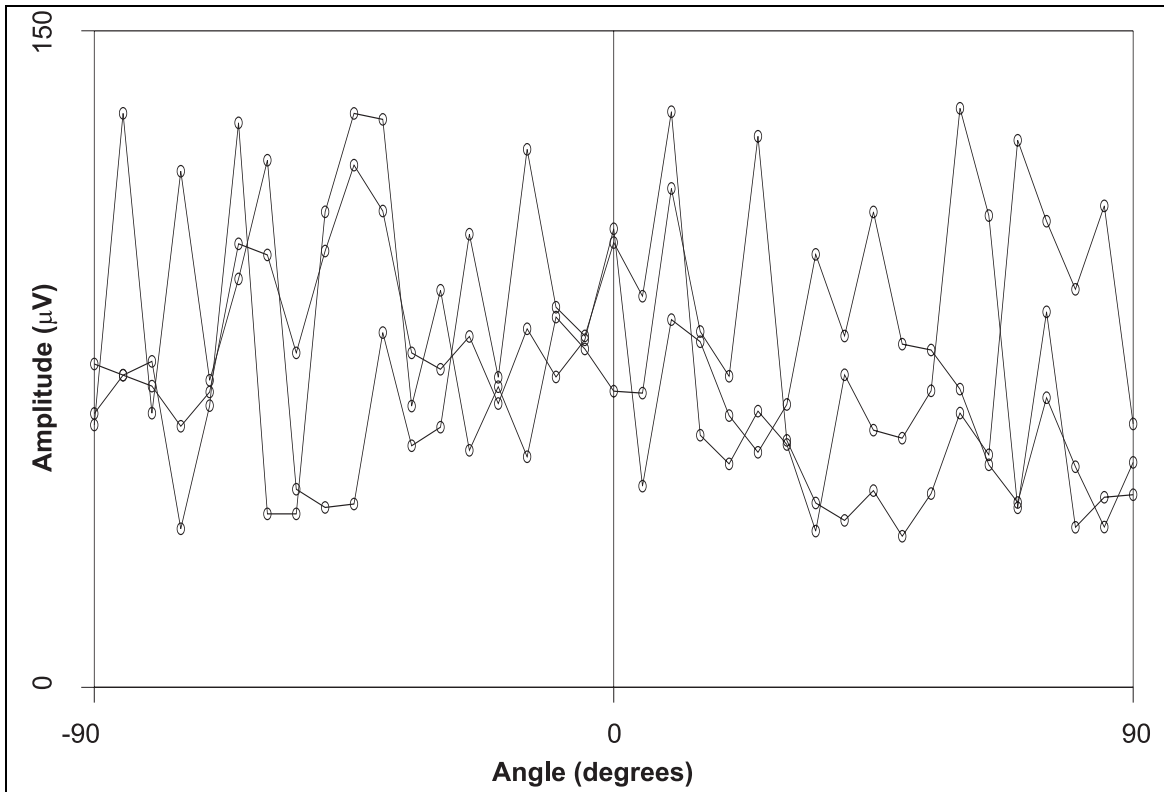


Figure 6.17 Three sets of angular cross section measurements through the acoustic field from a point source before being corrected for coupling inconsistencies.

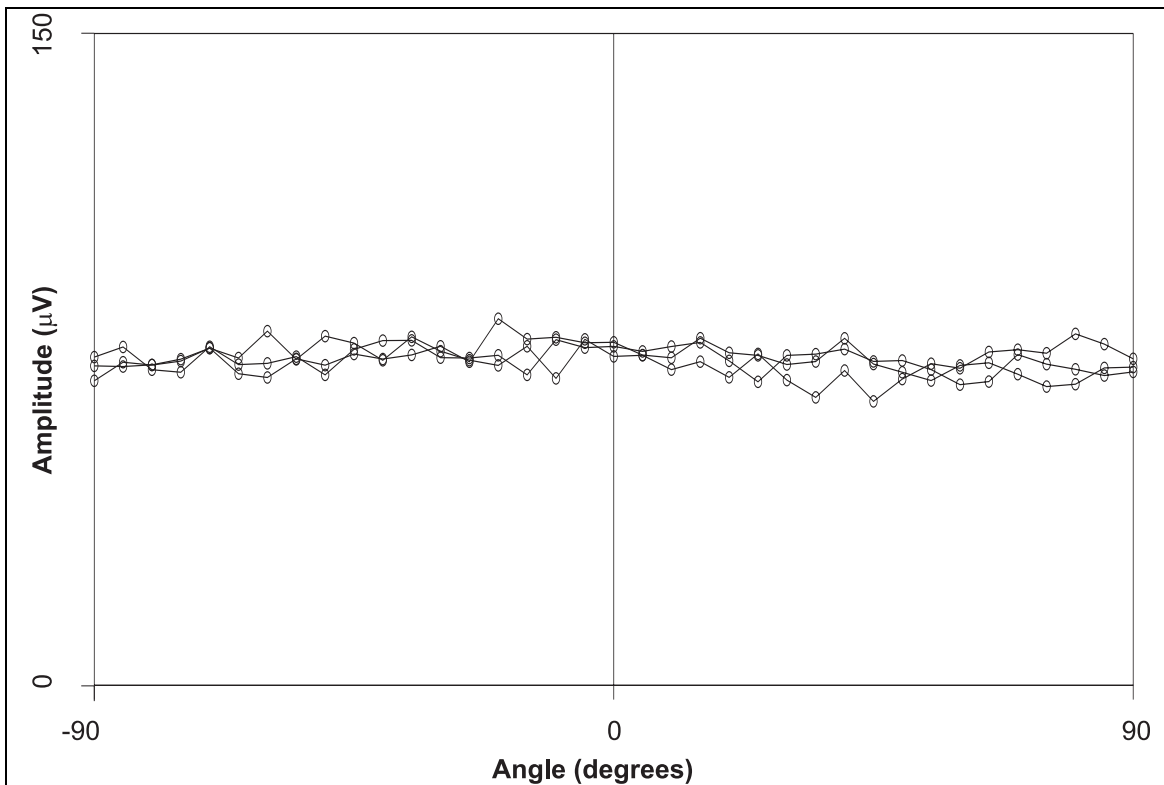


Figure 6.18 The three sets of angular cross section measurements from figure 6.17 after being corrected for coupling inconsistencies by **technique 3**.

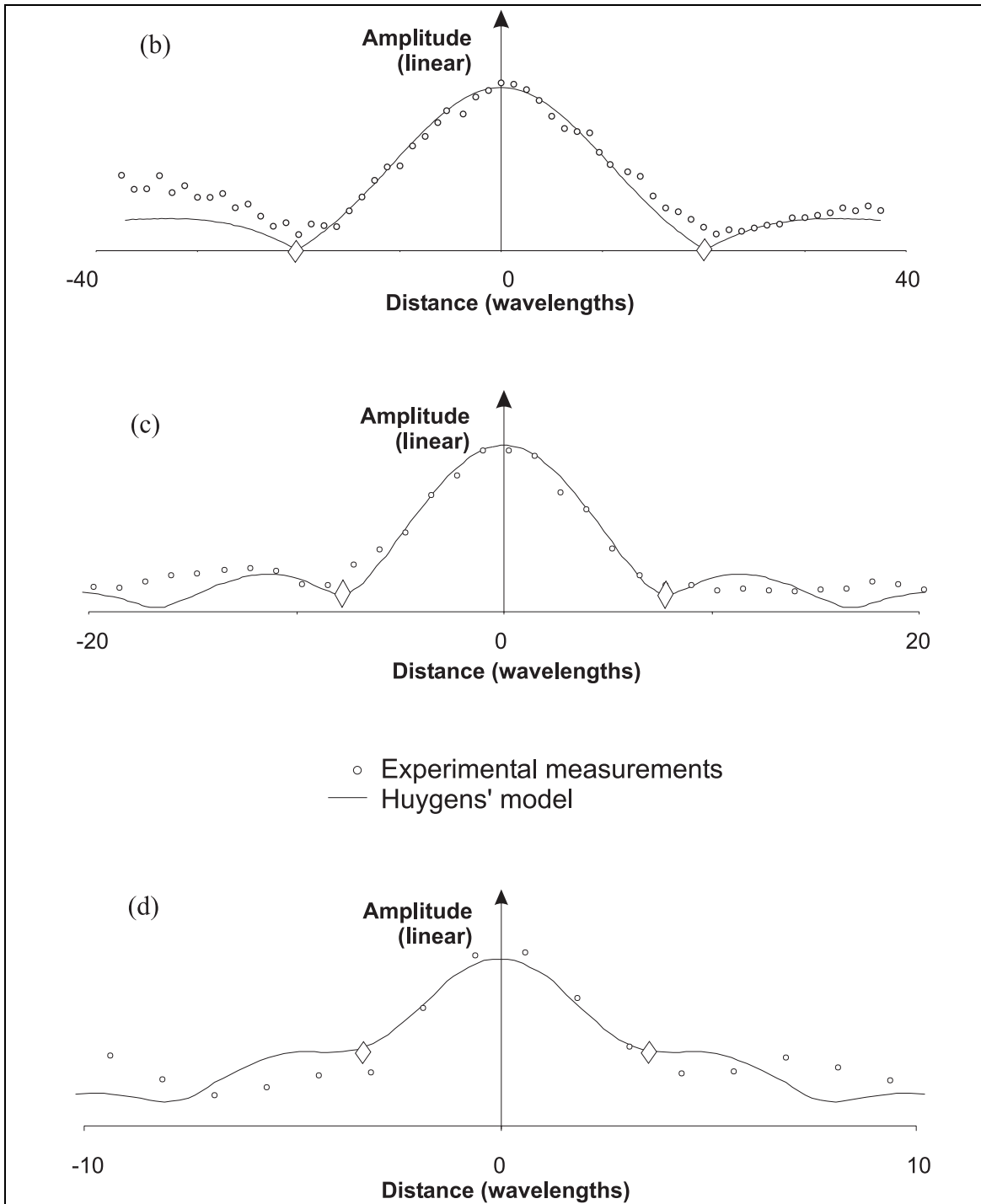


Figure 6.19 Measured cross sections through the acoustic fields from single straight fingers of lengths 2, 5 and 10 wavelengths. Predicted cross sections from Huygens' model are also shown. The diamonds on the cross sections indicate the minima on either side of the main lobe of the beam.

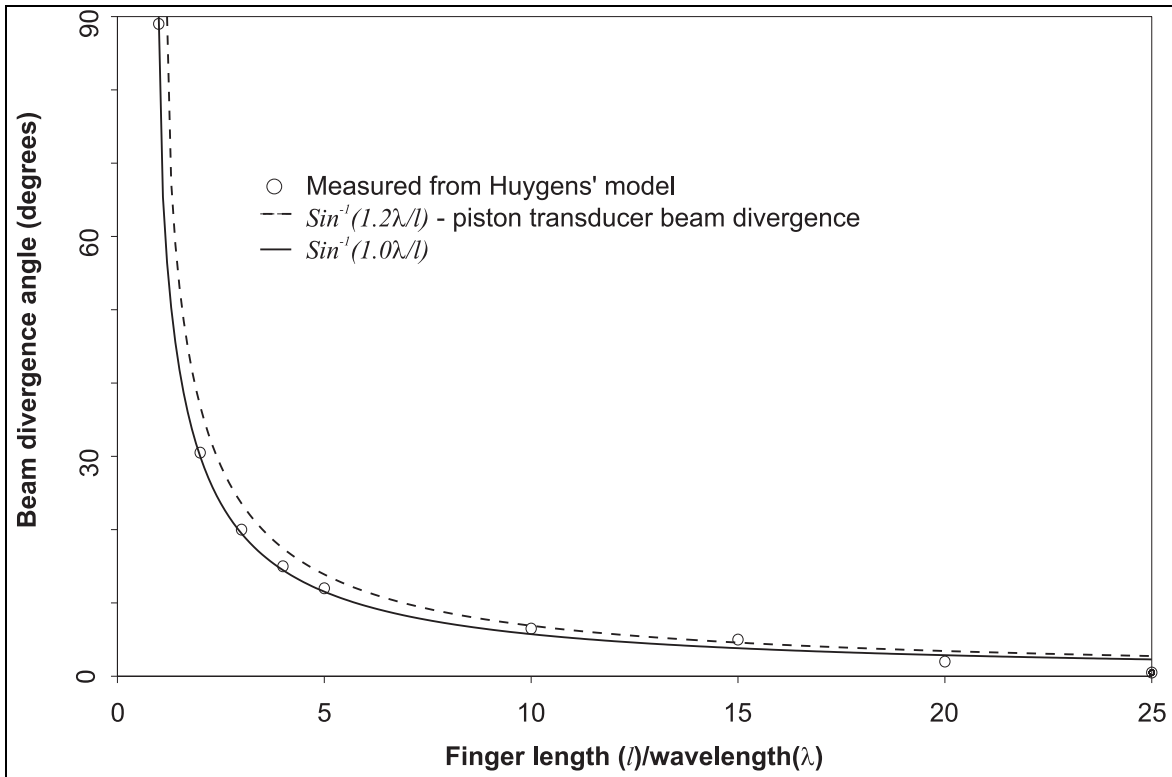


Figure 6.20 Predicted beam divergence angle as a function of finger length for a single straight finger. The function for the beam divergence of a bulk wave transducer with diameter equal to the finger length is indicated by the dashed line. An improved curve fitted to the predicted beam divergences is also plotted.

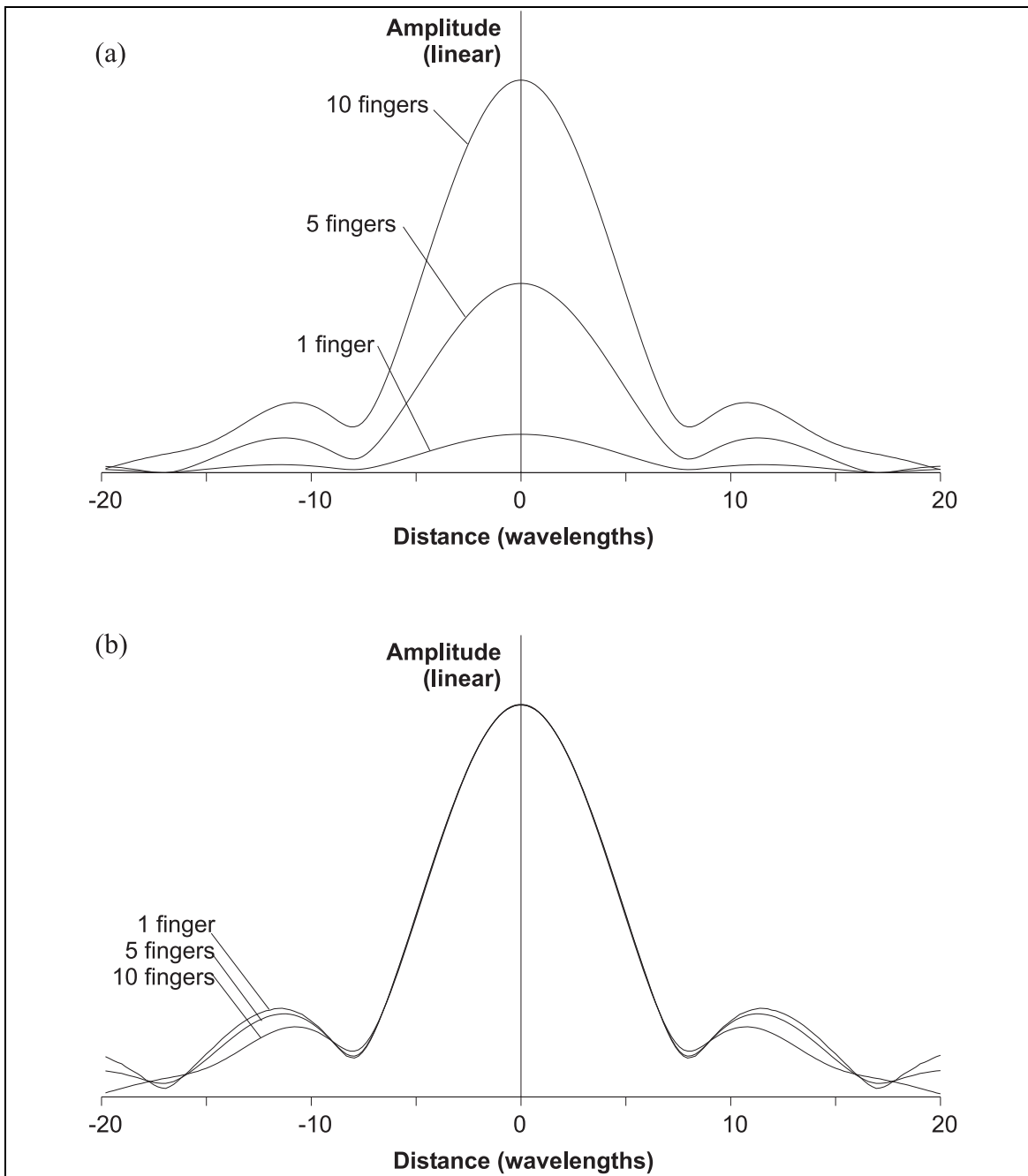


Figure 6.21 Predicted beam cross sections through the acoustic field from a straight finger IDT, 10 wavelengths wide, and with 1, 5 and 10 fingers. In (a) the relative amplitudes of the three fields are correct, but in (b) the amplitude of each cross section has been normalised by the number of fingers.

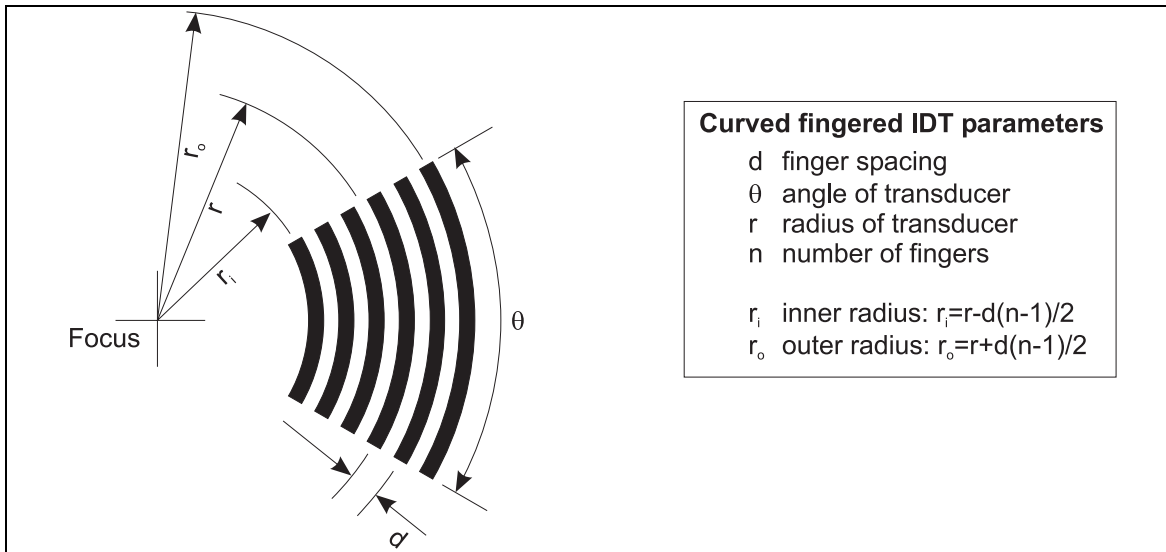


Figure 6.22 Nomenclature used to describe a curved finger IDT.

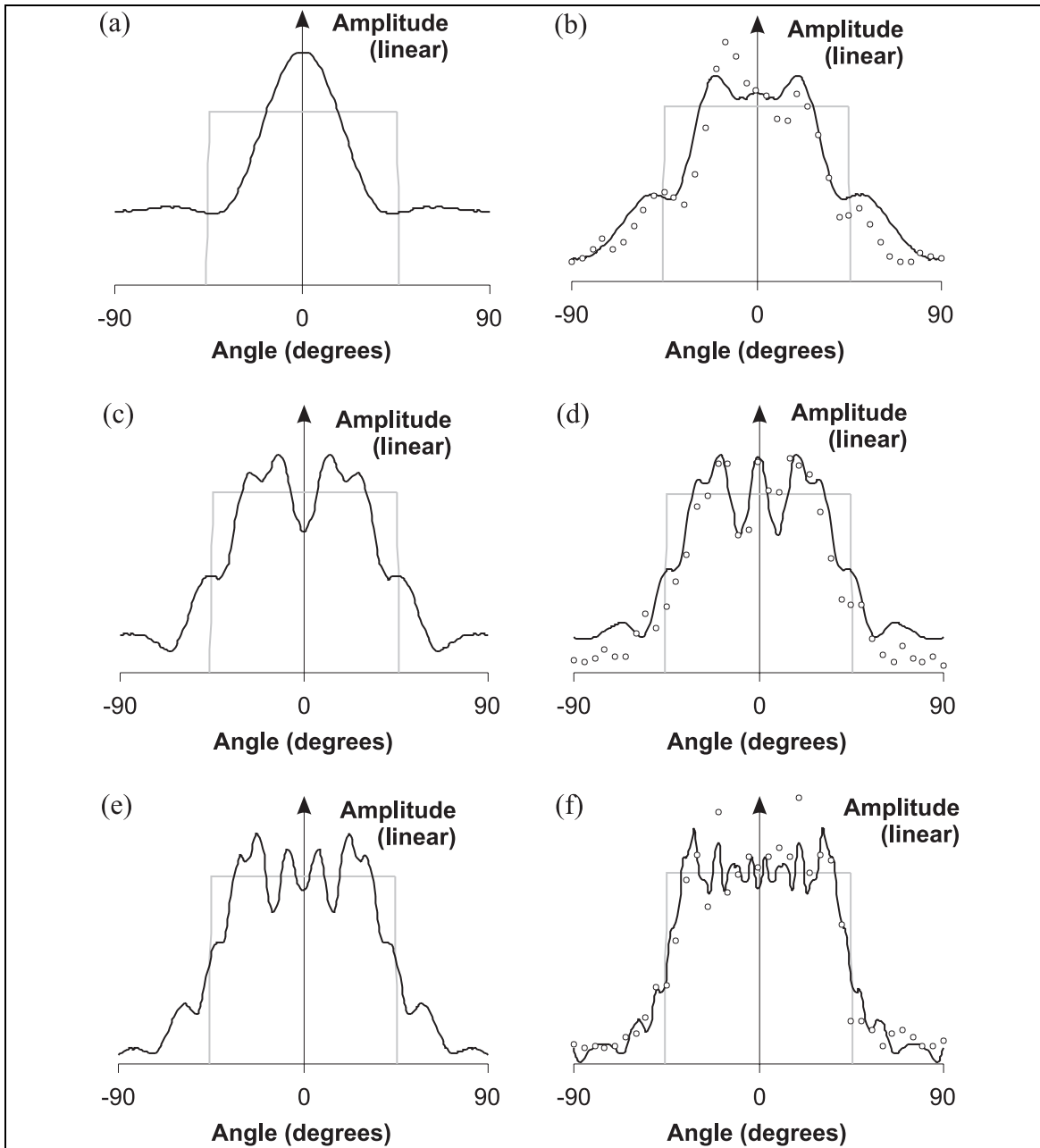


Figure 6.23 Predicted angular cross sections through the acoustic field from an IDT with a single curved finger of angle  $90^\circ$  as the radius of the finger is increased from (a) 1, (b) 2, (c) 3, (d) 4, (e) 5 and (f) 10 wavelengths. Cross sections through the ideal fields are shown with lighter lines and where applicable, experimental measurements are shown by black circles.

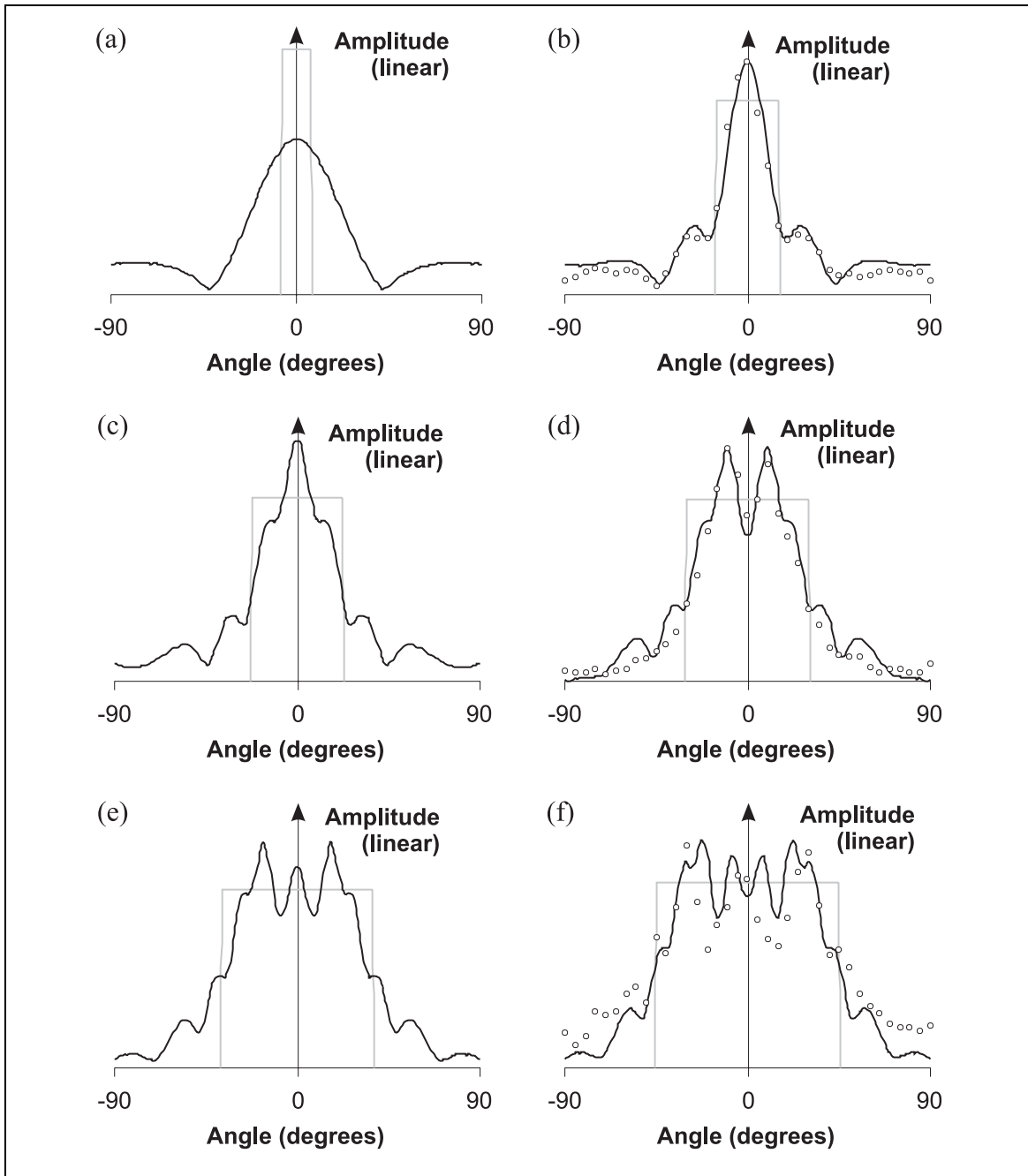


Figure 6.24 Predicted angular cross sections through the acoustic field from an IDT with a single curved finger of radius 5 wavelengths as the angle of the finger is increased from (a) 15°, (b) 30°, (c) 45°, (d) 60°, (e) 75° and (f) 90°. Cross sections through the ideal fields are shown with lighter lines and where applicable, experimental measurements are shown by black circles.

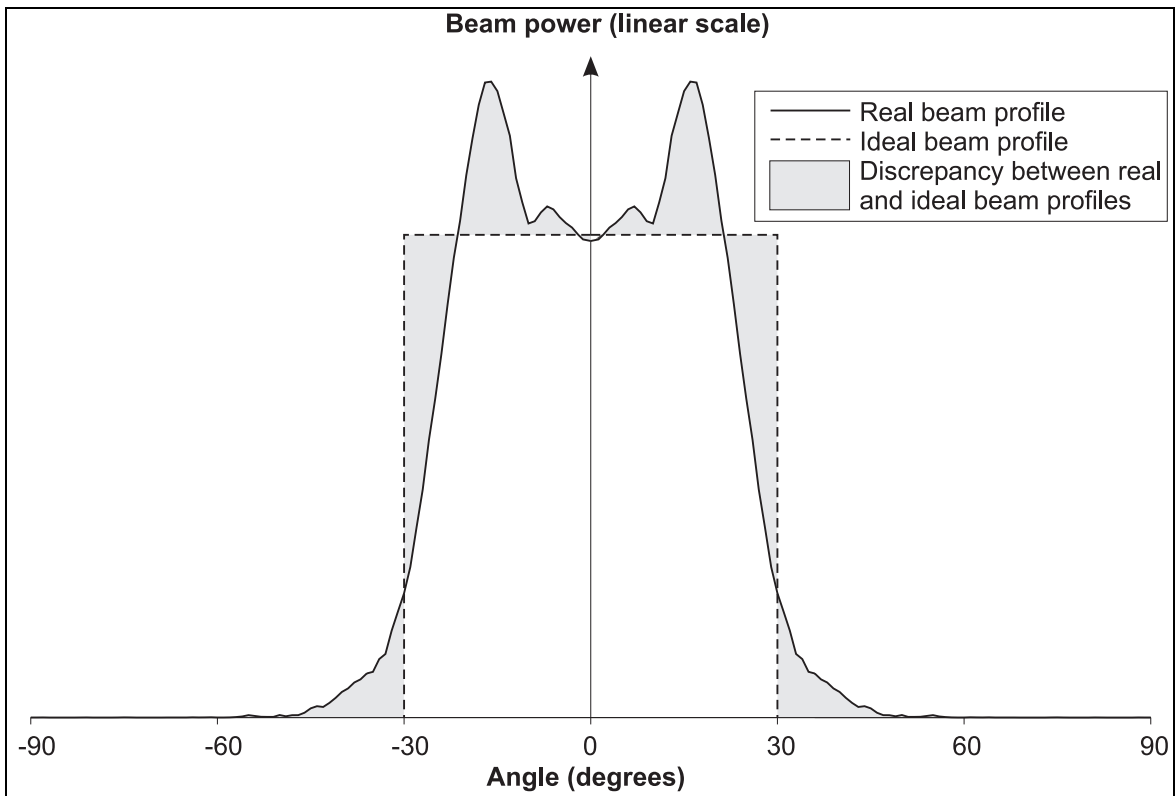


Figure 6.25 Schematic diagram illustrating the discrepancy between the actual and ideal angular beam profiles from a curved finger IDT.

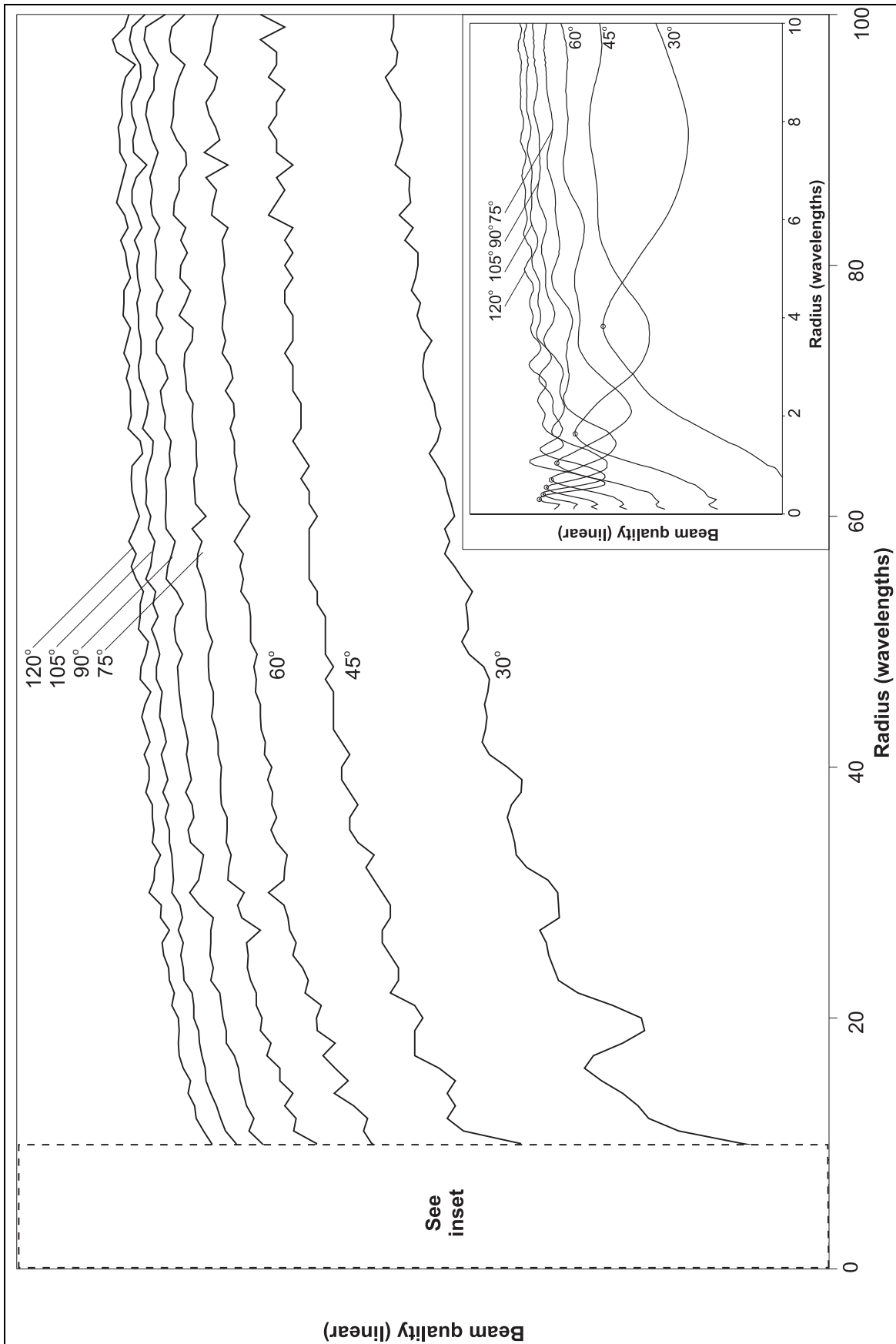


Figure 6.26 Predicted beam quality of a single curved finger IDT as a function of radius of finger for various angles of finger. The critical radius is indicated by circles in the inset graph of the low radius region.

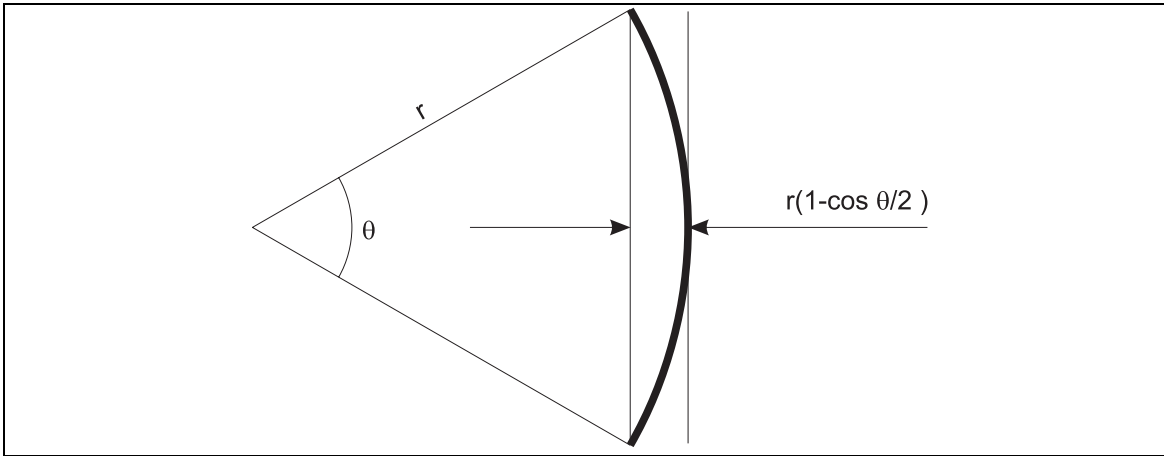


Figure 6.27 Critical radius of a single curved finger.

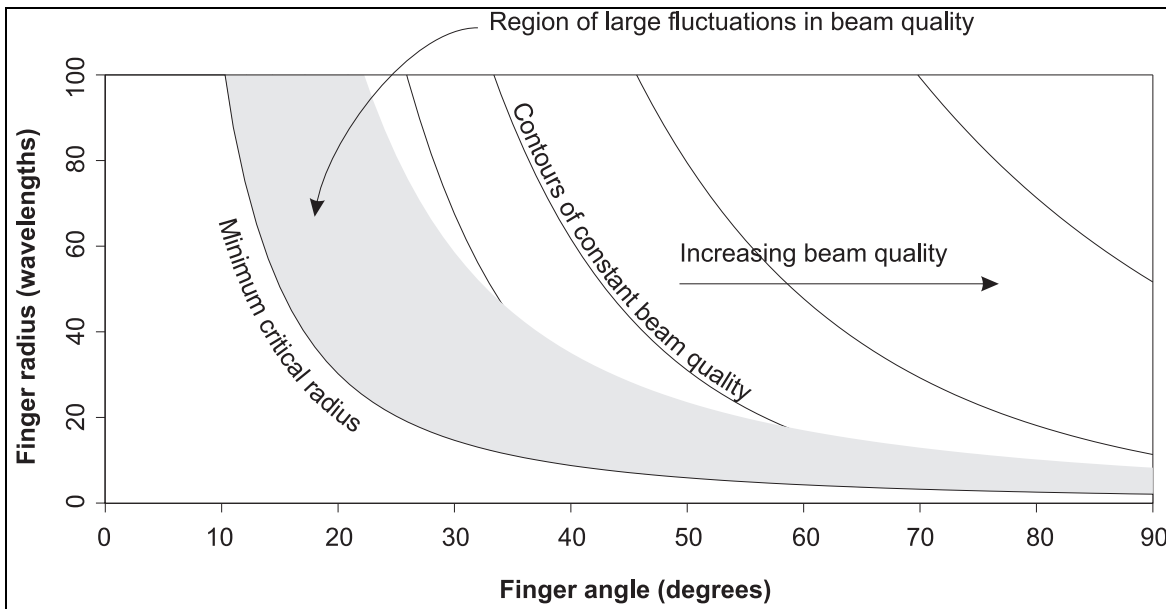


Figure 6.28 Radius and angle combinations required to produce particular beam qualities for an IDT with a single curved finger. The critical radius is also plotted.

## 7. Conclusions and future work

---

### 7.1 REVIEW OF THESIS

This thesis has investigated several fundamental areas relevant to the general title ‘Lamb wave inspection of large structures using permanently attached transducers’.

In chapter 2, Lamb wave theory was reviewed and two new areas were analysed. The first of these concerned the development of equations which cover guided wave propagation in curved plates. The second was an examination of the effect of dispersion on long range inspection using Lamb waves. Several methods of making quantitative comparisons of the degree of dispersion at different points on dispersion curves were presented.

Chapter 3 described the development of a one-dimensional model for a layered bulk wave transducer system. This model was validated using 110  $\mu\text{m}$  thick PVDF film which was taken as a candidate material from which to construct permanently attached transducers. The one-dimensional model was subsequently used in chapters 4 and 6 as a tool for predicting the frequency response of inter-digital transducers (IDTs).

The first generation of high frequency PVDF IDTs to transmit and receive Lamb waves at frequencies above 750 kHz was described in chapter 4. A modified form of Lamb wave phase velocity dispersion curves plotted on dimensionless logarithmic axes was introduced as a tool to assist in the initial design of an IDT to select a particular mode. Results were presented which demonstrated the use of these IDTs to transmit and receive the  $A_0$  mode in 1-2 mm thick plates, and to transmit and receive the  $A_2$  and  $S_4$  modes in 6.5 mm thick ductile iron pipe.

The development and validation of a model based on Huygens’ principle for predicting the acoustic field for different IDT finger geometries was described in chapter 5. The development of this model required an analytical investigation of the excitability of different Lamb wave modes in order to be able to predict the axi-symmetric acoustic field generated by the application of a time dependent point force normal to the surface of a plate.

Chapter 6 returned to the subject of IDT construction, this time describing the development of low frequency PVDF IDTs for transmitting and receiving the  $A_0$  mode in thicker structures. Results were presented which illustrated the operation of these IDTs on a 12.65 mm thick aluminium beam at around 100 kHz and on a 5 mm thick aluminium plate at around 65 kHz. On the latter structure, a four phase IDT was described which could transmit a uniformly divergent acoustic beam from one side of the transducer only. The remainder of chapter 6 described experiments performed with very simple low frequency IDTs, the results from which were used in conjunction with predictions obtained from Huygens’ model to elucidate some general guidelines for the geometry of IDT fingers. As part of this experimental work, an improved technique was developed for measuring the strength of the acoustic field at a point in a plate.

## 7.2 SUMMARY OF FINDINGS

### 7.2.1 *Effect of curvature on Lamb wave propagation*

The phase velocity curves for wave propagation in curved plates appear very similar to those for a flat plate except when the ratio of the radius of curvature to the plate thickness is below around 5:1. However, the group velocity dispersion curves for a curved plate show much larger deviations from those for a flat plate, even when the radius of curvature to the plate thickness is around 10:1. This is caused by some of the mode crossing points in phase velocity space changing to being points of mode repulsion for curved plates even when the curvature is only moderate. As the curvature is increased, the repulsion and mode separation in these locations becomes greater and readily visible on the phase velocity dispersion curves.

### 7.2.2 *Effect of dispersion on Lamb wave propagation*

Previous workers (Alleyne and Cawley 1992) have suggested that the points of maximum group velocity on Lamb wave dispersion curves are ideal operating points from the point of view of obtaining long range propagation with minimum dispersion. Here various measures have been proposed which enable the amount of dispersion at different points to be quantitatively compared. Firstly a quantity called dispersivity has been suggested as a measure of the rate of spatial spreading of a single mode Lamb wave signal as it propagates. This has been used to look at the original group velocity dispersion curves in two different ways: for input signals of constant duration they should be plotted on a linear frequency axis and for input signals of fixed shape (i.e. tonebursts with a fixed number of cycles) they should be plotted on a logarithmic frequency axis. The former case agrees with the original view that all points of maximum group velocity are potential low dispersion operating points, but only on the extra condition that the number of cycles used in input signals must be increased roughly in proportional to the operating frequency. On the other hand, the latter case favours the lower order modes and of particular interest is the fundamental  $A_0$  mode at low frequencies, which on a logarithmic frequency axis appears to have a surprisingly slowly changing group velocity. This result indicates that the  $A_0$  mode can be used for long range testing over a wide range of frequencies rather than just at the frequency of maximum group velocity.

For a particular propagation distance, it has been shown that there is a minimum resolvable distance associated with every point on the dispersion curves and a corresponding optimum shape of input signal required to achieve this. The minimum resolvable distance can be used as an unambiguous measure of the relative resolution which may obtainable at any point on the dispersion curves for a given propagation distance.

### 7.2.3 *Inter-digital transducers*

Although the first generation of IDTs worked very well as transmitters and receivers of the  $A_0$  mode in 1-2 mm thick plates, their frequency response restricted them to higher order modes when used on thicker structures. Although some success was demonstrated when using these transducers to transmit and receive the  $A_2$  and  $S_4$  modes in a 6.5 mm thick ductile iron pipe, serious problems of achieving modal selectivity were encountered.

Attenuation was also shown to severely limit the propagation distance of these modes even in an air-loaded structure. From these results, it has been concluded that the use of higher order Lamb wave modes is not likely to be suitable for long range inspection purposes. If only lower order modes are used, it is clear that the operating frequencies associated with transducers must be reduced as the thickness of plates is increased.

### 7.2.4 *Inspection of thick plate-like structures*

For low profile IDTs generating out-of-plane surface tractions, it has been shown that the operating frequency can be reduced by using a thin layer of dense backing material behind the piezoelectric layer to provide mass loading. The successful use of PVDF IDTs of this construction has been demonstrated at frequencies as low as 65 kHz. It is hoped that similar techniques of improving the low frequency response could be directly applied to other piezoelectric materials suitable for IDTs such as 0-3 composites (Tran-Huu-Hue *et al.* 1997) and ceramic platelet matrices (Gachagan *et al.* 1996). It has also been shown that with careful design, a curved finger IDT driven from a four phase signal source can be constructed that will emit a uniformly divergent beam from one side of the transducer only. Such an acoustic field pattern would be ideal for monitoring a sector of a structure.

### 7.2.5 *Huygens' modelling of the field from inter-digital transducers*

A model based on Huygens' principle has been shown to be a fast and accurate method of predicting the acoustic field generated by an IDT, subject to the IDT satisfying the assumption that waves which pass beneath it are not significantly affected by the presence of the IDT.

Using this model and experimental data, the design of straight and curved finger IDTs has been investigated in more detail. It has been shown that a single straight finger of an IDT is the Lamb wave analogue of a conventional plane bulk wave transducer. The beam divergence angle associated with such a finger can be calculated using a similar formula to that which is used to calculate the beam divergence angle from a conventional transducer. The use of an IDT with multiple fingers of equal length does not affect the beam divergence angle, nor does it significantly affect the overall acoustic field pattern.

In the case of an IDT with curved fingers generating a divergent beam, the situation is more complicated, and a quantity called the beam quality has been introduced to enable quantitative comparisons to be made between the beams generated by different IDTs. By firstly investigating the acoustic field from a single curved finger, it has been shown that the beam quality tends to improve as either the radius of the finger is increased or the angle subtended by the finger is increased. It also appears that for a given angle of curved finger, there is a minimum radius, below which the finger behaves more like a straight finger. The practical implication for the design of a curved finger IDT to produce a divergent beam over a given angle is that the mean radius of the IDT must be several times greater than the minimum radius required for that angle.

## 7.3 FUTURE WORK

This thesis has investigated some aspects of the basic science necessary for the development of an integral structural inspection system using Lamb waves. Several topics

have been covered in some detail, and in this section future work in these areas is proposed. This section does not attempt to address wider issues necessary for the development of an integral structural inspection system such as telemetry and data processing.

### 7.3.1 *Effect of curvature on Lamb wave propagation*

The dispersion curves for curved plates need validation either experimentally, or more likely, by using finite element modelling. Such validation was not performed at the time when the analytical work was done as the effect of curvature on the phase velocity dispersion curves was minor at the degrees of curvature likely to be encountered in the structures described here. However, the major effect which curvature appears to have on the group velocity dispersion curves definitely warrants further investigation.

A practical use which is envisaged for the phase velocity dispersion curves of plates with varying degrees of curvature is to obtain a first approximation of the likely transmission or reflection coefficients for Lamb waves incident on a fold in an otherwise flat plate. Whether or not the assumption that such coefficients can be inferred from the change in phase velocity between a flat and curved section of plate is correct would again need extensive finite element or experimental validation.

### 7.3.2 *Inter-digital transducers*

In addition to continuing investigations into other piezoelectric materials, the design of IDTs to generate in-plane rather than out-of-plane surface tractions is a high priority. This would increase the number of modes which could be used in long range Lamb wave inspection, and would potentially enable liquid loaded structures such as pipes and oil storage tanks to be inspected. Many options are being considered, including the idea of exploiting Poisson's ratio effects in thin piezoelectric films (including PVDF) in order to obtain the necessary tractions. The use of piezoelectric materials that undergo a shearing rather than expanding motion when an electric field is applied also needs to be examined. Such materials would probably be employed in piezo-ceramic platelet matrices (Gachagan *et al.* 1996) rather than in monolithic form.

### 7.3.3 *Huygens' modelling of inter-digital transducers*

In the work described here, the predictions made using Huygens' model have all used continuous excitation of the IDT in order to calculate the acoustic field strength. This is because if toneburst excitation is used the acoustic field must be recalculated at every instant in time in order to calculate the peak amplitude at each point, which makes the overall calculation take considerably longer. The difference between the acoustic fields predicted by the two methods is usually minimal, but in certain cases it can be significant, particularly when the dimensions of the IDT are large compared to the spatial length of the toneburst. Since toneburst rather than continuous excitation is used in practical applications, this area needs further investigation to determine under exactly what conditions the continuous model ceases to be a valid approximation.

The examination of the acoustic fields from curved finger IDTs needs to be completed by investigating the effect of multiple fingers.

## References

---

Alers (1994) 'Application of special wave modes to industrial inspection problems' *Wave propagation and emerging technologies - ASME AMD - Vol 188*, pp. 1 - 9

Alers and Burns (1987) 'EMAT designs for special applications' *Materials evaluation* **45**, pp. 1184-1189

Alleyne (1991) 'The nondestructive testing of plates using ultrasonic Lamb waves' PhD thesis, Department of Mechanical Engineering, Imperial College of Science, Technology and Medicine, London

Alleyne and Cawley (1992a) 'The interaction of Lamb waves with defects' *IEEE transactions on ultrasonics, ferroelectrics and frequency control* **39**(3), pp. 381-397

Alleyne and Cawley (1992b) 'Optimization of Lamb wave inspection techniques' *NDT and E international* **25**, pp. 11-22

Alleyne and Cawley (1994a) 'The long range detection of corrosion in pipes using Lamb waves' in *Annual review of progress in quantitative NDE* edited by Thompson and Chimenti. Plenum Press, New York

Alleyne and Cawley (1994b) 'The practical excitation and measurement of Lamb waves using piezoelectric transducers' pp. 181-188 in *Annual review of progress in quantitative NDE* edited by Thompson and Chimenti, Plenum Press, New York

Auld (1990) 'Acoustic fields and waves in solids', Krieger Publishing Company, Florida

Bainton, Hillier and Silk (1980) 'An easily constructed, broad bandwidth ultrasonic probe for research purposes AERE-R-9769' United Kingdom Atomic Energy Authority, Harwell

Ball and Shewing (1973) 'Some problems in the use of Lamb waves for the inspection of cold-rolled steel sheet and coil' *Non-destructive Testing* **3**(6)

Blanquet, Demol and Delebarre (1996) 'Application of array transducers to health monitoring of aeronautic structures' presented at *World Conference on Non-destructive Testing*, New Delhi, India.

Brekhovskikh and Goncharov (1985) 'Mechanics of continua and wave dynamics'. Springer-Verlag, Berlin

Brown and Carlson (1989) 'Ultrasound transducer models for piezoelectric polymer films' *IEEE transactions on ultrasonics, ferroelectrics and frequency control* **36**(3), pp. 313-318

Brown and Mason (1995) 'Disposable PVDF ultrasonic transducers for non-destructive testing applications' presented at *IEEE ultrasonics symposium*

Bui, Shaw and Zitelli (1977) 'Study of acoustic wave resonance in piezoelectric PVF2 film' *IEEE transactions on sonics and ultrasonics* **SU-24**(5), pp. 331-336

Chen and Payne (1995) 'Industrial applications of piezoelectric polymer transducers' *Measurement science technology* **6**, pp. 249-267

Chen (1983) 'Analysis of the high-field losses of polyvinylidene fluoride transducers' *IEEE transactions on sonics and ultrasonics* **SU-30**(4), pp. 238-249

Chimenti and Nayfeh (1990) 'Ultrasonic reflection and guided wave propagation in biaxially laminated composite plates' *Journal of the acoustical society of America* **87**(4), pp. 1409-1415

Chimenti and Lobkis (1997) 'Effect of rough surfaces on guided waves in plates' pp. 169-176 in *Annual review of progress in quantitative NDE* edited by Chimenti and Thompson, Plenum Press, New York

Clark (1998) 'Smart materials: the spatially resolved chemistry dimension' presented at *How intelligent are smart materials*, IMechE Headquarters, IMechE, London

Datta, Al-Nasser and Shah (1991) 'Lamb wave scattering by a surface breaking crack in a plate' pp. 97-104 in *Annual review of progress in quantitative NDE* edited by Thompson and Chimenti, Plenum Press, New York

Degertekin and Khuri-Yakub (1996) 'Single mode Lamb wave excitation in thin plates by Hertzian contacts' *Applied physics letters* **69**(2), pp. 146-148

Demol, Blanquet and Delebarre (1996) 'Optimization of linear array transducers for Lamb waves in composite plates' presented at *World conference on non-destructive testing*, New Delhi, India.

Desilets, Fraser and Kino (1978) 'The design of efficient broad-band piezoelectric transducers' *IEEE transactions on sonics and ultrasonics* **SU-25**(3), pp. 115-125

Dias, Das-gupta, Hinton and Shufford (1993) 'Polymer/ceramic composites for piezoelectric sensors' *Sensors and actuators* **A37**(38), pp. 343-347

Ditri, Rose and Pilarski (1993) 'Generation of guided waves in hollow cylinders by wedge and comb type transducers' pp. 211-218 in *Annual review of progress in quantitative NDE* edited by Thompson and Chimenti, Plenum Press, New York

Ditri, Pilarski, Rose and Pavlakovic (1994a) 'Generation of guided waves in a plate by axisymmetric normal surface loading' pp. 133-140 in *Annual review of progress in quantitative NDE* edited by Thompson and Chimenti, Plenum Press, New York

- Ditri and Rose (1994b) 'Excitation of guided waves in generally anisotropic layers using finite sources' *Journal of applied mechanics* **61**, pp. 330-338
- Epstein (1976) 'Circumferential waves in composite circular cylinder' *Journal of sound and vibration* **48**(1), pp. 57-71
- Epstein (1979) 'Circumferential waves for a cylindrical shell in smooth contact with a continuum' *Journal of sound and vibration* **64**(2), pp. 209-221
- Evans (1997) 'The use of diffuse field measurements for acoustic emission' PhD thesis, Department of Mechanical Engineering, Imperial College of Science, Technology and Medicine, London
- Farlow and Hayward (1994) 'Real-time ultrasonic techniques suitable for implementing non-contact NDT systems employing piezoceramic composite transducers' *Insight* **36**(12), pp. 926-935
- Fitch (1963) 'Observation of elastic-pulse propagation in axially symmetric and nonaxially symmetric longitudinal modes of hollow cylinders' *Journal of the acoustical society of America* **35**(5), pp. 706-708
- Freedman (1990a) 'The variation with the Poisson ratio of Lamb Modes in a free plate. 1. General spectra' *Journal of sound and vibration* **137**(2), pp. 209-230
- Freedman (1990b) 'The variation with the Poisson ratio of Lamb Modes in a free plate. 2. At transitions and coincidence values' *Journal of sound and vibration* **137**(2), pp. 231-248
- Freedman (1990c) 'The variation with the Poisson ratio of Lamb Modes in a free plate. 3. Behaviour of individual modes' *Journal of sound and vibration* **137**(2), pp. 249-266
- Gachagan, Reynolds, Hayward and McNab (1996) 'Construction and evaluation of a new generation of flexible ultrasonic transducers' *IEEE Ultrasonics Symposium*, pp. 1-4
- Gazis (1958) 'Exact analysis of the plane-strain vibrations of thick-walled hollow cylinders' *Journal of the acoustical society of America* **30**(8), pp. 786-794
- Gazis (1959) 'Three dimensional investigation of the propagation of waves in hollow circular cylinders' *Journal of the acoustical society of America* **31**(5), pp. 568-578
- Greenspan (1987) 'The NBS conical transducer: analysis' *Journal of the acoustical society of America* **81**(1), pp. 173-183
- Guo and Cawley (1992) 'Lamb waves for the NDE of composite laminates' pp. 1443-1450 in *Review of progress in quantitative NDE* edited by Thompson and Chimenti, Plenum Press, New York
- Haskell (1953) 'The dispersion of surface waves on multi-layered media' *Bulletin of the American seismological society* **43**, pp. 17-34

- Hassan and Nagy (1997) 'Circumferential creeping waves around a fluid-filled cylindrical cavity in an elastic medium' *Journal of the acoustical society of America* **101**(5), pp. 2496-2503
- Hayward, McLeod and Durrani (1984) 'A systems model of the thickness mode piezoelectric transducer' *Journal of the acoustical society of America* **76**(2), pp. 369-382
- Hayward and Hossack (1990) 'Unidimensional modelling of 1-3 composite transducers' *Journal of the acoustical society of America* **88**(2), pp. 599-608
- Hitchings (1997) 'FE77 user manual version 2.45' Imperial College of Science Technology and Medicine, London
- Howatson, Lund and Todd (1972) 'Engineering tables and data' Chapman and Hall, London
- Jia (1996) 'Modal analysis of lamb wave generation in elastic plates by liquid wedge transducers' *Journal of the acoustical society of America* **101**(2), pp. 834-842
- Jin and Joshi (1991) 'Coupling of interdigital transducer to ultrasonic Lamb waves' *Applied physics letters* **58**(17), pp. 1830-1832
- Kaduchak and Marston (1995) 'Traveling wave decomposition of surface displacements associated with scattering by a cylindrical shell: numerical evaluation displaying guided forward and backward wave properties' *Journal of the acoustical society of America* **98**(6), pp. 3501-3507
- Kawai (1969) 'The piezoelectricity of poly (vinylidene fluoride)' *Japanese journal of applied physics* **8**, pp. 975-976
- Kawald, Desmet, Lauriks, Glorieux and Thoen (1996) 'Investigation of the dispersion relations of surface acoustic waves propagating on layered cylinder' *Journal of the acoustical society of America* **99**(2), pp. 926-930
- Khuri-Yakub, Pei and Degerketin (1996) 'In situ simultaneous measurement of temperature and thin film thickness with ultrasonic techniques' presented at *Non-destructive evaluation for process control and manufacturing*, Scottsdale, Arizona, SPIE, USA.
- Kimura and Ohigashi (1988) 'Analysis of impulse response characteristics of polymer ultrasonic transducers' *Japanese journal of applied physics* **27**(4), pp. 540-546
- Kino (1987) 'Acoustic waves: devices, imaging and analogue signal processing', Prentice-Hall Inc, New Jersey
- Krautkramer and Krautkramer (1983) 'Ultrasonic testing of materials', Springer-Verlag, Berlin, Heidelberg, New York

- Kumar (1971) 'Flexural vibrations of fluid-filled circular cylindrical shells' *Acoustia* **24**, pp. 137-146
- Kumar (1972) 'Dispersion of axially symmetric waves in empty and fluid-filled cylindrical shells' *Acoustia* **27**(6), pp. 317-329
- Lamb (1917) 'On waves in an elastic plate' pp. 114-128 in *Proceedings of the royal society* **93**(PT Series A), London
- Leedom, Krimholtz and Matthaei (1971) 'Equivalent circuits for transducers having arbitrary even or odd-symmetry piezoelectric excitation' *IEEE transactions on sonics and ultrasonics* **SU18**(3), pp. 128-141
- Lehfeltdt and Holler (1967) 'Lamb waves and lamination detection' *Ultrasonics*, pp. 255-257
- Leung and Yung (1980) 'Internal losses in polyvinylidene fluoride (PVF2) ultrasonic transducers' *Journal of applied physics* **50**, pp. 8031-8033
- Lewis (1980) 'A matrix technique for analysing the performance of multilayered front matched and backed piezoceramic transducers' pp. 395-416 in *Acoustical imaging* **8**(4), Plenum Press, New York
- Lockett (1973) 'Lamb and torsional waves and their use in flaw detection in tubes' *Ultrasonics*, pp. 31-37
- Lockwood and Foster (1994) 'Modelling and optimization of high frequency ultrasound transducers' *IEEE transactions on ultrasonics, ferroelectrics and frequency control* **41**(2), pp. 225-230
- Lowe (1995) 'Matrix techniques for modelling ultrasonic waves in multilayered media' *IEEE transactions on ultrasonics, ferroelectrics and frequency control* **42**(4), pp. 525-542
- Mal, Xu and Bar-Cohen (1990) 'Leaky Lamb waves for the ultrasonic non-destructive evaluation of adhesive bonds' *Journal of engineering materials & technology* **112**(3), pp. 255-259
- Malvern (1969) 'Introduction to the mechanics of a continuous medium' Prentice-Hall, New Jersey
- Mason (1948) 'Electromechanical transducers and wave filters' Van Nostrand, New York
- Mattiocco, Dieulesaint and Ryer (1980) 'PVF2 transducers for Rayleigh waves' *Electronic letters* **16**(7), pp. 250-251
- Maxfield, Kuramoto and Hulbert (1987) 'Evaluating EMAT designs for selected application' *Materials evaluation* **45**, pp. 1166-1183

Metsaveer and Klauson (1996) 'Influence of the curvature on the dispersion curves of a submerged cylindrical shell' *Journal of the acoustical society of America* **100**(3), pp. 1551-1560

Monkhouse, Wilcox and Cawley (1997a) 'Flexible interdigital PVDF Lamb wave transducers for the development of smart structures' pp. 877-884 in *Annual review of progress in quantitative NDE* edited by Chimenti and Thompson, Plenum Press, New York

Monkhouse, Wilcox and Cawley (1997b) 'Flexible interdigital PVDF transducers for the generation of Lamb waves in structures' *Ultrasonics* **35**, pp. 489-498

Murayama, Fujisawa, Fukuoka and Hirao (1996) 'Development of an on-line evaluation system of formability in cold-rolled steel sheets using electromagnetic acoustic transducers (EMATs)' *NDT and E international* **29**(3), pp. 141-146

Numerich and Dale (1984) 'Generation and exploitation of plate waves in submerged, air-filled shells' *Advances in fluid structures interaction (ASME)* **64**, pp. 59-74

Ohigashi (1976) 'Electromechanical properties of polarized polyvinylidene fluoride films as studied by the piezoelectric resonance method' *Journal of applied physics* **47**(3), pp. 949-955

Ohigashi, Itoh, Kimura, Nakanishi and Suzuki (1988) 'Analysis of frequency response characteristics of polymer ultrasonic transducers' *Japanese journal of applied physics* **27**(3), pp. 354-360

Ohigashi, Koga, Suzuki, Nakanishi, Kimura and Hashimoto (1984) 'Piezoelectric and ferroelectric properties of P(VDF-TrFE) copolymers and their application to ultrasonic transducers' *Ferroelectrics* **60**, pp. 263-276

Pao and Mindlin (1960) 'Dispersion of flexural waves in an elastic, circular cylinder' *Journal of applied mechanics* **27**, pp. 513-520

Pavlakovic, Lowe, Alleyne and Cawley (1997) 'Disperse: a general purpose program for creating dispersion curves' pp. 155-192 in *Annual review of progress in quantitative NDE* edited by Thompson and Chimenti, Plenum Press, New York

Qu, Berthelot and Li (1996) 'Dispersion of guided circumferential waves in a circular annulus' pp. 169-176 in *Annual Review of Progress in Quantitative NDE* edited by Thompson and Chimenti, Plenum Press, New York

Rayleigh (1885) 'On waves propagating along the plane of an elastic solid' *Proceedings of the London mathematical society* **17**

Rose (1995) 'Recent advances in guided wave NDE' presented at *IEEE ultrasonics symposium*, Seattle, IEEE, USA

- Rose, Jiao and Spanner (1996) 'Ultrasonic guided wave NDE for piping' *Materials evaluation* **54**(11), pp. 1310-1313
- Rulf (1968) 'Rayleigh waves on curved surfaces' *Journal of the acoustical society of America* **45**(2), pp. 493-499
- Sachse and Hsu (1979) 'Ultrasonic transducers for materials testing and their characterisation' pp. 277-406 in *Physical acoustics* **14**, Academic, New York
- Safaenili, Lobkis and Chimenti (1995) 'Air-coupled ultrasonic characterisation of composite plates' *Material evaluation* **53**(10), pp. 1186-1190
- Silk (1983) 'Extended model of the ultrasonic transducer' *Measurement science instrumentation* **16**, pp. 879-887
- Silk (1984) 'Ultrasonic transducers for nondestructive testing' Adam Hilger Ltd, Bristol
- Sittig (1967) 'Transmission parameters of thickness driven piezoelectric transducers arranged in multilayer configurations' *IEEE transactions on sonics and ultrasonics* **SU14**(4), pp. 167-174
- Swartz and Plummer (1980) 'On the generation of high frequency acoustic energy with polyvinylidene fluoride' *IEEE transactions on sonics and ultrasonics* **SU27**(6), pp. 295-303
- Szilard (1980) 'Ultrasonic testing' John Wiley and Sons, New York
- Thompson, Elsley, Peterson and Vasile (1979) 'An EMAT system for detecting flaws in steam generator tubes' *Ultrasonics symposium*, pp. 246-249
- Thomson (1950) 'Transmission of elastic waves through a stratified solid medium' *Journal of applied physics* **21**, pp. 89-93
- Toda and Ikenohira (1980) 'Highly temperature dependant performance of a polyvinylidene Lamb wave device' *Journal of applied physics* **51**(11), pp. 5657-5660
- Toda and Sawaguchi (1992) 'Ultrasonic system for detecting defects in IC package using leaky Lamb wave device' *Non-destructive testing evaluation* **10**, pp. 137-144
- Tran-Huu-Hue, Levassort, Lethiecq, Certon and Patat (1997) 'Characterisation of the piezoelectric and dielectric relaxation parameters of 0-3 composites and PVDF materials in the thickness mode' *Ultrasonics* **35**, pp. 317-324
- Viktorov (1967) 'Rayleigh and Lamb waves: Physical theory and applications' Plenum Press, New York
- Viktorov, Zubova and Kaekina (1965) 'Investigation of Lamb wave excitation by the "wedge" method' *Soviet physics - acoustics* **10**(4), pp. 354-359

Whittington (1989) 'EMAT - generated Lamb waves applied to hot aluminium strip profile measurement with temperature compensation' *British journal of nondestructive testing* **31**(3)

Wilcox, Monkhouse, Cawley, Lowe and Auld (1998a) 'Development of a computer model for an ultrasonic polymer film transducer system' *NDT and E international* **31**(1), pp. 51-64

Wilcox, Monkhouse, Lowe and Cawley (1998b in press) 'The use of Huygens' principle to model the acoustic field from inter-digital Lamb wave transducers' in *Annual review of progress in quantitative NDE* edited by Chimenti and Thompson, Plenum Press, New York

Wolf (1990) 'The life and work of Christiaan Huygens' presented at *Huygens' principle 1690-1990: theory and applications*, Elsevier, Holland.

Worlton (1961) 'Experimental confirmation of Lamb waves at megacycle frequencies' *Journal of applied physics* **32**(6), pp. 967-971

## Appendix A: Equations for wave propagation in a curved plate

---

The following potential functions were shown to satisfy the wave equation (equation 2.11):

$$\begin{aligned}\phi &= \left( A^{l+} H_{k_\theta}^{(1)}(rk_l) + A^{l-} H_{k_\theta}^{(2)}(rk_l) \right) \exp i(k_\theta \theta - \omega t) \\ \psi_z &= \left( A^{t+} H_{k_\theta}^{(1)}(rk_t) + A^{t-} H_{k_\theta}^{(2)}(rk_t) \right) \exp i(k_\theta \theta - \omega t)\end{aligned}\quad (\text{A.1})$$

where  $r$  is the radial coordinate,  $\theta$  is the angular coordinate,  $k_l$  is the bulk longitudinal wavenumber,  $k_t$  is the bulk transverse wavenumber,  $k_\theta$  is the angular wavenumber,  $\omega$  is the circular frequency,  $t$  is the time and the values of  $A^{l+}$ ,  $A^{l-}$ ,  $A^{t+}$  and  $A^{t-}$  are the amplitudes of longitudinal and transverse partial waves. From these, the particle displacement fields may be calculated from the definition of the potential functions:

$$\begin{aligned}u_r &= \frac{\partial \phi}{\partial r} + \frac{1}{r} \frac{\partial \psi_z}{\partial \theta} \\ u_\theta &= \frac{1}{r} \frac{\partial \phi}{\partial \theta} - \frac{\partial \psi_z}{\partial r} \\ u_z &= 0\end{aligned}\quad (\text{A.2})$$

To obtain:

$$\begin{aligned}u_r &= \frac{\omega r^2}{2v_l} \left[ J_{k_\theta-1}(\omega r/v_l) - J_{k_\theta+1}(\omega r/v_l) \right] A^{l+} \\ &+ \frac{\omega r^2}{2v_l} \left[ Y_{k_\theta-1}(\omega r/v_l) - Y_{k_\theta+1}(\omega r/v_l) \right] A^{l-} \\ &+ ik_\theta r J_{k_\theta}(\omega r/v_l) A^{t+} \\ &+ ik_\theta r Y_{k_\theta}(\omega r/v_l) A^{t-}\end{aligned}\quad (\text{A.3})$$

and

$$\begin{aligned}u_\theta &= ik_\theta r J_{k_\theta}(\omega r/v_l) A^{l+} \\ &+ ik_\theta r Y_{k_\theta}(\omega r/v_l) A^{l-} \\ &- \frac{\omega r^2}{2v_t} \left[ J_{k_\theta-1}(\omega r/v_t) - J_{k_\theta+1}(\omega r/v_t) \right] A^{t+} \\ &- \frac{\omega r^2}{2v_t} \left[ Y_{k_\theta-1}(\omega r/v_t) - Y_{k_\theta+1}(\omega r/v_t) \right] A^{t-}\end{aligned}\quad (\text{A.4})$$

The displacement field is the first of the two fields which is required in order to solve multi-layered propagation problems using the global matrix method. The second field required is the stress field and this is obtained firstly by calculating the strain field from the displacement field using:

$$\begin{aligned}
 \varepsilon_{rr} &= \frac{\partial u_r}{\partial r} \\
 \varepsilon_{\theta\theta} &= \frac{u_r}{r} + \frac{1}{r} \frac{\partial u_\theta}{\partial \theta} \\
 \varepsilon_{r\theta} &= \frac{\partial u_\theta}{\partial r} - \frac{u_\theta}{r} + \frac{1}{r} \frac{\partial u_r}{\partial \theta}
 \end{aligned} \tag{A.5}$$

The stress field is calculated from the strain field using Hooke's law (Howatson *et al.* 1972):

$$\begin{aligned}
 \sigma_{rr} &= \lambda(\varepsilon_{rr} + \varepsilon_{\theta\theta} + \varepsilon_{zz}) + 2\mu\varepsilon_{rr} \\
 \sigma_{\theta\theta} &= \lambda(\varepsilon_{rr} + \varepsilon_{\theta\theta} + \varepsilon_{zz}) + 2\mu\varepsilon_{\theta\theta} \\
 \sigma_{zz} &= \lambda(\varepsilon_{rr} + \varepsilon_{\theta\theta} + \varepsilon_{zz}) + 2\mu\varepsilon_{zz} \\
 \sigma_{r\theta} &= \mu\varepsilon_{r\theta} \\
 \sigma_{rz} &= \mu\varepsilon_{rz} (= 0) \\
 \sigma_{\theta z} &= \mu\varepsilon_{\theta z} (= 0)
 \end{aligned} \tag{A.6}$$

Which yields:

$$\begin{aligned}
 \sigma_{rr} &= \left[ \begin{aligned} &-k_\theta^2 \lambda J_{k_\theta}(\omega r/v_l) + \frac{\lambda \omega r}{2v_l} \{J_{k_\theta-1}(\omega r/v_l) - J_{k_\theta+1}(\omega r/v_l)\} \\ &+ \frac{(\lambda + 2\mu)\omega^2 r^2}{4v_l^2} \{J_{k_\theta-2}(\omega r/v_l) - 2J_{k_\theta}(\omega r/v_l) + J_{k_\theta+2}(\omega r/v_l)\} \end{aligned} \right] A^{l+} \\
 &+ \left[ \begin{aligned} &-k_\theta^2 \lambda Y_{k_\theta}(\omega r/v_l) + \frac{\lambda \omega r}{2v_l} \{Y_{k_\theta-1}(\omega r/v_l) - Y_{k_\theta+1}(\omega r/v_l)\} \\ &+ \frac{(\lambda + 2\mu)\omega^2 r^2}{4v_l^2} \{Y_{k_\theta-2}(\omega r/v_l) - 2Y_{k_\theta}(\omega r/v_l) + Y_{k_\theta+2}(\omega r/v_l)\} \end{aligned} \right] A^{l-} \\
 &+ \left[ -2ik_\theta \mu J_{k_\theta}(\omega r/v_t) + \frac{ik_\theta \mu \omega r}{v_t} \{J_{k_\theta-1}(\omega r/v_t) - J_{k_\theta+1}(\omega r/v_t)\} \right] A^{t+} \\
 &+ \left[ -2ik_\theta \mu Y_{k_\theta}(\omega r/v_t) + \frac{ik_\theta \mu \omega r}{v_t} \{Y_{k_\theta-1}(\omega r/v_t) - Y_{k_\theta+1}(\omega r/v_t)\} \right] A^{t-}
 \end{aligned} \tag{A.7}$$

and

$$\begin{aligned}
 \sigma_{r\theta} = & \left[ -2ik_{\theta}\mu J_{k_{\theta}}(\omega r/v_l) + \frac{ik_{\theta}\mu\omega r}{v_l} \{J_{k_{\theta}-1}(\omega r/v_l) - J_{k_{\theta}+1}(\omega r/v_l)\} \right] A^{l+} \\
 & + \left[ -2ik_{\theta}\mu Y_{k_{\theta}}(\omega r/v_l) + \frac{ik_{\theta}\mu\omega r}{v_l} \{Y_{k_{\theta}-1}(\omega r/v_l) - Y_{k_{\theta}+1}(\omega r/v_l)\} \right] A^{l-} \\
 & + \left[ \begin{aligned} & -k_{\theta}^2 \lambda J_{k_{\theta}}(\omega r/v_t) + \frac{\lambda\omega r}{2v_t} \{J_{k_{\theta}-1}(\omega r/v_t) - J_{k_{\theta}+1}(\omega r/v_t)\} \\ & + \frac{(\lambda + 2\mu)\omega^2 r^2}{4v_t^2} \{J_{k_{\theta}-2}(\omega r/v_t) - 2J_{k_{\theta}}(\omega r/v_t) + J_{k_{\theta}+2}(\omega r/v_t)\} \end{aligned} \right] A^{t+} \\
 & + \left[ \begin{aligned} & -k_{\theta}^2 \lambda Y_{k_{\theta}}(\omega r/v_t) + \frac{\lambda\omega r}{2v_t} \{Y_{k_{\theta}-1}(\omega r/v_t) - Y_{k_{\theta}+1}(\omega r/v_t)\} \\ & + \frac{(\lambda + 2\mu)\omega^2 r^2}{4v_t^2} \{Y_{k_{\theta}-2}(\omega r/v_t) - 2Y_{k_{\theta}}(\omega r/v_t) + Y_{k_{\theta}+2}(\omega r/v_t)\} \end{aligned} \right] A^{t-}
 \end{aligned} \tag{A.8}$$

The expressions for  $u_r$ ,  $u_{\theta}$ ,  $\sigma_{rr}$  and  $\sigma_{r\theta}$  given by equations A.3, A.4, A.7 and A.8 respectively may now be used to obtain the components,  $a_{ij}$ , in the field matrix for circumferential wave propagation in a cylindrical layer:

$$\begin{bmatrix} u_r \\ u_{\theta} \\ u_z \\ \sigma_{rr} \\ \sigma_{r\theta} \\ \sigma_{rz} \end{bmatrix} = \begin{bmatrix} a_{11} & a_{12} & a_{13} & a_{14} & 0 & 0 \\ a_{21} & a_{22} & a_{23} & a_{24} & 0 & 0 \\ 0 & 0 & 0 & 0 & 0 & 0 \\ a_{41} & a_{42} & a_{43} & a_{44} & 0 & 0 \\ a_{51} & a_{52} & a_{53} & a_{54} & 0 & 0 \\ 0 & 0 & 0 & 0 & 0 & 0 \end{bmatrix} \begin{bmatrix} A^{l+} \\ A^{l-} \\ A^{t+} \\ A^{t-} \\ A^{h+} \\ A^{h-} \end{bmatrix} \tag{A.9}$$

This matrix is in the correct form to be implemented in a global matrix algorithm for computing modal solutions to wave propagation in cylindrical layered systems. For the work described in this thesis, this solution for circumferentially propagating waves has been implemented into *Disperse* (Pavlakovic *et al.* 1997). The terms  $A^{h+}$  and  $A^{h-}$  are the amplitudes of partial transverse waves polarised in the  $z$  direction. These are the curved plate analogue of *SH* waves in a flat plate, and have not been considered here.

## Appendix B: Bandwidths of Hanning windowed tonebursts

---

Consider a Hanning windowed toneburst with centre frequency  $f_0$ ,  $n$  cycles and centred in time at  $t = 0$ . Its duration,  $2\tau$ , is  $n/f_0$  and its shape is thus given by:

$$x(t) = \frac{1}{2} \left[ 1 + \cos\left(\frac{2\pi f_0 t}{n}\right) \right] \sin(2\pi f_0 t) \quad \left. \vphantom{x(t)} \right\} \quad -\tau \leq t \leq \tau \quad (\text{B.1})$$

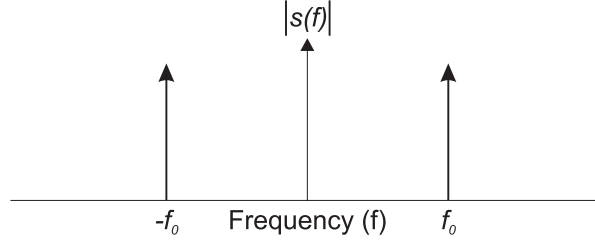
$$= h(t)s(t)$$

where  $h(t)$  is the Hanning envelope, and  $s(t)$  is the pure sine wave. Since this is the product of two functions, the Fourier transform may be expressed as the convolution of the transforms of each of the functions:

$$x(f) = h(f) * s(f) \quad (\text{B.2})$$

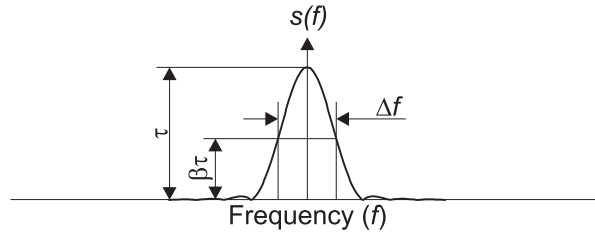
The Fourier transform of the sine wave,  $s(f)$  is given by (Howatson *et al.* 1972):

$$s(f) = j \frac{1}{2} \{ -\delta(f - f_0) + \delta(f + f_0) \} \quad (\text{B.3})$$



and the Fourier transform of the Hanning window is given by (Howatson *et al.* 1972):

$$h(f) = \frac{\sin(2\pi f \tau)}{2\pi f (1 - 4f^2 \tau^2)} \quad (\text{B.4})$$



The bandwidth,  $\Delta f$ , of the Hanning window is defined by the frequencies,  $-\Delta f/2$  and  $\Delta f/2$ , at which the amplitude of  $h(f)$  falls to some (fixed) fraction,  $\beta$ , of its maximum value,  $\tau$ . Thus from equation B.4:

$$\beta\tau = \frac{\sin(\pi\Delta f\tau)}{\pi\Delta f(1 - (\Delta f)^2\tau^2)} \quad (\text{B.5})$$

and so:

$$\beta = \frac{\sin(\pi(\Delta f\tau))}{\pi(\Delta f\tau)(1 - (\Delta f\tau)^2)} \quad (\text{B.6})$$

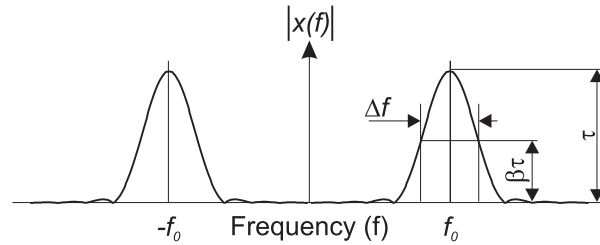
$$= \beta(\Delta f\tau)$$

Thus, for a fixed value of  $\beta$ :

$$\Delta f\tau = k \quad (\text{B.7})$$

where  $k$  is a function of  $\beta$ .

The frequency spectrum of the original signal,  $x(f)$ , given by the convolution described by equation B.2 appears thus:



If the centre frequency,  $f_0$ , is small compared to the bandwidth of  $h(f)$ , then the two portions of  $x(f)$  corresponding to convolution with the two delta functions in equation B.3 may overlap at low frequencies. However, in most cases (typically when the input signal has more than 2 cycles) this overlap may be ignored for the purposes of calculating the bandwidth of  $x(f)$ . Thus equation B.7 may be re-arranged to give the bandwidth of the original toneburst in terms of the number of cycles and the centre frequency:

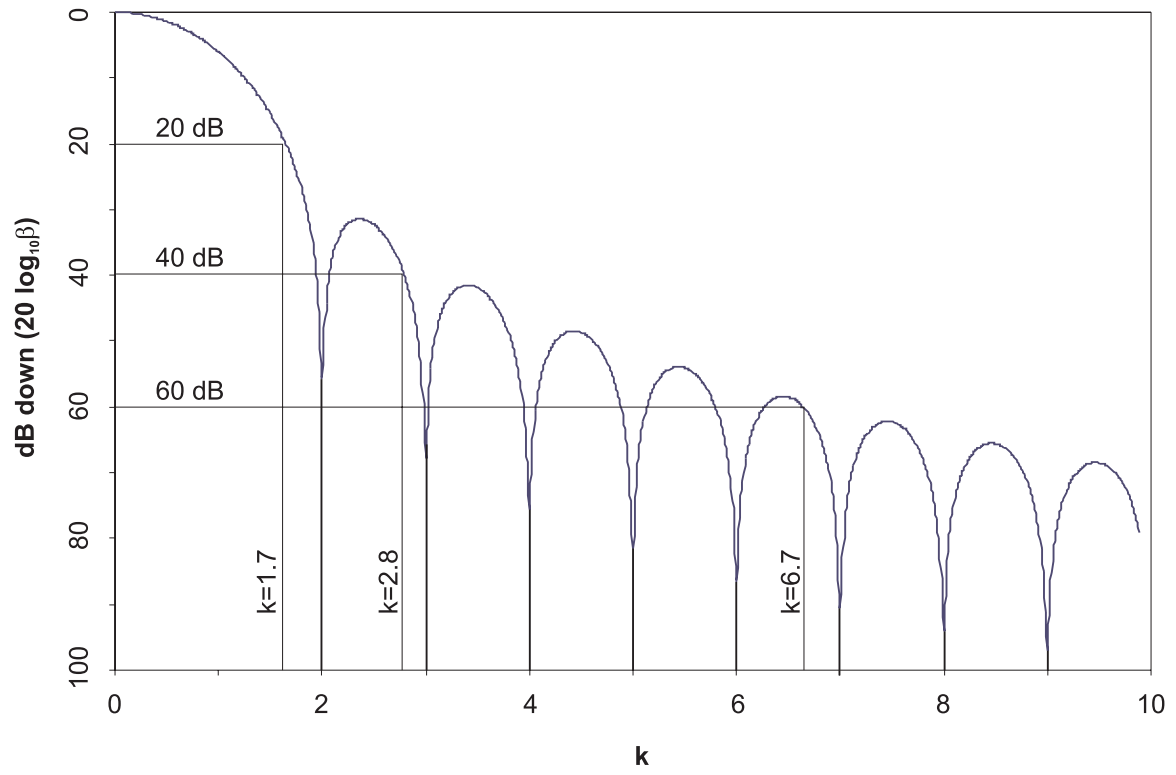
$$\Delta f = \frac{2kf_0}{n} \quad (\text{B.8})$$

Hence the frequency spectrum of the original toneburst is defined by the limits:

$$f_{\min} = f_0 - \frac{\Delta f}{2} = f_0 \left(1 - \frac{k}{n}\right) \quad (\text{B.9})$$

$$f_{\max} = f_0 + \frac{\Delta f}{2} = f_0 \left(1 + \frac{k}{n}\right)$$

And the value of  $k$  necessary for different bandwidth measures may be calculated from equation B.6 as illustrated in the graph below:



## Appendix C: Publications list

---

Wilcox, Castaings, Monkhouse, Cawley and Lowe (1997) 'An example of the use of inter-digital PVDF transducers to generate and receive a high order Lamb wave mode in a pipe' pp 919-926 in *Annual Review of Progress in Quantitative NDE* edited by Chimenti and Thompson. Plenum Press, New York

Wilcox, Monkhouse, Cawley, Lowe and Auld (1998) 'Development of a computer model for an ultrasonic polymer film transducer system' *NDT & E International* **31**(1), pp 51-64

Wilcox, Monkhouse, Lowe and Cawley (1998 in press) 'The use of Huygens' principle to model the acoustic field from inter-digital Lamb wave transducers' in *Annual Review of Progress in Quantitative NDE* edited by Chimenti and Thompson. Plenum Press, New York

Wilcox, Cawley and Lowe (1998 in press) 'New transducers for non-destructive testing: Acoustic fields from inter-digital transducers' *IEE Proceedings - Science, Measurement and Technology*

### **The current author also contributed to the following publications:**

Monkhouse, Wilcox and Cawley (1997) 'Flexible interdigital PVDF Lamb wave transducers for the development of smart structures' pp 877-884 in *Annual Review of Progress in Quantitative NDE* edited by Chimenti and Thompson. Plenum Press, New York

Monkhouse, Wilcox and Cawley (1997) 'Flexible inter-digital PVDF transducers for the generation of Lamb waves in structures' *Ultrasonics* **35**, pp 489-498